EXPLAINING DARK MATTER AND NEUTRINO MASSES BY BEYOND STANDARD MODEL PHYSICS

By
SARIF KHAN
PHYS08201305001

Harish-Chandra Research Institute, Prayagraj

A thesis submitted to the
Board of Studies in Physical Sciences
In partial fulfillment of requirements
for the Degree of
DOCTOR OF PHILOSOPHY
of
HOMI BHABHA NATIONAL INSTITUTE

August, 2019

Homi Bhabha National Institute[1]

Recommendations of the Viva Voce Committee

As members of the Viva Voce Committee, we certify that we have read the dissertation prepared by Sarif Khan entitled "Explaining Dark Matter and Neutrino masses by Beyond Standard Model Physics " and recommend that it may be accepted as fulfilling the thesis requirement for the award of Degree of Doctor of Philosophy.

Chairman - Prof. S. Naik **Date:** 31/10/19
S. Naik

Guide /Convener - Prof. Sandhya Choubey **Date:** 31/10/19
Sandhya Choubey

Examiner - Prof. Sourov Roy Sourov Roy **Date:** 31/10/19

Member 1- Prof. Raj Gandhi **Date:** 31/10/19

Member 2 - Prof. Aseshkrishna Datta **Date:** 31/10/19

Member 3 - Prof. Aditi Sen (De) **Date:** 31/10/19
Aditi Sen (De)

Final approval and acceptance of this thesis is contingent upon the candidate's submission of the final copies of the thesis to HBNI.

I/We hereby certify that I/we have read this thesis prepared under my/our direction and recommend that it may be accepted as fulfilling the thesis requirement.

Date: 31.10.2019

Place: Prayagraj

Sandhya Choubey
Prof. Sandhya Choubey
Guide
31/10/19

---

[1] This page is to be included only for final submission after successful completion of viva voce.

STATEMENT BY AUTHOR

This dissertation has been submitted in partial fulfillment of requirements for an advanced degree at Homi Bhabha National Institute (HBNI) and is deposited in the Library to be made available to borrowers under rules of the HBNI.

Brief quotations from this dissertation are allowable without special permission, provided that accurate acknowledgement of source is made. Requests for permission for extended quotation from or reproduction of this manuscript in whole or in part may be granted by the Competent Authority of HBNI when in his or her judgment the proposed use of the material is in the interests of scholarship. In all other instances, however, permission must be obtained from the author.

Sarif Khan.

Sarif Khan

DECLARATION

I, hereby declare that the investigation presented in the thesis has been carried out by me. The work is original and has not been submitted earlier as a whole or in part for a degree / diploma at this or any other Institution / University.

Sarif Khan
Sarif Khan

List of Publications arising from the thesis

Journal

1. "Galactic gamma ray excess and dark matter phenomenology in a $U(1)_{B-L}$ model", Anirban Biswas, Sandhya Choubey and Sarif Khan, *JHEP*, **2016**, 08, 114.
2. "Neutrino Mass, Dark Matter and Anomalous Magnetic Moment of Muon in a $U(1)_{L_\mu - L_\tau}$ Model", Anirban Biswas, Sandhya Choubey and Sarif Khan, *JHEP*, **2016**, *09*, 147.
3. "FIMP and Muon $(g-2)$ in a $U(1)_{L_\mu - L_\tau}$ Model", Anirban Biswas, Sandhya Choubey and Sarif Khan, *JHEP*, **2017**, *02*, 123.
4. "Neutrino mass, leptogenesis and FIMP dark matter in a $U(1)_{B-L}$ model", Anirban Biswas, Sandhya Choubey and Sarif Khan, *Eur. Phys. J. C*, **2017**, *77 no. 12*, 875.
5. "Explaining the 3.5 keV X-ray Line in a $L_\mu - L_\tau$ Extension of the Inert Doublet Model", Anirban Biswas, Sandhya Choubey, Laura Covi and Sarif Khan, *JCAP*, **2018**, *02*, 002.
6. "Singlet-Triplet Fermionic Dark Matter and LHC Phenomenology", Sandhya Choubey, Sarif Khan, Manimala Mitra and Subhadeep Mondal, *Eur. Phys. J. C*, **2018**, *78 no. 4*, 302.

List of Publications not included in the thesis

1. "Inverse seesaw and dark matter in a gauged B-L extension with flavour symmetry", Anirban Biswas, Sandhya Choubey and Sarif Khan, *JHEP*, **2018**, *08*, 062.
2. "Neutrino and Collider Implications of a Left-Right Extended Zee Model", Sarif Khan, Manimala Mitra and Ayon Patra, *Phys. Rev. D*, **2018**, *98 no. 11*, 115038.
3. "Common origin of baryon asymmetry, dark matter and neutrino mass", Anirban Biswas, Sandhya Choubey, Laura Covi and Sarif Khan, *JHEP*, **2019**, *05*, 193.
4. "Doubly-charged Higgs boson at a future electron-proton collider", P. S. Bhupal Dev, Sarif Khan, Manimala Mitra and Santosh Kumar Rai, *Phys. Rev. D*, **2019**, *99, no. 11*, 115015.
5. "FIMP dark matter candidate(s) in a $B-L$ model with inverse seesaw mechanism", Waleed Abdallah, Sandhya Choubey and Sarif Khan, *JHEP*, **2019**, *06*, 095.

Conferences

1.Invisible 16 School, SISSA, Trieste, Italy, 5-9 September, 2016, presented a poster.

2.Invisible 16 Workshop, INFN Padova, Italy, 12-16 September, 2016, gave a talk and presented a poster.

3.XXII DAE-BRNS HIGH ENERGY PHYSICS SYMPOSIUM 2016, University of Delhi, India, 12-16 December, 2016, presented a poster.

4.Workshop on High Energy Physics Phenomenology XV, 14-23 December 2017, IISER Bhopal, India, gave a talk.

5.Nu HoRIzons VII,21-23 February, 2018,Harish-Chandra Research Institute, Allahabad, India, presented a poster.

6.Invisible 18 School, TUM, Burghausen, Germany, 28 August-1 September, 2018, presented a poster.

7.Invisible 18 Workshop, KIT, Karlsruhe, Germany, 3-7 September, 2018, gave a talk and presented a poster.

8.International Meeting on High Energy Physics-2019, IOP, Bhubaneswar, India, 17-22 January, 2019, gave a talk.

9.Invisible 19 School, LSC, Canfranc, Spain, 3 June-7 June, 2019, presented a poster.

10.Invisible 19 Workshop, IFIC, Valencia, Spain, 10 June-14 June, 2019, presented a poster.

Sarif Khan

Sarif Khan

Dedicated

To the ones I love

ACKNOWLEDGEMENTS

Acknowledging the people is the most difficult thing because there is a fair amount of chance to forget many names who had an impact during this PhD journey of my life. Taking this fact granted I am grateful to all the people whomever I have interacted during my PhD tenure.

First and foremost, I am heartily grateful to my Supervisor Prof. Sandhya Choubey who has helped me in many ways not only just guiding me excellently but also allowed me to think and work independent way. I am indebted to Prof. Sandhya in a great many ways. I have enjoyably passed my PhD journey I could have ever imagined.

Secondly, I owe very special gratitude to Prof. Laura Covi for all the collaborative works and very fruitful discussions that immensely helped me in learning Physics. I am highly grateful to Dr Manimala Mitra for introducing me to the collide physics.

It gives me immense pleasure to thank all my collaborators. I am always thankful to Prof. Santosh Kumar Rai and Dr P. S. Bhupal Dev for giving me the opportunity to learn from them. I am always grateful to Dr Anirban Biswas who has helped me in many ways. I am thankful to Dr Shubhadeep Monadal, Dr Ayon Patra and Dr Waleed Abdallah for the collaborative work.

I sincerely express my gratitude to Prof. Ashoke Sen, Prof. Jayanta K. Bhattacharjee and Dr. Anirban Basu, for the excellent teaching and discussions.

I especially thank all the people whomever I have encountered during my PhD tenure at HRI.

Last but not the least, I am forever grateful to my loving parents and my family members for the patience and support whenever I needed them.

Contents

SUMMARY

Standard model (SM) is a very successful theory of nature which contains three fundamental forces namely the strong force, weak force and electromagnetic force. Particle spectrum of SM has been completed with the discovery of Higgs boson. Despite its tremendous success so far, SM suffers from few drawbacks which need beyond standard model (BSM) physics. The well-known inadequacies of SM which will be addressed in this thesis are the absence of a suitable dark matter (DM) candidate, neutrinos are massless, matter-antimatter asymmetry of the Universe and the disagreement between the experimental and theoretical value of muon $(g-2)$. This thesis deals with the BSM models which are an extension of SM by extra gauge groups such as $U(1)_{B-L}$, $U(1)_{L_\mu-L_\tau}$ or $\mathbb{Z}_2$ and additional particles. By overcoming the SM drawbacks these BSM models always contain a suitable DM candidate which is stable in the Universe time scale. Moreover, we have discussed DM production by two mechanisms, one is the freeze-out mechanism (WIMP, weakly interacting massive particle, type DM) and another one is the freeze-in mechanism (FIMP, feebly interacting massive particle, type DM). In our case as well, WIMP type DM interacts with the visible sector by the usual annihilation or co-annihilation processes mediated by the Higgses and the extra gauge boson. At freeze-out temperature, DM decouples from the cosmic soup and freezes out to that particular value of the co-moving number density which determines its relic density. By choosing the suitable value of the model parameters, we can satisfy the DM relic density, in the resonance regions of the Higgses, in the correct ballpark value put by WMAP and Planck. We have predicted that WIMP type DM can be tested in future at different direct detection, indirect detection and collider experiments. Moreover, WIMP type DM can also explain the $1-3$ GeV γ-ray excess in the galactic canter observed by Fermi-LAT satellite. The null result so far after the rigorous search of WIMP type DM has forced the physicist to think of any alternate way of DM production. Freeze-in mechanism is one of them where DM feebly couples with rest of the particles and is very hard to detect it in any terrestrial experiment. In this the-

sis, we have explored different regimes of the parameter space for FIMP DM production and have shown that DM can be produced both from decay and annihilation dominantly. Moreover, we find regions in the parameter space where either decay or annihilation is dominant. Due to the feeble coupling of FIMP type DM they are difficult to detect at different DM detection experiments, indeed we have shown that two-component FIMP type DM (the mass difference between them is around 3.5 keV) can interpret the unknown 3.5 keV line detected by the XMM-Newton and Chandra satellites at the galaxies clusters and galactic canter.

Neutrino mass has been confirmed by many oscillation experiments and this is one of the major problems of SM. In this thesis, depending on the model construction we have generated neutrino mass as well, besides DM, either by tree level process or radiatively. With the advancement of detector technology, presently there is a tight bound on the neutrino oscillation parameters (two mass squared differences, three mixing angles and one CP phase) range obtained from different oscillation experiments. We have constrained our model parameters by using these oscillation parameter bounds and have shown that there exist correlations (anticorrelations) among the model parameters.

We generate the lepton asymmetry from the decay of the right-handed neutrinos, which help in generating the neutrino mass as well, to explain the correct value of the baryon asymmetry of the Universe through resonant leptogenesis. Interestingly, we find a regime of FIMP type DM mass where it can be produced entirely from the annihilation of the same right-handed neutrinos which are mentioned just before. Therefore, we concluded that right-handed neutrinos affect all the three major problems. Since we have considered $U(1)_{L_\mu - L_\tau}$ gauged symmetry, it can give MeV order gauge boson after evading all the existing bounds. This gauge boson can contribute to muon $(g-2)$ through one loop diagram and for the MeV order gauge boson mass and $\mathcal{O}(10^{-3})$ gauge coupling one can fill the gap between the experimental and theoretical value of muon $(g-2)$.

List of Figures

List of Tables

1

Introduction

1.1 Standard Model

Standard Model (SM) of particle physics is a very successful theory so far in describing nature. The more and more experimental tests happen to validate the SM, the more and more successful SM becomes a complete theory of nature. Although it is a very successful theory of nature, indeed it has a few drawbacks which we will discuss later in this chapter. This thesis is basically to explain those subtleties of the SM by staying in its footstep. The complete gauge group of the SM is $\mathrm{SU}(3)_c \times \mathrm{SU}(2)_L \times \mathrm{U}(1)_Y$ where c corresponds to colour charge, L corresponds to the left-handed fields which are doublets and Y is the hypercharge. Particle spectrum of the SM is shown in Table 1.1. We will discuss the SM briefly in this section and in the later part we will summarize the limitations of SM.

Gauge Group	Baryon Fields			Lepton Fields		Scalar Fields
	$Q^i_L = (u^i_L, d^i_L)^T_I$	u^i_{RI}	d^i_{RI}	$L^i_L = (\nu^i_L, e^i_L)^T$	e^i_R	$\phi_h = (\phi^+, \phi_0)^T$
$\mathrm{SU(3)_C}$	3	3	3	1	1	1
$\mathrm{SU(2)_L}$	2	1	1	2	1	2
$\mathrm{U(1)_Y}$	1/6	2/3	−1/3	−1/2	−1	1/2
$U(1)_{em}$	$(2/3, -1/3)^T$	2/3	−1/3	$(0, -1)^T$	−1	$(+1, 0)^T$

Table 1.1: Particle contents and their corresponding charges under SM gauge group. i represents the generation index and I represents color charge.

1.1.1 Electroweak Sector $SU(2)_L \times U(1)_Y$

The electroweak sector consists of $SU(2)_L$ and $U(1)_Y$ gauge groups. Once the Higgs develops a vacuum expectation value (*vev*), v, then the aforementioned gauge groups break to $U(1)_{em}$,

$$SU(2)_L \times U(1)_Y \rightarrow U(1)_{em} \,. \tag{1.1}$$

$U(1)_Y$ is the high energy abelian symmetry related to hypercharge (Y) and $U(1)_{em}$ is the low energy abelian symmetry related to the electromagnetic charge. We will see later that the massless photon, which is a mediator of electromagnetic interaction, is a combination of $SU(2)_L$ and $U(1)_Y$ gauge bosons.

Once the neutral component of Higgs multiplet, ϕ_h, develops *vev*, it not only breaks $SU(2)_L \times U(1)_Y$ gauge symmetry but is also responsible for the mass generation of the gauge bosons and fermions.

The complete Lagrangian containing the spin-0 and spin-1 fields looks like as follows,

$$\mathcal{L}_{EW} \;=\; -\frac{1}{4}\sum_{a=1}^{3} W^a_{\mu\nu}W^{a\mu\nu} - \frac{1}{4}F_{\mu\nu}F^{\mu\nu} + \left(D_\mu\phi_h\right)^\dagger\left(D_\mu\phi_h\right) + \mu_h^2\left(\phi_h^\dagger\phi_h\right) - \lambda_h\left(\phi_h^\dagger\phi_h\right)^2 \,, \tag{1.2}$$

where B_μ is the hypercharge gauge boson and $B_{\mu\nu} = \partial_\mu B_\nu - \partial_\nu B_\mu$ is the $U(1)_Y$ field strength tensor, W^a_μ (a =1, 2, 3) gauge bosons are related to the $SU(2)_L$ gauge symmetry and the field strength tensor $W^a_{\mu\nu}$ is expressed as,

$$W^a_{\mu\nu} = \partial_\mu W^a_\nu - \partial_\nu W^a_\mu + g_2\epsilon^{abc}W^b_\mu W^c_\nu \,, \tag{1.3}$$

g_2 is the $SU(2)_L$ gauge coupling, ϵ^{abc} is the Levi-Civita symbol and structure function for the $SU(2)_L$ gauge group. The covariant derivative for the Higgs boson is given by,

$$D_\mu\phi_h = \left(\partial_\mu - ig_2W^a_\mu\tau^a - ig_1YB_\mu\right)\phi_h \,. \tag{1.4}$$

Here, g_2 and g_1 are the $SU(2)_L$ and $U(1)_Y$ gauge couplings, respectively, $Y = \frac{1}{2}$ is the hypercharge of the Higgs multiplet. The Higgs potential is given by,

$$V(\phi_h) = -\mu_h^2 \left(\phi_h^\dagger \phi_h\right) + \lambda_h \left(\phi_h^\dagger \phi_h\right)^2 , \tag{1.5}$$

under the conditions $\mu_h^2 > 0$, $\lambda_h > 0$, the neutral component of Higgs mass acquire a *vev*. Without loss of any generality, we can write the Higgs multiplet in the following way,

$$\phi_h = e^{\frac{2i\pi^a \tau^a}{v}} \begin{pmatrix} 0 \\ \frac{v+h}{\sqrt{2}} \end{pmatrix}, \tag{1.6}$$

where v is the *vev*, $\tau^a = \frac{\sigma^a}{2}$ is the canonically normalised $SU(2)$ generators, h is the real scalar field. π^a can be made associated with the Goldstone bosons which impart their physical degree of freedom (dof) to the gauge bosons as the longitudinal mode of them and make the gauge bosons massive. Therefore, after the electro-weak symmetry breaking, among the four dof of Higgs multiplet three of them go as the longitudinal component of the charged bosons ($W^\pm$, defined later) and neutral boson (Z, defined later). For simplicity, we use here the unitary gauge which means no unphysical dof are allowed, hence we can safely take, $\pi^a = 0$. Therefore, putting

$$\phi_h = \begin{pmatrix} 0 \\ \frac{v+h}{\sqrt{2}} \end{pmatrix}, \tag{1.7}$$

in the kinetic term of Higgs multiplet (as given in the Eq. (1.2)), we get the following terms which we discuss step by step.

Gauge boson mass terms

We focus on the kinetic term of the Higgs boson which gives mass to the gauge bosons,

$$\begin{aligned}
\left[\left(D_\mu\phi_h\right)^\dagger(D^\mu\phi_h)\right]_{GBmass} &= \frac{g^2v^2}{8}\begin{pmatrix}0 & 1\end{pmatrix}\begin{pmatrix}\frac{g_1}{g_2}B_\mu + W^3_\mu & W^1_\mu - iW^2_\mu \\ W^1_\mu + iW^2_\mu & \frac{g_1}{g_2}B_\mu - W^3_\mu\end{pmatrix}^2\begin{pmatrix}0\\1\end{pmatrix} \\
&= \frac{g^2v^2}{8}\left[(W^1_\mu)^2 + (W^2_\mu)^2 + \left(\frac{g_1}{g_2}B_\mu + W^3_\mu\right)^2\right], \qquad (1.8)
\end{aligned}$$

the above expression gives the mass terms for the gauge bosons. Since, the kinetic term for the B_μ and W^a_μ are canonically normalised, we don't need to rescale them and to get the mass basis we just rotate by the Weinberg angle, θ_w. The gauge basis and the mass basis are related in the following way,

$$\begin{pmatrix}B_\mu \\ W^3_\mu\end{pmatrix} = \begin{pmatrix}\cos\theta_w & -\sin\theta_w \\ \sin\theta_w & \cos\theta_w\end{pmatrix}\begin{pmatrix}A_\mu \\ Z_\mu\end{pmatrix}, \qquad (1.9)$$

with $\tan\theta_w = \frac{g_1}{g_2}$. Define, $W^\pm_\mu = \frac{W^1_\mu \mp iW^2_\mu}{\sqrt{2}}$ are the charged gauge bosons. Therefore, the kinetic terms, mass terms and the interaction terms among the gauge bosons take the following form,

$$\begin{aligned}
\mathcal{L}_{gauge} &= -\frac{1}{4}F^2_{\mu\nu} - \frac{1}{4}Z^2_{\mu\nu} - \frac{1}{2}W^+_{\mu\nu}W^-_{\mu\nu} + \frac{1}{2}M^2_Z Z_\mu Z^\mu + M^2_W W^+_\mu W^-_\mu \\
&\quad -ie\cot\theta_w\left[\partial_\mu Z_\nu(W^+_\mu W^-_\nu - W^+_\nu W^-_\mu) + Z_\nu(W^+_\mu W^-_{\mu\nu} + W^-_\mu W^+_{\nu\mu})\right] \\
&\quad -ie\left[\partial_\mu A_\nu(W^+_\mu W^-_\nu - W^+_\nu W^-_\mu) + A_\nu(W^+_\mu W^-_{\mu\nu} + W^-_\mu W^+_{\nu\mu})\right] \\
&\quad -\frac{e^2}{2\sin^2\theta_w}(W^+_\mu W^-_\mu W^+_\nu W^-_\nu - W^+_\mu W^+_\mu W^-_\nu W^-_\nu) - e^2\cot^2\theta_w(Z_\mu W^+_\mu Z_\nu W^-_\nu - Z_\mu W^+_\nu Z_\mu W^-_\nu) \\
&\quad +e^2\cot\theta_w\left[A_\mu W^+_\mu W^-_\nu Z_\nu + A_\mu W^+_\nu W^-_\mu Z_\nu - A_\nu W^+_\mu W^-_\mu Z_\nu\right] \\
&\quad +e^2(A_\mu W^+_\mu A_\nu W^-_\nu - A_\mu W^+_\nu A_\mu W^-_\nu) \qquad (1.10)
\end{aligned}$$

where

$$\begin{aligned}
F_{\mu\nu} &= \partial_\mu A_\nu - \partial_\nu A_\mu\,, \\
Z_{\mu\nu} &= \partial_\mu Z_\nu - \partial_\nu Z_\mu\,, \\
W^{\pm}_{\mu\nu} &= \partial_\mu W^{\pm}_\nu - \partial_\nu W^{\pm}_\mu\,, \\
e &= g_2 \sin\theta_w = g_1 \cos\theta_w = \frac{g_1 g_2}{\sqrt{g_1^2 + g_2^2}}\,, \qquad (1.11)
\end{aligned}$$

and the mass term for the $W^{\pm}$ and Z bosons are given by,

$$M_W = \frac{g_2 v}{2}\,,\;\; M_Z = \frac{v}{2}\sqrt{g_2^2 + g_1^2} = \frac{M_W}{\cos\theta_w}\,. \qquad (1.12)$$

Higgs Boson

After symmetry breaking, physical Higgs boson appear in the SM particle spectrum which has self interaction as well as interaction with the gauge bosons. The terms related with the Higgs boson are,

$$\begin{aligned}
\mathcal{L}_{Higgs} &= \frac{1}{2}\partial_\mu h \partial^\mu h - \frac{1}{2}M_h^2 h^2 - \frac{g_2 M_h^2}{4M_W}h^3 - \frac{g_2^2 M_h^2}{32 M_W^2}h^4 + \frac{2h}{v}\left(M_W^2 W_\mu^+ W_\mu^- + \frac{1}{2}M_Z^2 Z_\mu Z^\mu\right) \\
&\quad + \left(\frac{h}{v}\right)^2 \left(M_W^2 W_\mu^+ W_\mu^- + \frac{1}{2}M_Z^2 Z_\mu Z^\mu\right). \qquad (1.13)
\end{aligned}$$

The vertices of Higgs with the gauge bosons are very much important to make the SM a unitary theory. More explicitly, the theory becomes non-perturbative when we compute the $2-2$ scattering processes among the gauge bosons at high energy regime and the increasing behaviour of cross section is diminished by the Higgs mediated diagrams. Hence, because of the interaction of Higgs boson with the gauge bosons the theory remains finite at high energy. The mass term of the Higgs boson, $M_h^2 = 2\lambda_h v^2$, does not depend on the other independent parameter after symmetry breaking, e, $\sin^2\theta_w$ and M_W. Finally, before electroweak symmetry breaking we started with the four independent parameters μ_h^2, g_1, g_2, λ_h and after symmetry breaking we remain with the same number of independent variables namely, e, θ_w, M_h and M_W.

Experiments have measured the value of the following parameters very accurately,

$$\alpha_e(M_e) = \frac{e^2}{4\pi} = \frac{1}{137}\,, M_Z = 91.2\,\text{GeV}\,, M_W = 80.399\,\text{GeV}\,\text{and}\, M_h = 126.0\,. \tag{1.14}$$

Using the above values we get the following value of the other parameters, which are,

$$\begin{aligned} e &= \sqrt{4\pi\alpha_e(M_e)} = 0.303\,, \sin^2\theta_w = 0.23\,, g_2 = \frac{e}{\sin\theta_w} = 0.65\,, g_1 = \frac{e}{\cos\theta_w} = 0.34\,,\text{ and} \\ v &= \frac{2M_W}{g_2} = 251\,\text{GeV}\,. \end{aligned} \tag{1.15}$$

This is the one technique by which we determine the above mentioned values. For example from muon decays we get the value of *vev* as well which is $v = 246$ GeV.

1.1.2 Fermionic Sector

In the SM, left handed leptons $(e, \nu_e, \mu, \nu_\mu, \tau, \nu_\tau)_L$ pair transforms non-trivially under the $SU(2)_L$ gauge group, as do the left handed quarks $(d, u, s, c, b, t)_L$. There are three generations both for leptons as well as quarks,

$$\begin{aligned} L_L^i &= \begin{pmatrix} \nu_{eL} \\ e_L \end{pmatrix}, \begin{pmatrix} \nu_{\mu L} \\ \mu_L \end{pmatrix}, \begin{pmatrix} \nu_{\tau L} \\ \tau_L \end{pmatrix}, \\ Q_{LI}^i &= \begin{pmatrix} u_L \\ d_L \end{pmatrix}_I, \begin{pmatrix} c_L \\ s_L \end{pmatrix}_I, \begin{pmatrix} t_L \\ b_L \end{pmatrix}_I, \end{aligned}$$

where i is the generation index, and I is the color index. These fields transform as left handed field under the Lorentz group *i.e.* in $\left(\frac{1}{2}, 0\right)$ representation of the Lorentz group. On the other hand the right handed Weyl-spinor transform in the $\left(0, \frac{1}{2}\right)$ representation of the Lorentz group and they are singlet under $SU(2)_L$ gauge group. We define the right handed Weyl-fermions by the first generation symbol as,

$$\begin{aligned} u^i_{RI} &= (u_R, c_R, t_R)_I\,,\ d^i_{RI} = (d_R, s_R, b_R)_I\,, \\ e^i_R &= (e_R, \mu_R, \tau_R)\,, \end{aligned}$$

where again i is the generation index and I is the color index.

The Lagrangian for the fermions under $SU(2)_L \times U(1)_Y$ gauge groups takes the form,

$$\begin{aligned} \mathcal{L}_f &= i\bar{L}^i_L(\not{\partial} - ig_2\not{W}^a\tau^a - ig_1Y_L\not{B})L^i_L + i\bar{Q}^i_L\left(\not{\partial} - ig_2\not{W}^a\tau^a - ig_1Y_Q\not{B}\right)Q^i_L \\ &\quad + i\bar{e}^i_R(\not{\partial} - ig_1Y_e\not{B})e^i_R + i\bar{u}^i_R(\not{\partial} - ig_1Y_u\not{B})u^i_R + i\bar{d}^i_R(\not{\partial} - ig_1Y_d\not{B})d^i_R\,, \qquad (1.16) \end{aligned}$$

where $\not{A} = \gamma^\mu A_\mu$ and Y_L, Y_Q are the hypercharges for the lepton and quark doublets and happen to be same for all the generators. Y_e, Y_u, Y_d are the hypercharges for the right handed counterparts and again same for all generations. R, L are the index for the left handed and the right handed. In the two component notation, one can always write

$$\begin{aligned} \bar{Q}^i_L\not{\partial}Q^i_L &= Q^{i\dagger}_L\bar{\sigma}_\mu\partial_\mu Q^i_L\,, \\ \bar{u}^i_R\not{\partial}u^i_R &= u^{i\dagger}_R\sigma_\mu\partial_\mu u^i_R\,. \qquad (1.17) \end{aligned}$$

In the 4-component or Dirac fermion notation, we introduce left handed and right handed projectors for the handedness, $P_L = \frac{1-\gamma_5}{2}$ and $P_R = \frac{1+\gamma_5}{2}$. Therefore, we can write the terms in the following way,

$$\begin{aligned} \bar{Q}^i_L\not{\partial}Q^i_L &= Q^{i\dagger}_L\gamma^0\gamma^\mu P_L\partial_\mu Q^i\,, \\ \bar{u}^i_R\not{\partial}u^i_R &= u^{i\dagger}_R\gamma^0\gamma^\mu P_R\partial_\mu u^i_R\,. \qquad (1.18) \end{aligned}$$

Neutral Currents

In the covariant derivative, considering the terms which contain W_μ^3 and B_μ, then it gives the interaction of the fermions with the neutral gauge bosons,

$$\begin{aligned} D_\mu &= \partial_\mu - ig_2 W_\mu^3 T^3 - ig_1 B_\mu Y \\ &= \partial_\mu - ieA_\mu \left(T^3 + Y\right) - ieZ_\mu \left(\cot\theta_w T^3 - \tan\theta_w Y\right). \end{aligned} \tag{1.19}$$

Define, $Q = T^3 + Y$, it actually measures the electric charge,

$$Q\begin{pmatrix} 0 \\ e_L \end{pmatrix} = \begin{pmatrix} \frac{1}{2} - \frac{1}{2} & 0 \\ 0 & -\frac{1}{2} - \frac{1}{2} \end{pmatrix}\begin{pmatrix} 0 \\ e_L \end{pmatrix} = -\begin{pmatrix} 0 \\ e_L \end{pmatrix}, \tag{1.20}$$

it shows that electron has electric charge -1. By considering the fact that left handed fields have both $SU(2)_L$ and $U(1)_Y$ charges, and right handed fields have only hypercharge ($Q = Y$). Therefore, we can write the generic Lagrangian in the following way,

$$\mathcal{L}_{NC} = i\bar{\psi}_L^j \left(\partial\!\!\!/ - ig_2 W\!\!\!\!/^3 T^3 - ig_1 B\!\!\!/ Y_L^j\right)\psi_L^j + i\bar{\psi}_R^j \left(\partial\!\!\!/ - ig_1 B\!\!\!/ Y_R^j\right)\psi_R^j \tag{1.21}$$

where $\psi_L^j = L_L^j, Q_L^j$, $\psi_R^j = e_R^j, u_R^j, d_R^j$, j is the generation index. By using Eq. (1.9), we can rewrite W_μ^3, B_μ in terms of A_μ, Z_μ,

$$\mathcal{L} = ... + \frac{e}{\sin\theta_w} Z_\mu J_\mu^Z + eA_\mu J_\mu^{EM} \tag{1.22}$$

where J_μ^Z and J_μ^{EM} are given by,

$$\begin{aligned} J_\mu^Z &= \cos\theta_w J_\mu^3 - \frac{\sin^2\theta_w}{\cos\theta_w} J_\mu^Y, \\ J_\mu^Y &= \sum_j \left(Y_L^j \bar{\psi}_L^j \gamma_\mu \psi_L^j + Y_R^j \bar{\psi}_R^j \gamma_\mu \psi_R^j\right), \\ J_\mu^3 &= \sum_j \bar{\psi}_L^j \gamma_\mu T^3 \psi_L^j \end{aligned}$$

$$J_\mu^{EM} = \sum_j Q_j \left(\bar{\psi}_L^j \gamma_\mu \psi_L^j + \bar{\psi}_R^j \gamma_\mu \psi_R^j\right) \tag{1.23}$$

Fermion mass and Charged Currents

So far we have not discussed the mass generation of the fermions and will address it now. We can not simply write the mass term like $m(\bar{e}_L e_R + h.c.)$, then the immediate problem will arise is that this term is not gauged invariant under SM gauge groups. Therefore, we have to use Higgs doublet to generate the mass term for the fermions, we discuss first the lepton mass generation after that the quark mass generation.

Lepton mass

The mass term for the leptons can be easily written in the gauge invariant way by the following terms,

$$\mathcal{L}_{Yuk}^{lepton} = -y_{ij}^l \bar{L}_L^i \tilde{\phi}_h e_R^j + h.c., \tag{1.24}$$

where $\tilde{\phi}_h = i\sigma_2 \phi_h^*$. Once the neutral component of Higgs doublet acquire a vev, it will generate the mass term for the leptons, $-m_l^{ij}(\bar{e}_L^i e_R^j + h.c.)$, where,

$$m_l^{ij} = \frac{y_l^{ij} v}{\sqrt{2}}. \tag{1.25}$$

y_l^{ij} is the 3×3 complex matrix and by rotating the flavor basis, we can always make the lepton mass matrix into diagonalised form. As we will see that it is not difficult like finding the mass basis for quarks because in SM neutrinos are massless.

Quark mass

In the case of quarks, the down type quark mass can be generated in the similar way we generate mass for the leptons. In contrary to this, for up-type quark we need to define

Higgs with opposite hypercharge in the following way,

$$\tilde{\phi}_h = i\sigma_2 \phi_h^* \tag{1.26}$$

which is $SU(2)_L$ doublet and has hypercharge value, $Y = -1/2$. Finally, we can write the Yukawa terms for both up-type and down-type quarks in the following way,

$$\mathcal{L}_{Yuk}^{Quark} = -y_{ij}^u \bar{Q}_L^i \tilde{\phi}_h u_R^j - y_{ij}^d \bar{Q}_L^i \phi_h d_R^j + h.c.. \tag{1.27}$$

Here, both the terms are $SU(3)_c \times SU(2)_L \times U(1)_Y$ gauge invariant. After Higgs *vev* development, quarks generate mass,

$$\mathcal{L}_{mass}^{Q} = -\frac{y_{ij}^u v}{\sqrt{2}} \bar{u}_L^i u_R^j - \frac{y_{ij}^d v}{\sqrt{2}} \bar{d}_L^i d_R^j + h.c. \tag{1.28}$$

where y^u, y^d are the 3×3 complex matrices. We want the mass basis for the quarks. To that end, we introduce two unitary matrices U_u, U_d and two diagonal matrices M_u, M_d such that,

$$y^u y^{u\dagger} = U_u M_u^2 U_u^\dagger, \; y^d y^{d\dagger} = U_d M_d^2 U_d^\dagger. \tag{1.29}$$

It is very obvious that $yy^\dagger$ is hermitian matrix and hence it has real eigenvalues. We can write y in the following way,

$$y^u = U_u M_u K_u^\dagger, \; y^d = U_d M_d K_d^\dagger \tag{1.30}$$

for any unitary matrices K_u, K_d. Therefore, the mass term can be written as,

$$\mathcal{L}_{mass}^{Q} = -\frac{v}{\sqrt{2}} \left[\bar{d}_L U_d M_d K_d^\dagger d_R + \bar{u}_L U_u M_u K_u^\dagger u_R + h.c. \right] \tag{1.31}$$

To get the mass basis we can rotate the basis in the following way,

$$u_L \rightarrow U_u u_L\,,\; d_L \rightarrow U_d d_L\,,\; u_R \rightarrow K_u u_R\,,\; d_R \rightarrow K_d d_R\,. \tag{1.32}$$

These new basis are called mass basis and the mass terms take the following form,

$$\mathcal{L}^{Q}_{mass} = -m^u_j \bar{u}^j_L u^j_R - m^d_j \bar{d}^j_L d^j_R + h.c. \tag{1.33}$$

where $m^u_j = \frac{v}{\sqrt{2}} M^j_u$, $m^d_j = \frac{v}{\sqrt{2}} M^j_d$. We will focus on the charged current (CC) interactions and we will see that these basis transformations have significant role there.

Charged Current Interaction

We have already discussed the neutral current interaction for the leptons and quarks in Section 1.1.2. Here, we will only describe the charged current interaction and exception will happen for the quark case where we will also consider the neutral current case as well. The charged current interaction terms for the leptons take the following form,

$$\begin{aligned} \mathcal{L}^{leptons}_{CC} &= i\begin{pmatrix} \bar{\nu}^i_L & \bar{e}^i_L \end{pmatrix}\left[\not{\partial} - i\gamma^\mu \begin{pmatrix} \ldots & \frac{g_2}{\sqrt{2}} W^+_\mu \\ \frac{g_2}{\sqrt{2}} W^-_\mu & \ldots \end{pmatrix}\right]\begin{pmatrix} \nu^i_L \\ e^i_L \end{pmatrix} \\ &= \ldots + \frac{g_2}{\sqrt{2}} W^+_\mu \bar{\nu}^i_L \gamma_\mu P_L e^i_L + h.c.\,. \end{aligned} \tag{1.34}$$

Since in the SM, we don't have mass term for the neutrinos, hence we can freely rotate the basis and make the lepton mass matrix diagonalised without any difficulty. Now, we will talk about the CC interaction for the quarks and will see that these basis rotation in the quark sector have effect on the CC interactions for the quarks. We consider here both charged and neutral current for the quarks because it will help to describe the effect of basis rotation properly. More explicitly, we will see later that the basis rotations as shown in Eq. (1.32) have effect in the charged current interaction and no effect in the neutral current interaction. The interaction terms both for CC and NC interactions and also the mass term for the quarks take the following form,

$$\begin{aligned}\mathcal{L}_{flavor-basis} &= \begin{pmatrix}\bar{u}_L^i & \bar{d}_L^i\end{pmatrix}\left[\not{\partial}+\gamma^\mu\begin{pmatrix}\frac{g_1}{6}B_\mu+\frac{g_2}{2}W_\mu^3 & \frac{g_2}{\sqrt{2}}W_\mu^+\\ \frac{g_2}{\sqrt{2}}W_\mu^- & \frac{g_1}{6}B_\mu-\frac{g_2}{2}W_\mu^3\end{pmatrix}\right]\begin{pmatrix}u_L^i\\ d_L^i\end{pmatrix}\\ &+\bar{u}_R^i\left(i\not{\partial}+\frac{2g_1}{3}\not{B}\right)u_R^i+\bar{d}_R^i\left(i\not{\partial}-\frac{g_1}{3}\not{B}\right)d_R^i\\ &-\frac{v}{\sqrt{2}}\left[\bar{d}_L U_d M_d K_d^\dagger d_R+\bar{u}_L U_u M_u K_u^\dagger u_R+h.c.\right], \end{aligned} \tag{1.35}$$

when we make the rotation $d_R \to K_d d_R$ and $u_R \to K_u u_R$, the matrix K_d, K_u drop out from the Lagrangian completely because interaction related to hypercharge is diagonal generation wise. For the rotation $u_L \to U_u u_L$ and $d_L \to U_d d_L$, the B_μ, W_μ^3 interaction terms does not affect because these are also diagonal in generation wise. For the $W_\mu^\pm$ interaction case it mixes the up-type quark to down-type quark and these rotation matrix do not go away. Therefore, Eq. (1.35) takes the following form after the basis rotation,

$$\begin{aligned}\mathcal{L}_{mass-basis} &= \frac{e}{\sin\theta_w}Z_\mu J_\mu^Z+eA_\mu J_\mu^{EM}-\left(m_j^u\bar{u}_L^j u_R^j+m_j^d\bar{d}_L^j d_R^j+h.c.\right)\\ &+\frac{e}{\sqrt{2}\sin\theta_w}\left[W_\mu^+\bar{u}_L^i\gamma^\mu V^{ij}d_L^j+h.c.\right]\end{aligned} \tag{1.36}$$

where $V = U_u^\dagger U_d$, known as the Cabibbo-Kobayashi-Maskawa (CKM) matrix. One can easily check that V is a unitary matrix. If we consider $N \times N$ unitary matrix then the number of real parameters required to specify it is N^2, among them $(2N-1)$ number of parameters can be absorbed in the fields. Number of physical parameters we are left with is $(N-1)^2$. Of these, $\frac{N(N-1)}{2}$ parameters are for rotation and the remaining ones are phases. In the present case $N = 3$, so number of rotation angles are three $(\theta_{12}, \theta_{13}, \theta_{23})$ and one CP phase (δ_{CKM}). We can write down the matrix V as follows,

$$V=\begin{pmatrix} c_{12}c_{13} & s_{12}c_{13} & s_{13}e^{-i\delta_{CKM}}\\ -s_{12}c_{23}-c_{12}s_{23}s_{13}e^{i\delta_{CKM}} & c_{12}c_{23}-s_{12}s_{23}s_{13}e^{i\delta_{CKM}} & s_{23}c_{13}\\ s_{12}s_{23}-c_{12}c_{23}s_{13}e^{i\delta_{CKM}} & -c_{12}s_{23}-s_{12}c_{23}s_{13}e^{i\delta_{CKM}} & c_{23}c_{13}\end{pmatrix} \tag{1.37}$$

where $c_{ij} = \cos\theta_{ij}$, $s_{ij} = \sin\theta_{ij}$. From experiments, these mixing angles are measured very precisely,

$$\theta_{12} = 13.02^0 \pm 0.04^0,\ \theta_{23} = 2.30^0 \pm 0.08^0,\ \theta_{13} = 0.20^0 \pm 0.02^0 \text{ and } \delta_{CKM} = 69^0 \pm 5^0.$$

1.1.3 Color Sector $SU(3)_c$

After Electroweak symmetry breaking (EWSB), we can generate mass for all the fermions, gauge bosons and Higgs. So, we will discuss the strong interaction of the quarks which has mass m_q. After EWSB, the color symmetry, $SU(3)_c$, is still intact with the Lagrangian. Since, $SU(3)_c$ never breaks, hence there are eight massless gluon fields in the theory. The Lagrangian looks like as follows,

$$\mathcal{L}_{QCD} = -\frac{1}{4}G^a_{\mu\nu}G^{a\mu\nu} + \sum_f \bar{q}_f(i\gamma^\mu D_\mu - m_q)q_f \tag{1.38}$$

where

$$\begin{aligned} G^a_{\mu\nu} &= \partial_\mu G^a_\nu - \partial_\nu G^a_\mu + g_3 f^{abc} G^b_\mu G^c_\nu \\ D_\mu &= \partial_\mu - i g_3 \frac{\lambda^a}{2} G^a_\mu, \end{aligned} \tag{1.39}$$

f^{abc} is the structure constant for the $SU(3)_c$ gauge symmetry, λ^a ($a = 1$ to 8) is the Gell-Mann matrices. After decomposition, the above Lagrangian can be written as,

$$\begin{aligned} \mathcal{L}_{QCD} = &-\frac{1}{4}(\partial_\mu G^a_\nu - \partial_\nu G^a_\mu)^2 + \sum_f \bar{q}_f\left(i\gamma^\mu\partial_\mu - m_q\right)q_f + g_3 G^a_\mu \sum_f \bar{q}_f\gamma^\mu\frac{\lambda^a}{2}q_f \\ &-\frac{g_3}{2}f^{abc}(\partial^\mu G^{a\nu} - \partial^\nu G^{a\mu})G^b_\mu G^c_\nu - \frac{g_3^2}{4}f^{abc}f_{ade}G^\mu_b G^\nu_c G^d_\mu G^e_\nu. \end{aligned} \tag{1.40}$$

First two terms gives the kinetic term for the gluons and the quarks, third term in the first line gives the interaction term of quarks with the gluons, and the terms in the second line imply the self interaction among the gluons and present purely due to the non-abelian gauge structure of the $SU(3)_c$ gauge group.

1.2 Drawbacks of SM

1.2.1 Hierarchy of Higgs mass

At LHC we have measured the SM Higgs mass which is around 125 GeV confirmed from the $h \to \gamma\gamma$ channel. This value is consistent from many sides and one of them is the Lee-Quigg-Thacker [1] bound which put a constraint on the upper value of the Higgs mass,

$$M_h \leq \sqrt{\frac{16\pi}{3}} v \sim 1 \text{ TeV}. \tag{1.41}$$

If the above constraint is not followed at the tree level then the two to two scattering processes among the gauge bosons violate unitarity at the high energy scale and weak interaction becomes strong at the high energy scale. In SM, the immediate problem to the above constraints comes when we take one-loop correction to its Higgs mass mediated by the t-quark, as shown in Fig. 1.1. Due to this contribution Higgs mass gets contribution

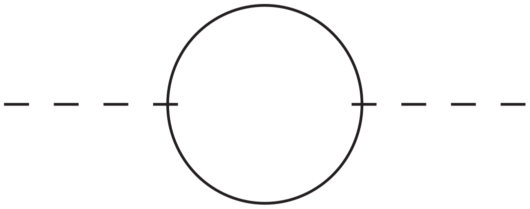

Figure 1.1: Higgs mass correction from fermionic loop.

which is proportional to the quadratic power of the cut off scale of the theory. Quantitatively the correction comes out as,

$$\Delta M_h^2 = -\frac{|\lambda_f^2|}{8\pi^2}\left[\Lambda_{UV}^2 + ...\right] \tag{1.42}$$

where Λ_{UV} is the cut off scale of the theory means after that energy scale theory is not valid. If we consider Λ_{UV} around the Planck scale then it is a very huge correction and around 10^{34} times higher than the observed Higgs mass. This is called the hierarchy problem of the SM. To tackle this we need to extend the SM and there are many proposals to solve this hierarchy problem which are yet to be confirmed as a final theory of nature. Most promising one is the SUperSYmmetry (SUSY) theory where each particle has their superpartner with a spin-$\frac{1}{2}$ difference.

1.2.2 Absence of Dark Matter Candidate

The presence of DM in the universe is an inevitable fact, it contains around 26% of the total energy budget of the Universe which is around five times the visible matter content of the Universe. We have many pieces of evidence regarding the presence of DM like Zwicky's missing mass conclusion in Coma Cluster, the flatness of galaxy rotation curve, observation of bullet cluster, WMAP and Planck collaboration have measured the amount of DM present in the Universe. Therefore, we need a suitable candidate for DM in the particle spectrum of nature. Although, it is not fully correct that SM does not contain any DM candidate. It is neutrino in the SM which can satisfy all the properties of DM. Unfortunately, they are present in the Universe with very small fraction and also another problem is that they are relativistic so can not form the halo. The amount of neutrino present in our Universe must follow the relation,

$$\Omega_\nu h^2 \leq 0.0062 \; at \; 95\% \; CL. \tag{1.43}$$

In the next Section 1.3, we will have more discussion on DM, mainly on its evidences, possible particle candidate and detection techniques. Therefore, not having a suitable DM candidate in the SM is a serious flaw of it. So, we need beyond the standard model which has a suitable DM candidate.

1.2.3 Observation of Neutrino mass

Neutrino mass is a proven fact and SM can not explain it. We have observed neutrino oscillation among the flavours in many experiments such as atmospheric neutrino experiment Super-Kamiokande [2], solar neutrino experiment SNO [3], reactor neutrino experiment KamLand [4], reactor neutrino experiments with short baselines Daya Bay [5], RENO [6], Double Chooz [7], and accelerator neutrino experiments T2K [8, 9], NOνA [10, 11]. To explain neutrino oscillation we need neutrino mass. In SM, there is no right-handed counterpart for the neutrinos, hence we can not simply write down the Dirac mass term for the neutrinos. Therefore, in SM neutrinos are massless. To give them mass we can extend SM particle spectrum in many ways and it will be discussed in detail in Section 1.9. Since neutrinos are neutral, we can write down Majorana mass term for them as well. To generate tiny neutrino masses we can follow the tree level seesaw mechanisms or radiative mass generation by loop diagrams. Neutrino mass can not be explained by the SM and we need some beyond SM theory to explain the neutrino mass.

1.2.4 Matter antimatter asymmetry of the Universe

In our Universe, we have observed slight excess of matter over antimatter. The numerical value of the slight difference [12] lies around, $Y_B = (8.24 - 9.38) \times 10^{-10}$. This is one of the unsolved puzzle so far. In 1967, Sakharov showed [13] that in order to explain matter-antimatter asymmetry of the Universe microscopic system must satisfy the following three conditions,

- Baryon number violation ,
- C and CP violation ,
- The process which generate this asymmetry must be out of equilibrium process.

If one of the above conditions fails then there should not be any excess of matter over antimatter. Surprisingly, all of the Sakharov conditions are satisfied in the SM, we have baryon number violation through anomaly, we have CP violation in the quark sector because it contains three generation of quark, and as the universe cools due to expansion of it and the electroweak phase transition are out of equilibrium. Unfortunately, these are not sufficient to produce enough matter-antimatter asymmetry of the Universe. In particular, we need more CP violation and strong first order phase transition. Therefore, the observed baryon asymmetry can not be explained in the context of the SM and hence we need to consider beyond SM scenario. One of the popular BSM solutions is the leptogenesis technique in which we generate lepton asymmetry and this lepton asymmetry can be converted to baryon asymmetry through sphaleron process. Another one is the R-parity violating SUSY where one can directly produce the observed matter antimatter asymmetry of the Universe.

1.2.5 Strong CP problem

Apart from the weak CP phase there is another source of CP violation. If we consider a chiral symmetry $\psi \to e^{i\gamma_5\theta}\psi$, then this is a classical symmetry of the Lagrangian but not the quantum symmetry. This symmetry will change the weight in the path integral formalism,

$$\int \mathcal{D}\bar{\psi}\mathcal{D}\psi \to \int \mathcal{D}\bar{\psi}\mathcal{D}\psi \; exp\left(i\theta \int d^4x \frac{g_3^2}{32\pi^2}\epsilon^{\alpha\beta\mu\nu}G^a_{\alpha\beta}G^a_{\mu\nu}\right). \tag{1.44}$$

This term will contribute in the Lagrangian,

$$\mathcal{L}_\theta = \theta_{QCD}\frac{g_3^2}{32\pi^2}\epsilon^{\alpha\beta\mu\nu}G^a_{\alpha\beta}G^a_{\mu\nu} \tag{1.45}$$

Again when we make chiral rotation in the Yukawa sector, we get similar type of contribution and hence the resulting Lagrangian will look like,

$$\mathcal{L}_\theta = \bar{\theta}\frac{g_3^2}{32\pi^2}\epsilon^{\alpha\beta\mu\nu}G^a_{\alpha\beta}G^a_{\mu\nu} \tag{1.46}$$

where $\bar{\theta} = \theta_{QCD} - \theta_Y$ and $\theta_Y = arg\,(det(Y_dY_u))$. This $\bar{\theta}$ is a physical parameter because any more chiral rotation can be adjusted between $\theta_{QCD}$and θ_Y. Therefore, we should observe this $\bar{\theta}$ parameter in experiments. We observe the effect $\bar{\theta}$ in computing the neutron electric dipole moment (EDM) and theoretically neutron EDM comes out as, $|d_n| = 5.2\times10^{-16}$ e cm $\bar{\theta}$. There is also experimental bound on d_n which is, $|d_n| < 2.9\times10^{-26}$ e cm. Therefore, from the above two observation we get bound on the $\bar{\theta}$ parameter,

$$\bar{\theta} < 10^{-10}. \tag{1.47}$$

The value of $\bar{\theta}$ is very small as compared to the weak scale CP violation and this is called the strong CP problem. One of the solution in the context of SM was proposed which was if one of the quark is massless then we can rotate away the θ parameters and make $\bar{\theta} = 0$. But this is not the case because in SM all the quarks are massive. Another BSM solution of this problem is the Peccei-Quinn symmetry which makes this $\bar{\theta}$ parameter as dynamical variable and in that case, it can take zero value and solve the strong CP problem.

1.2.6 Gravitational force

In nature, we have four kinds of interaction namely electromagnetic interaction, weak interaction, strong interaction and gravitational interaction. SM does not contain any information about the gravitational force and talks about the remaining three forces. Moreover, SM has no clue why the gravitational interaction is so weak compared to the other three interactions namely electromagnetic, weak and strong. Therefore, SM can not become a complete theory of nature and surely we need to extend the SM. One of these theories is the minimal supergravity where all the four interactions are included. Finally, the absence of gravitational force in the SM can also be one of the important reason to demand a beyond standard model theory.

1.2.7 Gauge coupling unification

SM gauge group consists of $SU(3)_c \times SU(2)_L \times U(1)_Y$ and each group is associated with their corresponding gauge coupling which are g_3, g_2, g_1 (g_N for $SU(N)$). If we assume that in the early Universe all these gauge couplings are unified to a single gauge coupling as predicted in the grand unified theories (GUT). If we study the running of the gauge couplings then we need to calculate the β-function which evolve the gauge couplings by the following equation,

$$\frac{dg_i}{dln\mu} = \mu\frac{dg_i}{d\mu} = \beta_i(g_i) = \frac{b_i}{4\pi}g_i^3 . \qquad (1.48)$$

If we make substitution, $\alpha_i = \frac{g_i^2}{4\pi}$, then the above equation takes the following form,

$$\begin{aligned} \frac{d}{dlnQ}\left(\frac{1}{\alpha_i}\right) &= \frac{b_i}{4\pi} \\ \frac{1}{\alpha_i(Q)} &= \frac{1}{\alpha_i(Q_0)} + \frac{b_i}{2\pi}ln\left(\frac{Q_0}{Q}\right) \end{aligned} \qquad (1.49)$$

where Q is the energy running scale of the theory and b_i is given by,

$$b_i = -\frac{11}{3}C_2(Adj) + \sum_R\left(n_{WF}I(R) + \frac{1}{6}n_S(R)I(R)\right), \qquad (1.50)$$

the first term is the contribution of the gauge bosons, $C_2(Adj)$ is the Casimir operator in adjoint representation for $SU(N)$ which is $C_2(Adj) = N$. The second term (first term in the bracket) represents the contribution due to the Weyl fermions, $n_{WF}(R)$ is the number of Weyl fermion in representation R, and $I(R) = \frac{1}{2}$ for fundamental representation. Remaining term is coming from the contribution of complex scalar, $n_S(R)$ is the number of complex scalars in the representation R. In the case of SM, b_i comes in the following order,

$$b_3 = -7,\ b_2 = -\frac{19}{6},\ \text{and}\ b_1 = \frac{2}{3}, \tag{1.51}$$

b_3, b_2 which are associated with $SU(3)_c$ and $SU(2)_L$ are asymptotically free and b_1, corresponding to $U(1)$, is not asymptotically free. In Fig. 1.2, the running of all the three

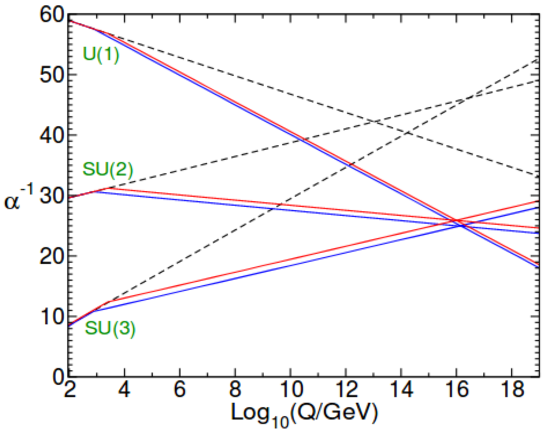

Figure 1.2: Gauge coupling unification for SM (dashed lines) and SUSY (solid lines). The image has been borrowed from, A Supersymmetry primer by S Martin (Adv.Ser.Direct.High Energy Phys. 21 (2010) 1-153).

gauge couplings have been shown by dashed lines and clearly, they never coincide to the single coupling at high energy. On the other hand in SUSY theory, b_i changes their magnitude as well as sign and it is possible to unify them as shown by the solid lines.

1.3 Evidences for dark matter

There are many pieces of evidence which support the presence of dark matter in the Universe and will be discussed briefly in this section.

1.3.1 Study of Galaxy Cluster

The hint for the presence of the dark matter (DM) was first observed by the Swedish scientist F. Zwicky when he was studying the Coma cluster. The detailed study regarding this can be found in [14] and we will briefly summarize the result here. As we will see in the subsequent paragraph that the most important thing in Zwicky's study was the determination of the nebulae masses. He used three techniques in doing so and are as follows,

- virial theorem of classical mechanics,
- observation of gravitational lens effect among the nebulae and
- using statistical mechanics.

  We briefly discuss here the virial theorem approach to determine the nebulae mass only while the details and the other two methods can be found in [14].

Virial theorem : We consider a nebulae (a) is at a distance $\vec{r}_a$ with mass m_a and it feels the external force $\vec{F}_a$

$$\vec{F}_a = m_a \frac{d^2\vec{r}_a}{dt^2} \tag{1.52}$$

After dot product with $\vec{r}_a$ and summing over a we get,

$$\begin{aligned}\sum_a \frac{1}{2}\frac{d^2(m_a^2 r_a^2)}{dt^2} &= \sum_a \vec{r}_a \cdot \vec{F}_a + \sum_a m_a \left(\frac{d\vec{r}_a}{dt}\right)^2 \\ \frac{1}{2}\frac{d^2 I_{MI}}{dt^2} &= W_{vir} + 2K \qquad (1.53)\end{aligned}$$

where $I_{MI} = \sum m_a r_a^2$ is the moment of inertia of the cluster, $W_{vir} = \sum_a \vec{r}_a \cdot \vec{F}_a$ is called the Virial of the cluster and K represents the sum of the kinetic energy for all nebulae in the cluster. If the cluster is stationary then its I_{MI} fluctuates around a mean value, say I_{MI}^0, then time average of its derivative vanishes. Therefore, we are left with the following equation,

$$W_{vir} + 2K = 0 \qquad (1.54)$$

Considering the fact that Newton's inverse square law describes the dynamics of the nebulae accurately, one can easily show that

$$\begin{aligned}W_{Vir} &= \sum_a \vec{r}_a \cdot \vec{F}_a \\ &= -\frac{1}{2}\sum_{a,a\neq b} \frac{G m_a m_b}{|\vec{r}_a - \vec{r}_b|} \qquad (1.55)\end{aligned}$$

which is the total gravitational energy of the system, G is the Newton's gravitational constant. If we assume uniform distribution of matter in the galaxy then we can estimate the Virial energy of the system in the following way,

$$\begin{aligned}W_{vir} &= -\int_0^R G \frac{(\frac{4\pi r^3 \rho}{3}) 4\pi r^2 \rho dr}{r} \\ &= -\frac{3GM^2}{5R}. \qquad (1.56)\end{aligned}$$

Taking the average velocity one more time over the whole cluster (define as $\bar{\bar{v}}$), we can write,

$$\sum m_a v_a^2 = M\bar{\bar{v^2}} \tag{1.57}$$

where M is the total mass of the cluster. Substituting the above expressions in Eq. 1.54, we get the total mass of the cluster as follows,

$$M = \frac{5R\bar{\bar{v^2}}}{3G}\,. \tag{1.58}$$

Using the velocity of the nebulae which was available at that time $\bar{\bar{v^2}} \sim 5\times 10^{15}$ cm^{2}sec^{-2}, astronomer F. Zwicky gave the bound on the mass of the coma cluster which is $M > 9\times 10^{46}$ gm. The Coma cluster contains around 1000 nebulae, hence the mass associated to each nebulae would be $M > 9\times 10^{43}$ gm $\sim 4.5\times 10^{10} M_\odot$. This result is somewhat unexpected to the value which we get after measuring the luminosity of the cluster which is roughly around $M \sim 8.5\times 10^{7} M_\odot$. Therefore, we need a multiplicative factor of 500 to match these two number. The inevitable consequence of this result is that in the coma cluster a large fraction of non-luminous matter is present and in other word it is the evidence of the presence of the dark matter in the cluster.

1.3.2 Flatness of the Galaxy rotation curve

Four decades after the study of F. Zwicky, Rubin-Ford studied the velocity of the stars in Galaxy [15] and they drew the same conclusion and hinted the presence of the excess matter in the Galaxy. Their idea was based on the classical object of mass, m, rotating around a heavy object of mass M at a distance r. To keep the system in orbit, the gravitational and the centrifugal force has to be equal which is,

$$\frac{mv^2}{r} = \frac{GMm}{r^2}\,. \tag{1.59}$$

Considering mass is uniformly distributed in the Galaxy bulge with mass density ρ, then

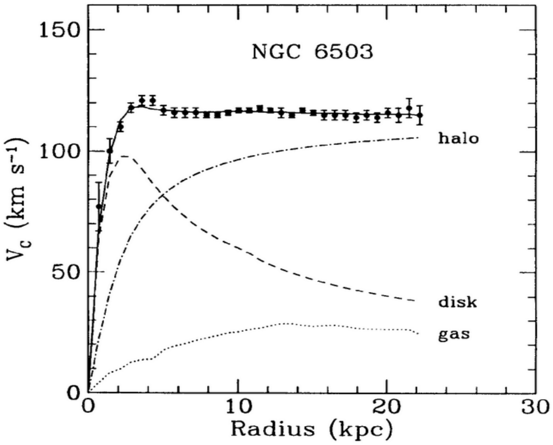

Figure 1.3: Galactic rotation curve.

mass contained within radius r is, $M = \frac{4}{3}\pi r^3 \rho$. Therefore within the Galactic bulge, we expect the velocity of an object increases with the distance *i.e* $v \propto r$ (obtained from Eq. 1.59). If we go outside of the Galactic bulge then the mass is fixed and the velocity must fall with the square root of the distance,

$$v \propto \frac{1}{\sqrt{r}}. \tag{1.60}$$

But instead of this falling behaviour of the velocity with distance, they observed the constant value of the velocity of the star with the distance which is moving outside the galactic bulge. This behaviour can be explained if we consider that the mass is linearly increased with the distance, $M \propto r$, then the velocity of the object does not depend on the distance *i.e.* v = constant. Therefore, there exists a huge amount of non-luminous matter namely dark matter in the galaxy. The other possible solution of the flatness of the galaxy rotation curve can be explained by the modified Newtonian dynamics, proposed by Milgrom which will be discussed in the latter part of this section.

1.3.3 Observation of Bullet cluster

In 2006, astronomers working on HST (Hubble Space Telescope) and Chandra X-ray observatory disclosed the observation of bullet cluster [16–18] at a distance around 4-billions light-years away from the earth. Bullet cluster is the phenomenon of the collision between two galaxy clusters. The observation of the bullet cluster implies the direct evidence of the presence of the extra non-luminous matter namely the DM in the universe. In bullet cluster, two measurement techniques are used to measure the center of mass, one of them is the X-ray observation and another one is the gravitational lensing. The bullet cluster is a high-speed collision between the two clusters. Because of the collision the gases in each cluster collide with each other and emit high energy X-ray. From this X-ray observatory point, we get the information about the centre of the baryonic matter. This collision implies (as shown in Fig. 1.4) that the ordinary matter interacts with each other and try to merge each other. In Fig. 1.4, this phenomenon is shown by the red regions.

Figure 1.4: Observation of bullet cluster. Image credit: NASA, CXC, STScl.

On the other hand to get the information about the total mass, one can use the gravitational lensing technique by determining the bending of the light. Therefore, for gravitational lensing to happen successfully, we need a background light source and the light will pass through the heavy object and finally reach the observatory. Since light bends due to the heavy objects in space-time which is $\alpha_{bend} = \frac{4GM_{lens}}{R}$, where α_{bend} is the bending angle, M_{lens} is the total lensing mass and R is the radius of it. Therefore, by determining the bending angle we can infer the mass of the cluster and its centre of mass as well. The blue regions obtained in Fig. 1.4 are obtained by the gravitational technique. From the figure, it is very much clear to us that the centre of mass which we obtained from the luminous object does not coincide with the centre of mass of the cluster. Therefore, the observation of bullet cluster provide us with useful pieces of information which are as follows,

- this is the phenomenon just after the collision of the two galaxy clusters.
- the centre of mass and the centre of the ordinary matter (which is the X-ray emitting points) do not coincide. It indicates that there exist excess matter namely the dark matter.
- Another information which we get is that the ordinary matter interact with each other hence trying to merge each other (red regions). But the DM is very less interactive and hence they pass through each other *i.e.* DM is almost collisionless.

1.3.4 CMB anisotropy

The measurement of the cosmic microwave background (CMB) temperature by the Wilson and Penzias not only solidify the base of the Big-Bang theory, but further investigation on the CMB spectrum and finding the anisotropies in the spectrum implies the amount of baryonic matter and the dark matter present in the Universe. In explaining the anisotropy in the CMB spectrum [19, 20] as shown in Fig. 1.5, we assume that there exists a density fluctuation in the Universe which might originate either during the inflation epoch or some sort of the topological defects present at the early evolution of the Universe. Due to these density fluctuations, in the early universe baryonic acoustic oscillation (BAO) happen. BAO reveals two types of regions, one of them is more densed for the baryonic matter, hence have more interaction with the photon and the other one contains less baryonic matter but more non-baryonic matter, hence this region is more gravitationally interacting than the repulsive force which generate due to the baryon matter interaction with

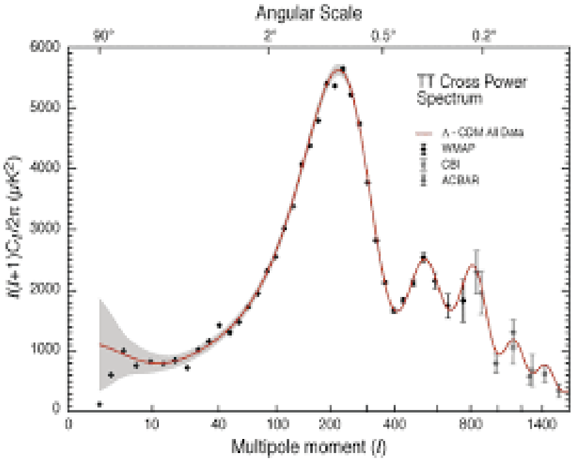

Figure 1.5: CMB power spectrum measured by WMAP [19] and Planck [20].

photon. Therefore, due to these force variation among the matter, rarefaction and compression kind of phenomenon must have been happened. When photon decouples from the cosmic plasma then only gravitational interaction dominates and the CMB anisotropy is the imprints of these rarefaction and compression events which were happening before the photon decoupling. The odd peaks (first, third, etc) happen due to the compression and the even peaks (second, fourth, ...) happen due to the rarefaction. From these CMB anisotropies, we get much useful information quantitatively like the amount of matter present in the universe, Hubble constant value and also the geometry of the Universe. The first peak imply the geometry of the universe and suggest that the universe is spatially flat, the ratio between the first and the second peak gives us the amount of baryonic matter present in the Universe, the ratio between the first and the third peak estimate the total amount of matter present and the tail towards the high l value gives us the value of the expansion rate of the Universe which is the Hubble constant.

1.4 Alternative Explanation of dark matter

Before going to the particle candidate for the dark matter, here we explain two well known alternative scenario where we don't need to extend the SM. The two proposals are the modified Newtonian dynamics (MOND) and massive astrophysical compact halo object

(MACHO).

1.4.1 Modified Newtonian dynamics

There exist an alternative theory called modified Newtonian dynamics proposed by the Milgrom in 1982 [21]. Instead of considering the idea of dark matter they tried to explain the flatness of the rotation curve in the galaxy by modifying the Newtonian dynamics at the Galactic scale. Newton's law is well tested when the object moves very fast near to the galaxy but when the object is outside of the galactic centre then they move slowly. Therefore, one needs to modify Newton's dynamics and this is the main statement of the MOND theory. The modification is very simple and we just need to modify Newton's second law in the following way,

$$F = m\mu(x)a\,, \tag{1.61}$$

where F is the force on the moving object, $x = \frac{a}{a_0}$, a is the acceleration of a m mass object, and a_0 is some constant value which differentiates between the Newtonian regime and the MOND regime. The new function $\mu(x)$ is called the interpolation function with the following two limits,

$$\begin{aligned} \mu(x) &= 1 \text{ for } x \gg 1 \\ &= x \text{ for } x \ll 1\,, \end{aligned} \tag{1.62}$$

and in between one can formulate this as $\mu(x) = \frac{x}{1+x}$. From Eq. 1.61, we have the following form of the velocity in the regime $x \ll 1$,

$$\begin{aligned} F &= m\frac{a^2}{a_0} \\ \frac{GmM}{r^2} &= m\frac{\left(\frac{v^2}{r}\right)^2}{a_0} \\ v &= (GMa_0)^{\frac{1}{4}}\,. \end{aligned} \tag{1.63}$$

By fitting the data with rotation curve, $a_0 = 1.2 \times 10^{-10}$ ms^{-2}. Although, MOND theory can explain flatness of the rotation curve and now they are proceeding to explain the phenomenon related to gravitational lensing [22]. But there are many things which are still unexplained from the MOND theory perspectives and are as follows,

- The general theory of relativity (GTR) is a very successful theory of gravity and prime examples are our GPS where GTR is used and the recent discovery of the gravitational wave by LIGO collaboration.
- When it comes to the fact of explaining the CMB anisotropy then this theory has no clue and one of the big drawback of the MOND theory.
- The observation of the bullet cluster indicates that the centre of mass of the clusters and the centre of the luminous part do not coincide and it can not be explained just by modifying the Newtonian dynamics.

There are many things to be explained by MOND before we accept it as the successful theory of DM.

1.4.2 MACHO type objects

A massive astrophysical compact halo object (MACHO) is an astronomical object and its presence in enough amount can explain the mystery of dark matter. Generally, MACHO objects are non-luminous and hence hard to detect by the terrestrial observatory which used techniques other than gravitational lensing. MACHO type objects are made of by baryonic matter and are not associated with any planetary system. The popular candidates which fall in the MACHO category are a primordial black hole (PBH), neutron stars, brown dwarfs, white dwarfs, red dwarfs and unassociated planets. The detection technique of MACHO type objects is based on the principle of gravitational lensing. In particular, it works on the microlensing technique which means that when MACHO type

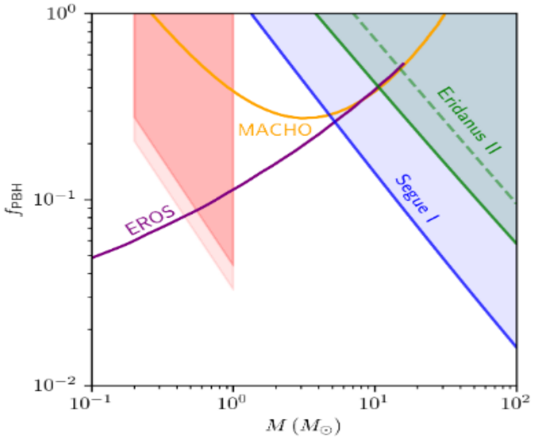

Figure 1.6: Bound on the fraction of the MACHO type objects contains in the total amount of dark matter. The bounds from the different collaboration are listed in the following Refs. [23–26] in detail.

objects move around and passes between the luminous background object and the detector, then at particular alignment of the three objects (background source, MACHO object and the detector) there will be a peak in the source light and we can confirm in this way that something has passed through this region. This works on the principle of microlensing light amplification. There are experimental collaborations who are trying to detect MACHO type objects and the familiar ones are the EROS2 [23] and MACHO [27] collaboration. MACHO claimed that they have observed the MACHO type of objects which can be around 20% of the total amount of the dark matter. But their claim has been challenged by the survey of the EROS2 and Hubble space telescope. The bound on the MACHO type of objects mass and its fraction to the total amount of the dark matter [28] has been displayed very beautifully in Fig. 1.6.

There is also a strong constraint on this type of MACHO objects which are made of the baryonic matter from the baryonic acoustic oscillation in CMB and the large scale structure of the Universe. We know from these collaborations precisely the amount of baryonic matter present in comparison to the total matter content of the Universe. Therefore, to explain these extra matters we need to consider the presence of the extra non-baryonic and non-luminous matter.

1.5 Particle candidate for dark matter

It is clear to us that we have a large amount of non-baryonic matter whose particle origin is still unknown to us. The percentwise amount of dark matter is 26% (Ω_{DM}), baryonic matter is around 5 % (Ω_B) and the remaining 69% of the energy density of the universe is called the dark energy (Ω_Λ). Although we don't have any confirmation about the DM candidate still to become a DM candidate it has to pass all the following ten criterion as listed in [29],

- it has to give the correct value of the DM relic density which we obtained from WMAP [19] and Planck data [20],
- it has to be cold,
- it has to be electrically neutral,
- need to check whether consistent with BBN or not,
- no effect in the stellar evolution,
- should follow the constraints from self-interaction,
- need to obey the bound from the direct detection of DM,
- constraint from γ-rays,
- other astrophysical bounds,
- prospects for its detection in the current earth-based experiments.

If we look into the SM we find that the candidate which satisfy many of the criteria listed above is the neutrino. But, it has been shown in the literature that neutrino is a relativistic particle and can not form halo structure which we observe in the Universe. Moreover, neutrinos are in eV scale, hence it cannot be the sole component of the dark matter. So, the only option for us to accommodate the DM candidate in the SM is to extend it by new particles and also a new gauge group if needed. In literature, a vast study in this direction exist and many authentic ideas about the DM candidate exist. The most popular ones are described very briefly below,

- In SUperSYmmetry (SUSY) the superpartner of the W-bosons (SU(2) gauge bosons) and the B-boson ($U(1)_Y$ gauge boson) mix with each other and in the mass basis the lightest component of them becomes a suitable DM candidate under R-parity or $\mathbb{Z}_2$ symmetry. This DM candidate is called neutralino. Therefore, in the SUSY extension under R-parity, a DM candidate appears naturally in the model.

- Lightest Kaluza-Klein (KK) particle, if we take motivation from string theory and consider a 5-dimensional universe and try to compactify it to our observed 4-dimensional universe, then under compactification of the extra space, Kaluza-Klein tower of particles appear in the theory. Under KK-parity symmetry, these particles can be viable DM candidates.

- Axion dark matter, as mentioned in Section 1.2.5 there exists a strong CP-problem *i.e.* we need a very small θ-parameter to explain the neutron electric dipole moment. Under Peccei-Quinn (PQ) symmetry this problem can be solved by making the θ parameter dynamical and it also gives a new CP-odd scalar particle which can be a viable DM candidate.

- Inert doublet model (IDM), in this type of model, SM is extended by a doublet and right handed fermions which are odd under some additional discrete symmetry $\mathbb{Z}_2$. The neutral component of the inert doublet or the right handed neutrino (depending on their masses) can be a very good DM candidate.

- SM can also be extended by scalars and fermions and under some suitable symmetry, they become stable and can be very good DM candidate with the minimal extension of the SM. Among them, the most popular ones are the DM annihilation via

Higgs-portal, gauge boson mediated processes and also the DM con-annihilation process. In this thesis, we will mostly focus on this type of dark matter candidate easily obtained by extending the SM and in some cases, we also extend the SM gauge group by some additional abelian or non-abelian gauge groups.

1.6 Determining the relic density of dark matter

The number density of a particle is governed by the Boltzmann equation (BE) and take the following form,

$$\mathcal{L}\Big[f_{\phi}(p^{\mu}_{\phi}, x^{\mu})\Big] = C\Big[f_{\phi}(p^{\mu}_{\phi}, x^{\mu})\Big]\,, \tag{1.64}$$

where p^{μ}_{ϕ} is the four momentum of the particle species ϕ at space time point x^{μ} while $\mathcal{L}$ and C are the Lioville's operator and collision operator, respectively. For the Friedmann–Lemaitre–Robertson–Walker (FLRW) metric, the Lioville's operator takes the following form,

$$\mathcal{L}\Big[f_{\phi}(E_{\phi}, t)\Big] = E_{\phi}\frac{\partial f_{\phi}}{\partial t} - H|\vec{p}_{\phi}|^2\frac{\partial f_{\phi}}{\partial E_{\phi}}\,, \tag{1.65}$$

where $H = \frac{\dot{a}(t)}{a(t)}$ is called the Hubble parameter.

The number density ($n_{\phi}(t)$) of the particle species ϕ at any stage of time can be expressed by using its distribution function in the following way,

$$n_{\phi}(t) = \frac{g_{\phi}}{(2\pi^3)}\int f_{\phi}(E_{\phi}, t)d^3p_{\phi}\,. \tag{1.66}$$

Using the above definition of number density, one can easily show that,

$$\frac{g_{\phi}}{(2\pi^3)}\int \frac{\mathcal{L}\Big[f_{\phi}(E_{\phi}, t)\Big]}{E_{\phi}}d^3p_{\phi} \;=\; \frac{\partial n_{\phi}}{\partial t} + 3Hn_{\phi}\,. \tag{1.67}$$

Therefore, for the process $\phi + i \to a + b$, Eq. (1.64) looks like as follows,

$$\frac{\partial n_\phi}{\partial t} + 3Hn_\phi \;=\; \frac{g_\phi}{(2\pi)^3}\int \frac{C\left[f_\phi(E_\phi,t)\right]}{E_\phi} d^3p_\phi \,. \tag{1.68}$$

Using the standard definition of the collision term, the right hand side of the above equation for the process $\phi + i \to a + b$ can be written as,

$$\frac{g_\phi}{(2\pi)^3}\int \frac{C\left[f_\phi(E_\phi,t)\right]}{E_\phi} d^3p_\phi = -\sum_{\text{spin}}\int d\Pi_\phi d\Pi_i d\Pi_a d\Pi_b \times (2\pi)^4\delta^4(p_\phi + p_i - p_a + p_b)$$
$$\times\left[|M|^2_{\phi+i\to a+b} f_\phi f_i (1\pm f_a)(1\pm f_b) - |M|^2_{a+b\to\phi+i} f_a f_b (1\pm f_\phi)(1\pm f_i)\right], \tag{1.69}$$

where $d\Pi_\alpha$ is the phase space density for the α^{th} particle and defined as,

$$d\Pi_\alpha = \frac{d^3p_\alpha}{2E_\alpha(2\pi)^3}\,, \tag{1.70}$$

and f_α is the distribution function of the species α and $+(-)$ sign implies for the fermions (bosons). $f_\alpha(p)$ implies the probability of the species α in that state for the incoming particle where $(1 \pm f_\alpha)$ factor implies the probability of the emptiness of the α species in the final state. The momentum, as well as energy conservation, are ensured by the 4-dimensional Dirac-delta function. $|M|^2_{\phi+i\to a+b}$ implies the modulus square of the amplitude for the process $\phi + i \to a + b$ after taking the average over the spin for the initial state particles and sum over the spin for the final state particles.

In order to simplify the Eq. (1.69), we make few well accepted assumptions by following the laws of physics which are the following,

- we assume that the final state particles reach thermal equilibrium as soon as they are produced. This is trivially true for the charged final state particles because it will see free photon roaming around for the interaction. This is even true for the neutral particle as well in most of the cases. Therefore, for the final state particle we use f^{eq}_α. Moreover, if we assume detail balance for any process then we can simply write,

$$n_a^{eq} n_b^{eq} = n_\phi^{eq} n_i^{eq} \,. \tag{1.71}$$

- for any process $\phi + i \rightarrow a + b$, we can write the following relation by the virtue of the unitarity of the S-matrix,

$$\sum_{\text{spin}} \int d\Pi_a d\Pi_b (2\pi)^4 \delta^4 (p_\phi + p_i \rightarrow p_a + p_b) |M|^2_{a+b\rightarrow\phi+i} = \sum_{\text{spin}} \int d\Pi_a d\Pi_b$$
$$\times (2\pi)^4 \delta^4 (p_\phi + p_i \rightarrow p_a + p_b) |M|^2_{\phi+i\rightarrow a+b} \,. \tag{1.72}$$

- the other relevant assumption is the use of the classical Maxwell-Boltzmann distribution for all the species without distinguishing between the Fermi-Dirac (for the fermions) and Bose-Einstein (for the bosons) distribution. Due to this assumption there will be no Bose condensation or Fermi degeneracy. Therefore, we can safely neglect the blocking or stimulated factor in Eq. (1.69) *i.e.* $1 + f_\alpha \simeq 1$ while $f_\alpha = e^{\frac{E_\alpha - \mu}{k_B T}}$, μ is the chemical potential and k_B is the Boltzmann constant.

The cross section for the process $\phi + i \rightarrow a + b$ are defined in the following way,

$$\sigma_{\phi+i\rightarrow a+b} = \frac{1}{4E_\phi E_i g_\phi g_i v} \int d\Pi_a d\Pi_b (2\pi)^4 \delta^4 (p_\phi + p_i \rightarrow p_a + p_b) \sum_{\text{spin}} |M|^2_{\phi+i\rightarrow a+b} \,, \tag{1.73}$$

where E_α, g_α are the energy and the internal degree of freedom of the species α, v corresponds to the relative velocity between the two incoming particles ϕ and i and have the following form in terms of the momentums and energies,

$$v = \frac{\sqrt{(p_\phi \cdot p_i)^2 - m_\phi^2 m_i^2}}{E_\phi E_i} \,. \tag{1.74}$$

Finally using the assumptions as stated above and the expression of the cross section, we can write the collision term in the following way,

$$\begin{aligned}\frac{g_\phi}{(2\pi)^3}\int\frac{C\left[f_\phi(E_\phi,t)\right]}{E_\phi}d^3p_\phi &= -\int\sigma_{\phi+i\rightarrow a+b}v\left(dn_\phi dn_i - dn_\phi^{eq}dn_i^{eq}\right)\\ &= -\langle\sigma v\rangle\left(n_\phi n_i - n_\phi^{eq}n_i^{eq}\right), \qquad (1.75)\end{aligned}$$

where the thermal average of the cross section times velocity implies the following form,

$$\langle\sigma_{\phi+i\rightarrow a+b}v\rangle = \frac{\int\sigma_{\phi+i\rightarrow a+b}v\,dn_\phi^{eq}dn_i^{eq}}{\int dn_\phi^{eq}dn_i^{eq}}\,. \qquad (1.76)$$

The above expression of the thermal average of the cross section times velocity has a practical form in terms of the Bessel function and given by,

$$\begin{aligned}f_1 &= \sqrt{s^2+(M_\phi^2-M_i^2)^2-2\,s\,(M_\phi^2+M_i^2)},\\ f_2 &= \sqrt{s-(M_\phi-M_i)^2}\,\sqrt{s-(M_\phi+M_i)^2}\,,\\ \langle\sigma v_{\phi+i\rightarrow a+b}v\rangle &= \frac{1}{8\,M_\phi^2M_i^2\,T\,\mathrm{K}_2\left(\frac{M_\phi}{T}\right)\mathrm{K}_2\left(\frac{M_i}{T}\right)}\times\\ &\quad\int_{(M_\phi+M_i)^2}^{\infty}\frac{\sigma_{\phi i\rightarrow ab}}{\sqrt{s}}\,f_1\,f_2\,\mathrm{K}_1\left(\frac{\sqrt{s}}{T}\right)\mathrm{d}s, \qquad (1.77)\end{aligned}$$

where M_ϕ and M_i correspond to the mass for ϕ and i, respectively, T is the evolution temperature of the Universe and K_2 is the Bessel function of the second kind. Therefore, if we substitute the collision term in Eq. (1.68) then we get the familiar form of the Boltzmann equation which is,

$$\frac{\partial n_\phi}{\partial t}+3Hn_\phi = -\langle\sigma_{tot}v\rangle\left(n_\phi n_i - n_\phi^{eq}n_i^{eq}\right), \qquad (1.78)$$

where $\sigma_{tot}=\sum_{a,b}\sigma_{\phi+i\rightarrow a+b}$, means after considering all the annihilation mode of ϕ and i. In the above equation if we assume that the initial density of ϕ and i are same *i.e.* $n_\phi = n_i = n$, then the above equation depends only on number density n. Moreover, a factor of 1/2 will appear in the right hand side of the above equation if the initial particle is not its own self conjugate. The above equation looks like as follows,

$$\frac{\partial n}{\partial t}+3Hn=-\langle\sigma_{tot}v\rangle\left(n^2-n^{eq2}\right). \tag{1.79}$$

We can further simplify the above equations by defining the co-moving number density

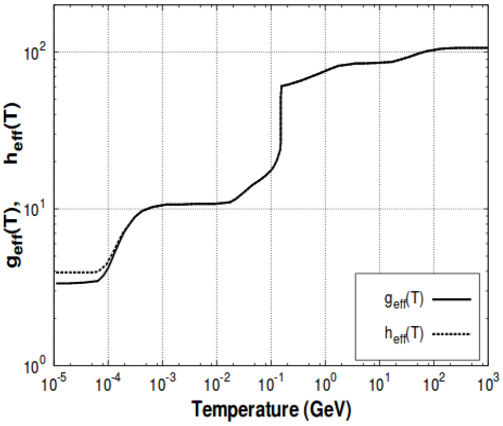

Figure 1.7: Variation of $g_{eff}(T)$ and $h_{eff}(T)$ with the temperature of the Universe.

(Y) which is the ratio between the number density and the entropy, $Y=\frac{n}{s}$, where s is the entropy of the Universe. Define a new variable which is the inverse of the temperature, $z=\frac{m}{T}$. By using the time temperature relation, Hubble in terms of matter density, matter density and entropy in terms of temperature, which are as follows,

$$\begin{aligned}\frac{dt}{dT} &= -\frac{1}{HT}\left(1+\frac{Th'_{eff}(T)}{3h_{eff}(T)}\right),\\ H &= \sqrt{\frac{8\pi G\rho}{3}},\\ \rho &= g_{eff}(T)\frac{\pi^2T^4}{30},\\ s &= h_{eff}(T)\frac{2\pi^2T^3}{45}.\end{aligned} \tag{1.80}$$

We can write the Eq. (1.79) in the following form [30],

$$\frac{dY}{dz}=-\left(\frac{45G}{\pi}\right)^{-1/2}\frac{g_*^{1/2}m}{z^2}\langle\sigma_{tot}v\rangle\left(Y^2-Y^{eq2}\right), \tag{1.81}$$

where $g_*^{1/2}$ is defined in the following way,

$$g_*^{1/2} = \frac{h_{eff}(T)}{\sqrt{g_{eff}(T)}}\left(1 + \frac{T h'_{eff}(T)}{3 h_{eff}(T)}\right), \tag{1.82}$$

where G is the Newton's gravitational constant, $g_{eff}(T)$ and $h_{eff}(T)$ are the matter and the entropy degree of freedom [1]. Moreover, the quantities $g_{eff}(T)$ and $h_{eff}(T)$ are related to the relativistic degree of freedom of the Universe at the time of its evolution and at temperature T and describe in the following way,

$$\begin{aligned} g_{eff}(T) &= \sum_{b=bosons} g_b \left(\frac{T_b}{T}\right)^4 + \frac{7}{8}\sum_{f=fermions} g_f \left(\frac{T_f}{T}\right)^4 , \\ h_{eff}(T) &= \sum_{b=bosons} g_b \left(\frac{T_b}{T}\right)^3 + \frac{7}{8}\sum_{f=fermions} g_f \left(\frac{T_f}{T}\right)^3 , \end{aligned} \tag{1.83}$$

where g_b, g_f are the internal degree of freedom of the bosonic and fermionic fields, respectively at temperature T. The variation of $g_{eff}(T)$ and $h_{eff}(T)$ with the temperature of the Universe have been shown in Fig. 1.7. These two values match each other for the entire evolution of the Universe and start deviating when the neutrino decouple from the thermal plasma which happens between 1-3 MeV.

Finally, we can determine the co-moving number density of the DM today by solving Eq. (1.81) easily because all the necessary information to solve the equation are known. Relic density of DM (of mass m) can be determined by the following relation,

$$\Omega h^2 = 2.755 \times 10^8 \left(\frac{m}{\text{GeV}}\right) Y(T \to 0), \tag{1.84}$$

where $Y(T \to 0)$ is the co-moving number density of DM today. In the recent time, the

---

[1] Sometime we use the notation $g_\rho(T)$ and $g_s(T)$ instead of $g_{eff}(T)$ and $h_{eff}(T)$ in the later part of the thesis.

observed value of the dark matter relic density given by the Planck collaboration [20], is

$$\Omega_{DM}h^2 = 0.1197 \pm 0.0022. \tag{1.85}$$

In this thesis we have used the above relic density bound.

1.7 Types of Dark Matter

Assuming the fact that DM is mostly non-baryonic, we can classify the DM in two ways. One of them is by its way of production and another one is depending on its mass. First, we discuss its distinguished nature from the production viewpoint and next, we distinguish them by their masses.

1.7.1 DM classification by thermal history

The production mechanism of DM from the thermal point of view can be classified in two ways namely thermal production of DM and non-thermal production of DM. We briefly discuss the two different way of DM production.

Thermal production of DM

In this mechanism, one assumes that DM produce simultaneously with the visible matter and remain in thermal equilibrium until the Universe temperature goes below DM mass. During its thermal equilibrium with the cosmic soup, DM number density varies differently with temperature depending on its relativistic and non-relativistic nature,

$$\begin{aligned} n^{eq} &= \frac{g_{eff}}{\pi^2}\zeta(3)T^3 \text{ for relativistic species} \\ &= g_{eff}\left(\frac{mT}{2\pi}\right)^{\frac{3}{2}} e^{-\frac{m}{T}} \text{ for non-relativistic species}. \end{aligned} \tag{1.86}$$

The number density of the particle decrease with the temperature and hence at a particular value of the Universe's temperature its interaction rate $\Gamma = n^{eq}\langle\sigma v\rangle$ become smaller than the Hubble rate of the Universe. As a result, the DM particle can not interact with each other and its number density freezes-out to that particular value. The temperature at which the freeze-out or decoupling of the DM from the thermal plasma happens is called the freeze-out temperature and we can be determine its numerical value by equating the DM interaction rate with the Hubble rate of the Universe in the following way,

$$n^{eq}\langle\sigma v\rangle = H\,. \tag{1.87}$$

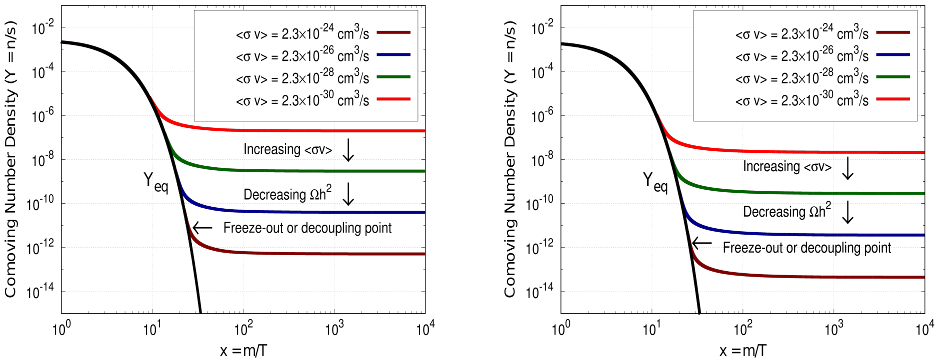

Figure 1.8: DM production by the freeze-out mechanism for two different values of the DM mass.

In this type of DM production, the co-moving number density is inversely proportional to the thermal average of the cross-section times velocity *i.e.* $Y \propto \frac{1}{\langle\sigma v\rangle}$. Therefore, more the value of $\langle\sigma v\rangle$ less amount of DM present in the Universe. This can be easily seen in Fig. 1.8. The DM produced by this mechanism is called weakly interacting massive particle (WIMP). In this mechanism, DM can be successfully produced in the correct ballpark value (given by WMAP and Planck) for $\mathcal{O}(1)$ coupling strength, hence it is conceptually easy to design the detection technique for this type of DM. So far vastly used techniques to detect this type of DM are the direct detection, indirect detection and collider search which we briefly discuss in the next section. In Chapters [2, 3, 4], we discuss this type of DM in this thesis. For the numerical study of this type of DM, we use the well known package micrOMEGAs [31–33].

Non-thermal production of DM

The DM production by the freeze-out mechanism is very charming and conceptually easy to make a detector to detect them. But after extensive study of this type of DM at the direct detection, indirect detection and collider, we are unable to find the hint of this type of DM. Therefore, we need to go beyond the usual freeze-out mechanism. One of the beyond freeze-out scenarios is the non-thermal way of DM production and this mechanism is called the freeze-in mechanism. In the left panel (LP) of Fig. 1.9, one can see that for the freeze-in mechanism we need very small coupling strength as compared to the freeze-out mechanism. The price we pay for such small coupling is that this type of non-thermal DM is very difficult to detect at any terrestrial experiments. One known possibility to detect this type of DM is to look for the long-lived particle by observing the displaced vertex type of signature. The production mechanism of freeze-in mechanism [34] has been displayed in the right panel (RP) of Fig. 1.9. Due to the feeble coupling of the DM, this type of DM can never reach thermal equilibrium with the cosmic soup. In producing the DM by the freeze-in mechanism, we make the crucial assumption that in the very early time DM is

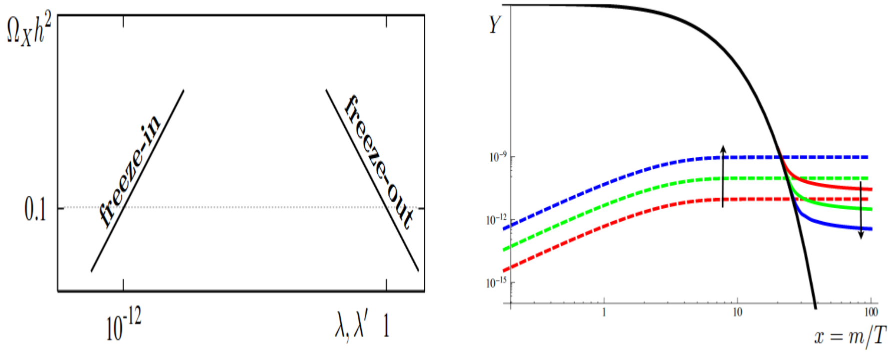

Figure 1.9: LP: Schematic diagram shows the order of the coupling strength for freeze-in and freeze-out. RP: Variation of co-moving number density with the inverse of temperature for the freeze-out and the freeze-in mechanisms. Figures borrowed from [34].

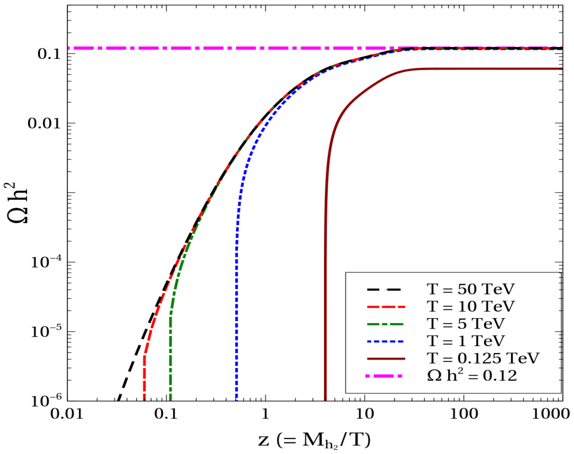

Figure 1.10: Variation of relic density with the inverse of temperature for different initial value where the coupling strength is $\mathcal{O}(10^{-11})$ and DM mass is 50 GeV.

produced in a negligible fraction from the inflaton decay after the inflation. Moreover, its production is independent of the UV quantities like the reheat temperature of the Universe and the production is IR dominated *i.e.* depends on the low-temperature regime which is around the DM mass. In this mechanism as opposed to the freeze-out mechanism, DM is produced more with the increasing of the coupling strength as shown in Fig. 1.9. In the freeze-in mechanism, DM is mostly produced when the Universe temperature goes below DM mass. A particular variation of relic density of the DM produced by the freeze-in mechanism with the inverse of the temperature has been shown in Fig. 1.10.

1.7.2 DM classification depending on masses

DM can also be classified depending on their masses or more appropriately by comparing its free streaming length (FSL) with the FSL of the photo galaxy. Depending on FSL, we get three types of DM which are cold, warm and hot dark matter. For cold DM, its FSL is smaller than the FSL of photo galaxy. This type of DM mass can range from Solar mass (MACHO type object) to MeV scale mass. Neutralino, gravitino, heavy sterile neutrino and many more DM candidates fall in this category. Another one is warm DM where its FSL is comparable to FSL of photo galaxy. The warm DM mass range varies from 300 eV to 3000 eV. This type of DM suffer from the absence of many suitable DM candidate and the most promising ones are the light sterile neutrino. In the hot DM category, its FSL is much larger than the FSL of photo galaxy. Generally eV scale mass falls in this category. In SM, the neutrino is a suitable candidate for hot DM candidate. We describe all the three DM detection methods briefly in the subsequent part.

1.8 Detection of Dark Matter

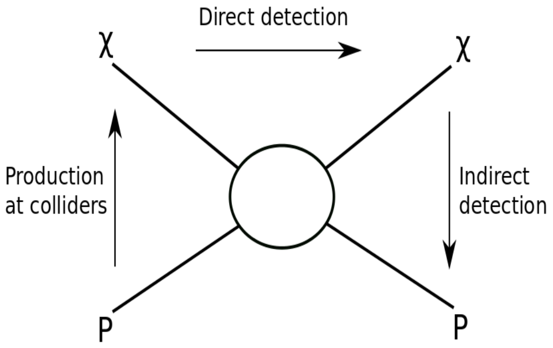

Figure 1.11: Schematic diagram of DM detection by direct detection, indirect detection and collider search. Figure is taken from [35].

As mentioned earlier WIMP type DM can be detected by the three techniques which are direct detection (DD) of DM, indirect detection (ID) of DM and collider search. In Fig. 1.11, the three types of DM detection have been shown schematically.

1.8.1 Direct Detection

DD detection experiments primary aim to detect the WIMP type DM particle (denoted by ϕ). If we assume that our Milky way is composed of WIMP type DM then the flux in the vicinity of the earth is of the order of $10^5 \times \left(\frac{100\,\text{GeV}}{M_\phi}\right)\,\text{cm}^{-2}\text{s}^{-2}$. This is sufficiently large flux, hence we can expect to detect them at the terrestrial detectors even if WIMP type DM interacts weakly with the detector nuclei. DD experiments focus to detect WIMP by observing the recoil of the nucleus or quantitatively they try to measure the rate, R, recoil energy, E_R, and and in some cases direction of the incident WIMP if the detector has directional sensitivity.

The differential event rate for the WIMP type DM (of mass M_ϕ) colliding with the nucleus of M_N is given by,

$$\frac{dR}{dE_R} = \frac{\rho_0}{M_N M_\phi} \int_{v_{min}}^{\infty} v f(v) \frac{d\sigma_{WN}(v, E_R)}{dE_R} dv, \tag{1.88}$$

where $\rho_0 = 0.3$ GeV cm^{-3} at a distance 8 kpc from the center of the Milky way galaxy, $f(v)$ is the isotropic, Gaussian velocity of DM near earth,

$$f(v) = \frac{1}{\sqrt{2\pi}\sigma} exp\left(-\frac{|v|^2}{2\sigma^2}\right), \tag{1.89}$$

where the speed dispersion, σ, is related to the circular velocity, v_c, by $\sigma = \sqrt{3/2}\, v_c$ and $v_c = 220 \pm 20$ km s^{-1}, E_R is the recoil energy and can be written in terms of the scattering angle (θ^*) as,

$$E_R = \frac{\mu^2 v^2 (1 - \cos\theta)}{M_N}, \tag{1.90}$$

where $\mu = \frac{M_N M_\chi}{M_N + M_\chi}$ is the reduced mass of WIMP and nucleus. The lower limit in the velocity integration in Eq. (1.88) implies the minimum velocity is required to handover E_R amount of recoil energy to the nucleus and expressed as, $v_{min} = \sqrt{\frac{M_N E_R}{2\mu^2}}$. On the other hand the upper limit of integration is infinite but in principle it can not exceed the escape velocity of the Milky way galaxy which is, $v_{esc} = 650$ km s^{-1}. The quantity $\frac{d\sigma_{WN}(v, E_R)}{dE_R}$ is called the WIMP-nucleus differential cross section. In determining this quantity we need the microscopic physics input that means how DM interact with the nucleus and it contains lots of uncertainties in the nuclear form factor. In general, interactions are two types one of them is spin independent (happens due to the scalar and vector interaction of DM) and another one is the spin dependent interaction (happens due to the axial vector interaction) and the total differential cross section is sum of these two contributions,

$$\frac{d\sigma_{WN}}{dE_R} = \left(\frac{d\sigma_{WN}}{dE_R}\right)_{SI} + \left(\frac{d\sigma_{WN}}{dE_R}\right)_{SD}. \tag{1.91}$$

Finally, the total WIMP-nucleus cross section is measured by taking the coherent sum of the WIMP-nucleon cross section. A form factor $F(E_R)$ is introduced to account for the contribution of non-zero momentum transfer, $q = \sqrt{2M_N E_R}$, and the coherent loss which leads to the suppression in the event rate. Therefore, we can write the differential cross section as,

$$\frac{d\sigma_{WN}}{dE_R} = \frac{M_N}{2\mu^2 v^2}\left[\sigma_0^{SI} F_{SI}^2(E_R) + \sigma_0^{SD} F_{SD}^2(E_R)\right], \tag{1.92}$$

where σ_0^{SD} and σ_0^{SI} are the spin-dependent and spin-independent WIMP-nucleon cross section at zero momentum transfer.

Finally, the total event rate in the unit of $\mathrm{kg}^{-1}\mathrm{day}^{-1}$ can be obtained by integration over the recoil energy of the differential event rate,

$$R = \int_{E_T}^{\infty} dE_R \frac{\rho_0}{M_N M_\chi} \int_{v_{min}}^{\infty} v f(v) \frac{d\sigma_{WN}(v, E_R)}{dE_R} dv, \tag{1.93}$$

where E_T is the minimum threshold energy which can be recorded by the detector. There are many earth based DD experiments which try to detect this keV recoil energy of the nucleus. To reduce the background, mainly the cosmic rays, this type of detector is located underground. These experiments mostly work on two types of detector technologies, one is the cryogenic detector and another one is the noble gas. The cryogenic detector is maintained below the 100 mK temperature and it detects the heat produced by the collision of DM particle with the atom of the crystal detector such as germanium. CDMS, CRESST, EDELWESS, EURECA fall in this kind of detector. In the case of Nobel liquid, it detects the scintillation light produced by the DM collision with the atom of the liquid Xenon and argon. The experiments are Xenon, LUX, ZEPLIN, DarkSide, PandaX,

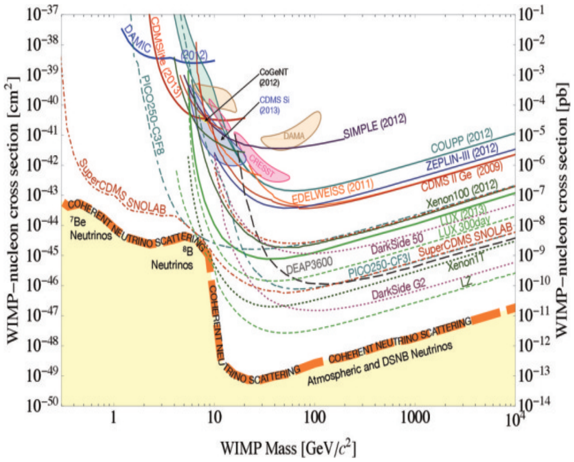

Figure 1.12: Bound on DM dd cross section from different experiments. Image source [36].

Darwin. The current bound and projected sensitivity of the proposed experiments [37] on the WIMP-nucleon DD cross-section are shown in Fig. 1.12.

1.8.2 Indirect Detection

Dark matter particles can also be detected indirectly by looking at the final state particles when they annihilate or when they decay to other particles. DM particle can annihilate to gamma rays, particle-antiparticle pair of the SM particle spectrum or if the DM is unstable, with the lifetime greater than the age of the Universe, then it can decay to SM particles. In indirect detection we look for the excess of gamma rays, anti-proton excess or positron excess in the high DM dense region (e.g. the centre of the Milky Way galaxy). The main difficulties of this type of detection are that the signal can be successfully explained by some unrecognised astrophysical source. Therefore, to claim any type of discovery by the indirect detection we have to be completely aware of the astrophysical source. We now discuss briefly the different indirect signal which we can have during DM annihilation or decay.

Gamma rays

The annihilation rate of DM to gamma rays which make an angle ψ with the galactic center is given by,

$$\phi_\gamma(\psi) \quad \simeq \quad 0.94\times10^{-13}\left(\frac{N_\gamma\sigma v}{\mathrm{cm}^3\mathrm{s}^{-1}}\right)\left(\frac{100\,GeV}{M_\chi}\right)^2 \mathcal{J}(\psi)\,\mathrm{cm}^{-2}\,\mathrm{s}^{-1}\,\mathrm{sr}^{-1}\,, \tag{1.94}$$

where the dimensionless parameter $\mathcal{J}(\psi)$ is defined as,

$$\mathcal{J}(\psi) = \frac{1}{8.5\,kpc}\left(\frac{1}{0.3\,GeV\,cm^{-3}}\right)^2 \int_{l.o.s}\rho^2(l)dl(\psi)\,, \tag{1.95}$$

$\rho(l)$ is the DM halo density along the line of sight (l.o.s) $l(\psi)$. $N_\gamma\sigma v$ is the annihilation rate times number of photon produced for the DM annihilation and it depends on the particular model on which we work. There are many experimental collaborations like HESS, MAGIC, CANGAROO, VERITAS and FermiLAT which are trying to observe the excess in the gamma rays. In 2012, Fermi-LAT collaboration [38] claimed the statistical evidence of 130 GeV gamma-ray excess and van be explained by DM annihilation. Several groups [39, 40] have pointed out the excess of gamma rays in the 1-3 GeV energy range after analysing the publicly available Fermi-LAT data [41]. This excess can be explained by the DM annihilation to different channels of SM particles. Another possible explanation of this excess is the millisecond pulsars [42, 43] but a recent study also disfavors this type of source for the excess.

Neutrino signal

We can also look for DM by observing the neutrino signal from its annihilation. Our solar system moves through the DM halo present in our galaxy. Although, the probability of scattering of DM with the sun's nuclei is very small, still in billion of years there would be sufficient accumulation of DM particle in the core of the sun. These accumulated DM particles annihilate and help in creating neutrino later on. Generally, neutrinos can be produced from the decay of the heavy quark, heavy gauge boson, other product of WIMP annihilation and they move towards the earth and can be identified by the large volume neutrino detector. If the capture rate and annihilation rate are large enough then they can reach thermal equilibrium and change of number density of DM will follow the equation below,

$$\frac{dN(t)}{dt} = C^{\odot} - A^{\odot} N(t)^2 - E^{\odot} N(t) , \tag{1.96}$$

where $C^{\odot}$ is called the capture rate of DM inside the sun, $A^{\odot}$ is the annihilation rate and $E^{\odot}$ implies the evaporation of DM. If DM mass is more than few GeV, we can neglect the evaporation term. Therefore, under $E^{\odot} \simeq 0$, we can solve the Eq. (1.96) easily and the annihilation rate takes the following form,

$$\begin{aligned} \Gamma_{anni-rate} &= \frac{1}{2} A^{\odot} N(t_{\odot})^2 \\ &= \frac{1}{2} C^{\odot} \tanh(\sqrt{C^{\odot} A^{\odot}}\, t_{\odot}) . \end{aligned} \tag{1.97}$$

where $t_{\odot}$ = 4.5 billion years is the age of our solar system. If the system satisfy the condition $\sqrt{C^{\odot} A^{\odot}}\, t_{\odot} \gg 1$, then we get,

$$\Gamma_{anni-rate} = \frac{C^{\odot}}{2} . \tag{1.98}$$

The above equation announces that the annihilation rate is determined by the capture rate and does not depend on the annihilation cross-section. Finally, the produced neutrinos heading towards earth can be detected by many experiments like IceCube, AMANDA and ANTARES.

Cosmic antimatter

The propagation of charged particle inside the Milky way is a very messy trajectory and cumbersome to figure out properly. The charged particles deflect due to the magnetic field and its irregularities. DM particle can create these charged particles inside the Milky way and when they propagate to earth detector, would give excess in the normal flux spectrum. In general different experiments like PAMELA, AMS-02, HAWC measure the antiproton, positron, antineutron, antihelium, antideuterium flux. These antiparticle can be produced from the DM annihilation,

$$\chi + \chi \rightarrow q\bar{q},\, W^+W^-, ... \rightarrow \bar{p},\, \bar{D},\, e^+,\, \gamma,\, \nu\,. \tag{1.99}$$

Although, it is a complex system, nevertheless we can write the master equation for space and energy distribution, $\Psi = \frac{dn}{dt}$ of the charged particle [44],

$$\partial_z(V_c\Psi) - K\Delta^2\Psi + \partial_E\left(b^{\text{loss}}(E)\Psi - K_{EE}(E)\partial_E\Psi\right) = q(X,E)\,, \tag{1.100}$$

where n is the number density, E is the energy, $V_c \sim 5$ to $10\ \text{km}\,\text{s}^{-1}$ measures the galactic convection wipes cosmic rays away from the disk, K is the spatial diffusion coefficient, K_{EE} is the diffusive coefficient, $b^{\text{loss}}(E)$ is the energy loss and $q(X,E)$ is the rates of production. The aforementioned master equation has been solved by using different techniques and all of them lead to the almost same flux at earth.

If the DM produce these cosmic antiparticles then we would expect a deviation in the normal flux. PAMELA and AMS-02 experiments have observed positron excess [45] in their flux. However, HAWC collaboration has challenged DM origin of this excess and hints that the flux is generated by the pulsars [46]. AMS-02 has also studied the antiproton data and they have found excess around 10 - 20 GeV and above 100 GeV. Although, the above 100 GeV antiproton excess can be explained by reacceleration of secondary antiproton due to the Supernovae remnants. AMS-02 has not yet published the data for the antideuterium and antihelium and could be a potential probe for the annihilating DM scenario.

Decaying DM

The gamma rays can also be produced from the decays of the decaying type DM. In general, we impose some additional symmetry to make the DM candidate stable for example R-parity conservation in SUSY. If we consider a model where the lifetime of DM is just greater than the age of the Universe then it is perfectly a suitable decaying type DM candidate. For such decaying DM, we can predict the flux of the gamma rays by the following relation,

$$\frac{d\phi_\gamma^{dec}}{dE} = \frac{2}{M_\chi}\frac{dN_\gamma}{dE}\frac{1}{8\pi\tau_\chi}\int_{l.o.s}\rho_\chi(l)dl, \tag{1.101}$$

where τ_χ is a decay lifetime of DM, in contrary to the annihilation flux decay flux is proportional to the halo density, $\rho_\chi(l)$, and $\frac{dN_\gamma}{dE}$ is the spectrum of produced gamma-rays from the hadronisation processes. These exist a 3.55 keV line reported by the XMM-Newton and Chandra satellites [47–49]. This signal can be explained by the decaying DM consideration. This signal can also be explained by considering the annihilating DM as well [50, 51].

1.8.3 Collider search

This is the era of the collider search because of the presence of the gigantic collider experiment Large Hadron Collider (LHC) and many more to come in future like International Linear Collider (ILC), Compact Linear Collider (CLIC). Collider search of DM implies to detect the DM directly by producing them at the collider, we focus on the LHC collider for DM detection. Since DM is a neutral and stable particle, hence it is difficult to track them at the collider. To understand the presence of the DM, we use the transverse missing energy kinematical variable, it is the missing part of the transverse momentum (p_T) in the transverse plane for the proton-proton (pp) collider like LHC. If we stay within SM then the missing energy signal can come from the neutrino (ν). At collider, to observe the DM we generally look for the signal like $\not{E}_T + n\,j + m\,l$, $n \geq 0$, $m \geq 0$, $n+m \geq 1$, j corresponds to the jets and l is for leptons. This type of signal always mimics by the SM particles. Therefore, one needs to have a very good understanding of the SM background before claiming any kind of discovery. If collider finds huge statistical significance of the above signal then we can interpret the signal in the following way by considering the beyond the standard model (BSM). For simplicity and to discuss it briefly we consider $n \geq 2$, $m = 0$ *i.e.* multi-jet + $\not{E}_T$ signal at the pp collider. To explain the signal by any BSM model we have to take care of the following main backgrounds (BKG) coming from SM which mimic the signal,

- $pp \to \text{QCD}\ (\leq 4j)$,
- $pp \to Z + 4j$,
- $pp \to W^{\pm} + \leq 4j$,
- $pp \to t\bar{t} + \leq 2j$,
- $pp \to W^{\pm}Z + \leq 2j$,
- $pp \to ZZ + \leq 2j$.

The production cross section of the above BKGs are huge, hence to survive the signal from the BKG, we need to use suitable cuts on different kinematical variables like p_T, $\not{E}_T$, invariant mass, rapidity (η) and so on. The aim of using different cuts is to reduce the BKGs without affecting the signal much and this way we can get the required statistical significance to explain the signal. This way we claim that this model is the probable model for the observed signal. There is a rigorous search to observe the SUSY model but so far null results have been observed for all channels and data is very much agreeing with the

SM. Another useful tool which people are using nowadays to distinguish the signal from the BKG very efficiently is machine learning. Therefore, by observing any new signal related to missing energy is a direct observation of DM at the collider.

1.9 Neutrino Mass

The presence of neutrino oscillation among the flavors is an inevitable consequence of neutrino mass and mixing. There is much experimental proof of neutrino oscillations, starting in the year 1967 as the outcome of Davis et. al. work [52, 53]. They were trying to measure solar electron neutrino (ν_e) flux by using the chlorine detector (ν_e + ^{37}Cl $\rightarrow$ e^- + ^{37}Ar) in the South Dakota's Homestake mine and found deficit in the neutrino flux in comparison to the standard solar model available that time [54, 55]. In the contemporary time of the Davis et. al. study, the oscillation phenomenon was not considered very seriously but came into consideration when many experiments in the later on like Kamiokande [56–59], Super-Kamiokande [60, 61], Gallex/GNO [62–65], and SAGE [66–69] also observed deficit in the solar neutrino flux.

The oscillation phenomenon was finally confirmed by the measurements at the Sudbary neutrino observatory in Canada (SNO) [3,70,71] using a heavy water detector (D_2O, D corresponds to the deuteron). In particular, they observed $1/3$ deficit in the solar ν_e flux for the charged current interaction ($\nu + D \rightarrow e^- + p + p$) and no deficit in the neutral current interaction ($\nu + D \rightarrow \nu + p + n$). Other experiments like KamLAND [4, 72, 73] in Japan and Borexino [74, 75] in Italy also played an important role in certifying the neutrino oscillation phenomenon during neutrinos travel.

The first confirmed evidence of neutrino oscillation (at 6.2σ statistical significance) came from the study of the atmospheric neutrinos by Super-Kamiokande collaboration [2, 76, 77]. These neutrinos are generated when the cosmic rays, mostly consisting of energetic proton, collide with the nucleon of the outer layer of the atmosphere producing mesons such as π^+, K^+. These produced mesons then decay to neutrinos in the following manner,

$$\pi^+, K^+ \to \nu_\mu \mu^+ \to \nu_\mu e^+ \nu_e \bar{\nu_\mu}\,,$$

$$\pi^-, K^- \to \bar{\nu_\mu} \mu^- \to \bar{\nu_\mu} e^- \nu_\mu \bar{\nu_e}\,,$$

which produced muon neutrino and electron neutrino fluxes. Around 1980, before SK data two experiments Irvine-Michigan-Brookhaven (IMB) [78–80] and KamiokaNDE [81,82] found the deficit in the atmospheric neutrino flux as well. More recently, K2K [83] and T2K [8,9] in Japan and MINOS [84,85] and NOνA [10,11] in USA have further studied neutrino oscillation and confirmed the existence of ν oscillation.

1.9.1 Theoretical Formulation of Oscillation

Neutrino oscillation implies the presence of neutrino mass. To formulate neutrino oscillation theoretically, consider a neutrino of flavor α, ν_α ($\alpha = e, \mu, \tau$), (which is produced with the same flavor charged lepton l_α in the charged current interaction), which is a coherent superposition of ν_i states ($i = 1, 2, 3$),

$$|\nu_\alpha\rangle = \sum_i U_{\alpha i} |\nu_i\rangle\,, \tag{1.102}$$

where U is a unitary matrix. An $N \times N$ unitary matrix U, has $\frac{N(N-1)}{2}$ mixing angles and $\frac{(N-1)(N-2)}{2}$ Dirac CP phase, and if the neutrinos are Majorana then $(N-1)$ Majorana phases. We will consider here the neutrinos as Majorana particles unless we specify. In the present case, the unitary matrix U (also called PMNS matrix [86–88]) for $N = 3$ has three mixing angles (θ_{12}, θ_{23}, θ_{13}), one Dirac CP phase (δ) and two Majorana phases (α_1, α_2) and can be expressed as,

$$U = \begin{pmatrix} c_{12}c_{13} & s_{12}c_{13} & s_{13}e^{-i\delta} \\ -s_{12}c_{23} - c_{12}s_{23}s_{13}e^{i\delta} & c_{12}c_{23} - s_{12}s_{23}s_{13}e^{i\delta} & s_{23}c_{13} \\ s_{12}s_{23} - c_{12}c_{23}s_{13}e^{i\delta} & -c_{12}s_{23} - s_{12}c_{23}s_{13}e^{i\delta} & c_{23}c_{13} \end{pmatrix} \begin{pmatrix} e^{i\frac{\alpha_1}{2}} & 0 & 0 \\ 0 & e^{i\frac{\alpha_2}{2}} & 0 \\ 0 & 0 & 1 \end{pmatrix}, \tag{1.103}$$

where $c_{ij} = \cos\theta_{ij}$, $s_{ij} = \sin\theta_{ij}$. To quantify the neutrino oscillation from the flavor α to flavor β, we can determine the following probability,

$$P_{\nu_\alpha\to\nu_\beta} = |\langle\nu_\beta|\nu_\alpha\rangle|^2\,. \tag{1.104}$$

Using the plane wave approximation and the unitarity condition, one can easily derive the oscillation probability for $\nu_\alpha \to \nu_\beta$ transition in the utrarelativistic limit as,

$$P_{\nu_\alpha\to\nu_\beta} = \delta_{\alpha\beta} - 4\sum_{k>j}\mathbb{R}\mathrm{e}\left[U^*_{\alpha k}U_{\beta k}U_{\alpha j}U^*_{\beta j}\right]\sin^2\left(\phi_{kj}\right) + 2\sum_{k>j}\mathbb{I}\mathrm{m}\left[U^*_{\alpha k}U_{\beta k}U_{\alpha j}U^*_{\beta j}\right]\sin\left(2\phi_{kj}\right), \tag{1.105}$$

where $\phi_{kj} = \frac{\Delta m^2_{kj}L}{4E}$, $\Delta m^2_{kj} = m^2_k - m^2_j$, m_k is the mass for the k$^{\text{th}}$ state, E is the energy of the neutrinos and L is the distance over which they have traveled.

Parameter	Hierarchy	Best fit	1σ range	2σ range	3σ range
$\delta m^2/10^{-5}$ eV^2	NH or IH	7.37	7.21 – 7.54	7.07 – 7.73	6.93 – 7.97
$\sin^2\theta_{12}/10^{-1}$	NH or IH	2.97	2.81 – 3.14	2.65 – 3.34	2.50 – 3.54
$\Delta m^2/10^{-3}$ eV^2	NH	2.50	2.46 – 2.54	2.41 – 2.58	2.37 – 2.63
$\Delta m^2/10^{-3}$ eV^2	IH	2.46	2.42 – 2.51	2.38 – 2.55	2.33 – 2.60
$\sin^2\theta_{13}/10^{-2}$	NH	2.14	2.05 – 2.25	1.95 – 2.36	1.85 – 2.46
$\sin^2\theta_{13}/10^{-2}$	IH	2.18	2.06 – 2.27	1.96 – 2.38	1.86 – 2.48
$\sin^2\theta_{23}/10^{-1}$	NH	4.37	4.17 – 4.70	3.97 – 5.63	3.79 – 6.16
$\sin^2\theta_{23}/10^{-1}$	IH	5.69	4.28 – 4.91 $\oplus$ 5.18 – 5.97	4.04 – 6.18	3.83 – 6.37
δ/π	NH	1.35	1.13 – 1.64	0.92 – 1.99	0 – 2
δ/π	IH	1.32	1.07 – 1.67	0.83 – 1.99	0 – 2
$\Delta\chi^2_{\mathrm{I-N}}$	IH–NH	+0.98			

Table 1.2: Best-fit values and allowed 1, 2 and 3σ ranges for the 3ν mass-mixing parameters [89].

The above equation implies that for neutrino oscillation we need a tiny mass difference between the neutrinos. The oscillation parameters are θ_{12}, θ_{13}, θ_{23}, Δm^2_{12}, Δm^2_{23} and δ_{CP}. The recent bound on the oscillation parameters [89] is shown in Table 1.2. If we look at the SM then the neutrinos are massless. Therefore, to generate neutrino mass with the renormalisable terms, we need to extend the SM as there is no other way to accommodate neutrino mass.

1.9.2 Neutrino Mass Theory

In SM we have two types of Weyl fermions, one is left handed chiral field and another one is the right handed chiral field defined in the following way,

$$\begin{aligned} \psi_{L,R} &= \frac{1 \mp \gamma_5}{2}\psi, \\ &= P_{L,R}\psi, \end{aligned} \tag{1.106}$$

where ψ is the four component spinor. In general, we can write two types of mass term, one is the Dirac mass term and other one is Majorana mass term expressed in the following way,

Dirac mass term:

$$\begin{aligned} \mathcal{L}_{Dirac} &= m_D\bar{\psi}\psi, \\ &= m_D\bar{\psi_L}\psi_R + h.c.. \end{aligned} \tag{1.107}$$

Majorana mass term:

$$\mathcal{L}_{Majorana} = m_L\bar{\psi_L}\psi_L^c + m_R\bar{\psi_R^c}\psi_R + h.c.. \tag{1.108}$$

where m_D is the Dirac mass and m_L, m_R are the Majorana mass term for the left and right handed fields. One can easily notice that for the Dirac type of mass term we need both left handed and right handed chiral fields like the mass term for the charged fermions in SM. If we add right handed neutrinos (N_R) to the SM, then we can write down the Yukawa term which gives the Dirac mass term naturally,

$$\mathcal{L}_{N_R}^{\text{Yuk}} = y_\nu\bar{L}\tilde{\phi}_h N_R + h.c.. \tag{1.109}$$

To achieve the neutrino mass in the eV scale, we need to assume that $y_\nu \ll y_e$, where y_e

is electron Yukawa coupling. As mentioned earlier, we have another option to generate the mass, namely, the Majorana mass. Since, neutrinos are neutral particles one can very easily generate Majorana mass for them. In the case of Majorana mass, we need only one kind of chiral fermion as shown in Eq. (1.108). Due to charge conservation we can not write Majorana mass for the charged particles. As mentioned previously, in SM we don't have any right handed counterpart of the neutrinos, hence it is difficult to write down the Dirac type mass term but we can write Majorana mass term by using the non-renormalisable dim-5 operator which consist of the SM fields,

$$\mathcal{L}_\nu = \frac{y^2}{\Lambda}\left(\bar{L}\tilde{\phi}_h\right)^2 + h.c., \tag{1.110}$$

where y is a dimensionless parameter and Λ is some high scale of the theory upto which the theory is valid. Once the EWSB happens spontaneously, the above term generates the neutrino mass,

$$m_\nu = \frac{y^2\langle\phi_h\rangle^2}{\Lambda}\bar{\nu_L}\nu_L^c + h.c.. \tag{1.111}$$

From the above expression when $\Lambda \gg \langle\phi_h\rangle$, then the neutrino mass automatically comes to the eV scale. As mentioned before, we consider here Majorana neutrinos for the rest of the discussion. This type of mass generation can be achieved in many UV complete beyond SM models, where ν mass is generated at tree level as well as loop level. We will discuss now some very popular techniques for generating the neutrino mass.

Tree level process

- Type-I Seesaw Mechanism: If we introduce three right handed neutrinos (N_{Rj}, j = 1,2,3) in the SM, then we can write down the following terms in the Lagrangian,

$$-\mathcal{L}_{Type-I} = y_\nu\bar{L}\tilde{\phi}_h N_R + \frac{M_N}{2}\bar{N_R^c}N_R + h.c.. \tag{1.112}$$

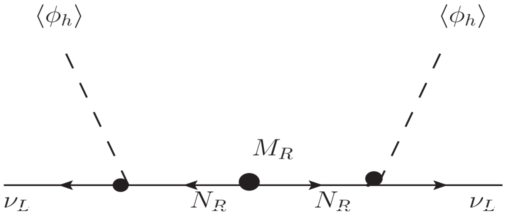

Figure 1.13: Schematic diagram of Type-I seesaw mechanism.

When the EWSB happens then we can write the above terms in the following way,

$$-2\mathcal{L}_{Type-I} = \sum_{i,j=1}^{3}\left[\bar{\nu_{iL}}(m_D)_{ij}N_{Rj} + \bar{N^c_{Rj}}(m_D)_{ji}\nu^c_{iL} + \bar{N^c_{Ri}}(M_R)_{ij}N_{jR} + h.c.\right], \tag{1.113}$$

where $m_D = y_\nu\langle\phi_h\rangle$ and we use the relation $\bar{\nu_L}N_R = \bar{N^c_R}\nu^c_L$. In matrix form we can write the above matrix in the following way,

$$\begin{aligned} -2\mathcal{L}_{Type-I} &= \begin{pmatrix}\bar{\nu_L} & \bar{N^c_R}\end{pmatrix}\begin{pmatrix}0 & m_D \\ m_D^T & M_R\end{pmatrix}\begin{pmatrix}\nu^c_L & N_R\end{pmatrix} + h.c., \\ &= \begin{pmatrix}\bar{\nu_L} & \bar{N^c_R}\end{pmatrix} M \begin{pmatrix}\nu^c_L & N_R\end{pmatrix} + h.c.. \end{aligned} \tag{1.114}$$

One can diagonalize the above 6×6 matrix, M, in the limit $m_D \ll M_R$ by the matrix V_I,

$$\begin{aligned} D_\nu &= V_I M V_I^T, \\ &\simeq \begin{pmatrix} m_D M_R^{-1} m_D^T & 0 \\ 0 & M_R\end{pmatrix}, \end{aligned} \tag{1.115}$$

where

$$V_I = \begin{pmatrix} I & (M_R^{-1}m_D^T)^\dagger \\ -M_R^{-1}m_D^T & I\end{pmatrix}\begin{pmatrix} iI & 0 \\ 0 & I\end{pmatrix}. \tag{1.116}$$

By defining the new basis we can write the above neutrino mass term in the following way,

$$-2\mathcal{L}_{Type-I} = m_\nu \bar{\nu}\nu + M_R \bar{N} N + h.c., \tag{1.117}$$

where

$$\begin{aligned} m_\nu &= m_D M_R^{-1} m_D^T, \\ M_R &= M_R. \end{aligned} \tag{1.118}$$

In the limit $M_R \gg m_D$, m_ν represents the the matrix for the light neutrinos and M_R denotes the mass matrix for the heavy neutrinos. The schematic view of the Type-I seesaw mechanism has been shown in Fig. 1.13.

- Type-II Seesaw Mechanism: Instead of extending the SM by three right handed neutrinos, we can extend the SM by a $SU(2)$ triplet scalar with hypercharge $Y = -2$. This $SU(2)$ triplet scalar will be useful because the combination $\bar{L}L^c$ also forms triplet under $SU(2)$ gauge group. When the triplet scalar combines with $\bar{L}L^c$ they form a singlet. The Lagrangian can be written in the following way,

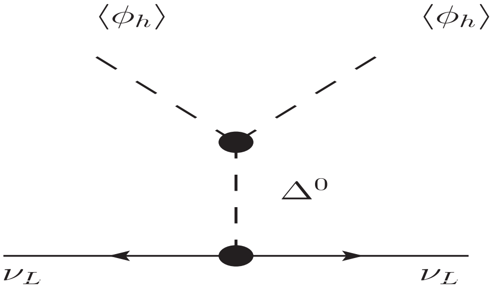

Figure 1.14: Schematic diagram of Type-II seesaw mechanism.

$$-\mathcal{L}_{Type-II} = \frac{Y_\Delta}{2}\bar{L} i\tau_2 \Delta L^c + \mu_\Delta \phi^T \Delta\phi + M_\Delta^2 \Delta^\dagger \Delta + h.c., \tag{1.119}$$

where $\tau_2 = \frac{\sigma_2}{2}$ and the triplet scalar is given by,

$$\Delta = \begin{pmatrix} \frac{\Delta^-}{\sqrt{2}} & \Delta^{--} \\ \Delta^0 & -\frac{\Delta^-}{\sqrt{2}} \end{pmatrix}. \tag{1.120}$$

Schematically the above terms are shown in Fig. 1.14. Once the EWSB occur, the neutral component of the triplet acquires induced *vev*. We can write down the neutrino mass term as,

$$\begin{aligned} m_{Type-II} &= \mu_\Delta Y_\Delta \frac{\langle\phi_h\rangle^2}{M_\Delta^2}, \\ &= \mu'_\Delta Y_\Delta \frac{\langle\phi_h\rangle^2}{M_\Delta}, \end{aligned} \tag{1.121}$$

where $\mu'_\Delta = \frac{\mu_\Delta}{M_\Delta}$. The above mass term exactly looks like the Eq. (1.111) when we assume $y^2 = \mu'_\Delta Y_\Delta$.

- Type-III Seesaw Mechanism: One can generate the neutrino mass at the tree level

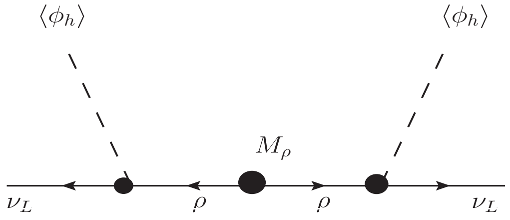

Figure 1.15: Schematic diagram of Type-III seesaw mechanism.

by introducing the $SU(2)$ triplet fermions as well instead of introducing the singlet fermions. If we introduce the triplet fermion with hypercharge zero, then we can write down a term with lepton doublet and Higgs doublet which is $SU(2)$ singlet. The Lagrangian looks like,

$$-\mathcal{L}_{Type-III} = Y_\rho \bar{L} i\tau_2 \rho \phi_h + M_\rho Tr[\bar{\rho^c}\rho] + h.c., \tag{1.122}$$

where the triplet fermion is expressed as,

$$\rho = \begin{pmatrix} \frac{\rho_0}{2} & \frac{\rho^+}{\sqrt{2}} \\ \frac{\rho^-}{\sqrt{2}} & -\frac{\rho_0}{2} \end{pmatrix}. \tag{1.123}$$

The above terms in the Lagrangian can generate the neutrino mass as shown in Fig. 1.15 schematically. After integrating out the heavy triplet field one can generate the neutrino mass in the following form,

$$m_{Type-III} = \langle\phi_h\rangle^2 Y_\rho M_\rho^{-1} Y_\rho^T . \tag{1.124}$$

Therefore, by setting $M_\rho \gg \langle\phi_h\rangle$, we can generate the light neutrino mass very easily.

One-loop process

- Inert Higgs doublet:

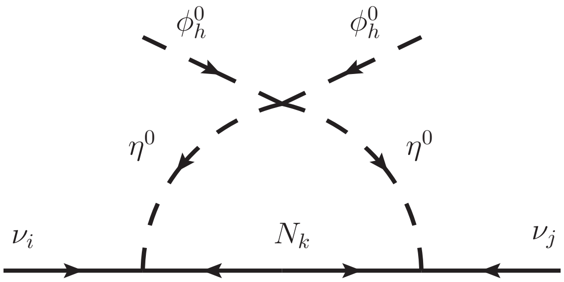

Figure 1.16: Light neutrino mass generation by one loop process with the inert Higgs doublet.

Like the tree level processes, one can generate neutrino mass by the loop diagram as well (as shown in Fig. 1.16) [90]. Here, one introduces three right handed neutrino and one doublet scalar which are odd under a $\mathbb{Z}_2$ symmetry and the SM fields are even under this discrete gauge group. We can write down the following term in the

Lagrangian,

$$\mathcal{L}_N = \sum_{i=e,\mu,\tau} \frac{i}{2}\bar{N}_i\gamma^\mu D_\mu N_i - \frac{1}{2}M\bar{N^c}N - \sum_{i,j=e,\mu,\tau} y_{ij}\bar{L}_i\tilde{\eta}N_j + h.c., \quad (1.125)$$

Scalar potential also gets few extra terms which are as follows,

$$\begin{aligned} V(\phi_h,\phi_H,\eta) &= -\mu_h^2\phi_h^\dagger\phi_h + \mu_\eta^2\eta^\dagger\eta + \lambda_1(\phi_h^\dagger\phi_h)^2 + \lambda_2(\eta^\dagger\eta)^2 \\ &\quad +\lambda_{12}(\phi_h^\dagger\phi_h)(\eta^\dagger\eta) + \lambda_4(\phi_h^\dagger\eta)(\eta^\dagger\phi_h) \\ &\quad +\frac{1}{2}\lambda_5\left((\phi_h^\dagger\eta)^2 + h.c.\right). \end{aligned} \quad (1.126)$$

Once the EWSB symmetry breaks resulting in the induced vev for the triplet Higgs, we can generate the neutrino mass (as shown in the Fig. 1.16) in the following form,

$$M^\nu_{ij} = \sum_k \frac{y_{ik}y_{jk}M_k}{16\pi^2}\left[\frac{M^2_{\eta^0_R}}{M^2_{\eta^0_R} - M^2_k}\ln\frac{M^2_{\eta^0_R}}{M^2_k} - \frac{M^2_{\eta^0_I}}{M^2_{\eta^0_I} - M^2_k}\ln\frac{M^2_{\eta^0_I}}{M^2_k}\right], \quad (1.127)$$

where $M_{\eta^0_{R,I}}$ are the mass of the real and imaginary part of the neutral component of the inert doublet and M_K is the mass of the right handed neutrino. If we consider the mass square difference between η^0_R and η^0_I i.e. $M^2_{\eta^0_R} - M^2_{\eta^0_I} = \lambda_5 v^2 << M_0^2$ where $M_0^2 = (M^2_{\eta^0_R} + M^2_{\eta^0_I})/2$ then the above expression reduces to the following form,

$$M^\nu_{ij} = \frac{\lambda_5 v^2}{16\pi^2}\sum_k \frac{y_{ik}y_{jk}M_k}{M_0^2 - M_k^2}\left[1 - \frac{M_k^2}{M_0^2 - M_k^2}\ln\frac{M_0^2}{M_k^2}\right]. \quad (1.128)$$

Therefore, by choosing the parameters value appropriately we can achieve the correct value of the neutrino mass. One advantage of this model is that the right handed neutrino or the neutral component of the inert Higgs doublet, depending on their masses, can be made a viable DM candidate.

- Zee model in Left-Right symmetric extension:

The initial proposal of Zee to generate the neutrino mass by one loop process [91]

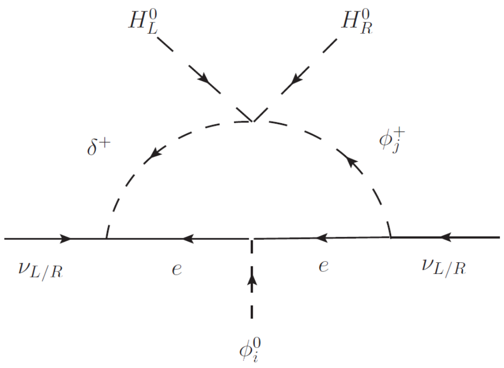

Figure 1.17: Light neutrino mass generation by one loop process with the inert Higgs doublet.

is already ruled out by the neutrino oscillation data [89]. If we implement the basic idea of the Zee model *i.e.* a charged singlet scalar in the left-right symmetric model, then we can still satisfy the allowed range of the neutrino oscillation parameters (schematic diagram shown in Fig. 1.17). We are discussing this particular left-right extension of the Zee model, since we have studied this version of Zee model in [92] and is not included in the thesis (detailed derivations are therein). The Yukawa terms which are relevant for the neutrino mass generation are as follows,

$$\mathcal{L}_Y = Y^{l1}_{ij}\bar{l}_{Li}\Phi l_{Rj} + Y^{l2}_{ij}\bar{l}_{Li}\widetilde{\Phi} l_{Rj} + \lambda_{L_{ij}} l^T_{Li} i\tau_2 l_{Lj}\delta^+ + \lambda_{R_{ij}} l^T_{Ri} i\tau_2 l_{Rj}\delta^+ + h.c., \tag{1.129}$$

where δ^+ is the additional charged scalar and the other particle contents are same with the left-right symmetric model. The structure of $\lambda_{L/R_{ij}}$ term is such that the only terms that will survive are the ones with $i \neq j$. This is exactly the same as in the Zee mechanism of neutrino mass generation. If we expand out any one of the terms involving δ^+ in the Yukawa Lagrangian we will get:

$$\mathcal{L} \supset \sum_{i \neq j} \nu_i e_j (\lambda_{ij} - \lambda_{ji}), \tag{1.130}$$

where ν_i and e_j are both in the flavor basis. Thus if we redefine the λ matrix to $\lambda'_{ij} = \lambda_{ij} - \lambda_{ji}$, then this new λ' matrix is completely anti-symmetric and the Lagrangian terms can now be written as:

$$\mathcal{L} \supset \sum_{i,j} \nu_i e_j \lambda'_{ij}. \tag{1.131}$$

The complete scalar potential is given in [92] and it contains the following terms which help in generating the neutrino mass,

$$V(\Delta,\Phi) \quad \supset \quad \left[i\alpha_1 \mathrm{Tr}(H_L^T \tau_2 \Phi H_R \delta^-) + i\alpha_2 \mathrm{Tr}(H_L^T \tau_2 \widetilde{\Phi} H_R \delta^-) + h.c.\right]. \tag{1.132}$$

The neutrino mass matrix takes the form,

$$M_\nu = \begin{bmatrix} M_\nu^L & M_\nu^D \\ (M_\nu^D)^T & M_\nu^R \end{bmatrix}, \tag{1.133}$$

where $M_\nu^D = Y^{l1} v_1 + Y^{l2} v_2$, $v_{1,2}$ are the *vevs* of the bidoublet. M_ν^L, M_ν^R are given by,

$$\begin{aligned}
(M_\nu^L)^{\alpha\gamma} \quad &= \frac{1}{4\pi^2}\lambda'_{L^{\alpha\beta}} m_{e_\beta} \sum_{i=1}^{3} \mathrm{Log}\left(\frac{M_{h_i}^2}{m_{e_\beta}^2}\right) \times V_{5i}\left[(Y_l^\dagger)^{\beta\gamma} V_{2i}^* - (\widetilde{Y}_l^\dagger)^{\beta\gamma} V_{1i}^*\right] \; + \; \alpha \leftrightarrow \gamma, \\
(M_\nu^R)^{\alpha\gamma} \quad &= \frac{1}{4\pi^2}\lambda'_{R^{\alpha\beta}} m_{e_\beta} \sum_{i=1}^{3} \mathrm{Log}\left(\frac{M_{h_i}^2}{m_{e_\beta}^2}\right) \times V_{5i}\left[(Y_l)^{\beta\gamma} V_{1i}^* - (\widetilde{Y}_l)^{\beta\gamma} V_{2i}^*\right] \; + \; \alpha \leftrightarrow \gamma,
\end{aligned} \tag{1.134}$$

where m_{e_β} is the lepton mass and V_{ij} (i,j = 1 to 5) is the unitary matrix which diagonalize the charged mass matrix of 5×5 dimension. If we diagonalize the Eq. (1.133) then we get the following mass term for the neutrinos,

$$M_\nu = M_\nu^L - M_\nu^{D^T} M_\nu^{R^{-1}} M_\nu^D. \tag{1.135}$$

With the suitable choice of the model parameters one can easily satisfy the present day neutrino oscillation data as done in Ref. [92].

1.10 An overview of the thesis

This thesis mainly on dark matter and neutrino mass models. We are convinced after knowing all the evidences of DM that it exists in nature and can not be explained by the SM. Another beyond SM problem is the existence of neutrino mass which has been proven by many experimental collaborations as discussed earlier. SM also has no clue to tackle this problem. Moreover, so far we have not discussed about the muon $(g-2)$ anomaly which says that the experimental value of muon $(g-2)$ and the theoretical value of muon $(g-2)$ after taking into account the loop diagrams based on SM do not agree each other. Therefore, to tackle all these beyond SM problems we have to extend SM by considering new particles as well as new gauge groups if it is necessary. Now we will describe very briefly the outline of each chapters contained in this thesis.

We discuss in chapter 2 the $U(1)_{B-L}$ extension of SM. The extra gauge group is local hence to cancel the gauge anomaly we have included three extra right handed neutrinos. Moreover, two singlet scalars have been introduced with nontrivial $(B-L)$ charge, one of them becomes a WIMP type DM candidate and other scalar spontaneously breaks the $U(1)_{B-L}$ gauge symmetry. We discuss the DM phenomenology in detail and its detection prospects at the direct detection experiments and also discuss that this DM candidate could be a possible source of the $1-3$ GeV Galactic center γ-ray excess observed by Fermi-LAT satellite.

In chapter 3, we discuss the $U(1)_{L_\mu - L_\tau}$ extension of the SM. Although, this abelian extension is gauge and gravitational anomaly free by its gauge structure still we have added three right handed neutrinos and two singlet scalars in order to explain the neutrino mass and DM. We can make the gauge boson light by obeying all the bounds, hence we can explain the muon $(g-2)$ anomaly by this model. We have discussed in detail the neutrino mass generation and allowed parameter space among the parameters after satisfying the neutrino oscillation data. We have also studied WIMP type DM and its detection at direct detection experiments.

Chapter 4 talks about extension of SM by $SU(2)_L$ triplet fermion, scalar and singlet fermion. Both the fermions are odd under extra $\mathbb{Z}_2$ symmetry and the remaining particles are even. The singlet fermion and the neutral component of triplet fermion can mix each other and lightest among them becomes a suitable WIMP DM candidate. We have studied in detail the detection of this type of DM by direct and indirect detection and also its collider search.

The gauge groups and the particle contents of chapter 5 are exactly same with the chapter 2. Here we have considered different way of DM production namely the freeze-in mechanism instead of freeze-out mechanism. Due to the feeble coupling of the FIMP type of DM, it never achieve thermal equilibrium with the cosmic soup. We have studied in detail its production mechanism from decay and annihilation of the other particles. Finally, we have also constrained the model parameters from the relic density bound. We have also discussed about the neutrino mass generation and the the baryon asymmetry of the Universe using resonant leptogenesis.

Chapter 6 mimic the same model as discussed in chapter 3. Here, also we have considered the FIMP type DM. We have done the detail study of its production from the decay and annihilation of the other particles. In particular we have constrained the $M_{Z_{\mu\tau}} - g_{\mu\tau}$ parameter space from the bound of muon $(g-2)$ and DM relic density.

In chapter 7, we have considered $U(1)_{L_\mu - \tau}$ extension of the inert doublet model. Here, we have considered the case when the mother particle (from which DM is produced dominantly) is also out of equilibrium and we have determined its number density by solving Boltzmann equation consist of Lioville's operator collision functions. We have successfully satisfied the observed value of the DM relic density. Finally, we have also explained the 3.5 keV line observed by the XMM-Newton and Chandra satellites.

Therefore, chapters (2 - 4) contain WIMP type DM candidate and the remaining ones, chapters (5 - 7), explain the FIMP type DM. Moreover, depending on the model construction we have also explained neutrino mass, matter antimatter asymmetry of the Universe and muon $(g-2)$.

2

Galactic Gamma Ray Excess and Dark Matter Phenomenology in a $U(1)_{B-L}$ Model

2.1 Introduction

This chapter is based on the work [93]. We consider an extension of the SM where the gauge sector of SM is enhanced by a local $U(1)_{\mathrm{B-L}}$ gauge group where B and L represent the baryon and lepton numbers respectively. In this model we have an extra neutral gauge boson Z_{BL} as the model Lagrangian possesses an additional local $U(1)_{\mathrm{B-L}}$ gauge invariance. In order to construct an anomaly free theory, the model needs three right handed neutrinos with $\mathrm{B-L}$ charge equal to -1. Thus, $\mathrm{B-L}$ extension of the SM is a well motivated beyond Standard Model (BSM) theory which can explain the origin of tiny neutrino masses through the type-I seesaw mechanism. Majorana mass terms of these three right handed neutrinos are generated in a gauge invariant way by introducing a SM gauge singlet scalar ϕ_H having $\mathrm{B-L}$ charge $+2$. The $U(1)_{\mathrm{B-L}}$ gauge symmetry breaks spontaneously when the scalar field ϕ_H gets a vacuum expectation value v_{BL}, thereby generating mass of the $\mathrm{B-L}$ gauge boson Z_{BL} and the right handed neutrinos. The mixing between the neutral components of ϕ_H and the SM Higgs doublet ϕ_h produces two physical scalars namely h_1 and h_2 where h_1 is identified as the SM-like Higgs boson with mass around 125.5 GeV. The $\mathrm{B-L}$ extension of SM [94–97] has been explored before in the context of dark matter phenomenology [98–106] and baryogenesis in the early Universe in Refs. [107–109]. In the present work we have introduced a complex scalar field ϕ_{DM} to the $U(1)_{\rm B-L}$ extension of SM. This complex scalar field ϕ_{DM} is singlet under the SM gauge group while it transforms nontrivially under $U(1)_{\rm B-L}$ gauge group. By choosing proper $\rm B-L$ charge, this scalar field ϕ_{DM} can be made stable and hence it can play the role of a viable dark matter candidate. In this present work, we have considered the low mass region 40 GeV to 55 GeV of DM masses to explain the Fermi-LAT gamma-ray excess from the Galactic Centre, whereas the high mass region has been studied in Ref. [105]. We have calculated the relic density of ϕ_{DM} by solving Boltzmann equation numerically. We have found that the gamma-ray flux produced from the annihilation of ϕ_{DM} and $\phi^{\dagger}_{DM}$ can reproduce the gamma-ray excess as observed by Fermi-LAT from the direction of GC. Moreover, in this work, we have taken into account all the possible existing theoretical as well as experimental constraints obtained from experiments like LHC, LEP, LUX, Planck.

2.2 Model

In the present work, we have considered "pure" $U(1)_{\rm B-L}$ extension of the Standard Model (SM) of elementary particles where the SM gauge group $SU(3)_{\rm c} \times SU(2)_{\rm L} \times U(1)_{\rm Y}$ is enhanced by an additional local $U(1)_{\rm B-L}$ gauge symmetry where B and L represent the baryon and lepton numbers, respectively. Therefore, all the SM (quarks and leptons) fields transform nontrivially under this $U(1)_{\rm B-L}$ gauge group. Besides the SM fields, we have to introduce three right handed neutrinos (N_i, $i = 1$ to 3) such that the present model becomes anomaly free. Further, in addition to the usual SM Higgs doublet ϕ_h, the scalar sector of the SM is also extended by adding two SM gauge singlet complex scalar fields, namely ϕ_H, ϕ_{DM} both of which possess nonzero $U(1)_{\rm B-L}$ charge. $U(1)_{\rm B-L}$ gauge symmetry breaks spontaneously when the scalar field ϕ_H gets a nonzero vacuum expectation value (VEV) v_{BL}. Consequently, we have one extra neutral massive gauge field Z_{BL} in the model. Moreover, after spontaneous breaking of $U(1)_{\rm B-L}$ symmetry, the

Majorana mass terms for the three right handed neutrinos can be generated in a gauge invariant way by choosing a suitable $U(1)_{\rm B-L}$ charge +2 of the scalar field ϕ_H. Also, if the value of the relevant model parameters are such that the VEV of ϕ_{DM} is zero then the complex scalar field ϕ_{DM} can be made stable by giving an appropriate $\rm B-L$ to it. Under such circumstances ϕ_{DM} can be a viable dark matter candidate. The $U(1)_{\rm B-L}$ charges as well as the SM gauge charges of all the fields present in the model are given in a tabular form (see Table 2.1).

Gauge Group	Baryon Fields			Lepton Fields			Scalar Fields		
	$Q_L^i=(u_L^i,d_L^i)^T$	u_R^i	d_R^i	$L_L^i=(\nu_L^i,e_L^i)^T$	e_R^i	N_R^i	ϕ_h	ϕ_H	ϕ_{DM}
$SU(2)_L$	2	1	1	2	1	1	2	1	1
$U(1)_Y$	1/6	2/3	−1/3	−1/2	−1	0	1/2	0	0
$U(1)_{B-L}$	1/3	1/3	1/3	−1	−1	−1	0	2	n_{BL}

Table 2.1: Particle content and their corresponding charges under various symmetry groups.

The Lagrangian of the present model including the SM Lagrangian $\mathcal{L}_{SM}$ is as follows

$$\begin{aligned}\mathcal{L} &= \mathcal{L}_{SM}+\mathcal{L}_{DM}+(D_\mu\phi_H)^\dagger(D^\mu\phi_H)-\frac{1}{4}F_{BL\mu\nu}F_{BL}{}^{\mu\nu}+\frac{i}{2}\bar{N}_i\gamma^\mu D_\mu N_i-V(\phi_h,\phi_H)\\ &\quad -\sum_{i=1}^{3}\frac{1}{2}\lambda_{N_i}\phi_H\bar{N_i^c}N_i-\sum_{i,j=1}^{3}y'_{ij}\bar{L}_i\tilde{\phi}_hN_j+h.c., \qquad (2.1)\end{aligned}$$

with $\tilde{\phi_h}=i\sigma_2\phi_h^*$, while $\mathcal{L}_{DM}$ represents the dark sector Lagrangian whose expression is given by

$$\begin{aligned}\mathcal{L}_{DM} &= (D^\mu\phi_{DM})^\dagger(D_\mu\phi_{DM})-\mu_{DM}^2\phi_{DM}^\dagger\phi_{DM}-\lambda_{Dh}(\phi_{DM}^\dagger\phi_{DM})(\phi_h^\dagger\phi_h)\\ &\quad -\lambda_{DH}(\phi_{DM}^\dagger\phi_{DM})(\phi_H^\dagger\phi_H)-\lambda_{DM}(\phi_{DM}^\dagger\phi_{DM})^2\,, \qquad (2.2)\end{aligned}$$

and the self interactions of ϕ_H and its mutual interaction with the SM Higgs doublet ϕ_h are described by $V(\phi_h,\phi_H)$ which can be written as

$$V(\phi_h,\phi_H)=\mu_H^2\phi_H^\dagger\phi_H+\lambda_H(\phi_H^\dagger\phi_H)^2+\lambda_{hH}(\phi_h^\dagger\phi_h)(\phi_H^\dagger\phi_H)\,. \qquad (2.3)$$

In Eq. (2.1), $F_{BL\mu\nu}=\partial_\mu Z_{BL\nu}-\partial_\nu Z_{BL\mu}$ is the field strength tensor of the $U(1)_{\rm B-L}$ gauge field Z_{BL}. Covariant derivative appearing in Eqs. (2.1, 2.2) is defined as

$$D_\mu\psi = (\partial_\mu + i\, g_{BL}\, Q_{BL}(\psi)\, Z_{BL\mu})\,\psi\,, \tag{2.4}$$

where $\psi = \phi_H$, ϕ_{DM}, N_i and $Q_{BL}(\psi)$ is the corresponding $U(1)_{\rm B-L}$ gauge charge which is given in Table 2.1. In general, the Majorana mass matrix for the three right handed neutrinos, obtained after spontaneous breaking of $\rm B-L$ symmetry, will contain *off diagonal* terms. However these off diagonal terms can be easily removed by changing the basis and therefore, we have considered the diagonal Majorana mass matrix for the three right handed neutrinos (or the right handed neutrinos N_i's are in mass basis).

After spontaneous breaking of $U(1)_{\rm B-L}$ symmetry the scalar fields ϕ_h and ϕ_H in unitary gauge take the following form

$$\phi_h = \begin{pmatrix} 0 \\ \dfrac{v+H}{\sqrt{2}} \end{pmatrix} \quad \phi_H = \begin{pmatrix} \dfrac{v_{BL}+H_{BL}}{\sqrt{2}} \end{pmatrix}\,, \tag{2.5}$$

where $v = 246$ GeV is the VEV of ϕ_h, which breaks the electroweak symmetry to a $U(1)$ symmetry ($U(1)_{em}$). On the other hand the VEV of ϕ_H, v_{BL}, is responsible for the breaking of $\rm B-L$ gauge symmetry of the Lagrangian and thereby generates masses for the three right handed neutrinos as well as the gauge boson Z_{BL},

$$\begin{aligned} M_{N_i} &= \frac{\lambda_{N_i}}{\sqrt{2}} v_{BL}\,, \\ M_{Z_{BL}} &= 2\, g_{BL}\, v_{BL}\,. \end{aligned} \tag{2.6}$$

In Eq. (2.5) H and H_{BL} are two neutral scalar fields of ϕ_h and ϕ_H respectively. There is also mixing between H and H_{BL} through the term λ_{hH} (see Eq. (2.3)). As a result, the mass matrix of H and H_{BL} contains off diagonal elements which are proportional to λ_{hH}, v and V_{BL}. Hence, H and H_{BL} are not representing any physical field. The scalar mass matrix with respect to the basis (H, H_{BL}) is given by

$$\mathcal{M}^2_{scalar} = \begin{pmatrix} 2\lambda_h v^2 & \lambda_{hH}\, v_{BL}\, v \\ & \\ \lambda_{hH}\, v_{BL}\, v & 2\lambda_H v^2_{BL} \end{pmatrix} . \tag{2.7}$$

In order to obtain the physical states we have to diagonalise the real [1] symmetric matrix $\mathcal{M}^2_{scalar}$ (Eq. (2.7)) by an orthogonal matrix. The physical fields or the mass eigenstates which are linearly related to H and H_{BL}, can be obtained through the following relations

$$\begin{aligned} h_1 &= H\cos\alpha + H_{BL}\sin\alpha\,, \\ h_2 &= -H\sin\alpha + H_{BL}\cos\alpha\,, \end{aligned} \tag{2.8}$$

where the scalar field h_1 is identified as the SM like Higgs boson and h_2 is the extra Higgs boson in the model, while α is the mixing angle between H and H_{BL} given as

$$\tan 2\alpha = \frac{\lambda_{hH}\, v_{BL}\, v}{\lambda_h v^2 - \lambda_H v^2_{BL}} . \tag{2.9}$$

We will see later that from LHC results, the allowed values of the mixing angle α are extremely small. The expressions of masses of the three physical scalar fields h_1, h_2 and ϕ_{DM} are

$$\begin{aligned} M^2_{h_1} &= \lambda_h v^2 + \lambda_H v^2_{BL} + \sqrt{(\lambda_h v^2 - \lambda_H v^2_{BL})^2 + (\lambda_{hH}\, v\, v_{BL})^2}\,, \\ M^2_{h_2} &= \lambda_h v^2 + \lambda_H v^2_{BL} - \sqrt{(\lambda_h v^2 - \lambda_H v^2_{BL})^2 + (\lambda_{hH}\, v\, v_{BL})^2}\,, \\ M^2_{DM} &= \mu^2_{DM} + \frac{\lambda_{Dh} v^2}{2} + \frac{\lambda_{DH} v^2_{BL}}{2} . \end{aligned} \tag{2.10}$$

Since h_1 is the SM like Higgs boson therefore we have taken $M_{h_1} = 125.5$ GeV.

In this model, besides the SM parameters, we have twelve unknown independent pa-

---

[1] In present model we have taken all the coupling constants and VEVs as real.

rameters, namely the masses of h_2, ϕ_{DM}, Z_{BL}, N_i, $U(1)_{\rm B-L}$ gauge coupling g_{BL}, $\rm B-L$ charge (n_{BL}) of dark matter (ϕ_{DM}), scalar mixing angle α and three quartic couplings λ_{DH}, λ_{Dh}, λ_{DM}. In terms of these independent parameters, the couplings appearing in the Lagrangian (Eqs. (2.1-2.3)) can be expressed as

$$\begin{aligned}
\lambda_H &= \frac{M_{h_1}^2 + M_{h_2}^2 + (M_{h_2}^2 - M_{h_1}^2)\cos 2\alpha}{4\, v_{BL}^2}\,, \\
\lambda_h &= \frac{M_{h_1}^2 + M_{h_2}^2 + (M_{h_1}^2 - M_{h_2}^2)\cos 2\alpha}{4\, v^2}\,, \\
\lambda_{hH} &= \frac{(M_{h1}^2 - M_{h_2}^2)\cos\alpha\sin\alpha}{v\, v_{BL}}\,, \\
\mu_{\phi_h}^2 &= -\frac{(M_{h_1}^2 + M_{h_2}^2)v + (M_{h_1}^2 - M_{h_2}^2)(v\cos 2\alpha + v_{BL}\sin 2\alpha)}{4\, v}\,, \\
\mu_{\phi_H}^2 &= \frac{-(M_{h_1}^2 + M_{h_2}^2)v_{BL} + (M_{h_1}^2 - M_{h_2}^2)(v_{BL}\cos 2\alpha - v\sin 2\alpha)}{4\, v_{BL}}\,, \qquad (2.11)
\end{aligned}$$

where $\mu_{\phi_h}^2$ and $\mu_{\phi_H}^2$ are the quadratic self coupling of the SM Higgs doublet ϕ_h and the extra Higgs singlet ϕ_H respectively. Moreover, the model parameters are subjected to satisfy certain conditions arising from theoretical constraints as well as relevant experimental results. These constraints are briefly discussed below.

- **Vacuum Stability:** In our model we choose the ground state (ϕ_h, ϕ_H, ϕ_{DM}) = (v, v_{BL}, 0). This requires the following constrains on the quadratic self couplings of the scalar fields,

  $$\mu_{\phi_h}^2 < 0, \;\; \mu_{\phi_H}^2 < 0 \;\text{ and }\; \mu_{DM}^2 > 0\,. \qquad (2.12)$$

  Also in order to obtained a stable ground state (*vacuum*), the quartic couplings, appearing in the Lagrangian, need to satisfy the following conditions

$$\begin{aligned}
&\lambda_h \geq 0, \lambda_H \geq 0, \lambda_{DM} \geq 0, \\
&\lambda_{hH} \geq -2\sqrt{\lambda_h \lambda_H}, \\
&\lambda_{Dh} \geq -2\sqrt{\lambda_h \lambda_{DM}}, \\
&\lambda_{DH} \geq -2\sqrt{\lambda_H \lambda_{DM}}, \\
&\sqrt{\lambda_{hH} + 2\sqrt{\lambda_h \lambda_H}}\sqrt{\lambda_{Dh} + 2\sqrt{\lambda_h \lambda_{DM}}}\sqrt{\lambda_{DH} + 2\sqrt{\lambda_H \lambda_{DM}}} \\
&+2\sqrt{\lambda_h \lambda_H \lambda_{DM}} + \lambda_{hH}\sqrt{\lambda_{DM}} + \lambda_{Dh}\sqrt{\lambda_H} + \lambda_{DH}\sqrt{\lambda_h} \geq 0 \ . \qquad (2.13)
\end{aligned}$$

- **Planck Limit:** The relic density $\Omega_{DM}h^2$ of the dark matter particle ϕ_{DM} at the present epoch should lie within the range reported by the satellite borne experiment Planck [20], which is

$$0.1172 \leq \Omega_{DM}h^2 \leq 0.1226 \quad \text{at } 68\% \text{ C.L.} \qquad (2.14)$$

- **Stability of dark matter:** We give a $U(1)_{\mathrm{B-L}}$ charge to the dark matter candidate (ϕ_{DM}) in such a way so that all possible decay terms are forbidden by the invariance of $U(1)_{\mathrm{B-L}}$ gauge symmetry which therefore ensures the stability of ϕ_{DM}. In general, the possible decay terms of ϕ_{DM} are like $\phi_{DM}\phi_h^p\phi_H^q$ (where $p+q \leq 3$ and p, q are integer can vary from 0 to 3) and $\phi_{DM}\bar{f}'f$, where f is N_i and $f' = N_i^c$ [2]. From Table 2.1 one can see that the $\mathrm{B-L}$ charges of ϕ_h and ϕ_H are 0 and +2 respectively. Therefore if we take $n_{BL} \neq -2\,q$ then we can not write the term $\phi_{DM}\phi_h^p\phi_H^q$, as it will violate the $U(1)_{\mathrm{B-L}}$ gauge symmetry. In addition, in our case, we have varied dark matter mass from 40 GeV to 55 GeV and $M_{DM} < M_{h_1}, M_{h_2}$ [3] as a result any decay modes of ϕ_{DM} to these scalar bosons are kinematically forbidden. Moreover, due to

---

[2] Since ϕ_{DM} is singlet under SM gauge group therefore a term like $\phi_{DM}f\bar{f}$ with f being any Standard Model fermion is forbidden.

[3] which is required to explain Fermi-LAT gamma excess [110], see section 2.5 for more detailed discussion.

the presence of $\phi_{DM}\bar{N_i^c}N_i$ term, the dark matter candidate can also decay into two Majorana type right handed neutrinos in the final state, if the kinematical condition ($M_{DM} > 2M_{N_i}$, $i = 1$ to 3) is satisfied, which can also destroy its stability. To get rid of this decay term we can not choose $n_{BL} = +2$ as the combination $\bar{N_i^c}N_i$ has B − L charge −2. Therefore, in order to avoid all the above mentioned decay terms (due to renormalizability of the Lagrangian we have considered operators only upto dimension 4) we need $n_{BL} \neq \pm 2q$ where q is any integer between 0 and 3.

- **LEP bound:** Since the SM fermions are charged under the gauge group $U(1)_{\rm B-L}$, therefore LHC should find some footprint of the B − L gauge boson Z_{BL} as it can directly interact with all the SM fermions. The nondetection of any signature of Z_{BL} puts a severe constraint on its mass ($M_{Z_{BL}}$) and B − L gauge coupling (g_{BL}). From LEP experiment the ratio $\frac{M_{Z_{BL}}}{g_{BL}}$ is bounded from below by the following condition [111, 112] [4]

$$\frac{M_{Z_{BL}}}{g_{BL}} \gtrsim 6-7\,\text{TeV}\,. \tag{2.15}$$

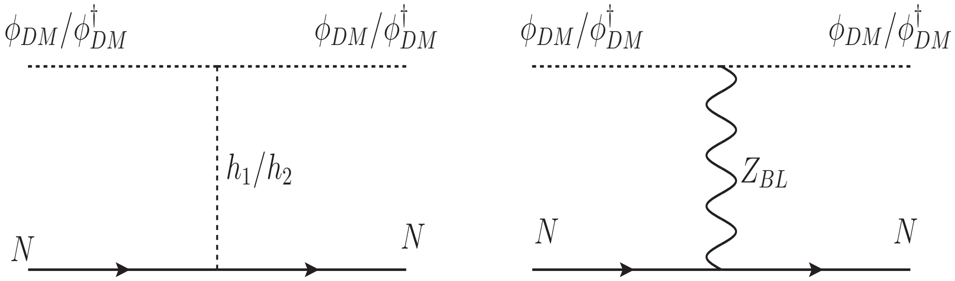

Figure 2.1: Feynmann diagrams for spin independent scattering cross section of dark matter particle/antiparticle with nucleon (N) through both Higgses (h_1, h_2) and gauge boson Z_{BL}.

- **LUX limit:** In this model, the complex scalar field ϕ_{DM} is our dark matter candidate. Therefore, both ϕ_{DM} and its antiparticle can elastically scatter off the detector

---

[4] Recent bounds on the mass and gauge coupling of $Z_{\rm BL}$ from ATLAS collaboration are given in Ref. [113].

nuclei through the exchange of neutral scalars h_1, h_2 and $U(1)_{\rm B-L}$ gauge boson Z_{BL}. Moreover, due to the presence of vector boson (Z_{BL}) mediator, the elastic scattering cross sections for the dark matter and its antiparticle are different. If we take the number densities of the dark matter and its antiparticle to be equal at the present epoch (which is true if the species has negligible chemical potential [30]), then we have to multiply the elastic scattering cross sections of dark matter and its antiparticle by a factor $1/2$ while comparing these scattering cross sections, obtained from the present model, with the experimental upper limits reported by the direct detection experiment LUX [114, 115]. The reason behind this is the exclusion regions in $\sigma_{SI} - M_{DM}$ plane reported by different dark matter direct detection experiments are computed assuming the existence of only one type of dark matter particle (and also self-conjugate) in the Universe. Although our model too has only one kind of dark matter candidate, however, it has a different antiparticle and they do not possess equal interaction strengths with the detector nuclei. Feynman diagrams for the elastic scattering of both ϕ_{DM} and $\phi^{\dagger}_{DM}$ with the nucleon (N) are shown in Fig. 2.1. These processes are mediated through the exchange of h_1, h_2 and Z_{BL}. The expressions of spin independent scattering cross sections off the nucleon (N) for both ϕ_{DM} and $\phi^{\dagger}_{DM}$ are given by

$$\sigma_{\phi_{DM}\,(\phi^{\dagger}_{DM})} = \frac{\mu^2}{4\pi}\left[\frac{M_N\, f_N\, \cos\alpha}{M_{DM}\, v}\left(\frac{\tan\alpha\, g_{\phi_{DM}\phi^{\dagger}_{DM}h_2}}{M^2_{h_2}} - \frac{g_{\phi_{DM}\phi^{\dagger}_{DM}h_1}}{M^2_{h_1}}\right) - (+)\frac{2\, n_{BL}\, g^2_{BL}\, f_{Z_{BL}}}{3\, M^2_{Z_{BL}}}\right]^2, \tag{2.16}$$

where $g_{\phi_{DM}\phi^{\dagger}_{DM}h_i}$ is the vertex factor for a vertex involving fields $\phi_{DM}\,\phi^{\dagger}_{DM}\,h_i$ ($i = 1$, 2) and its expression is given in Table 2.1. The reduced mass between nucleon N (proton or neutron) and DM particle is denoted by μ. Moreover, the nuclear form factor for the scalar mediated processes is $f_N \sim 0.3$ [116] while that for Z_{BL} mediated diagram is $f_{Z_{BL}} = 3.0$ [5]. From the expression of spin independent scattering cross section it is seen that although, the elastic scattering cross sections of ϕ_{DM} and $\phi^{\dagger}_{DM}$ with N are identical when the scattering processes are mediated through the scalar bosons only, however, if we include the Z_{BL} mediated diagram then the elastic scattering cross sections for both ϕ_{DM} and $\phi^{\dagger}_{DM}$ become different from each other. It is due to the fact that the momentum dependent vertex factors for the vertices $\phi_{DM}\phi_{DM}Z_{BL}$ and $\phi^{\dagger}_{DM}\phi^{\dagger}_{DM}Z_{BL}$ [6] are differ by a -ve sign (due to the change in sign of momentum while go from particle to anti particle scenario) from each other which results in a difference between $\sigma_{\phi_{DM}}$ and $\sigma^{\dagger}_{\phi_{DM}}$ arising from the interaction terms between Z_{BL} and scalar bosons mediated diagrams. If σ^{exp}_{SI} represents the upper limit of the spin independent scattering cross section reported by the LUX experiment for a particular dark matter mass then for a viable dark matter model both $\sigma_{\phi_{DM}}$ and $\sigma_{\phi^{\dagger}_{DM}}$ must satisfy the following condition

$$\sigma_{\phi_{DM}} + \sigma_{\phi^{\dagger}_{DM}} < 2\sigma^{exp}_{SI} \,, \tag{2.17}$$

- **LHC constraints:**
  - **Signal Strength of SM-like Higgs:** The signal strength of h_1 for a particular decay channel $h_1 \to X\bar{X}$ (X is any SM particle such as gauge boson, quark or lepton) is defined as

    $$R_{X\bar{X}} = \frac{\sigma\, BR(h_1 \to X\bar{X})}{[\sigma\, BR(h \to X\bar{X})]_{SM}} \,, \tag{2.18}$$

    where σ and $BR(h_1 \to X\bar{X})$ are the production cross section of h_1 and its branching ratio for $X\bar{X}$ decay channel. In the denominator of the above equa-

---

[5] $N\bar{N}Z_{\rm BL}$ coupling $g_{N\bar{N}Z_{\rm BL}} = \sum_{q=ud} f^{N}_{V_q} \times g_{q\bar{q}Z_{\rm BL}}$ [32] with $g_{q\bar{q}Z_{\rm BL}} = -\frac{g_{\rm BL}\gamma^{\mu}}{3}$ is the coupling for the vertex containing fields $q\bar{q}Z_{\rm BL}$ (see Table 2.2). Now for proton p (neutron n) $f^{p}_{V_u} = 2$, $f^{p}_{V_d} = 1$ ($f^{n}_{V_u} = 1$, $f^{n}_{V_d} = 2$) [32]. Therefore, for both the nucleon N (n and p) the coupling $g_{N\bar{N}Z_{\rm BL}} = f_{Z_{\rm BL}} \times g_{q\bar{q}Z_{\rm BL}}$ with $f_{Z_{\rm BL}} = \sum_{q=ud} f^{N}_{V_q} = 3$. Thus in this model form factors of proton and neutron are same for $Z_{\rm BL}$ mediated diagram.

[6] see the expression of $g_{\phi_{DM}\phi^{\dagger}_{DM}Z_{BL}}$ in Table 2.2

tion $[\sigma BR(h \to X\bar{X})]_{SM}$ represent the same quantities for the SM Higgs boson (h). If the neutral boson h_1 is similar to the SM Higgs boson then according to LHC result the signal strength ratio $R_{X\bar{X}}$ should be > 0.8 [7] [117]. We will see later, in Fig. 2.3 (Section 2.4) that the above condition will impose severe constrain on the allowed values of scalar mixing angle α.

- **Invisible decay width of Higgs boson:** In the present model, the SM like Higgs boson h_1 can decay into a pair of ϕ_{DM} and $\phi_{DM}^{\dagger}$ if the kinematical condition $M_{h_1} \geq 2M_{DM}$ is satisfied. Such decay channel is known as the invisible decay model of h_1. The expression of partial decay width of h_1 into $\phi_{DM}\phi_{DM}^{\dagger}$ final state is

$$\Gamma_{h_1 \to \phi_{DM}\phi_{DM}^{\dagger}} = \frac{g^2_{h_1\phi_{DM}\phi^{\dagger}_{DM}}}{16\pi M_{h_1}} \sqrt{1 - \frac{4M_{DM}^2}{M_{h_1}^2}}\,, \tag{2.19}$$

where $g_{h_1\phi_{DM}\phi^{\dagger}_{DM}}$ is the vertex factor for the vertex involving $h_1\phi_{DM}\phi^{\dagger}_{DM}$. Throughout this work we have considered the partial width of this invisible decay channel of h_1 to be less than 20% [118, 119] of its total decay width.

- **Fermi-LAT gamma excess from Galactic Centre:** In order to explain the Fermi-LAT observed gamma-ray excess from the Galactic Centre using a self-conjugate annihilating dark matter, one needs a dark matter particle of mass $48.7^{+6.4}_{-5.2}$ GeV [110]. If we assume an NFW halo profile with $\gamma = 1.26$, $\rho_{\odot} = 0.4$ GeV/cm^3, $r_{\odot} = 8.5$ kpc and $r_s = 20$ kpc then the annihilation cross section of dark matter particle for the $b\bar{b}$ annihilation channel should lie in the range $\langle\sigma \mathrm{v}\rangle_{b\bar{b}} \sim 1.75^{+0.28}_{-0.26} \times 10^{-26}$ cm^3/s [110]. However, if we take into account the uncertainties of DM halo profile parameters (mentioned above) then the quantity $\langle\sigma \mathrm{v}\rangle_{b\bar{b}}$ can vary in the range $\mathcal{A} \times 1.75^{+0.28}_{-0.26} \times 10^{-26}$ cm^3/s with $\mathcal{A} = [0.17, 5.3]$ [110]. We will discuss about the Fermi-LAT gamma-ray excess elaborately in Section 2.5 where we will see that the

---

[7] We have considered the central value of the combined signal strength of the SM Higgs boson reported by the CMS collaboration [117].

required value of $\langle\sigma \mathrm{v}\rangle_{b\bar{b}}$ for a non-self-conjugate DM (which is true for the present model) is different from a dark matter candidate whose particles and antiparticles are same.

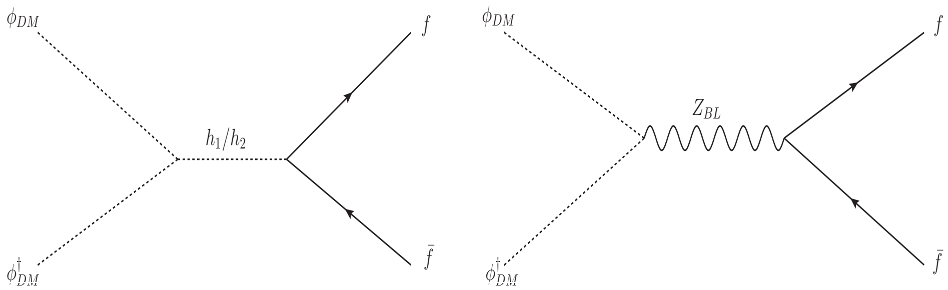

Figure 2.2: Feynman diagrams for dark matter annihilation through both scalar bosons (h_1, h_2) and gauge boson Z_{BL}.

2.3 Relic Density

The evolution of total number density (n) of both ϕ_{DM} and $\phi^\dagger_{DM}$ is governed by the Boltzmann equation as given in Eq. (1.81). To calculate $\langle\sigma v\rangle$ (as defined in Eq. (1.76)), we need to calculate the cross section for the process $\phi_{DM}\phi^\dagger_{DM} \to f\bar{f}$, mediated by the exchange of h_1, h_2 and Z_{BL} as given in Fig. 2.2, which is as follows,

$$\begin{aligned}\sigma \;=\; & \frac{3}{8\pi s}\sqrt{\frac{s-4m_f^2}{s-4M_{DM}^2}}\Bigg\{A^2\,(s-4m_f^2)\left|\frac{g_{h_1\phi_{DM}\phi^\dagger_{DM}}}{(s-M_{h_1}^2)+i\Gamma_{h_1}M_{h_1}}-\frac{\tan\alpha\; g_{h_2\phi_{DM}\phi^\dagger_{DM}}}{(s-M_{h_2}^2)+i\Gamma_{h_2}M_{h_2}}\right|^2 \\ & +\frac{2}{9}\frac{g_{BL}^4 n_{BL}^2}{(s-M_{Z_{BL}})^2+(\Gamma_{Z_{BL}}M_{Z_{BL}})^2}(s-4M_{DM}^2)(s+2m_f^2)\Bigg\}, \qquad (2.20)\end{aligned}$$

where Γ_i is the total decay width of the particle i ($i = h_1$, h_2, Z_{BL}), m_f is the mass of the SM fermion f and $\sqrt{s}$ is centre of mass energy. $g_{i\phi_{DM}\phi^\dagger_{DM}}$ is the vertex factor for the vertex involving the fields $i\phi_{DM}\phi^\dagger_{DM}$ ($i = h_1$, h_2) and its expression is given in Table 2.2.

Vertex abc	Vertex Factor g_{abc}
$q\bar{q}h_1$	$-\frac{M_q}{v}\cos\alpha$
$q\bar{q}h_2$	$\frac{M_q}{v}\sin\alpha$
$q\bar{q}Z_{BL}$	$-\frac{g_{BL}}{3}\gamma^{\mu}$
$l\bar{l}h_1$	$-\frac{M_l}{v}\cos\alpha$
$l\bar{l}h_2$	$\frac{M_l}{v}\sin\alpha$
$l\bar{l}Z_{BL}$	$g_{BL}\gamma^{\mu}$
$\phi_{DM}\phi^{\dagger}_{DM}h_1$	$-\frac{1}{2g_{BL}}(2g_{BL}v\lambda_{Dh}\cos\alpha + M_{Z_{BL}}\lambda_{DH}\sin\alpha)$
$\phi_{DM}\phi^{\dagger}_{DM}h_2$	$\frac{1}{2g_{BL}}(2g_{BL}v\lambda_{Dh}\sin\alpha - M_{Z_{BL}}\lambda_{DH}\cos\alpha)$
$\phi_{DM}\phi^{\dagger}_{DM}Z_{BL}$	$n_{BL}g_{BL}(p_2-p_1)^{\mu}$
$\phi_{DM}\phi^{\dagger}_{DM}h_1h_1$	$-(\lambda_{Dh}\cos^2\alpha + \lambda_{DH}\sin^2\alpha)$
$\phi_{DM}\phi^{\dagger}_{DM}h_2h_2$	$-(\lambda_{Dh}\sin^2\alpha + \lambda_{DH}\cos^2\alpha)$
$\phi_{DM}\phi^{\dagger}_{DM}h_1h_2$	$\sin\alpha\cos\alpha(\lambda_{Dh} - \lambda_{DH})$
$\phi_{DM}\phi^{\dagger}_{DM}Z_{BL}Z_{BL}$	$2g^2_{BL}n^2_{BL}$
$\phi_{DM}\phi^{\dagger}_{DM}\phi_{DM}\phi^{\dagger}_{DM}$	$-4\lambda_{DM}$

Table 2.2: All possible vertex factors related to dark matter annihilation for the present model.

2.4 Results

In this section we have shown how the relic density of DM varies with various model parameters namely α, g_{BL}, n_{BL}, M_{h_2}, M_{DM}, $M_{Z_{BL}}$, λ_{Dh}, λ_{DH}. In order to compute the DM relic density, we have solved the Boltzmann equation (Eq. (1.81)) numerically using the micrOMEGAs [33] package while the information of the present model is supplied to micrOMEGAs through the LanHEP [120] package. All the constraints on the model parameters, listed in Section 2.2, are also taken into account in the numerical calculations.

In the left panel (right panel) of Fig. 2.3 we plot the variation of DM relic density Ωh^2 with the scalar mixing angle α for three different values of $\lambda_{DH} = -0.005$ ($\lambda_{Dh} = 0.008$) (green dashed line), -0.0104 (0.001) (red solid line) and -0.015 (0.004) (blue dashed-dotted line) while the values of other parameters are kept fixed at $g_{BL} = 0.01$, $M_{DM} = 52.0$ GeV, $M_{h_2} = 102.8$ GeV, $M_{Z_{BL}} = 104.1$ GeV, $\lambda_{Dh} = 0.001$ ($\lambda_{DH} = -0.0104$) and $n_{BL} = 0.15$. In this plot, magenta dotted line represents the central value of DM relic density as reported by the Planck collaboration ($\Omega h^2 = 0.1199$). From the Table 2.2 we see that the Z_{BL} mediated diagram is independent of the mixing angle α, so its contribution does not depend on α. On the other hand the two Higgs scalars h_1, h_2 mediated diagrams are dependent on the mixing angle α. It is seen from Fig. 2.3 that the dark matter relic density is practically independent of the mixing angle α when α becomes too small ($\alpha < 3\times10^{-3}$). This can be explained as follows, in this region $\sin\alpha \sim 0$ and the h_2 mediated diagram does not contribute since the $l\bar{l}h_2$ vertex is suppressed and it is mostly the Z_{BL} and h_1 mediated diagrams that contribute. For very small α, even the h_1 mediated diagram is independent of α since $\cos\alpha \sim 1$, making Ωh^2 constant with α. We also note from left (right) panel of Fig. 2.3 that in this region, Ωh^2 has no dependence on λ_{DH} (λ_{Dh}). This again can be explained using the fact that here only the h_1 mediated diagram (in addition to the Z_{BL} mediated diagram which is anyway independent of α, λ_{DH} and λ_{Dh}) contributes and Table 2.2 reveals that for small α we have impact of only λ_{Dh} on Ωh^2.

On the other hand if we start increasing the mixing α after the value ($\alpha > 3\times10^{-3}$), the scalars h_1 and h_2 both start contributing along with $\mathrm{B-L}$ gauge boson Z_{BL} in the DM annihilation process, which enhances $\langle\sigma \mathrm{v}\rangle_{b\bar{b}}$. Therefore the relic density which is approximately inverse of $\langle\sigma \mathrm{v}\rangle_{b\bar{b}}$ decreases with increase of mixing angle α. Again we notice from Table 2.2 that the $\cos\alpha$ dependent term in the vertex $\phi_{DM}\phi^{\dagger}_{DM}h_2$ and the $\sin\alpha$ dependent term in the vertex $\phi_{DM}\phi^{\dagger}_{DM}h_1$ is proportional to λ_{DH}. This makes the relic density decrease with increasing λ_{DH} for larger values of α, as is evident from the left panel of Fig. 2.3. Likewise the right panel shows the dependence of the relic density on λ_{Dh} which comes from the first term of the $\phi_{DM}\phi^{\dagger}_{DM}h_1$ vertex. This explains the decrease of the relic density with λ_{Dh}. In this figure, we have also shown the excluded region for mixing angle α from LUX and LHC experiment. The crossed region is excluded by both LUX and LHC experiment, whereas the forward lines is only excluded by LHC experiment.

Left panel of Fig. 2.4 represents the variation of Ωh^2 with $U(1)_{\mathrm{B-L}}$ gauge coupling g_{BL} for three different chosen values of λ_{DH}. Here green dashed-dotted line is for $\lambda_{DH} = -0.015$, red solid line is for $\lambda_{DH} = -0.0104$ whereas the plot for $\lambda_{DH} = -0.015$ is shown by blue dashed line. Like the previous figures here also, the central value of Planck limit

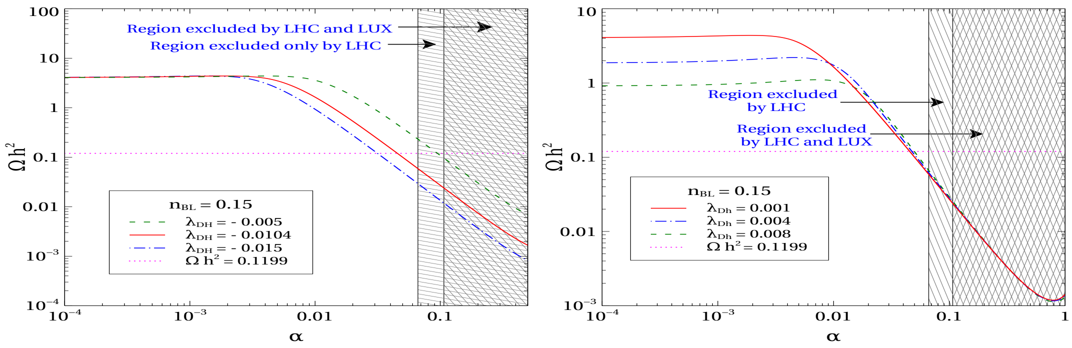

Figure 2.3: Left (Right) panel: Variation of relic density Ωh^2 with mixing angle α for $n_{BL} = 0.15$ and three different values of λ_{DH} (λ_{Dh}) while other parameters value have been kept fixed at $g_{BL} = 0.01$, $M_{DM} = 52.0$ GeV, $M_{h_2} = 102.8$ GeV, $M_{Z_{BL}} = 104.1$ GeV, $\lambda_{Dh} = 0.001$ ($\lambda_{DH} = -0.0104$).

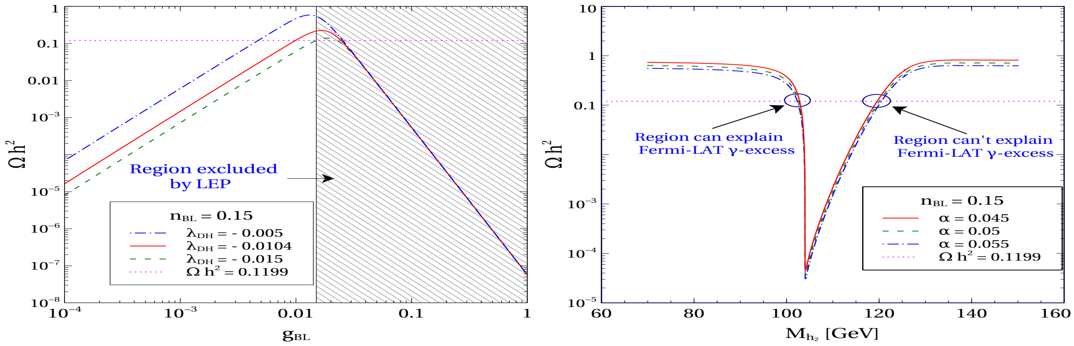

Figure 2.4: Left (Right) panel: Variation of relic density Ωh^2 with g_{BL} (M_{h_2}) for $n_{BL} = 0.15$ and three different values of λ_{DH} (α) while other parameters value have been kept fixed at $M_{DM} = 52.0$ GeV, $M_{Z_{BL}} = 104.1$ GeV, $M_{h_2} = 102.8$ GeV, $\lambda_{Dh} = 0.001$, $\alpha = 0.045$ ($\lambda_{DH} = -0.0104$). For discussion about the two marked regions see text below of this figure.

on DM relic density is indicated by magenta dotted line. It is seen from the left panel of Fig. 2.4 that initially the relic density increases with g_{BL} and attains a maximum value at $g_{BL} \sim 0.01$, thereafter it starts decreasing with g_{BL}. The initial rise of Ωh^2, for low g_{BL}, is due to s channel process of $\phi_{DM}\phi^\dagger_{DM} \rightarrow f\bar{f}$, mediated by h_1 and h_2. In this case, the relevant couplings ($\phi^\dagger_{DM}\phi_{DM}h_i$, $i = 1, 2$) are inversely proportional to g_{BL} (see Table 2.2). However, as g_{BL} becomes large ($g_{BL} \gtrsim 0.01$), the other s channel process mediated by B − L gauge boson starts dominating over the scalar exchange processes. From Table 2.2, one can easily see that the coupling $\phi^\dagger_{DM}\phi_{DM}Z_{BL}$ is proportional to g_{BL}, which makes $\langle\sigma \mathrm{v}\rangle_{f\bar{f}}$ (via Z_{BL} exchange) proportional to fourth power of g_{BL} [8]. The dominance of s

---

[8] $f\bar{f}Z_{BL}$ coupling is also proportional to g_{BL}.

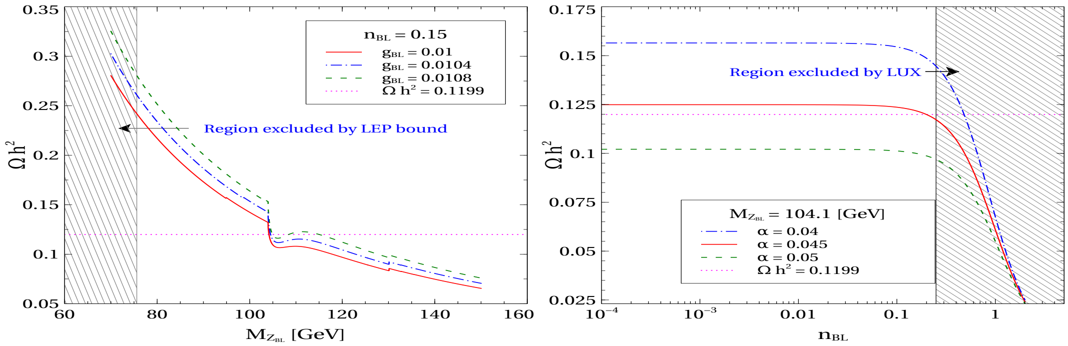

Figure 2.5: Left panel: Variation of relic density Ωh^2 with the mass of Z_{BL} for three different values of g_{BL}. Right panel: Variation of DM relic density with its B − L gauge charge n_{BL} for three different values of α. Both the plots are drawn for $M_{DM} = 52.0$ GeV, $M_{h_2} = 102.8$ GeV, $\lambda_{Dh} = 0.001$, $\lambda_{Dh} = -0.0104$.

channel Z_{BL} exchange annihilation process over the scalar mediated ones is indicated by the fact that in this region (higher value of g_{BL}, $g_{BL} \gtrsim 0.01$) Ωh^2 (or $\langle \sigma \mathrm{v} \rangle_{f\bar{f}}$) does not depend on the coupling λ_{DH}. We show by the hatched region the values of g_{BL} excluded by LEP.

In the right panel of Fig. 2.4 we show the variation of Ωh^2 with the mass of the non-standard Higgs boson h_2 for three different values of its mixing angle with SM Higgs, namely $\alpha = 0.045$, 0.05, 0.055. From this plot, it is seen that for all the chosen values of α the relic density satisfies the Planck limit only near the resonance region when $M_{DM} \sim M_{h_2}/2$. The figure shows that in this region Ωh^2 becomes practically independent of α. We see that there are two sets of values of M_{h_2} for which the model can predict the correct dark matter relic density. Of these two regions which are marked in the figure, one of them with $M_{h_2} \sim 100$ GeV produces $\langle \sigma \mathrm{v} \rangle_{b\bar{b}}$ in the right ballpark value of $\sim 10^{-26}\,\mathrm{cm}^3/\mathrm{s}$, thus can explain the Fermi-LAT gamma-ray excess [110]. Whereas the other region labelled as "Region can't explain Fermi-LAT γ excess" ($M_{h_2} \sim 120$ GeV) produces $\langle \sigma \mathrm{v} \rangle_{b\bar{b}} \sim 10^{-29}\,\mathrm{cm}^3/\mathrm{s}$ (see Fig. 2.9 also).

Variation of Ωh^2 with the mass of B − L gauge boson is shown in left panel of Fig. 2.5. In this figure three different plots are computed for three different values of B − L gauge coupling (g_{BL}). Here, red solid line is for $g_{BL} = 0.01$ while $g_{BL} = 0.0108$ and

0.0104 are represented by green dashed line and blue dashed-dotted line, respectively. This figure is drawn for fixed values of other parameters, namely, $\alpha = 0.045$, $M_{DM} = 52.0$ GeV, $M_{h_2} = 102.8$ GeV, $\lambda_{Dh} = 0.001$, $\lambda_{DH} = -0.0104$, $n_{BL} = 0.15$. From this plot it is seen that for a fixed value of $M_{Z_{BL}}$, DM relic density increases with g_{BL}, which is consistent with the plot in left panel of Fig. 2.4 (cf. red line in the left panel of Fig. 2.4 where the maxima of Ωh^2 occurs for $g_{BL} \gtrsim 0.015$). The presence of resonance due to Z_{BL} (when $\sqrt{s} \simeq M_{Z_{BL}}$) is also seen from this figure and like the previous case for h_2 here also the Planck limit is satisfied only near the resonance. However, the resonance due to Z_{BL} is not as sharp as it is due to h_2 because in this region of parameter space the decay width of Z_{BL} is nearly two orders of magnitude larger than that of h_2. Here in the left panel the shaded region is not allowed by the LEP bound on Z_{BL}. Right panel of Fig. 2.5 describes the variation of Ωh^2 with the $B-L$ gauge charge (n_{BL}) for three different values of neutral scalar mixing angle namely $\alpha = 0.04$ (blue dashed-dotted line), 0.045 (red solid line) and 0.05 (green dashed line), respectively. From this figure it is seen that as the $\mathrm{B-L}$ charge of the DM candidate ϕ_{DM} decreases, its relic density increases sharply and eventually the DM relic density saturates after a certain value of $n_{BL} \lesssim 0.1$. A possible explanation of this nature of Ωh^2 could be as follows. For large value of n_{BL} ($n_{BL} \sim 1$) the maximum contribution to DM annihilation cross section comes from $\mathrm{B-L}$ gauge boson mediated channel as the cross section for this channel is directly proportional to n_{BL}^2. Hence $\langle \sigma \mathrm{v} \rangle_{f\bar{f}}$ becomes practically independent of the mixing angle α. However as n_{BL} decreases from unity the scalar mediated s channel processes become significant and consequently after a certain value of n_{BL} ($n_{BL} \lesssim 0.1$) the annihilation cross section $\langle \sigma \mathrm{v} \rangle_{f\bar{f}}$ becomes nearly insensitive to n_{BL} and depends strongly on the mixing angle α. In the right panel, we have given upper bound on the DM charge n_{BL}, which we get from LUX limit on spin independent direct detection cross section.

Variation of Ωh^2 with dark matter mass for two different values of n_{BL} are shown in Fig. 2.6. In this figure, the left panel is for $n_{BL} = 0.15$ while the right panel is for $n_{BL} = 0.2$. In each panel the three different lines represent the variation of Ωh^2 with n_{BL}

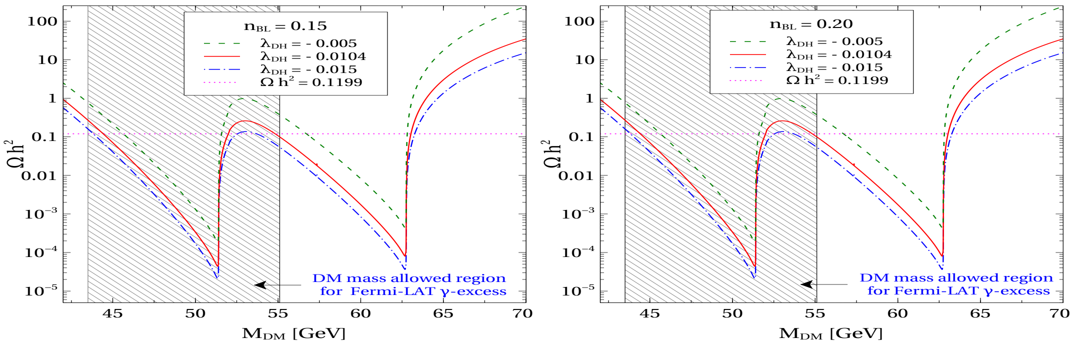

Figure 2.6: Left (Right) panel: Variation of relic density Ωh^2 with mass of ϕ_{DM} for $n_{BL} = 0.15$ ($n_{BL} = 0.20$) and three different value of λ_{DH} while other parameters value have been kept fixed at $\alpha = 0.045$, $g_{BL} = 0.01$, $M_{h_2} = 102.8$ GeV, $M_{Z_{BL}} = 104.1$ GeV, $\lambda_{Dh} = 0.001$.

for three chosen values of $\lambda_{DH} = -0.005$, -0.0104 and -0.015 respectively. From both panels of Fig. 2.6 it is seen that there are two resonance regions where the first one is for the non-standard Higgs boson h_2 ($M_{h_2} \sim 104$ GeV) while the second one corresponds to the SM Higgs boson of mass 125.5 GeV. In both panels the DM relic density satisfies the Planck limit (indicated by the magenta dotted line) only near the resonance regions. In both the panel of Fig. 2.6, we have shown allowed region of DM mass for explaining Fermi-LAT gamma-ray excess from GC.

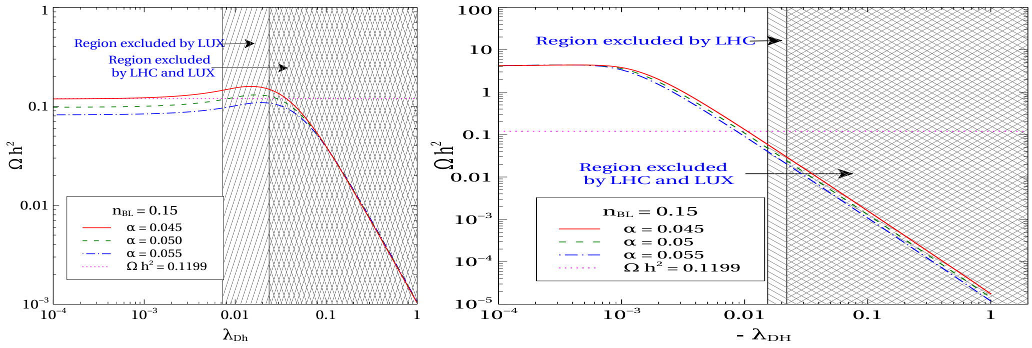

Figure 2.7: Left (Right) panel: Variation of relic density Ωh^2 with λ_{Dh} (λ_{DH}) for $n_{BL} = 0.15$ and three different values of mixing angle α while other relevant parameters value have been kept fixed at $M_{DM} = 52.0$ GeV, $M_{h_2} = 102.8$ GeV, $M_{Z_{BL}} = 104.1$ GeV, $\lambda_{DH} = -0.0104$ ($\lambda_{Dh} = 0.001$).

We finally show the variation of Ωh^2 with two remaining model parameters λ_{Dh} and λ_{DH} in left and right panel of Fig. 2.7, respectively. In each panel we have shown the variation of Ωh^2 for three different values of mixing angle α namely $\alpha = 0.045$, 0.05 and

0.055. From the left panel of Fig. 2.7 it is seen that for small value of the parameter λ_{Dh} ($\lambda_{Dh} < 0.03$) relic density remains unaffected with respect to the change in value of λ_{Dh} as in this region DM annihilation cross section is controlled by the coupling λ_{DH} which is considered to be $|\lambda_{DH}| \sim 0.01$. Also from Table 2.2 we see that when $\lambda_{DH} \gg \lambda_{Dh}$, the couplings $g_{h_1\phi_{DM}\phi^\dagger_{DM}} \propto \sin\alpha$ and $g_{h_2\phi_{DM}\phi^\dagger_{DM}} \propto \cos\alpha$. However, the term within the modulus in Eq. (2.20) is proportional to $\sin^2\alpha$. Therefore, inspite of being small in value, the variation of α produces a significant change in σ and hence in relic density. Similarly, using Eq. (2.20) and Table 2.2 one can easily see that for higher value of λ_{Dh} (when $\lambda_{DH} \ll \lambda_{Dh}$), the scalar mediated term in σ (term within modulus in Eq. (2.20)) mainly depends on $\cos\alpha$ and λ_{Dh}. Consequently, for the higher value of λ_{Dh}, there is no observable change in relic density with respect to α and it decreases with the increase of λ_{Dh}. In right panel of Fig. 2.7 we have shown the variation of Ωh^2 with λ_{DH}. It is seen from this figure that, the behaviour of DM relic density with respect to the coupling λ_{DH} is same as it is with λ_{Dh} i.e. initially for small value of λ_{DH} relic density remains unchanged and therefore after a certain value of λ_{DH} (when $\lambda_{DH} > \lambda_{Dh}$, $\lambda_{Dh} \sim 10^{-3}$) relic density falls gradually with the increase of λ_{DH}. However, by comparing both the plots in Fig. 2.7 one finds that with respect to α the behaviour of Ωh^2 Vs λ_{DH} curve is exactly opposite to the curve Ωh^2 Vs λ_{Dh} (shown in the left panel) which can be easily understood from Table 2.2 and Eq. (2.20). In both the panel we have shown allowed regions for the coupling constant λ_{Dh} and λ_{DH} respectively. The crossed regions are excluded by both LHC and LUX, whereas for left panel the backward line region is excluded by LUX and for right panel the forward line region is excluded by LHC.

In the left panel of Fig. 2.8, we show how the average value of spin independent scattering cross section $\frac{1}{2}(\sigma_{\phi_{DM}} + \sigma_{\phi^\dagger_{DM}})$ of ϕ_{DM} and $\phi^\dagger_{DM}$ with the detector nuclei varies as a function of dark matter mass for $n_{BL} = 0.15$. While computing this plot, we have varied the mass of $\mathrm{B-L}$ gauge boson in range of $2\,M_{DM}{}^{+70}_{-30}$ GeV for a particular value of DM mass (M_{DM}) since the relic density is satisfied only near the respective resonance regions of Z_{BL} and h_2 where $M_{h_2}, M_{Z_{BL}} \sim 2M_{DM}$ (see Figs. 2.4, 2.5). The other relevant

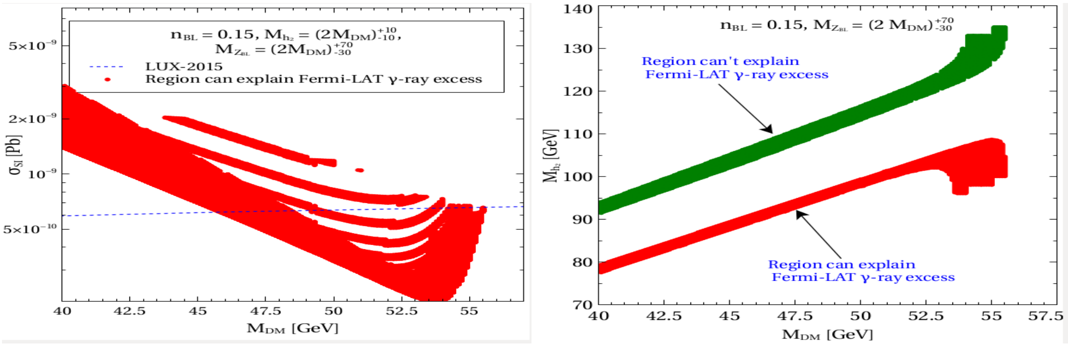

Figure 2.8: Left panel: Spin independent cross section σ_{SI} between and dark matter particle (ϕ_{DM}) and the detector nucleon for $n_{BL} = 0.15$. Blue dashed lines in this panel represent upper limit on σ_{SI} reported by LUX collaboration. Right panel: Allowed regions in $M_{DM} - M_{h_2}$ plane which satisfy the observed relic density, Fermi-LAT gamma-ray excess ($\langle \sigma v \rangle_{b\bar{b}} \sim 10^{-26}$ cm^3/s for red coloured region only) and LHC constraints listed in Section 2.2.

parameters are kept fixed at $\alpha = 0.045$, $g_{BL} = 0.01$, $\lambda_{DH} = -0.0104$, $\lambda_{Dh} = 0.001$. The experimental upper limits on the DM spin independent scattering cross section with the detector nuclei is also shown by blue dashed line. Here all the points within the red and green patches satisfy all the necessary constraints namely Planck limit on relic density, LHC bounds on invisible decay width and signal strength of SM-like Higgs boson (h_1), lower limit on $\frac{M_{Z_{BL}}}{g_{BL}}$ from LEP and also the vacuum stability conditions. From this plot it is seen that although the dark matter mass between 40 GeV to 55 GeV satisfies all the constrains mentioned above, the lower mass region between 40 GeV to 45 GeV has already been excluded by the upper limit on spin independent scattering cross section reported by the LUX collaboration. Therefore in this model with the considered ranges of model parameters, dark matter mass of 45 GeV to 55 GeV is still allowed by all possible experimental as well as theoretical constraints. This allowed region can be tested in near future by the upcoming “ton-scale” direct detection experiments like XENON 1T.

As we have seen earlier in Fig. 2.4 (right panel), that for two values of M_{h_2} Planck’s relic density central value is satisfied. If we consider the higher value of M_{h_2} ($M_{h_2} \sim 120$ GeV) then the annihilation cross section for the channel $\phi_{DM}\phi^{\dagger}_{DM} \to b\bar{b}$ comes in around $\langle \sigma v \rangle_{b\bar{b}} \sim 10^{-29}$ cm^3 s^{-1}, which cannot explain Fermi-LAT gamma excess [110]. On the other hand the lower value of M_{h_2} ($M_{h_2} \sim 100$ GeV) produces $\langle \sigma v \rangle_{b\bar{b}}$ in the right ballpark value of 10^{-26} cm^3 s^{-1} which is required to explain the Fermi-LAT gamma excess. To find the allowed region which can satisfy all the constraints as mentioned in Section 2.2 we have varied M_{h_2} and $M_{Z_{BL}}$ in the ranges $2\,M_{DM}{}^{+25}_{-10}$ GeV and $2\,M_{DM}{}^{+70}_{-30}$ GeV respectively. The allowed region in $M_{DM}-M_{h_2}$ plane is shown in the right panel of Fig. 2.8. In this plot red coloured region around $\sim 2\times M_{DM}$ corresponds to the lower value of M_{h_2} which can explain the Fermi-LAT γ-ray excess while the higher allowed value of M_{h_2} is indicated by green coloured patch which is unable to explain the GC γ-ray excess. As we have discussed above, here also the region corresponds to dark matter mass of 40 GeV to 45 GeV is ruled out by the results of LUX direct detection experiment. The region beyond the dark matter mass of 45 GeV satisfies all the constraints listed in Section 2.2.

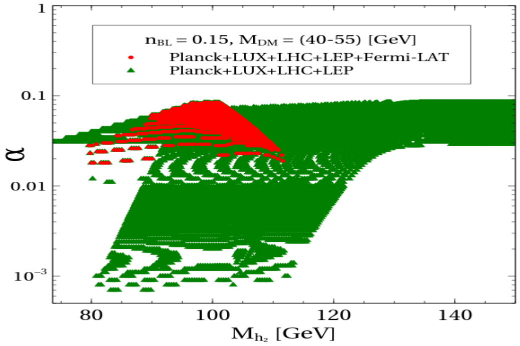

Figure 2.9: Allowed region in M_{h_2}-α plane satisfied by various experimental constraints considered in this work. Other relevant parameters are kept fixed at $\lambda_{Dh} = 0.001$, $\lambda_{DH} = -0.0104$, $M_{Z_{\rm BL}} = 104.1$ GeV and $g_{\rm BL} = 0.01$.

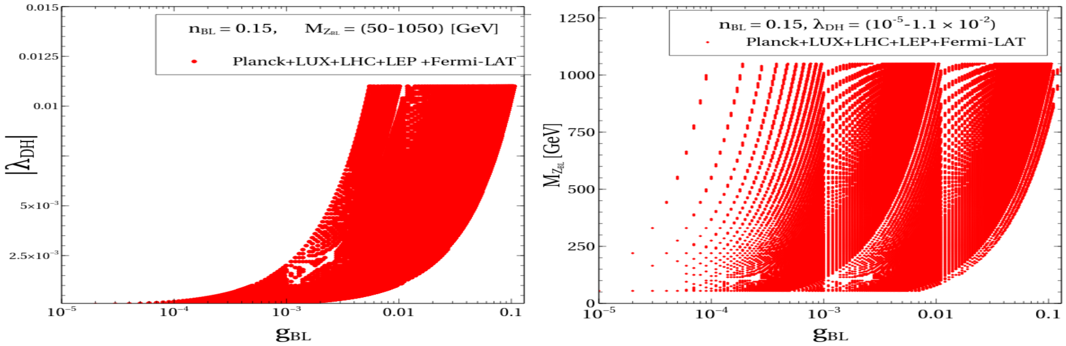

Figure 2.10: Left panel (Right panel): Allowed region in $g_{\rm BL}$-λ_{DH} ($g_{\rm BL}$-$M_{Z_{\rm BL}}$) plane satisfied by all the experimental constraints considered in this work. Other relevant parameters are kept fixed at $\lambda_{Dh} = 0.001$, $\alpha = 0.045$, $M_{DM} = 52$ GeV and $M_{h_2} = 102.8$ GeV.

In Fig. 2.9 we show the allowed region in M_{h_2}-α plane for $40\,\text{GeV} \leq M_{DM} \leq 55$

GeV, $M_{Z_{\rm BL}} = 104.1$ GeV, $n_{\rm BL} = 0.15$, $\lambda_{Dh} = 0.001$, $\lambda_{DH} = -0.0104$ and $g_{\rm BL} = 0.01$. Here, green coloured region satisfies all the constraints except Fermi-LAT bound on dark matter annihilation cross section into $b\bar{b}$ final state while the values of α and M_{h_2} lying within the red coloured patch are allowed by all the experimental constraints listed in Section 2.2. The region in $\lambda_{DH} - g_{\rm BL}$ plane which satisfies simultaneously the results of Planck, LUX, LHC, LEP and Fermi-LAT experiments is shown by a red coloured patch in the left panel of Fig. 2.10. While computing this plot we have varied the mass of the extra neutral gauge boson $Z_{\rm BL}$ in the range of 50 GeV to 1050 GeV and the values of other relevant parameters are kept fixed at $M_{DM} = 52$ GeV, $M_{h_2} = 102.8$ GeV, $\alpha = 0.045$, $\lambda_{Dh} = 0.001$ and $n_{\rm BL} = 0.15$. From this figure it is evident that $g_{\rm BL} \lesssim 0.1$ and $|\lambda_{DH}| \lesssim 0.011$ are allowed for $50\,{\rm GeV} \leq M_{Z_{\rm BL}} \leq 1050$ GeV. On the other hand from the right panel of Fig. 2.10 one can see that all the considered range of $M_{Z_{\rm BL}}$ ($50\,{\rm GeV} \leq M_{Z_{\rm BL}} \leq 1050$ GeV), except the extreme right region with $g_{\rm BL}$ lies between 0.01 to 0.1 (LEP excluded region), is allowed with respect to the variation of $\rm U(1)_{B-L}$ gauge coupling constant $g_{\rm BL}$.

2.5 Gamma-ray flux

In this present model the pair annihilation of $\phi_{DM}\phi^\dagger_{DM}$ produces b and $\bar{b}$ at the final state[9]. Therefore, these b quarks undergo hadronisation processes and produce γ-rays. The differential gamma-ray flux from the pair annihilation of ϕ_{DM} and $\phi^\dagger_{DM}$ at the Galactic Centre region is given by

$$\frac{d\Phi_\gamma}{d\Omega dE} = \frac{1}{2}\frac{r_\odot}{8\pi}\left(\frac{\rho_\odot}{M_{DM}}\right)^2 \bar{J}\,\langle\sigma {\rm v}\rangle_{b\bar{b}}\frac{dN^{\rm b}_\gamma}{dE}\,, \tag{2.21}$$

where $r_\odot = 8.5$ kpc is the distance of solar system from the centre of our Milky way galaxy and dark matter density near the solar neighbourhood is denoted by $\rho_\odot$ which is taken to be 0.4 GeV/cm^3. Similar to Eqs. (1.81), here also the half factor appearing in the

---

[9] One can extrapolate this work and can explain the Fermi-LAT gamma-ray excess by studying different channels such as $\tau^+\tau^-$, W^+W^-, $q\bar{q}$ and $h_1 h_1$.

expression of the differential gamma-ray flux is due the non-self-conjugate nature of ϕ_{DM}. Moreover, $\frac{dN_{\gamma}^{\rm b}}{dE}$ is the spectrum of produced gamma-rays from the hadronisation processes of b quarks and we have adopted the numerical values of $\frac{dN_{\gamma}^{\rm b}}{dE}$ for different values of photon energy from ref. [121]. Annihilation cross section for the channel $\phi_{DM}\phi_{DM}^{\dagger} \to b\bar{b}$ which acts as the seed mechanism for the Galactic Centre gamma-excess, is denoted by $\langle\sigma {\rm v}\rangle_{b\bar{b}}$. Further, $\bar{J}$ is the averaged of "astrophysical J factor" over a solid angle $\Delta\Omega$. The value of solid angle $\Delta\Omega$ around the Galactic Centre depends on the choice of a particular region of interest (ROI). In the present work we have adopted the same ROI as considered by Calore *et. al.* [110] which is $|l| < 20^0$ and $2^0 < |{\rm b}| < 20^0$ with l and b are the galactic longitude and latitude respectively. Therefore, the expression of $\bar{J}$ is given by

$$\bar{J} = \frac{4}{\Delta\Omega}\int\int d{\rm b}\, dl \cos{\rm b}\; J({\rm b}, l)\,, \tag{2.22}$$

with

$$J(l, {\rm b}) = \int_{\rm l.o.s} \frac{d\mathfrak{s}}{r_{\odot}}\left(\frac{\rho(r)}{\rho_{\odot}}\right)^2\,, \tag{2.23}$$

and

$$\Delta\Omega = 4\int dl \int d{\rm b}\cos{\rm b}\,, \tag{2.24}$$

$$r = \left(r_{\odot}^2 + \mathfrak{s}^2 - 2\, r_{\odot}\, \mathfrak{s}\cos{\rm b}\cos l\right)^{1/2}\,, \tag{2.25}$$

where the integration of Eq. (2.23) is performed along the line of sight (l.o.s) distance $\mathfrak{s}$ which can be defined using Eq. (2.25). In the definition of "astrophysical J factor" (Eq. (2.23)), $\rho(r)$ represents the variation of dark matter density with respect to the distance r from the Galactic Centre, which is also known as the density profile of dark matter. As the actual form of the density profile is still unknown to us there are many approximate dark matter density profiles available in the literature such as NFW profile [122], Einasto profile [123], Isothermal profile [124], Moore profile [125]. Therefore, as in ref. [110], in this work also, we have used NFW halo profile with $\gamma = 1.26$, $r_s = 20$ kpc. Using Eqs. (2.22-2.25) and a NFW dark matter halo profile we have found the value of $\bar{J} = 57.47$ for the above mentioned ROI ($|l| < 20^0$ and $2^0 < |\mathrm{b}| < 20^0$). However, due to our poor knowledge about the halo profile parameters ($\rho_\odot$, γ, r_s) the value of $\bar{J}$ may vary from its canonical value $\bar{J} = 57.47$ obtained for $\gamma = 1.26$, $r_s = 20$, $\rho_\odot = 0.4$ GeV/cm^3. Now in order to include such uncertainties into the value of $\bar{J}$, which exist within the values of DM density profile parameters, we have redefined $\bar{J}$ in the following way

$$\bar{J} = \mathcal{A}\,\bar{J}_{canonical}\,, \tag{2.26}$$

where $\bar{J}_{canonical} = 57.47$, i.e. the value of $\bar{J}$ for $\gamma = 1.26$, $r_s = 20$, $\rho_\odot = 0.4$ GeV/cm^3 and the quantity $\mathcal{A}$ can vary in the range 0.19 to 5.3 [110]. Therefore, the values of $\bar{J}$ and $J_{canonical}$ coincide when $\mathcal{A} = 1$.

Using Eqs. (2.21-2.26), we have computed the γ-ray flux due to the pair annihilation of $\phi_{DM}\phi^{\dagger}_{DM}$ into $b\bar{b}$ final state and it is plotted in Fig. 2.11. In this plot, Fermi-LAT observed gamma-ray flux from the direction of Galactic Centre is denoted by black triangle shaped points with the black vertical lines represent the uncorrelated statistical errors while the correlated systematics are described by yellow coloured boxes. The red solid line denotes the gamma-ray flux which is computed for an annihilating non-self-conjugate dark matter particle of mass $M_{DM} = 52$ GeV using the present model. We have found that the gamma-flux obtained from the present model agrees well with the flux observed by Fermi-LAT if the product of $\mathcal{A}\langle\sigma \mathrm{v}\rangle_{b\bar{b}} = 4.7 \times 10^{-26}$ cm^3/s. Therefore, if we use the canonical values of the halo profile parameters (when $\mathcal{A} = 1$ and $\bar{J} = 57.47$) then in order to reproduced Fermi-LAT observed gamma-ray flux from the pair annihilation of a non-self-conjugate dark matter of mass 52 GeV its annihilation cross section for the $b\bar{b}$ channel must be 4.7×10^{-26} cm^3/s. For the other values of $\mathcal{A}$ which are not equal to unity, the quantity $\langle\sigma\mathrm{v}\rangle_{b\bar{b}}$ will be scaled accordingly.

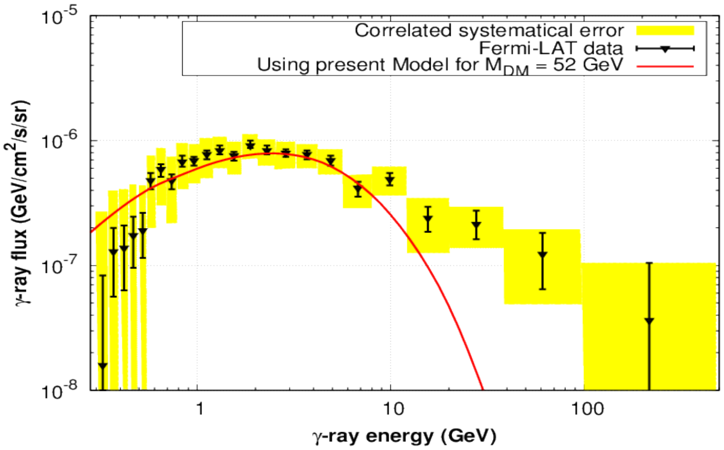

Figure 2.11: Gamma-ray flux produced from dark matter annihilation at the Galactic Centre.

Three allowed values of $\langle\sigma\mathrm{v}\rangle_{b\bar{b}}$ that we have obtained from the present model for $M_{DM} = 52$ GeV, which are also satisfying all the constrains listed in Section 2.2, are given in Table 2.3.

M_{DM} [GeV]	n_{BL}	M_{h_2} [GeV]	$M_{Z_{BL}}$ [GeV]	Ωh^2	$<\sigma\mathrm{v}>_{b\bar{b}}$ [cm^{3}s^{-1}]	$\mathcal{A}$
52.0	0.15	103.3	77.1	0.1208	7.005×10^{-26}	0.67
		102.8	104.2	0.1191	4.545×10^{-26}	1.03
		101.4	168.6	0.1199	2.853×10^{-26}	1.65

Table 2.3: Allowed values of $\langle\sigma\mathrm{v}\rangle_{b\bar{b}}$ and $\mathcal{A}$ for three randomly chosen benchmark points M_{h_2} and $M_{Z_{\mathrm{BL}}}$. The values of other relevant parameters are $g_{\mathrm{BL}} = 0.01$, $\alpha = 0.045$, $\lambda_{DH} = -0.0104$ and $\lambda_{Dh} = 0.001$.

3

Neutrino Mass, Dark Matter and Anomalous Magnetic Moment of Muon in a $\mathrm{U}(1)_{L_\mu - L_\tau}$ Model

3.1 Introduction

This chapter contains the paper [126] where we have considered the gauged $\mathrm{U}(1)_{L_\mu - L_\tau}$ extension of the SM. The main motivations for choosing this model is that it provides $\mu - \tau$ flavor symmetry which could naturally explain the peculiar neutrino mixing parameters (See Table 1.2) wherein θ_{23} is close to maximal and θ_{13} is small. As mentioned above, this model can also explain the muon $(g-2)$ anomaly [127–131] for a range of $Z_{\mu\tau}$ mass and $g_{\mu\tau}$ consistent with collider constraints. We will further extend this model with a complex scalar, which will become a viable DM candidate. $\mathrm{U}(1)_{L_\mu - L_\tau}$ extended Ma model [90] has been studied earlier in the context of small neutrino mass generation in one loop level [132] and dark matter [133]. A review on earlier works about $\mu - \tau$ flavour symmetry in neutrino sector can be found in [134] and references therein. In order to generate neutrino masses through the Type-I seesaw mechanism [135–138] in the present scenario, we have introduced three right handed neutrinos (N_e, N_μ, N_τ) with $L_\mu - L_\tau$ charges 0, 1 and -1 respectively in the fermionic sector of SM. The scalar sector of the model is also enlarged by the addition of two complex scalar singlets (ϕ_H and ϕ_{DM}) with nonzero $L_\mu - L_\tau$ charge. The proposed $L_\mu - L_\tau$ symmetry is broken spontaneously when ϕ_H acquires vacuum expectation value (VEV) $v_{\mu\tau}$ and thereby making $Z_{\mu\tau}$ massive. The breaking of $L_\mu - L_\tau$ symmetry also results in additional terms in the neutrino mass matrix. In particular, the $\mu - \tau$ symmetry is broken and we can generate neutrino masses and mixing parameters consistent with current bounds. We show that the complex scalar ϕ_{DM} is stable in our model and hence becomes the DM candidate satisfying the constraints from Planck, LUX and LHC results. We show that a sub-region of the parameter space that is consistent with Planck, LUX and LHC results can also explain the Galactic Centre gamma ray excess observed by Fermi-LAT.

3.2 Model

In this present work, we have considered a minimal extension of the SM where we have imposed an extra local $\mathrm{U}(1)_{L_\mu - L_\tau}$ symmetry to the SM Lagrangian, where L_μ and L_τ denote the muon lepton number and tau lepton number respectively. Therefore, the Lagrangian of the present model remains invariant under the $\mathrm{SU}(3)_\mathrm{c} \times \mathrm{SU}(3)_c \times \mathrm{SU}(2)_L \times \mathrm{U}(1)_Y \times \mathrm{U}(1)_{L_\mu - L_\tau}$ gauge symmetry. This model is free from axial vector and mixed gravitational gauge anomalies as these anomalies cancel between second and third generations of leptons without the requirement of any additional chiral fermion. The full particle content of our model and their respective charges under $\mathrm{SU}(3)_c \times \mathrm{SU}(2)_L \times \mathrm{U}(1)_Y \times \mathrm{U}(1)_{L_\mu - L_\tau}$ gauge groups are listed in Tables 3.1 and 3.2. In order to break the $\mathrm{U}(1)_{L_\mu - L_\tau}$ symmetry spontaneously, we need a complex scalar field ϕ_H with a non-trivial $L_\mu - L_\tau$ charge assignment such that the $L_\mu - L_\tau$ symmetry is broken spontaneously when ϕ_H picks up a vacuum expectation value $v_{\mu\tau}$. Spontaneous breaking of the $L_\mu - L_\tau$ symmetry generates mass for the extra neutral gauge boson $Z_{\mu\tau}$. It has been shown that the spontaneously broken $L_\mu - L_\tau$ model can explain the anomalous muon $g - 2$ signal. The $L_\mu - L_\tau$ symmetry is a flavor symmetry and hence can be used to explain the peculiar mixing pattern of the neutrinos [139]. In our model we generate small neutrino masses through the Type-I seesaw mechanism. To that end we introduce three right handed neutrinos (N_e, N_μ, N_τ) with

$L_\mu - L_\tau$ charges of 0, 1 and -1 respectively, such that their presence do not introduce any further anomaly. In the $\mathrm{U}(1)_{L_\mu - L_\tau}$ symmetric limit the right-handed neutrino mass has exact $\mu - \tau$ symmetry. We will show that the spontaneous breaking of the gauged $\mathrm{U}(1)_{L_\mu - L_\tau}$ symmetry leads to additional terms in the right-handed neutrino mass matrix, providing a natural explanation of the neutrino masses and mixing parameters observed in neutrino oscillation experiments, given in Table 1.2. We also add another complex scalar field ϕ_{DM} in the model, with a chosen $L_\mu - L_\tau$ charge $n_{\mu\tau}$ such that the Lagrangian does not contain any term with odd power of ϕ_{DM}. Also the scalar field ϕ_{DM} does not acquire any VEV and consequently in this model ϕ_{DM} becomes odd under a remnant $\mathbb{Z}_2$ symmetry after the spontaneous breaking of the gauged $\mathrm{U}(1)_{L_\mu - L_\tau}$ symmetry, which ensure its stability. Hence ϕ_{DM} can be a viable dark matter candidate. We now write the Lagrangian of present model, which is given by

Gauge Group	Baryon Fields			Lepton Fields			Scalar Fields		
	$Q^i_L = (u^i_L, d^i_L)^T$	u^i_R	d^i_R	$L^i_L = (\nu^i_L, e^i_L)^T$	e^i_R	N^i_R	ϕ_h	ϕ_H	ϕ_{DM}
$\mathrm{SU(2)_L}$	2	1	1	2	1	1	2	1	1
$\mathrm{U(1)_Y}$	1/6	2/3	−1/3	−1/2	−1	0	1/2	0	0

Table 3.1: Particle contents and their corresponding charges under SM gauge group.

Gauge Group	Baryonic Fields	Lepton Fields			Scalar Fields		
	(Q^i_L, u^i_R, d^i_R)	(L^e_L, e_R, N^e_R)	$(L^\mu_L, \mu_R, N^\mu_R)$	$(L^\tau_L, \tau_R, N^\tau_R)$	ϕ_h	ϕ_H	ϕ_{DM}
$\mathrm{U}(1)_{L_\mu - L_\tau}$	0	0	1	−1	0	1	$n_{\mu\tau}$

Table 3.2: Particle contents and their corresponding charges under $\mathrm{U}(1)_{L_\mu - L_\tau}$.

$$\mathcal{L} \;=\; \mathcal{L}_{SM} + \mathcal{L}_N + \mathcal{L}_{DM} + (D_\mu \phi_H)^\dagger (D^\mu \phi_H) - V(\phi_h, \phi_H) - \frac{1}{4} F^{\alpha\beta}_{\mu\tau} F_{\mu\tau_{\alpha\beta}}, \qquad (3.1)$$

where $\mathcal{L}_{SM}$ is the usual SM Lagrangian while the Lagrangian for the right handed neutrinos containing their kinetic energy terms, mass terms and Yukawa terms with the SM lepton doublets, is denoted by $\mathcal{L}_N$ which can be written as

$$\begin{aligned}\mathcal{L}_N &= \sum_{i=e,\mu,\tau} \frac{i}{2}\bar{N}_i\gamma^\mu D_\mu N_i - \frac{1}{2}M_{ee}\,\bar{N}_e^c N_e - \frac{1}{2}M_{\mu\tau}\,(\bar{N}_\mu^c N_\tau + \bar{N}_\tau^c N_\mu) \\ &\quad -\frac{1}{2}h_{e\mu}(\bar{N}_e^c N_\mu + \bar{N}_\mu^c N_e)\phi_H^\dagger - \frac{1}{2}h_{e\tau}(\bar{N}_e^c N_\tau + \bar{N}_\tau^c N_e)\phi_H \\ &\quad - \sum_{i=e,\mu,\tau} y_i \bar{L}_i\tilde{\phi}_h N_i + h.c. \end{aligned} \tag{3.2}$$

with $\tilde{\phi}_h = i\sigma_2\phi_h^*$ and M_{ee}, $M_{\mu\tau}$ are constants having dimension of mass while the Yukawa couplings $h_{e\mu}$, $h_{e\tau}$ and y_i are dimensionless constants. In Eq. (3.1), $\mathcal{L}_{DM}$ represents the dark sector Lagrangian including the interactions of ϕ_{DM} with other scalar fields. The expression of $\mathcal{L}_{DM}$ is given by

$$\begin{aligned}\mathcal{L}_{DM} &= (D^\mu\phi_{DM})^\dagger(D_\mu\phi_{DM}) - \mu_{DM}^2\phi_{DM}^\dagger\phi_{DM} - \lambda_{DM}(\phi_{DM}^\dagger\phi_{DM})^2 \\ &\quad -\lambda_{Dh}(\phi_{DM}^\dagger\phi_{DM})(\phi_h^\dagger\phi_h) - \lambda_{DH}(\phi_{DM}^\dagger\phi_{DM})(\phi_H^\dagger\phi_H)\,. \end{aligned} \tag{3.3}$$

Moreover, the quantity $V(\phi_h, \phi_H)$ in Eq. (3.1) contains all the self interaction of ϕ_H and its interaction with SM Higgs doublet. Therefore,

$$V(\phi_h, \phi_H) = \mu_H^2\phi_H^\dagger\phi_H + \lambda_H(\phi_H^\dagger\phi_H)^2 + \lambda_{hH}(\phi_h^\dagger\phi_h)(\phi_H^\dagger\phi_H)\,. \tag{3.4}$$

The expressions of all the covariant derivatives appearing in Eqs. (3.1)-(3.3) can be written in a generic form which is given as

$$D_\nu X = (\partial_\nu + i\,g_{\mu\tau}\,Q_{\mu\tau}(X)\,Z_{\mu\tau_\nu})\,X\,, \tag{3.5}$$

where X is any field which is singlet under SM gauge group but has a $L_\mu - L_\tau$ charge $Q_{\mu\tau}(X)$ (see Table 3.2) and $g_{\mu\tau}$ is the gauge coupling of the $\mathrm{U}(1)_{L_\mu - L_\tau}$ group. Furthermore, the last term in Eq. (3.1) represents the kinetic term for the extra neutral gauge boson $Z_{\mu\tau}$ in terms of its field strength tensor $F_{\mu\tau}^{\alpha\beta} = \partial^\alpha Z_{\mu\tau}^\beta - \partial^\beta Z_{\mu\tau}^\alpha$.

The $L_\mu - L_\tau$ symmetry breaks spontaneously when ϕ_H acquires VEV and consequently the corresponding gauge field $Z_{\mu\tau}$ becomes massive, $M_{Z_{\mu\tau}} = g_{\mu\tau}\, v_{\mu\tau}$. In the unitary gauge, the expressions of ϕ_h and ϕ_H after spontaneous breaking of the $\mathrm{SU}(3)_c \times \mathrm{SU}(2)_L \times \mathrm{U}(1)_Y \times \mathrm{U}(1)_{L_\mu - L_\tau}$ gauge symmetry are

$$\phi_h = \begin{pmatrix} 0 \\ \dfrac{v+H}{\sqrt{2}} \end{pmatrix}, \quad \phi_H = \begin{pmatrix} \dfrac{v_{\mu\tau} + H_{\mu\tau}}{\sqrt{2}} \end{pmatrix}, \tag{3.6}$$

where v and $v_{\mu\tau}$ are the VEVs of ϕ_h and ϕ_H respectively. Presence of the mutual interaction term in Eq. (3.4) between ϕ_h and ϕ_H introduces mass mixing between the scalar fields H and $H_{\mu\tau}$. The scalar mass matrix with off-diagonal elements proportional to λ_{hH} is given by

$$\mathcal{M}^2_{scalar} = \begin{pmatrix} 2\lambda_h\, v^2 & \lambda_{hH}\, v_{\mu\tau}\, v \\ & \\ \lambda_{hH}\, v_{\mu\tau}\, v & 2\lambda_H\, v_{\mu\tau}^2 \end{pmatrix}. \tag{3.7}$$

From the expression of $\mathcal{M}^2_{scalar}$ it is evident that if $\lambda_{hH} = 0$ (i.e. the interaction between ϕ_h and ϕ_H is absent), there is no mixing between H and $H_{\mu\tau}$ and hence they can represent two physical states. In our model however $\lambda_{hH} \neq 0$ and consequently the states representing the physical scalars will be obtained after the diagonalization of matrix $\mathcal{M}^2_{scalar}$. The new physical states which are linear combinations of H and $H_{\mu\tau}$ can be written as

$$\begin{aligned} h_1 &= H\cos\alpha + H_{\mu\tau}\sin\alpha\,, \\ h_2 &= -H\sin\alpha + H_{\mu\tau}\cos\alpha\,. \end{aligned} \tag{3.8}$$

The mixing angle α and the corresponding eigenvalues (masses of h_1 and h_2) are given by

$$\begin{aligned}
\tan 2\alpha &= \frac{\lambda_{hH}\, v_{\mu\tau}\, v}{\lambda_h v^2 - \lambda_H v_{\mu\tau}^2}\,, && (3.9)\\
M_{h_1}^2 &= \lambda_h v^2 + \lambda_H v_{\mu\tau}^2 + \sqrt{(\lambda_h v^2 - \lambda_H v_{\mu\tau}^2)^2 + (\lambda_{hH}\, v\, v_{\mu\tau})^2}\,, && (3.10)\\
M_{h_2}^2 &= \lambda_h v^2 + \lambda_H v_{\mu\tau}^2 - \sqrt{(\lambda_h v^2 - \lambda_H v_{\mu\tau}^2)^2 + (\lambda_{hH}\, v\, v_{\mu\tau})^2}\,. && (3.11)
\end{aligned}$$

We have considered h_1 as the SM-like Higgs boson [1] which has recently been discovered by ATLAS [140] and CMS [141] collaborations. Therefore its mass M_{h_1} and VEV v are kept fixed at 125.5 GeV and 246 GeV respectively. The mass of dark matter candidate ϕ_{DM} takes the following form

$$M_{DM}^2 = \mu_{DM}^2 + \frac{\lambda_{Dh}\, v^2}{2} + \frac{\lambda_{DH}\, v_{\mu\tau}^2}{2}\,. \tag{3.12}$$

In this model our ground state is defined as $\langle\phi_h\rangle = \frac{v}{\sqrt{2}}$, $\langle\phi_H\rangle = \frac{v_{\mu\tau}}{\sqrt{2}}$ and $\langle\phi_{DM}\rangle = 0$ this requires

$$\mu_h^2 < 0,\ \mu_H^2 < 0 \text{ and } \mu_{DM}^2 > 0. \tag{3.13}$$

The stability of the ground state (vacuum) requires the following inequalities [93] among the quartic couplings of scalar fields

$$\begin{aligned}
&\lambda_h \geq 0, \lambda_H \geq 0, \lambda_{DM} \geq 0,\\
&\lambda_{hH} \geq -2\sqrt{\lambda_h \lambda_H},\\
&\lambda_{Dh} \geq -2\sqrt{\lambda_h \lambda_{DM}},\\
&\lambda_{DH} \geq -2\sqrt{\lambda_H \lambda_{DM}},\\
&\sqrt{\lambda_{hH} + 2\sqrt{\lambda_h \lambda_H}}\sqrt{\lambda_{Dh} + 2\sqrt{\lambda_h \lambda_{DM}}}\sqrt{\lambda_{DH} + 2\sqrt{\lambda_H \lambda_{DM}}}\\
&+2\sqrt{\lambda_h\lambda_H\lambda_{DM}} + \lambda_{hH}\sqrt{\lambda_{DM}} + \lambda_{Dh}\sqrt{\lambda_H} + \lambda_{DH}\sqrt{\lambda_h} \geq 0\ . && (3.14)
\end{aligned}$$

---

[1] Eq. (3.10, 3.11) are valid when $M_{h_1} > M_{h_2}$. On the other hand, the expressions of M_{h_1} and M_{h_2} will be interchanged for $M_{h_2} > M_{h_1}$ resulting an change in sign to the mixing angle α.

Besides the above inequalities, the upper bound on quartic, gauge and Yukawa couplings can be obtained from the condition of perturbativity. For a scalar quartic coupling λ ($\lambda = \lambda_h,\ \lambda_H,\ \lambda_{DM},\ \lambda_{hH},\ \lambda_{Dh},\ \lambda_{DH}$) this condition will be ensured when [142]

$$\lambda < 4\pi\,, \tag{3.15}$$

while for gauge coupling $g_{\mu\tau}$ and Yukawa coupling y ($y = y_e$, y_μ, y_τ, $h_{e\mu}$ and $h_{e\tau}$) it is [142]

$$g_{\mu\tau}, y < \sqrt{4\pi}\,. \tag{3.16}$$

The above quadratic and quartic couplings of scalars fields ϕ_h and ϕ_H namely μ_h^2, μ_H^2, λ_h, λ_H and λ_{hH} can be expressed in terms of physical scalar masses (M_{h_1}, M_{h_2}), mixing angle α and VEVs (v, $v_{\mu\tau}$), which have been given in [93].

3.3 Muon $(g-2)$

It is well known that from the Dirac equation, the magnetic moment of muon $\vec{M}$ can be written in terms of its spin ($\vec{S}$), which is

$$\vec{M} = g_\mu \frac{e}{2m_\mu}\vec{S}, \tag{3.17}$$

where m_μ is the mass of muon and $g_\mu = 2$ is the gyromagnetic ratio. However, if we calculate g_μ using QFT then contributions arising from loop corrections slightly shift the value of g_μ from 2. Hence one can define a quantity a_μ which describes the deviation of g_μ from its tree level value,

$$a_\mu = \frac{g_\mu - 2}{2}\,. \tag{3.18}$$

In general, the contribution to the theoretical value of a_μ ($a_\mu^{\rm th}$) comes from the following sources [117]

$$a_\mu^{\rm th} = a_\mu^{\rm QED} + a_\mu^{\rm EW} + a_\mu^{\rm Had}\,, \tag{3.19}$$

where the contributions arising from Quantum Electrodynamics (QED), Electroweak theory and hadronic process are denoted by $\mathrm{a}_\mu^{\rm QED}$, $\mathrm{a}_\mu^{\rm EW}$ and $\mathrm{a}_\mu^{\rm Had}$, respectively. The SM prediction of a_μ including the above terms is [143]

$$a_\mu^{\rm th} = 1.1659179090(65)\times 10^{-3}\,. \tag{3.20}$$

On the other hand, a_μ has been precisely measured experimentally, initially by the CERN experiments and later on by the E821 experiment, and the current average experimental value is [128]

$$a_\mu^{\rm exp} = 1.16592080(63)\times 10^{-3}\,. \tag{3.21}$$

From the above one can see that although the theoretically predicted and the experimentally measured values of a_μ are quite close to each other, there still exists some discrepancy between these two quantities at the 3.2σ significance which is [143],

$$\Delta a_\mu = a_\mu^{\rm exp} - a_\mu^{\rm th} = (29.0 \pm 9.0)\times 10^{-10}\,. \tag{3.22}$$

Therefore, in order to reduce the difference between $a_\mu^{\rm exp}$ and $a_\mu^{\rm th}$ we need to explore BSM scenarios where we can get extra contributions from some extra diagrams. In our $\mathrm{U}(1)_{L_\mu - L_\tau}$ model we have an additional one loop diagram compared to the SM, which is mediated by the extra neutral gauge boson $Z_{\mu\tau}$ and gives nonzero contribution to $a_\mu^{\rm th}$ as shown in Fig. 3.1. The additional contribution to $a_\mu^{\rm th}$ from this diagram is given by

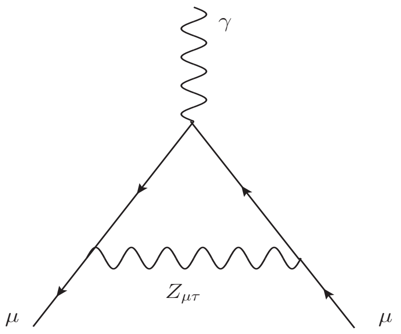

Figure 3.1: One loop Feynman diagram contributing to muon $(g-2)$, mediated by the extra gauge boson $Z_{\mu\tau}$.

[127, 144],

$$\Delta a_\mu(Z_{\mu\tau}) = \frac{g_{\mu\tau}^2}{8\pi^2}\int_0^1 dx \frac{2x(1-x)^2}{(1-x)^2 + rx}, \tag{3.23}$$

where, $r = (M_{Z_{\mu\tau}}/m_\mu)^2$ is the square of the ratio between masses of gauge boson $(Z_{\mu\tau})$ and muon. As mentioned in the Introduction, although a $\mathcal{O}(100\ \text{MeV})$ $Z_{\mu\tau}$ is allowed, its coupling strength $(g_{\mu\tau})$ is strongly constrained to be less than $\sim 10^{-3}$ from the measurement of neutrino trident cross section by experiments like CHARM-II [145] and CCFR [146]. In our analysis, we find that for $M_{Z_{\mu\tau}} = 100$ MeV and $g_{\mu\tau} = 9 \times 10^{-4}$ the value of $\Delta a_\mu = 22.6 \times 10^{-10}$, which lies around the ballpark value given in Eq. (3.22). In what follows, we will use $M_{Z_{\mu\tau}} = 100$ MeV and $g_{\mu\tau} = 9.0 \times 10^{-3}$ as our benchmark point for the analyses of neutrino masses and dark matter phenomenology.

3.4 Neutrino Masses and Mixing

Majorana neutrino masses are generated via the Type-I seesaw mechanism by the addition of three right handed neutrinos to the model. Using Eq. (3.2) we can write the Majorana mass matrix for the three right handed neutrinos as

$$\mathcal{M}_R = \begin{pmatrix} M_{ee} & \frac{v_{\mu\tau}}{\sqrt{2}}h_{e\mu} & \frac{v_{\mu\tau}}{\sqrt{2}}h_{e\tau} \\ \frac{v_{\mu\tau}}{\sqrt{2}}h_{e\mu} & 0 & M_{\mu\tau}\,e^{i\xi} \\ \frac{v_{\mu\tau}}{\sqrt{2}}h_{e\tau} & M_{\mu\tau}\,e^{i\xi} & 0 \end{pmatrix}, \tag{3.24}$$

where all parameters in M_R in general can be complex. However, by proper phase rotation one can choose all the elements expect the $\mu\tau$ component of M_R to be real [132]. Thus, M_R depends on the real parameters M_{ee}, $M_{\mu\tau}$, $h_{e\mu}$ and $h_{e\tau}$ and the phase ξ. On other hand, from the Yukawa term in Eq. (3.2) one can easily see that the Dirac mass matrix M_D between left handed and right handed neutrinos is diagonal and for simplicity we have chosen all the Yukawa couplings (y_e, y_μ and y_τ) are real. The expression of M_D is

$$M_D = \begin{pmatrix} f_e & 0 & 0 \\ 0 & f_\mu & 0 \\ 0 & 0 & f_\tau \end{pmatrix}, \tag{3.25}$$

where $f_i = \dfrac{y_i}{\sqrt{2}}v$ with $i = e$, μ and τ. Now, with respect to the basis $\left(\overline{\nu_{\alpha L}}\ \ \overline{(N_{\alpha R})^c}\right)^T$ and $((\nu_{\alpha L})^c\ \ N_{\alpha R})^T$ we can write the mass matrix of both left as well as right handed neutrinos which is given as

$$M = \begin{pmatrix} 0 & M_D \\ M_D^T & M_R \end{pmatrix}, \tag{3.26}$$

where M is a 6×6 matrix and both M_D and M_R are 3×3 matrices given by Eqs. (3.24) and (3.25). After diagonalization of the matrix M one obtains two fermionic states for each generation which are Majorana in nature. Therefore we have altogether six Majorana neutrinos, out of which three are light and rest are heavy. Using block diagonalisation technique, we can find the mass matrices for light as well as heavy neutrinos which are given as

$$m_\nu \simeq -M_D M_R^{-1} M_D^T, \tag{3.27}$$

$$m_N \simeq M_R. \tag{3.28}$$

Here both m_ν and m_N are complex symmetric matrices. Also Eqs. (3.27-3.28) are derived using an assumption that $M_D \ll M_R$ i.e. the eigenvalues of M_D is much less than those of M_R and therefore terms with higher powers of M_D/M_R are neglected. Using the expressions of M_R and M_D given in Eqs. (3.24-3.25) the light neutrino mass matrix in this model takes the following form

$$m_\nu = \frac{1}{2p}\begin{pmatrix} 2 f_e^2 M_{\mu\tau}^2 e^{i\xi} & -\sqrt{2} f_e f_\mu h_{e\tau} v_{\mu\tau} & -\sqrt{2} f_e f_\tau h_{e\mu} v_{\mu\tau} \\ -\sqrt{2} f_e f_\mu h_{e\tau} v_{\mu\tau} & \dfrac{f_\mu^2 h_{e\tau}^2 v_{\mu\tau}^2 e^{-i\xi}}{M_{\mu\tau}} & \dfrac{f_\mu f_\tau}{M_{\mu\tau}}(M_{ee} M_{\mu\tau} - p e^{-i\xi}) \\ -\sqrt{2} f_e f_\tau h_{e\mu} v_{\mu\tau} & \dfrac{f_\mu f_\tau}{M_{\mu\tau}}(M_{ee} M_{\mu\tau} - p e^{-i\xi}) & \dfrac{f_\tau^2 h_{e\mu}^2 v_{\mu\tau}^2 e^{-i\xi}}{M_{\mu\tau}} \end{pmatrix}, \tag{3.29}$$

where $p = h_{e\mu} h_{e\tau} v_{\mu\tau}^2 - M_{ee} M_{\mu\tau} e^{i\xi}$. The masses and mixing angles of the light neutrinos are found by diagonalising this matrix [147] and are compared against the corresponding experimentally allowed ranges obtained from global analysis of the data (see Table 1.2).

There are eight independent parameters in the light neutrino mass matrix m_ν, namely, f_e, f_μ, f_τ, $M_{\mu\tau}$, M_{ee}, $V_{e\tau} = \frac{v_{\mu\tau}}{\sqrt{2}} h_{e\tau}$, $V_{e\mu} = \frac{v_{\mu\tau}}{\sqrt{2}} h_{e\mu}$ and ξ. All of these parameters have mass dimension GeV except the dimensionless phase factor ξ which is in radian. In order to find the model parameter space allowed by the neutrino oscillation experiments, we have varied the above mentioned parameters in the following range

$$\begin{array}{ccccc} 0 & \leq & \xi\,[\mathrm{rad}] & \leq & 2\pi\,, \\ 1 & \leq & M_{ee},\, M_{\mu\tau}\,[\mathrm{GeV}] & \leq & 10^4\,, \\ 1 & \leq & V_{e\mu},\ V_{e\tau}\ [\mathrm{GeV}] & \leq & 280\,, \\ 0.1 & \leq & \dfrac{(f_e,\, f_\mu,\, f_\tau)}{10^{-4}}\,[\mathrm{GeV}] & \leq & 10\,. \end{array} \tag{3.30}$$

The allowed parameter space satisfies the following constraints from the neutrino sector

- cosmological upper bound on the sum of all three light neutrinos, $\sum_i m_i < 0.23$ eV at 2σ C.L. [20],
- mass squared differences $6.93 < \dfrac{\Delta m^2_{21}}{10^{-5}}\,\mathrm{eV}^2 < 7.97$ and $2.37 < \dfrac{\Delta m^2_{31}}{10^{-3}}\,\mathrm{eV}^2 < 2.63$ in 3σ range [89],
- all three mixing angles $30^\circ < \theta_{12} < 36.51^\circ$, $37.99^\circ < \theta_{23} < 51.71^\circ$ and $7.82^\circ < \theta_{13} < 9.02^\circ$ also in 3σ range [89].

All the Yukawa couplings appearing in the light as well as heavy Majorana neutrino mass matrices (m_ν and M_R) are enforced to always lie within the perturbative range mentioned in Eq. (3.16). Furthermore, we scan the allowed areas in the model parameter space for only for the normal mass ordering which corresponds to $\Delta m^2_{31} > 0$.

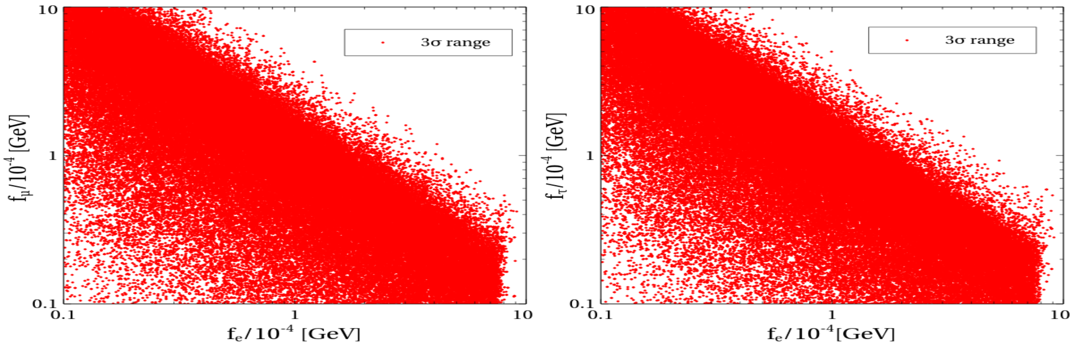

Figure 3.2: Left (Right) panel: Allowed region in $f_e - f_\mu$ ($f_e - f_\tau$) plane which satisfies all the experimental constraints considered in this work.

In the left and right panels of Fig. 3.2, we have shown the allowed regions in $f_e - f_\mu$

and $f_e - f_\tau$ planes respectively, where we have varied f_e, f_μ, f_τ in the range 10^{-5} GeV to 10^{-3} GeV while the other parameters have been scanned over the entire considered range as given in Eq. (3.30). From both the panels it is clear that there is (anti)correlation between the parameters $f_e - f_\mu$ and $f_e - f_\tau$. We find that for the lower values of f_e higher values of f_μ, f_τ are needed to satisfy the experimental constraints in the 3σ range and vice versa. Moreover, although there are smaller number of allowed points when both f_e and f_i ($i = \mu, \tau$) are small but the present experimental bounds on the observables of the neutrino sector forbid the entire region in the $f_e - f_\mu$ and $f_e - f_\tau$ planes for both f_e and $f_i > 2\times 10^{-4}$ GeV ($i = \mu, \tau$). Also, unlike the parameters f_μ and f_τ, we do not get any allowed values of f_e beyond 8×10^{-4} GeV.

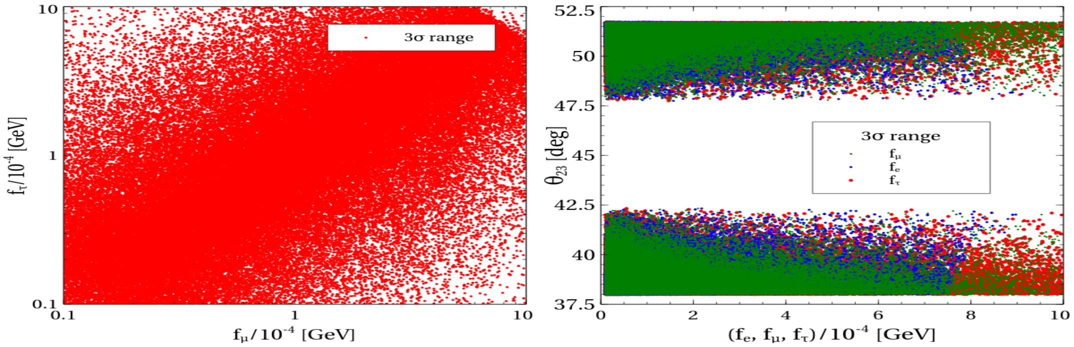

Figure 3.3: Left panel: Allowed region in $f_\mu - f_\tau$ plane. Right panel: Variation of θ_{23} with f_e (blue dots), f_μ (green dots) and f_τ (red dots).

The allowed parameter space in $f_\mu - f_\tau$ plane has been shown in the left panel of Fig. 3.3. From the figure it is seen that there is a correlation between the parameters f_μ and f_τ. That means unlike the previous plots here most of allowed points in $f_\mu - f_\tau$ plane are such that for the lower (higher) values of the parameter f_μ we also need lower (higher) values of f_τ to reproduce the experimental results. On the other hand, in the right panel of Fig. 3.3, we show the variation of θ_{23} with f_e (blue dots), f_μ (green dots) and f_τ (red dots). We see from the plot that the region around maximal θ_{23} mixing angle is ruled out in this model. The reason is that while in the $L_\mu - L_\tau$ symmetric limit, the neutrino mass matrix had a $\mu - \tau$ symmetry and hence $\theta_{23} = \pi/4$ and $\theta_{13} = 0$, once the $L_\mu - L_\tau$ symmetry is spontaneously broken, θ_{23} shifts away from maximal and θ_{13} becomes non-zero, making the model consistent with the neutrino oscillations data. The plot also shows that the allowed values of mixing angle θ_{23} lie in two separate ranges between $38^\circ \lesssim \theta_{23} \lesssim 42^\circ$ (lower octant, $\theta_{23} < 45^\circ$) and $48^\circ \lesssim \theta_{23} \lesssim 51.5^\circ$ (higher octant, $\theta_{23} > 45^\circ$) for the variation of entire considered range of parameters f_i $(i = e, \mu, \tau)$ from 10^{-5} GeV to 10^{-3} GeV. Therefore, we can conclude that our model is insensitive to the octant of θ_{23}.

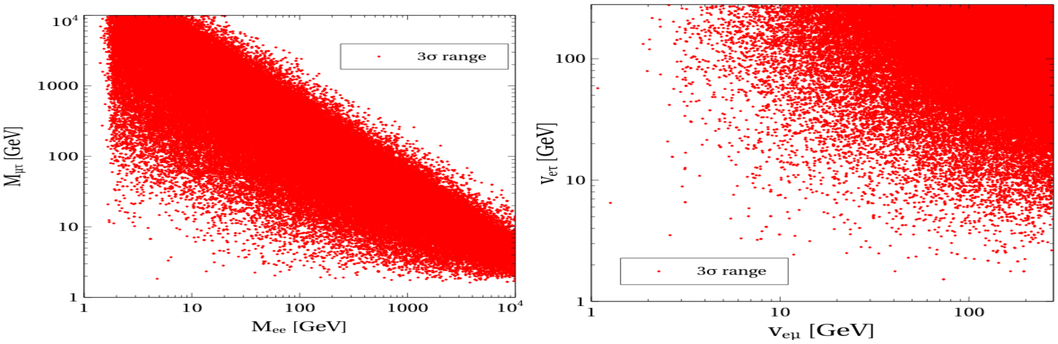

Figure 3.4: Left (Right) panel: Allowed region in $M_{ee} - M_{\mu\tau}$ $(V_{e\mu} - V_{e\tau})$ plane which satisfies all the experimental constraints considered in this work.

The allowed regions for the other remaining parameters $M_{ee} - M_{\mu\tau}$ and $V_{e\mu} - V_{e\tau}$ have been shown in Fig. 3.4. The left panel of Fig. 3.4 shows the (anti)correlation between the allowed values of the parameters M_{ee} and $M_{\mu\tau}$. The neutrino oscillation data rules out the parameter region $M_{ee} \gtrsim 500$ GeV, $M_{\mu\tau} \gtrsim 500$ GeV and $M_{ee} \lesssim 5$ GeV, $M_{\mu\tau} \lesssim 5$ GeV. In the right panel Fig. 3.4, we have shown the allowed region in the $V_{e\mu} - V_{e\tau}$ plane. In order to keep the Yukawa couplings $h_{e\mu}$ and $h_{e\tau}$ within the perturbative regime (see Eq. (3.16)) we have restricted variation of both $V_{e\mu}$ and $V_{e\tau}$ upto 280 GeV. From this plot it is clearly seen that the higher values of $V_{e\mu}$ and $V_{e\tau}$ ($V_{e\mu}$, $V_{e\tau} \gtrsim 10$ GeV) are mostly preferred by the neutrino experiments over the smaller ones.

In the left panel of Fig. 3.5, we have shown the variation of the phase ξ with respect to the parameter $M_{\mu\tau}$. Only a very narrow range of value of ξ, placed symmetrically with respect to the line $\xi = \pi$, are allowed, which reproduce the neutrino observables in the 3σ range. It is also seen from this figure that there are no points along $\xi = \pi$ line (blue dashed line), which indicates that for the present model, at least one element in the right

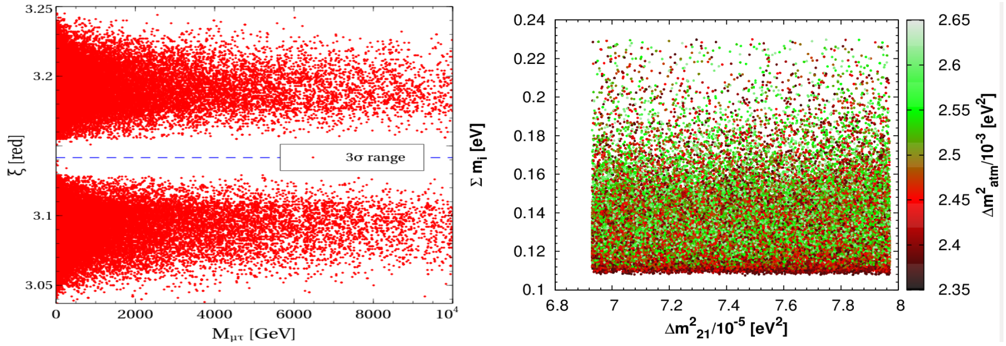

Figure 3.5: Left pane: Allowed values of the parameters $M_{\mu\tau}$ and ξ. Blue dashed line represents $\xi = \pi$. Right panel: Variation of $\sum_i m_{\nu_i}$ with the mass square differences Δm^2_{21} and Δm^2_{32}.

handed neutrino mass matrix (here we have considered 2×3 element of M_R) has to be a complex number to satisfy the experimental results. The variation of sum of all three neutrino masses with Δm^2_{21} is presented in the right panel of Fig. 3.5. The variation of Δm^2_{atm} is also shown in the same figure. From this plot, it is evident that in this model lower values of $\sum m_i$ ($\sum m_i \leq 0.18$ eV) are more favourable.

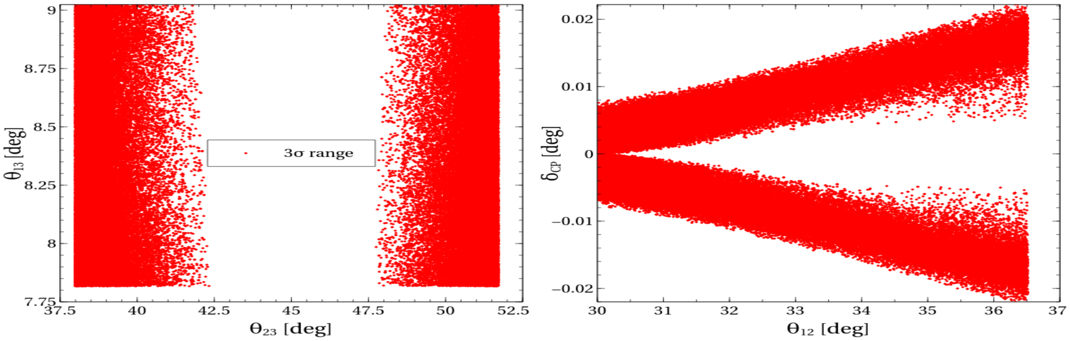

Figure 3.6: Left panel: Variation of θ_{13} with θ_{23}. Right panel: Variation of Dirac CP phase δ_{CP} with mixing angle θ_{12}.

In the left and right panels of Fig. 3.6, we have shown the predicted ranges of the mixing angles and the Dirac CP phase. The left panel shows that for both lower and higher octant, the whole range of θ_{13} is allowed here. In the right panel of Fig. 3.6, we have plotted the predicted Dirac CP phase with respect to the mixing angle θ_{12}. We find that in our model the predicted values of Dirac CP phase are very small and symmetric around 0°. One can also note that the absolute predicted value of $|\delta_{CP}|$ increases with the mixing angle θ_{12}.

3.5 Dark Matter

Being stable as well as electrically neutral, ϕ_{DM} can serve as a dark matter candidate. By following the 1.81, we can compute the relic abundance of ϕ_{DM} at the present epoch and its spin independent scattering cross section relevant for direct detection experiments is already discussed in section 2.2 by considering only the Higgses mediated diagrams as shown in Fig. 3.7. The viability of ϕ_{DM} as a dark matter candidate will be tested by comparing its relic abundance and spin independent scattering cross section with the results obtained from Planck and LUX experiments. Finally, at the end of this section we will compute the γ-ray flux due to the annihilation of ϕ_{DM} and compare this flux with Fermi-LAT observed γ-ray excess from the regions close to the Galactic Centre (GC).

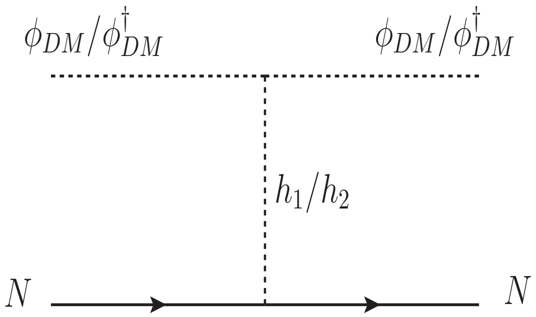

Figure 3.7: Feynman diagram for the elastic scattering of ϕ_{DM} and $\phi^{\dagger}_{DM}$ with detector nucleon (N).

3.5.1 Results

We have computed the relic density of DM using micrOMEGAs [33] package and the implementation of the present model in micrOMEGAS has been done using the LanHEP [148] package. For the relic density calculation, we have considered the following benchmark values of the parameters related to the neutrino sector,

- Masses of the three heavy neutrinos: M_{N_1} = 332.88 GeV, M_{N_2} = 279.06 GeV and M_{N_3} = 168.28 GeV,

Vertex abc	Vertex Factor g_{abc}
$q\bar{q}h_1$	$-\frac{M_q}{v}\cos\alpha$
$q\bar{q}h_2$	$\frac{M_q}{v}\sin\alpha$
$W^+W^-h_1$	$\frac{2M_W^2\cos\alpha}{v}$
$W^+W^-h_2$	$-\frac{2M_W^2\sin\alpha}{v}$
ZZh_1	$\frac{2M_Z^2\cos\alpha}{v}$
ZZh_2	$-\frac{2M_Z^2\sin\alpha}{v}$
$N_e N_\mu (N_\tau) h_1$	$\sqrt{2}\sin\alpha\, h_{e\mu}\,(h_{e\tau})$
$N_e N_\mu (N_\tau) h_2$	$\sqrt{2}\cos\alpha\, h_{e\mu}\,(h_{e\tau})$
$l\bar{l}h_1$	$-\frac{M_l}{v}\cos\alpha$
$l\bar{l}h_2$	$\frac{M_l}{v}\sin\alpha$
$l\bar{l}Z_{\mu\tau}$	$\pm g_{\mu\tau}\gamma^\rho$(+ for μ, − for τ)
$\phi_{DM}\phi^\dagger_{DM}h_1$	$-(v\lambda_{Dh}\cos\alpha + v_{\mu\tau}\lambda_{DH}\sin\alpha)$
$\phi_{DM}\phi^\dagger_{DM}h_2$	$(v\lambda_{Dh}\sin\alpha - v_{\mu\tau}\lambda_{DH}\cos\alpha)$
$\phi_{DM}\phi^\dagger_{DM}Z_{\mu\tau}$	$n_{\mu\tau}\,g_{\mu\tau}\,(p_2 - p_1)^\rho$
$\phi_{DM}\phi^\dagger_{DM}h_1h_1$	$-(\lambda_{Dh}\cos^2\alpha + \lambda_{DH}\sin^2\alpha)$
$\phi_{DM}\phi^\dagger_{DM}h_2h_2$	$-(\lambda_{Dh}\sin^2\alpha + \lambda_{DH}\cos^2\alpha)$
$\phi_{DM}\phi^\dagger_{DM}h_1h_2$	$\sin\alpha\cos\alpha(\lambda_{Dh} - \lambda_{DH})$
$\phi_{DM}\phi^\dagger_{DM}Z_{\mu\tau}Z_{\mu\tau}$	$2g^2_{\mu\tau}n^2_{\mu\tau}$
$\phi_{DM}\phi^\dagger_{DM}\phi_{DM}\phi^\dagger_{DM}$	$-4\lambda_{DM}$

Table 3.3: All relevant vertex factors required for the computation of DM annihilation as well as scattering cross sections.

- Yukawa couplings: $h_{e\mu} = 2.44$ and $h_{e\tau} = 1.28$.

We have checked that these adopted values of right handed neutrino masses and Yukawa couplings reproduce all the experimentally measurable quantities of the neutrino sector within their 1σ range [89]. Moreover like the previous section, here also we have used our benchmark point $M_{Z_{\mu\tau}} = 100$ MeV and $g_{\mu\tau} = 9\times10^{-4}$, which are required to explain the muon $(g-2)$ anomaly.

In the left panel of Fig. 3.8, we show the variation of the DM relic density with its mass for three different values of the scalar mixing angle, $\alpha = 0.01$ rad, 0.045 rad and 0.09 rad [2] respectively. From this plot it is clearly seen that DM relic density satisfies the central value of Planck limit ($\Omega_{DM}h^2 = 0.1197$) only around the two resonance regions where the mass of DM is nearly equal to half of the mediator mass i.e. $M_{DM} \sim M_{h_i}/2$ ($i = 1, 2$). Therefore the first resonance occurs when DM mass is around 62 GeV and it is due to the SM-like Higgs boson h_1 while the second one is due to extra Higgs boson h_2

---

[2] We have checked that these values of mixing angle α are allowed by the LHC results on Higgs signal strength [117] and invisible decay width [118].

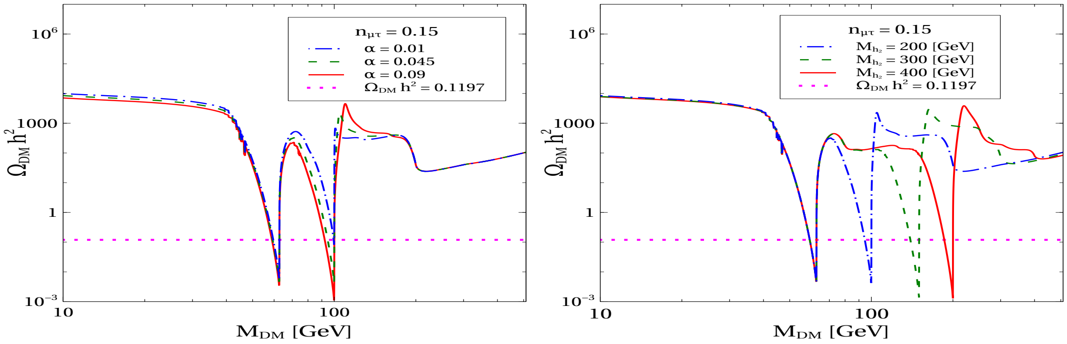

Figure 3.8: Left (Right) Panel: Variation of relic density $\Omega_{DM}h^2$ with respect to the DM mass M_{DM} for three different value of mixing angle α (M_{h_2}), while other the values of parameters have been kept fixed at $\lambda_{DH} = 0.01$, $\lambda_{Dh} = 0.001$, and $M_{h_2} = 200$ GeV ($\alpha = 0.045$ rad).

of mass 200 GeV. Like the left panel of Fig. 3.8, the right panel also shows the variation of $\Omega_{DM}h^2$ with M_{DM} but in this case three different plots are generated for three different values of $M_{h_2} = 200$ GeV (blue dashed dot line), 300 GeV (green dashed line) and 400 GeV (red solid line), respectively. Similar to the left panel, here also the DM relic density satisfies the Planck limit only around the resonance regions. However in this plot, as we have varied the mass of h_2, therefore instead of getting a single resonance region for h_2 (as in the left panel) we have found three resonance regions at $M_{DM} \sim 100$ GeV, 150 GeV and 200 GeV for $M_{h_2} = 200$ GeV, 300 GeV and 400 GeV, respectively. For all three cases the resonance due to the SM-like Higgs boson h_1 occurs at the same value of $M_{DM} \sim 62.5$ GeV as we have fixed the mass of h_1 at 125.5 GeV. Plots in both panels are generated for $n_{\mu\tau} = 0.15$.

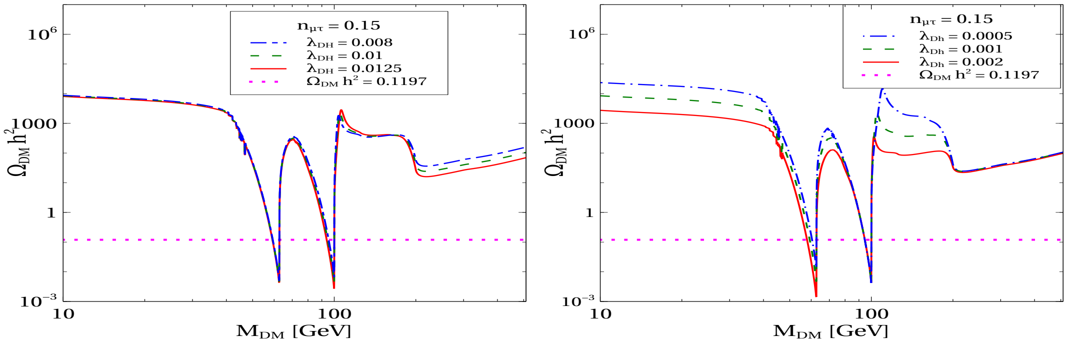

Figure 3.9: Left (Right) Panel: Variation of relic density Ωh^2 with respect to the mass of the dark matter M_{DM} for three different value of λ_{DH} (λ_{Dh}), while other parameters value are kept fixed at $M_{h_2} = 200$ GeV, $\alpha = 0.045$ rad and $\lambda_{Dh} = 0.001$ ($\lambda_{DH} = 0.01$).

Left and right panels of Fig. 3.9 represent the variation of relic density $\Omega_{DM}h^2$ with the dark matter mass ϕ_{DM} for there different values of parameter λ_{DH} and λ_{Dh}, respectively. These plots also show the appearance of two resonance regions due to the two mediating scalar bosons. However, from this figure one can notice the effect of parameters λ_{Dh} and λ_{DH} on the DM relic density with respect to the variation of M_{DM}. In the low mass region ($M_{DM} \lesssim 80$ GeV), SM-like Higgs boson mediated diagrams dominantly contribute to the pair annihilation processes of ϕ_{DM} and $\phi^\dagger_{DM}$ while the contribution of extra Higgs mediated diagrams become superior for the high DM mass region ($M_{DM} \gtrsim 80$ GeV). From the expression of $\phi_{DM}\phi^\dagger_{DM}h_1$ vertex factor given in Table 3.3, one can see that the effect of the parameter λ_{DH} on $\langle\sigma \mathrm{v}\rangle$ is mixing angle suppressed (i.e. multiplied by $\sin\alpha$). Therefore, in the left panel for low DM mass region the effect of λ_{DH} to $\Omega_{DM}h^2$ is small. On the other hand, in the expression of vertex factor of $\phi_{DM}\phi^\dagger_{DM}h_1$, the parameter λ_{Dh} appears with $\cos\alpha$ and hence we see a considerable effect of λ_{Dh} on $\Omega_{DM}h^2$ in the right panel (low DM mass region). For the extreme right region of both panels ($M_{DM} \gtrsim 200$ GeV), the dominant pair annihilation channel is $\phi_{DM}\phi^\dagger_{DM} \to h_2h_2$. Hence, the impact of λ_{DH} and λ_{Dh} to $\Omega_{DM}h^2$ can well be understood from the expression of $\phi_{DM}\phi^\dagger_{DM}h_2h_2$ vertex factor (see Table 3.3). In the intermediate region ($80\,\mathrm{GeV} < M_{DM} < 200\,\mathrm{GeV}$), $\phi_{DM}\phi^\dagger_{DM} \to W^+W^-$, ZZ and h_1h_1 channels mainly contribute to DM relic density and in the right panel for $100\,\mathrm{GeV} < M_{DM} < 200\,\mathrm{GeV}$, the variation of $\Omega_{DM}h^2$ with respect to λ_{Dh} resulting from DM pair annihilation into h_1h_1 final state.

In the left panel of Fig. 3.10, we show the allowed values of M_{h_2} which reproduce the correct DM relic density for the variation of M_{DM} in the range 30 GeV to 500 GeV. In this plot we have varied the mass of extra Higgs boson M_{h_2} in the range 60 GeV to 450 GeV and λ_{DH} from 0.001 to 0.1. From this plot it is evident that for a particular value of dark matter mass the corresponding allowed values of M_{h_2} lie around $2\,M_{DM}$. The reason behind this nature is that the relic abundance of dark matter (both ϕ_{DM} and $\phi^\dagger_{DM}$) satisfies the observed DM density only around the resonance regions (when mediator mass $M_{h_i} \sim 2 \times M_{DM}$, $i = 1, 2$ see Fig. 3.8 and Fig. 3.9). The allowed range of M_{h_2} for

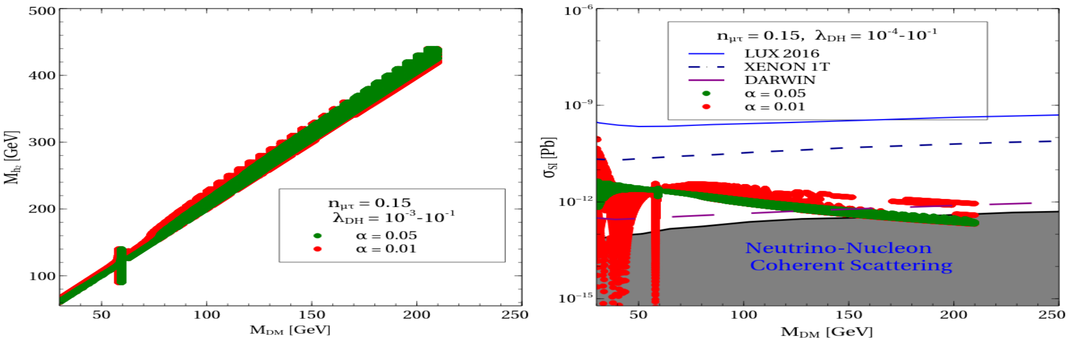

Figure 3.10: Left Panel: Allowed values of M_{h_2} with respect to the variation of the dark matter mass M_{DM} for two different value of mixing angle α. Right panel: Variation of spin independent scattering cross sections of dark matter with its mass. All the points in both plots satisfy the Planck limit on DM relic density in 1σ range ($\Omega_{\rm DM}h^2 = 0.1197 \pm 0.0022$ [20]) and these two plots are generated for $\lambda_{Dh} = 0.001$.

a particular DM mass does not vary much for the change of mixing angle α from 0.01 rad (red coloured region) to 0.05 rad (green colour region). Moreover, we restrict M_{h_2} upto 430 GeV to remain within the perturbative regime ($\lambda_H < 4\pi$) and hence the relic density condition is not satisfied beyond $M_{DM} = 215\,$GeV Furthermore, near $M_{DM} \sim 60$ GeV, one can see that a broad range of M_{h_2} values are allowed, which indicates that in this region the SM-like Higgs contributes dominantly giving the wide range of M_{h_2} values for which the DM relic density is satisfied. Spin independent elastic scattering cross section ($\sigma_{\rm SI}$) of DM with with its mass has been plotted in the the right panel of Fig. 3.10 for two different values of $\alpha = 0.01$ rad (green coloured region) and 0.05 rad (red coloured region) respectively. This plot is also generated for $60\,{\rm GeV} \leq M_{h_2} \leq 430$ GeV, $0.001 \leq \lambda_{DH} \leq 0.1$ and $\lambda_{Dh} = 0.001$ and all the points within the red and green coloured patch satisfy the Planck result. For comparison with current experimental limits on $\sigma^{\rm SI}$ from DM direct detection experiments we have plotted the result of LUX-2016 (blue solid line) in the same figure. Moreover, we have also shown the predicted results from the "ton-scale" direct detection experiments like XENON 1T [149] (blue dashed line) and DARWIN [150] (long dashed purple line). From this figure it is evident that the validity of our model can be explored in near future by these "ton-scale" experiments.

3.5.2 Indirect detection: Fermi-LAT γ-ray excess from the Galactic Centre

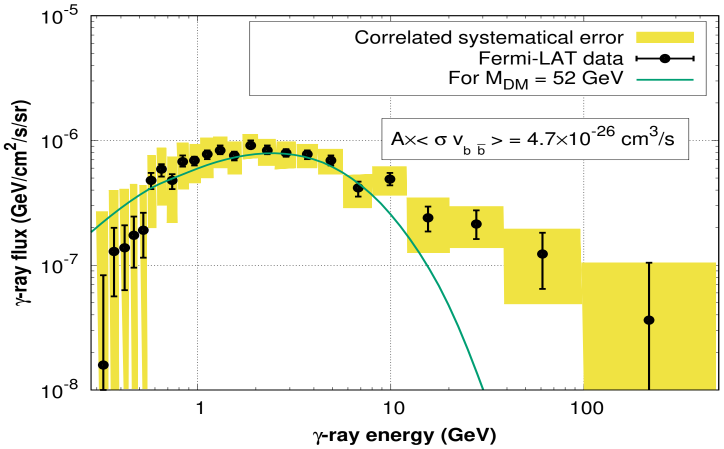

Figure 3.11: Gamma-ray flux obtained from the pair annihilation of ϕ_{DM} and $\phi^{\dagger}_{DM}$ at the Galactic Centre for $M_{DM} = 52$ GeV, $\langle \sigma \mathrm{v}_{b\bar{b}} \rangle = 3.856 \times 10^{-26}\,\mathrm{cm}^3/\mathrm{s}$ and $\mathcal{A} = 1.219$

Following the same procedure given in Section 2.5 we have found that, for the present model, the excess gamma-rays flux observed by Fermi-LAT can be reproduced for an annihilating dark matter of mass $M_{DM} = 52$ GeV and $\langle \sigma \mathrm{v}_{b\bar{b}} \rangle = 3.856 \times 10^{-26}\,\mathrm{cm}^3/\mathrm{s}$. In this case, DM annihilation to $b\bar{b}$ channel dominantly occurs through the resonance of extra Higgs boson (h_2) with resonating mass $M_{h_2} = 104.025$ GeV and coupling parameters $\lambda_{DH} = 0.01$, $\lambda_{Dh} = 0.001$ and scalar mixing angle $\alpha = 0.045$ rad.

In Fig. 3.11, green solid line represents the γ-ray flux that we have computed for a $M_{DM} = 52$ GeV while the value of $b\bar{b}$ annihilation cross section is $3.856 \times 10^{-26}\,\mathrm{cm}^3/\mathrm{s}$. The correlated systematic errors are represented by the yellow boxes while the Fermi-LAT uncorrelated statistical uncertainties are shown by the black error bars taken from [151]. We have found that in order to reproduced the Fermi-LAT observed γ-ray flux for a 52 GeV non-self-conjugate DM, the quantity $\mathcal{A} \times \langle \sigma \mathrm{v}_{b\bar{b}} \rangle$ must be $4.7 \times 10^{-26}\,\mathrm{cm}^3/\mathrm{s}$ [93]. This requires DM halo profile error parameter $\mathcal{A}$ to be ~ 1.22, well inside its allowed range between 0.17 to 5.3 [110].

4

Singlet-Triplet Fermionic Dark Matter and LHC Phenomenology

4.1 Introduction

This chapter is based on [152] which deals with an extension of the SM that accommodates both high as well as low mass fermionic DM such that it can be produced and tested at the 13 TeV run of the LHC. The low mass DM regime do not have any significant SE enhancement (because the DM mass becomes comparable to the mediator mass inside the loops) and hence are safe from the gamma ray indirect detection bounds put by the Fermi-LAT collaboration [153]. Our proposed extension of the particle content includes one SM singlet fermion and SM triplet fermion [154–158]. The scalar sector is also extended to include a SM triplet scalar. The $\mathbb{Z}_2$ charge of these BSM particles is arranged in such a way that there is a mixing between the neutral component of the triplet fermion and the singlet fermion, that generates two mass eigenstates for the neutral fermions. The lower mass eigenstate becomes the viable DM candidate. The neutral and charged components of the SM doublet and triplet scalars also mix, that gives rise to two physical neutral Higgs scalars and one charged Higgs scalar. The presence of these extra scalars opens up additional annihilation and co-annihilation processes between the two DM candidates which effectively reduces the mass of the DM for which the current DM relic density bound can be easily satisfied. For low mass DM we give the prediction for the annihilation of the

DM to two gamma rays by one loop process. In addition, these lower mass DM fermions ($\sim$ 100 GeV) can be observed with large production cross-section at the 13 TeV LHC. We perform a detailed collider phenomenology of the DM model. In this work we will consider multi jets + missing energy signal in the final state for searching the DM. We study in detail the dominant backgrounds for such type of signal. The SM backgrounds are reduced by applying suitable cuts that increases the statistical significance of detection for the fermionic DM with the low luminosity run of the LHC. A final comment is in order. It is possible to embed our model in a SO(10) GUT where the SU(2) triplet would belong to the 45 representation of SO(10) and would help in the gauge coupling unification, as was shown in [159, 160].

4.2 Triplet Fermionic Dark Matter

Gauge Group	Baryon Fields			Lepton Fields			Scalar Fields
	$Q_L^i = (u_L^i, d_L^i)^T$	u_R^i	d_R^i	$L_L^i = (\nu_L^i, e_L^i)^T$	e_R^i	ρ	ϕ_h
$SU(3)_c$	3	3	3	1	1	1	1
$SU(2)_L$	2	1	1	2	1	3	2
$U(1)_Y$	1/6	2/3	−1/3	−1/2	−1	0	1/2
$\mathbb{Z}_2$	+	+	+	+	+	−	+

Table 4.1: Particle content and their corresponding charges under various symmetry groups.

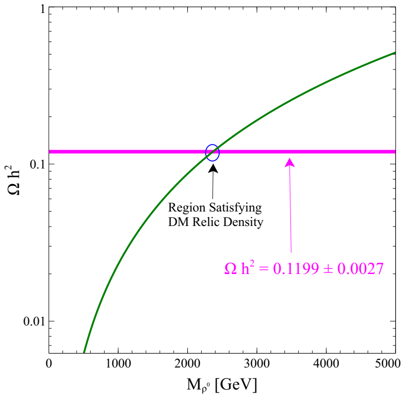

Figure 4.1: Variation of relic density Ωh^2 with the mass of the triplet DM $M_{\rho_1^0}$.

In this case the SM particle content is extended with just a left handed fermionic triplet field ρ [161, 162]. There is an additional $\mathbb{Z}_2$ symmetry imposed on the model such that the triplet is odd under it, while all SM particles are even under this symmetry. The particle content of the model and their charges under the symmetries of the model is given in Table 4.1. The $\mathbb{Z}_2$ symmetry forbids all the Yukawa couplings of ρ with the SM fermions and the complete Lagrangian includes just the additional kinetic energy term for the triplet ($\mathcal{L}_\rho$) along with the SM Lagrangian ($\mathcal{L}_{SM}$),

$$\mathcal{L} = \mathcal{L}_{SM} + \mathcal{L}_\rho\,. \tag{4.1}$$

The Lagrangian for triplet field ρ takes the following form,

$$\mathcal{L}_\rho = Tr[\bar{\rho}\, i\gamma^\mu D_\mu \rho]\,, \tag{4.2}$$

where the covariant derivative D_μ takes the following form,

$$D_\mu = \partial_\mu - ig\, T_i^{adj}\, W_i\,, \tag{4.3}$$

where g and W_i are the $SU(2)_L$ gauge coupling and gauge field, respectively, and T_i^{adj}'s are the $SU(2)_L$ generators in the adjoint representation. The $\mathbb{Z}_2$ symmetry makes ρ^0, the chargeless component of ρ stable and it becomes the DM. The annihilation and co-annihilation of the DM ρ_0, and $\rho^\pm$ proceed through SM gauge bosons, as shown in Fig. 4.2. In Fig. 4.1 we show the ρ^0 relic abundance as a function of its mass M_{ρ^0}. From the figure one can notice that with the increase of the DM mass, its relic density also increases. This is because in the present case the velocity times the DM annihilation and co-annihilation cross sections vary inversely with the square of the DM mass. Hence, as the DM mass is increased, the DM annihilation cross-section decreases and as a result the

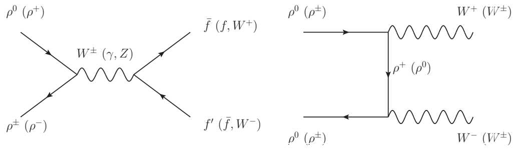

Figure 4.2: Pure triplet fermions DM annihilation and co-annihilation diagrams.

DM relic density increases as it is inversely proportional to the velocity times cross section. From the figure we note that the present day observed value of the DM relic density is satisfied around $M_{\rho^0} \sim 2370$ GeV. This has been also pointed out before in [162].

Note that, while the model can be tested in direct and indirect detection experiments, due to its heavy mass it is difficult to produce this DM candidate at the 13 TeV or 14 TeV LHC search. One will need a very high energy collider to test this DM model. Minimal extension of the model by adding a gauge singlet fermion and a triplet scalar opens up the possibility to test the model at collider. Below, we discuss in detail the required extensions and the model predictions.

4.3 Singlet Triplet Mixing

Gauge Group	Baryon Fields			Lepton Fields				Scalar Fields	
	$Q_L^i = (u_L^i, d_L^i)^T$	u_R^i	d_R^i	$L_L^i = (\nu_L^i, e_L^i)^T$	e_R^i	N'	ρ	ϕ_h	Δ
$SU(3)_c$	3	3	3	1	1	1	1	1	1
$SU(2)_L$	2	1	1	2	1	1	3	2	3
$U(1)_Y$	1/6	2/3	−1/3	−1/2	−1	0	0	1/2	0
$\mathbb{Z}_2$	+	+	+	+	+	−	−	+	+

Table 4.2: Particle content and their corresponding charges under various symmetry groups.

In this section, we present a minimal extension of the model, such that the mass of the DM can be suitably reduced and it can be produced at the LHC. To that end, we add an extra gauge singlet fermion which is also odd under the $\mathbb{Z}_2$ and an additional real triplet Higgs ($Y = 0$). The particle content of our model and their respective charges are displayed in the Table 4.2. The corresponding Lagrangian is given by,

$$\begin{aligned} \mathcal{L} &= \mathcal{L}_{SM} + Tr\left[\bar{\rho}\, i\gamma^\mu D_\mu \rho\right] + \bar{N'}\, i\gamma^\mu D_\mu N' + Tr[(D_\mu\Delta)^\dagger (D^\mu\Delta)] - V(\phi_h, \Delta) \\ &\quad - Y_{\rho\Delta}(Tr[\bar{\rho}\Delta]N' + h.c.) - M_\rho Tr[\bar{\rho^c}\rho] - M_{N'} \bar{N'^c} N' \end{aligned} \tag{4.4}$$

where the triplet fermion takes the following form,

$$\rho = \begin{pmatrix} \frac{\rho_0}{2} & \frac{\rho^+}{\sqrt{2}} \\ \frac{\rho^-}{\sqrt{2}} & -\frac{\rho_0}{2} \end{pmatrix} . \tag{4.5}$$

The complete form of the potential $V(\phi_h, \Omega)$ takes the following form,

$$\begin{aligned} V(\phi_h, \Delta) \;=\; & -\mu_h^2 \phi_h^\dagger \phi_h + \frac{\lambda_h}{4} (\phi_h^\dagger \phi_h)^2 + \mu_\Delta^2 Tr[\Delta^\dagger \Delta] + \lambda_\Delta (\Delta^\dagger \Delta)^2 + \lambda_1 (\phi_h^\dagger \phi_h) \mathrm{Tr}[\Delta^\dagger \Delta] \\ & + \lambda_2 \left(Tr[\Delta^\dagger \Delta] \right)^2 + \lambda_3 Tr[(\Delta^\dagger \Delta)^2] + \lambda_4 \phi_h^\dagger \Delta \Delta^\dagger \phi_h + (\mu \phi_h^\dagger \Delta \phi_h + h.c.) . \end{aligned} \tag{4.6}$$

In general, one can also insert a term like $\phi_h^\dagger \Delta^\dagger \Delta \phi_h$, but this term can be easily decomposed to two components that give contribution to the terms with λ_1 and λ_4 couplings. Hence, we do not write this term separately in the potential. We assume here that μ_Δ^2 is positive hence the neutral component of the Higgs triplet will get small induced vev, because it has coupling with the SM like Higgs, after electro weak symmetry breaking (EWSB) which takes the following form,

$$\langle \Delta_0 \rangle = v_\Delta = \frac{\mu v^2}{2\left(\mu_\Delta^2 + (\lambda_4 + 2\lambda_1)\frac{v^2}{4} + (\lambda_3 + 2\lambda_2)\frac{v_\Delta^2}{2} \right)} \tag{4.7}$$

The Higgs doublet and real triplet take the following form after taking the small fluctuation around the vevs v and v_Δ, respectively,

$$\phi_h = \begin{pmatrix} \phi^+ \\ \frac{v + H + i\xi}{\sqrt{2}} \end{pmatrix} \qquad \Delta = \begin{pmatrix} \frac{\Delta_0 + v_\Delta}{2} & \frac{\Delta^+}{\sqrt{2}} \\ \frac{\Delta^-}{\sqrt{2}} & -\frac{\Delta_0 + v_\Delta}{2} \end{pmatrix} . \tag{4.8}$$

Since ϕ_h takes vev spontaneously which breaks the EWSB and Δ gets induced vev, we need to satisfy the following criterion for the quadratic and quartic couplings,

$$\mu_h^2 > 0, \;\; \mu_\Delta^2 > 0, \;\; \lambda_h > 0 \;\text{ and }\; \lambda_\Delta > 0 . \tag{4.9}$$

After symmetry breaking the 2×2 mass matrix for the CP even Higgs scalars H and Δ_0 take the following form,

$$M_s = \frac{1}{2}\begin{pmatrix} \lambda v^2 & v v_\Delta(2\lambda_1+\lambda_4)-2\mu v \\ v v_\Delta(2\lambda_1+\lambda_4)-2\mu v & 2v_\Delta^2(\lambda_3+2\lambda_2)+\frac{\mu v^2}{v_\Delta} \end{pmatrix} \tag{4.10}$$

After diagonalisation of the above matrix we will get the physical Higgses h_1 and h_2 with masses M_{h_1} and M_{h_2}, respectively. If the mixing angle between h_1 and h_2 is α, then the mass and flavor eigenstates can be written in the following way,

$$\begin{aligned} h_1 &= \cos\alpha\, H + \sin\alpha\, \Delta_0 \\ h_2 &= -\sin\alpha\, H + \cos\alpha\, \Delta_0 \end{aligned} \tag{4.11}$$

The CP odd field ξ becomes Goldstone boson which is “eaten” by the SM gauge boson Z. In addition to the mixing between H and Δ_0, the charged scalars will also be mixed and one of them will be the Goldstone boson “eaten” by $W^\pm$. We can write them in the physical basis in the following way,

$$\begin{aligned} G^\pm &= \cos\delta\, \phi^\pm + \sin\delta\, \Delta^\pm \\ H^\pm &= -\sin\delta\, \phi^\pm + \cos\delta\, \Delta^\pm \end{aligned} \tag{4.12}$$

where the mixing angle depends on the strength of the vevs of doublet and triplet, *i.e.*,

$$\tan\delta = \frac{2v_\Delta}{v}. \tag{4.13}$$

The quadratic and quartic couplings have the following form in terms of the CP even Higgs masses M_{h_1} and M_{h_2}, the mixing angle between them α, the charge scalar mass and the mixing angle between the charged scalars δ:

$$\begin{aligned}
\mu &= \frac{M_{H^\pm}^2 \sin\delta\cos\delta}{v}, \\
\lambda_3 + 2\lambda_2 &= \frac{M_{h_1}^2 + M_{h_2}^2 + (M_{h_2}^2 - M_{h_1}^2)\cos 2\alpha - 2 M_{H^\pm}^2 \cos^2\delta}{2 v_\Delta^2}, \\
\lambda_h &= \frac{M_{h_1}^2 + M_{h_2}^2 + (M_{h_1}^2 - M_{h_2}^2)\cos 2\alpha}{v^2}, \\
\lambda_4 + 2\lambda_1 &= \frac{(M_{h_1}^2 - M_{h_2}^2)\sin 2\alpha + M_{H^\pm}^2 \sin 2\delta}{v v_\Delta}, \\
\mu_h^2 &= \lambda_h \frac{v^2}{4} + (\lambda_4 + 2\lambda_1)\frac{v_\Delta^2}{4} - \mu v_\Delta .
\end{aligned} \tag{4.14}$$

The vev of the Higgs triplet is constrained by the data on the ratio $\frac{M_W^2}{\cos^2\theta_w M_Z^2}$, which limits $v_\Delta < 12$ GeV [163, 164]. The value of M_{h_2} needs to satisfy the perturbativity limit on the quartic couplings which is $\lambda < 4\pi$. The quartic couplings are also bounded from the below [165] and as long as all the quartic couplings are positive, we do not need to worry about the lower bounds. From Eq. (4.14) we see that by choosing a suitable value for the free parameter μ which has mass dimension, we can keep all the quartic couplings in the perturbative regime.

In Eq. (4.4), $Y_{\rho\Delta}$ is the Yukawa term relating the fermionic triplet with the fermionic singlet. When the neutral component of Δ takes vev, the mass matrix for the fermions takes the following form,

$$M_F = \begin{pmatrix} M_\rho & \frac{Y_{\rho\Delta} v_\Delta}{2} \\ \frac{Y_{\rho\Delta} v_\Delta}{2} & M_{N'} \end{pmatrix}. \tag{4.15}$$

The lightest component of the eigenvalues of this matrix will be the stable DM. Relation between the the mass eigenstates and weak eigenstates are as follows:

$$\begin{aligned}
\rho_2^0 &= \cos\beta\rho_0 + \sin\beta N'^c \\
\rho_1^0 &= -\sin\beta\rho_0 + \cos\beta N'^c
\end{aligned} \tag{4.16}$$

Therefore, the tree level mass eigenstates are,

$$
\begin{aligned}
M_{\rho_1^0} &= \frac{1}{2}\left(M_\rho + M_{N'} - \sqrt{(M_\rho - M_{N'})^2 + 4\left(\frac{Y_{\rho\Delta} v_\Delta}{2}\right)^2}\right), \\
M_{\rho_2^0} &= \frac{1}{2}\left(M_\rho + M_{N'} + \sqrt{(M_\rho - M_{N'})^2 + 4\left(\frac{Y_{\rho\Delta} v_\Delta}{2}\right)^2}\right), \\
\tan 2\beta &= \frac{Y_{\rho\Delta} v_\Delta}{M_\rho - M_{N'}}. \qquad (4.17)
\end{aligned}
$$

In terms of $M_{\rho_1^0}$ and $M_{\rho_2^0}$ we can express the Yukawa coupling $Y_{\rho\Delta}$ in the following way:

$$
\begin{aligned}
Y_{\rho\Delta} &= \frac{(M_{\rho_2^0} - M_{\rho_1^0})\sin 2\beta}{2\, v_\Delta}, \\
&= \frac{\Delta M_{21} \sin 2\beta}{2 v_\Delta} \qquad (4.18)
\end{aligned}
$$

where $\Delta M_{21} = (M_{\rho_2^0} - M_{\rho_1^0})$ represents the mass difference between $M_{\rho_2^0}$ and $M_{\rho_1^0}$. Therefore, one can increase the Yukawa coupling $Y_{\rho\Delta}$ by increasing the mass difference ΔM_{21} or the singlet triplet fermionic mixing angle, or decreasing the triplet vev v_Δ. We have kept the mass of charged component ($\rho^\pm$) of triplet fermion equal to the mass of ρ_2^0 with the mass gap of pion *i.e.* $M_{\rho^\pm} = M_{\rho_2^0} + 0.16$ GeV.

A further discussion is in order. For the present model we can generate the neutrino mass by Type I seesaw mechanism just by introducing SM singlet right handed neutrinos. In other variants of the triplet fermionic DM model, neutrino masses were generated by using the Type III seesaw mechanism and radiatively by the authors of [166] and [154–156, 162], respectively.

4.4 Constraints used in Dark Matter Study

Below, we discuss different constraints that we take into account. This includes the constraints from relic density, the direct detection constraints, as well as the invisible Higgs

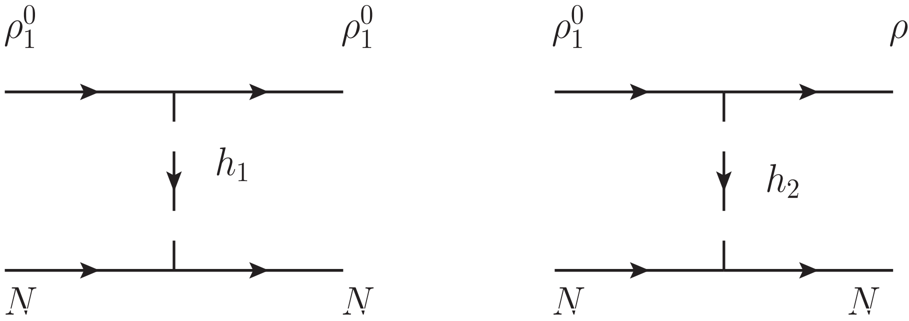

Figure 4.3: SI direct detection scattering processes between DM and nucleaon of the nucleus.

decay.

4.4.1 SI direct detection cross section

The Feynman diagrams in Fig. 4.3 show the spin independent (SI) direct detection (DD) scattering processes between the DM and the nucleon ($\rho_1^0 N \to \rho_1^0 N$), which are mediated by the two Higgses h_1 and h_2, respectively, through the t-channel process. Since DM interacts very weakly with the nucleon, one can safely calculate the cross-section for this process in the $t \to 0$ limit, where t is the Mandelstam variable corresponding to the square of the four-momentum transfer. The expression for the above process takes the following form,

$$\sigma_{SI} = \frac{\mu_{red}^2}{\pi}\left[\frac{M_N f_N}{v}\left(\frac{g_{\rho_1^0\rho_1^0 h_2}\sin\alpha}{M_{h_2}^2} - \frac{g_{\rho_1^0\rho_1^0 h_1}\cos\alpha}{M_{h_1}^2}\right)\right]^2 \tag{4.19}$$

where the quantity f_N is the nucleon form factor and it is equal to 0.3 [32] while μ_{red} is the reduced mass between the DM mass ($M_{\rho_1^0}$) and the nucleon mass (M_N) and is given by

$$\mu_{red} = \frac{M_N M_{\rho_1^0}}{M_N + M_{\rho_1^0}}, \tag{4.20}$$

The couplings in Eq. (4.19) $g_{\rho_1^0\rho_1^0h_1}$ and $g_{\rho_1^0\rho_1^0h_2}$ are given by,

$$\begin{aligned} g_{\rho_1^0\rho_1^0h_1} &= \frac{Y_{\rho\Delta}}{2}\sin 2\beta\,\sin\alpha\,, \\ g_{\rho_1^0\rho_1^0h_2} &= \frac{Y_{\rho\Delta}}{2}\sin 2\beta\,\cos\alpha\,, \end{aligned} \tag{4.21}$$

where $Y_{\rho\Delta}$, α and β have been defined in the previous section. We had seen in Eq. (4.18) that the Yukawa coupling $Y_{\rho\Delta}$ is linearly proportional to $\sin 2\beta$ for a given choice of mass splitting $\Delta M_{21} = (M_{\rho_2^0} - M_{\rho_1^0})$ and vev v_Δ. Therefore, inserting Eqs. (4.18) and (4.21) into Eq. (4.19) we get

$$\sigma_{SI} = \frac{\mu_{red}^2}{\pi}\left[\frac{M_N f_N}{v}\frac{\Delta M_{21}\sin^2 2\beta\sin 2\alpha}{4v_\Delta}\left(\frac{1}{M_{h_2}^2}-\frac{1}{M_{h_1}^2}\right)\right]^2 \tag{4.22}$$

Since σ_{SI} depends on the model parameters, and since the current limit from DD experiments need to be satisfied, they put a constraint on the our model parameter space. Also, the model could be tested and/or the parameter space can be constrained by the future DD experiments like LUX [115, 167], Xenon-1T [149, 168], Panda [169] and Darwin [150].

4.4.2 Invisible decay width of Higgs

If the DM candidate has mass less than half the SM-like Higgs mass then the SM-like Higgs could decay to pair of DM particles. This process would contribute to the decay width of the SM-like Higgs into invisible states. The Higgs decay width has been measured very precisely by the LHC which constrains the Higgs decay in such a way that its branching ratio to invisible states must be less than 34% at 95% C.L. [170]. In the present model the Higgs decay width to invisible states ρ_1^0 (since in the present work $M_{\rho_2^0} > \frac{M_{h_1}}{2}$, hence Higgs can not decay to ρ_2^0) is given by,

$$\Gamma_{h_1\to\rho_1^0\rho_1^0} = \frac{M_{h_1} g^2_{\rho_1^0\rho_1^0h_1}}{16\pi}\left(1-\frac{4M^2_{\rho_1^0}}{M^2_{h_1}}\right)^{3/2}\,, \tag{4.23}$$

where $g_{\rho_1^0 \rho_1^0 h_1}$ is given in Eq. (4.21). In order to satisfy the LHC limit, the model parameters have to satisfy the following constraint

$$\frac{\Gamma_{h_1 \to \rho_1^0 \rho_1^0}}{\Gamma_{h_1}^{Total}} \leq 34\% \text{ at } 95\% \text{ C.L.} \tag{4.24}$$

For the parameter range where the kinematical condition $M_{\rho_1^0} < \frac{M_{h_1}}{2}$ is satisfied we impose the condition given by Eq. (4.24) and only model parameter values that satisfy this constraints are used in our analysis.

4.4.3 Planck Limit

Relic density for the DM has been measured very precisely by the satellite borne experiments WMAP [19] and Planck [20]. In this work we have used the following bound on the DM relic density,

$$0.1172 \leq \Omega h^2 \leq 0.1226 \text{ at } 68\% \text{ C.L.}, \tag{4.25}$$

which is used to constrain the model parameters such that it is compatible with the Planck limit on DM abundance.

4.5 Dark Matter Relic Abundance

In analysing the DM phenomenology we implement the model in Feynrules [171]. We generate Calchep files using Feynrules and feed the output files into micrOmegas [33]. The relevant Feynman diagrams that determine the DM relic abundance are shown in Fig. 4.4. In presence of triplet as well as singlet states, additional channels mediated by the neutral and charged Higgs state opens up.

Different model parameters, such as, the mass of DM, neutral Higgs, mixing between

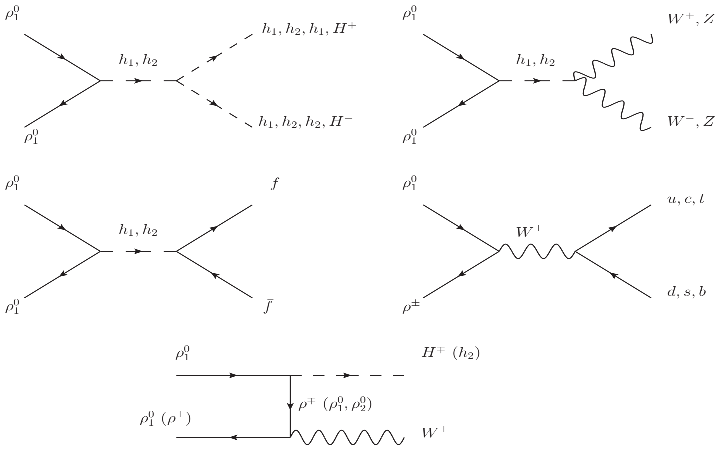

Figure 4.4: Feynman diagrams which dominantly participate in determining the relic density of DM.

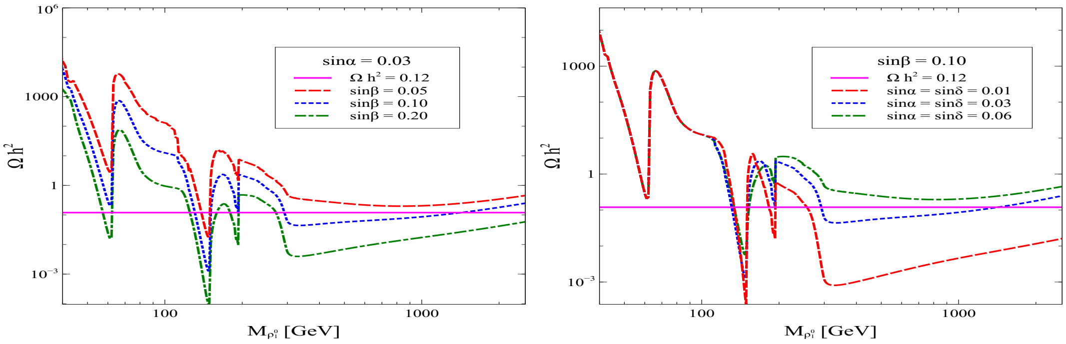

Figure 4.5: Left Panel: variation of DM relic density for three different values of the singlet triplet fermionic mixing angle sinβ. Right Panel: variation of DM relic density for three different values of the neutral Higgses mixing angle sinα. When the BSM Higgs value kept fixed at $M_{h_2} = 300$ GeV and we took sinδ equal neutral Higgs mixing angle for simplicity and kept the mass difference ΔM_{12} fixed at 50 GeV.

singlet and triplet fermions, as well as different Higgs states can impact the DM relic density. We analyse the dependence of the DM relic density on the model parameters and also study the correlation between them that follows from the DM relic density constraint. Fig. 4.5 shows the variation w.r.t the mass of DM taking into account the variation of the different mixing angles. In other figures, such as, Fig. 4.6, we explore the dependency on the mass-difference and the BSM Higgs masses. Few comments are in order:

- In the left panel (LP) of Fig. 4.5, we show the variation of the DM relic density with DM mass for three different values of the singlet-triplet mixing angle $\sin\beta$. The thin magenta band shows the 2σ experimentally allowed range of the DM relic density reported by the Planck collaboration. From the figure, this is evident, that there are four dip regions with respect to the DM mass. The first resonance occurs at $M_{\rho_1^0} \simeq M_{h_1}/2 \sim 62.5$ GeV. The SM-like Higgs mediated diagrams shown in Fig. 4.4 give the predominant contribution in this mass range. The second resonance occurs at $M_{\rho_1^0} \sim 150$ GeV, when the DM mass is approximately half the BSM Higgs mass ($M_{\rho_1^0} \simeq M_{h_2}/2$) assumed in this figure. The third dip is due to the t-channel diagram $\rho_1^0\rho_1^0 \to W^\pm H^\mp$ mediated by the $\rho^\pm$. This dip occurs when the DM mass satisfies the relation $M_{\rho_1^0} = \frac{M_{W^\pm}+M_{H^\mp}}{2}$ and happens due to the destructive interference term of the $W^\pm H^\mp$ final state. The fourth dip happens because of the threshold effect of the $W^\pm H^\mp$ final state and clear from the fact that with the variation of the charged scalar mass ($M_{H^\mp}$), this dip also changes its position with respect to the DM mass. For DM masses greater than this, the DM relic abundance is mainly dominated by the s-channel annihilation diagram where the final state contains H^+H^-, h_2h_2.

- This is to emphasize, in the present scenario even relatively lighter DM is in agreement with the observed relic density. The low mass DM can be copiously produced at LHC and hence can further be tested in the ongoing run of LHC. The lowering of DM mass is possible due to the addition of the extra SM gauge singlet fermion N' and the extra SM triplet Higgs Δ. This opens up additional annihilation and coannihilation diagrams shown in Fig. 4.4. As described before, this allows the three resonance regions and make the model compatible with the experimental constraint from Planck for DM masses accessible at LHC. This should be contrasted with the pure triplet model discussed in section 4.2, where the DM mass compatible with the Planck data is 2.37 TeV, well outside the range testable at LHC due to small production cross-section. In the next section, we will discuss in detail the prospects of testing the DM at LHC (see Fig. 4.11).

- The singlet triplet mixing angle β has significant effect on the relic density. With the increase of the mixing angle β, the DM relic density decreases. This happens because the $g_{\rho_1^0\rho_1^0 h_i}$ $(i = 1,2)$ coupling increases with β (cf. Eq. (4.21)), thereby increasing the cross-section of the annihilation processes. Since the relic density is inversely proportional to the velocity times cross-section $\langle\sigma v\rangle$, where σ is the annihilation cross-section of the DM particles and v is the relative velocity, increase of $\sin\beta$ causes the relic density of DM to decrease.

- Additionally, we also explore the effect of the Higgs mixing angle α. In the right panel (RP) of Fig. 4.5, we show the variation of the DM relic density for three different values of the doublet-triplet Higgs mixing angle α. The first resonance peak is seen to be nearly unaffected by any change in $\sin\alpha$. As the DM mass increases, the impact of $\sin\alpha$ increases and we see an increase in the DM relic density with increase of $\sin\alpha$. These features can be explained as follows. Inserting $Y_{\rho\Delta}$ from Eq. (4.18) into Eq. (4.21), and replacing v_Δ in terms of $\tan\delta$ using Eq. (4.13), we get

$$\begin{aligned} g_{\rho_1^0\rho_1^0 h_1} &= \frac{\Delta M_{21}\sin 2\beta}{2v}\frac{\sin\alpha}{\tan\delta}, \\ g_{\rho_1^0\rho_1^0 h_2} &= \frac{\Delta M_{21}\sin 2\beta}{2v}\frac{\cos\alpha}{\tan\delta}. \end{aligned} \tag{4.26}$$

In our analysis we have taken $\sin\alpha = \sin\delta$ for simplicity. Therefore, this results in partial cancellations between the the neutral scalars mixing angle and charged

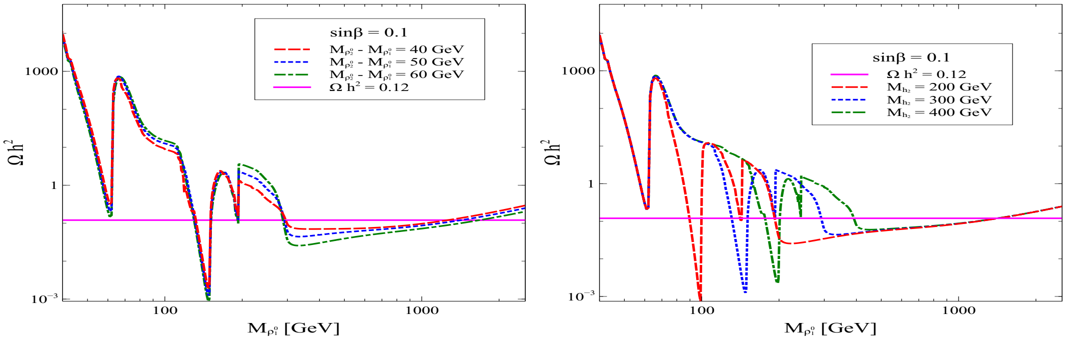

Figure 4.6: Left Panel: variation of DM relic density for three different value of mass difference ($M_{\rho_2^0} - M_{\rho_1^0}$) when the BSM neutral and charged Higgses values kept fixed at $M_{h_2} = M_{H^\pm} = 300$ GeV. Right Panel: variation of DM relic density for three different value of the BSM Higgs mass and we kept the mass difference fixed at $M_{\rho_2^0} - M_{\rho_1^0} = 50$ GeV. We took the other parameters value, $\sin\alpha = 0.03$, $\sin\delta = 0.03$.

scalars mixing angle, hence we get the following effective couplings for the h_1 and h_2 mediated diagrams, respective,

$$\begin{aligned} g_{\rho_1^0\rho_1^0 h_1} &= \frac{\Delta M_{21}\sin 2\beta}{2v}\cos\alpha\,, \\ g_{\rho_1^0\rho_1^0 h_2} &= \frac{\Delta M_{21}\sin 2\beta}{2v}\frac{\cos^2\alpha}{\sin\alpha}\,. \end{aligned} \tag{4.27}$$

Since the h_1 mediated diagrams effectively depend on $\cos\alpha$ and since $\cos\alpha$ remains close to 1 for all the three choices of $\sin\alpha$, taken in Fig. 4.5, we see no effect of $\sin\alpha$ variation for the h_1 resonance region. On the other hand, once the h_2 mediated diagrams start to dominate, the effect of $\sin\alpha$ variation starts to show up. For the h_2 resonance region, the cross-section decreases as $\sin\alpha$ increases (cf. Eq. (4.26)) and hence the relic density increases with $\sin\alpha$. In the vicinity of third resonance region t-channel diagrams dominate and for DM masses $M_{\rho_1^0} > M_{h_2}, M_{H^\pm}$, the s-channel mediated diagrams start contributing in the DM relic density and vary the relic density in the expected way with the variation of $\sin\alpha$ and $\sin\delta$.

Additionally, we also show the variation of relic density for different mass difference ΔM_{21} in the LP of Fig. 4.6. The first and second resonance regions show very little dependence on the mass difference ($M_{\rho_2^0} - M_{\rho_1^0}$), with the relic abundance being marginally less for higher $(M_{\rho_2^0} - M_{\rho_1^0})$. However, for the high DM mass we see that the decrease in DM relic abundance with increasing values of $(M_{\rho_2^0} - M_{\rho_1^0})$ is visible. The reason for this can be understood as follows. From Eq. (4.18), one can see that the singlet-triplet Yukawa coupling $Y_{\rho\Delta}$ is directly proportional to the mass difference $(M_{\rho_2^0} - M_{\rho_1^0})$. Both DM couplings $g_{\rho_1^0\rho_1^0 h_2}$ and $g_{\rho_1^0\rho_1^0 h_1}$ (see Eq. (4.21)) depend on the Yukawa coupling $Y_{\rho\Delta}$ and hence in first and second resonance regions where the s-channel processes dominate, *viz.*, at the resonance regions mainly, controlled by resonance, hence less effect. On the other hand for higher $M_{\rho_1^0}$ regions and *t*-channel dominated regions no such resonance exists, so vary linearly with the mass differences. Close to the third resonance region, the t-channel process dominates and here, the cross-section is suppressed due to the propagator mass $M_{\rho^\pm}$. Therefore, for regions of the parameter space where the t-channel process dominates, the relic abundance is seen to increase as $(M_{\rho_2^0} - M_{\rho_1^0})$ (here we considered $M_{\rho^\pm} - M_{\rho_2^0} = 160$ MeV) increases for a given $M_{\rho_1^0}$. One can see that there is clear cross over between the *t*-channel and *s*-channel diagrams for $M_{\rho_1^0} > M_{H^\pm}, M_{h_2}$, because after this value of DM mass $\rho_1^0\rho_1^0$ mainly annihilates to $h_2 h_2$ and $H^+ H^-$ by the *s*-channel process mediated by the Higgses.

Finally, we also explore the dependency on the mass of the neutral Higgs h_2. In the RP of Fig. 4.6, we show the variation of the relic density with DM mass for three different values of the BSM Higgs mass: $M_{h_2} = 200$ GeV, 300 GeV and 400 GeV, respectively. From the figure we see that the first resonance remains unchanged at $M_{\rho_1^0} \sim 62.5$ because the SM-like Higgs mass is fixed at $M_{h_1} = 125.5$ GeV. However, the second resonance occurs at three different values of the DM mass depending on the values of M_{h_2}, as the resonance occurs at $M_{\rho_1^0} \sim \frac{M_{h_2}}{2}$. Since here we vary only the BSM Higgs mass M_{h_2}, the couplings which are related to the Higgses remain unaffected, and all three curve merge for greater values of DM mass.

To summarise, the relic density depends crucially on the mixing angles between singlet and triplet states, as well as the SM and BSM Higgs, and their masses. The BSM

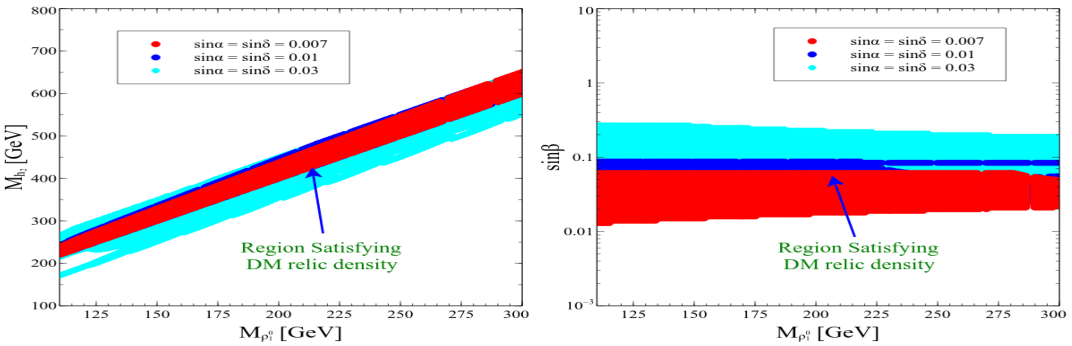

Figure 4.7: LP (RP): Allowed region in the $M_{\rho_1^0} - M_{h_2}$ ($M_{\rho_1^0} - \sin\beta$) plane after satisfying relic density bound. Other parameters values are $\Delta M_{12} = 50$ GeV, $M_{H^\pm} = M_{h_2}$ and the remaining parameters have been varied as shown in Table 4.3.

neutral Higgs state with mass M_{h_2} and the charged Higgs state with suitable mass can generate multiple resonance regions, where the DM relic abundance is satisfied. The relic abundance varies inversely with the fourth power of $\sin 2\beta$ *i.e.*, $\propto \frac{1}{\sin^4 2\beta}$, where β is the singlet-triplet mixing angle. The DM relic abundance is also seen to depend on the neutral Higgs mixing angle α. Below, we discuss the correlation between different model parameters.

Model Parameters	Range
$M_{\rho_1^0}$	110 - 300 [GeV]
M_{h_2}	$(2\,M_{\rho_1^0})^{100}_{-50}$ [GeV]
$\sin\beta$	10^{-3} - 1

Table 4.3: Parametsr varied in the above mentioned range at the time of generating the scatter plots.

4.6 Correlation between parameters

In the LP of Fig. 4.7 we show the allowed regions in M_{h_2} and $M_{\rho_1^0}$, where all the dots satisfy the relic density bound as given in Eq. 1.85. The three colors correspond to three different benchmark choices for the Higgs mixing angle α. From Figs. 4.5 and 4.6, one can see that the DM relic density can always be satisfied near the resonance regions. Hence, for a given BSM Higgs mass, there is only a range of DM masses that are allowed by the Planck bound. In generating the scatter plots we have varied the model parameters as shown in Table 4.3. We have kept the values of M_{h_2} near the resonance region. As expected, we get a sharp correlation between the mass of DM and the BSM Higgs mass as stressed above. On the other hand, in the RP of Fig. 4.7 we have shown the allowed region in the sine of singlet-triplet mixing angle ($\sin\beta$) and the DM mass ($M_{\rho_1^0}$) plane. Here we keep $\Delta M_{21} = 50$ GeV (ΔM_{21} as defined before), and the allowed region shows that for the given ranges as in Table 4.3, the DM relic density can be satisfied for $0.025 < \sin\beta < 0.27$. One interesting point to note here is that in the LP of Fig. 4.7 for $\sin\alpha$, $\sin\delta = 0.03$, correlation in the $M_{\rho_1^0} - M_{h_2}$ is wider compared to the other two lower values of $\sin\alpha$, $\sin\delta$. We can understand this as follows. From the RP of Fig. 4.7 for $\sin\alpha$, $\sin\delta = 0.03$, the DM relic density is satisfied for higher values of $\sin\beta$ (~ 0.3). From the LP of Fig. 4.5 we see that near the second resonance region ($M_{\rho_1^0} \sim M_{h_2}/2$) the DM relic density is satisfied for a wider range of $M_{\rho_1^0}$ for higher values of $\sin\beta$. Since, for $\sin\alpha$, $\sin\delta = 0.03$, we get higher values of $\sin\beta$ (as seen from the RP of Fig. 4.7), so the correlation in $M_{\rho_1^0} - M_{h_2}$ planes becomes wider.

The LP and RP of Fig. 4.8 show the allowed regions in the spin independent DD cross section and the DM mass ($\sigma_{SI} - M_{\rho_1^0}$) plane and the singlet-triplet mixing angle ($\sigma_{SI} - \sin\beta$) plane, respectively. The LP shows that the model parameter space is not constrained so-far by the results from the LUX experiment [167] (and Panda experiment [169]). However, a good part of the parameter space can be probed in by the Xenon 1T experiment [168] and in the future by the Darwin experiment [150]. The green, blue and red dots satisfy the present day relic density bound for three chosen values of $\sin\alpha$. In the RP we show the variation of the spin independent direct detection cross-section with the fermion singlet-triplet mixing angle. Since the DD cross section is directly proportional to the square of $\sin\beta$ we see this functional dependence in this figure and σ_{SI} is seen to increase with $\sin\beta$.

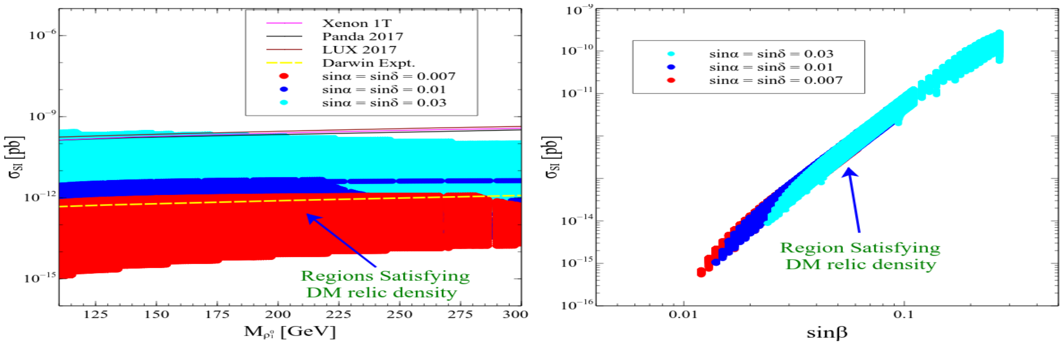

Figure 4.8: LP (RP): Allowed region in the $M_{\rho_1^0}-\sigma_{SI}$ ($\sin\beta-\sigma_{SI}$) plane after satisfying relic density bound. Other parameters values are $\Delta M_{12}=50$ GeV, $M_{H^\pm}=M_{h_2}=300$ GeV and the remaining parameters have been varied as shown in Table 4.3.

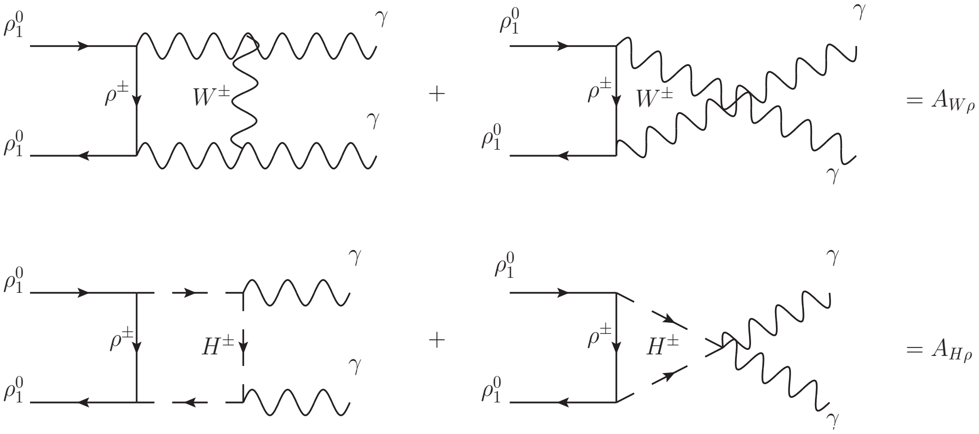

Figure 4.9: Feynman diagrams of the DM annihilation into the gamma rays by one loop diagrams mediated by the charge gauge boson $W^\pm$ and the charged scalar $H^\pm$.

4.7 Indirect Detection of Dark Matter by $\gamma\gamma$ observation

In addition to the detection of the DM in the ongoing direct detection experiments for the present model, it can also be detected by the indirect search of DM in different satelite borne experiments like Fermi-LAT [153, 172], HESS [173, 174] by detecting the gamma-rays signal which comes from the DM annihilation. In the present situation DM cannot annihilate to gamma-rays at tree level but certainly can annihiate at the one loop level mediated by the charged gauge boson $W^\pm$ and the charged scalar $H^\pm$ which is shown in Fig. 4.9. The average of the amplitude for the velocity times cross section for the Feynman

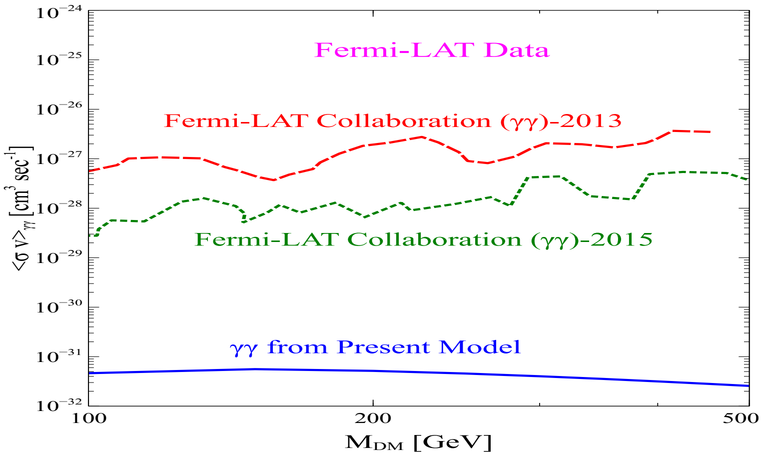

Figure 4.10: Fermi-LAT bounds and the prediction from the present model. In getting the prediction from the model, we have kept the parameters value fixed at $\sin\beta = 0.1$, $\Delta M_{21} = 50$ GeV, $M_{H^\pm} = M_{h_2} = 2M_{DM}$ and $\sin\alpha = \sin\delta = 0.03$.

diagrams which are shown in Fig. 4.9 takes the following form [175, 176],

$$\langle\sigma v\rangle_{\gamma\gamma} = \frac{\alpha_{EM}^2 M^2_{\rho_1^0}}{16\pi^3}|A|^2 \tag{4.28}$$

where $A = A_{W\rho} + A_{H\rho}$, $\alpha_{EM} = e^2/4\pi$ and $e = 0.312$. $A_{W\rho}$ and the $A_{H\rho}$ are the separate contribution from one loop diagrams as shown in Fig. 4.9 which are mediated by the $W^\pm$ and $H^\pm$, respectively. The individual amplitude for the diagrams which are shown in Fig. 4.9 take the following form,

$$\begin{aligned} A_{W\rho} &= -2C_1^2\Big[2I_3^a(M_W) + 2(M^2_{\rho^\pm} + M_W^2 - M^2_{\rho_1^0})I_4^a + 2M^2_{\rho^\pm}I_4^b + 3M^2_{\rho^\pm}I_4^c + I_3^b(M_W, M_{\rho^\pm})\Big] \\ &\quad +8C_1^2 M_{\rho^\pm}M_{\rho_1^0}(I_4^b + I_4^c), \\ A_{H\rho} &= C_2^2\Big[2M^2_{\rho^\pm}I_4^b + M^2_{\rho^\pm}I_4^c + I_3^b(M_{H^\pm}, M_{\rho_1^0})\Big] \end{aligned} \tag{4.29}$$

where the explicit form of I_3^i ($i = a,b$) and I_4^j ($j = a,b,c$) are given in the Appendix. The couplings C_1 and C_2 are $C_1 = -e\sin\beta/\sin\theta_w$, where θ_w is the Weinberg angle and $C_2 = \cos\alpha Y_{\rho\Delta}/2$, where $Y_{\rho\Delta}$ is given in Eq. (4.18).

In Fig. 4.10, we show the variation of $\langle\sigma v\rangle$ with the DM mass, $M_{\rho_1^0}$ by considering the relevant one loop diagrams. As the DM relic density for the pure triplet fermion is satisfied for DM mass of about 2.4 TeV and this is already ruled out by the Fermi-LAT data when we the Sommerfeld enhancement is taken into consideration. In the current work, we have taken the triplet fermion mixing with the singlet fermion with the help of the triplet scalar and DM relic density can be satisfied around the 100 GeV order DM mass. For such low mass range of the DM where $M_{\rho_1^0} \sim M_W \sim M_{H^\pm}$, the Sommerfeld enhancement factor will have no significant role in the increment of $\langle\sigma v\rangle_{\gamma\gamma}$. We have shown the Fermi-LAT-2013 [172] and Fermi-LAT-2015 [153] data in the $\langle\sigma v\rangle_{\gamma\gamma} - M_{\rho_1^0}$ plane by the red and green dash line, respectively. By blue solid line we have shown the $\langle\sigma v\rangle_{\gamma\gamma}$ variation with the DM mass which is suppressed by the one loop factor for the present model.

4.8 LHC Phenomenology

Although there has been no dedicated search for such a model at the LHC, one can in principle, derive limits on the masses of the exotic fermions ($\rho^0_{1,2}$, $\rho^\pm$) and the additional scalar states(h_2, $H^\pm$) from existing LHC analyses looking for similar particles. LHC has extensively searched for heavy neutral Higgs boson similar to h_2 and the non-observation of any such states puts stringent constraints on masses and branching ratios of such particles provided their decay modes are similar to that of the SM-like Higgs [177–179]. However, in our case, these bounds are significantly weakened because the decays of h_2 here are quite different compared to the conventional modes. h_2 mostly decays into $h_1 h_1$, $\rho_2^0\rho_1^0$ or $\rho_1^0\rho_1^0$ pair depending on the availability of the phase space. In absence of $\rho_2^0\rho_1^0$ mode, $\rho_1^0\rho_1^0$ always has a large (30% - 40%) branching ratio, which is a completely invisible mode and thus leads to weaker event rates in the visible final states. In the presence of $\rho_2^0\rho_1^0$ and(or) $h_1 h_1$ modes, a $b\bar{b}$ final state study can constrain the h_2 mass since ρ_2^0 always decays dominantly via $b\bar{b}$. However, the net branching ratio suppression results in weaker limits from the existing studies. Charged Higgs search at the LHC concentrates on the $\tau\bar{\nu}$, $c\bar{s}$, $c\bar{b}$ and $t\bar{b}$ decay modes depending on the mass of $H^\pm$ [180–183]. None of these decay modes are significant in our present scenario. Here $\rho^\pm$ decays via $\rho_1^0\rho^\pm$ and(or) $W^\pm Z$ depending on the particle masses. Thus the existing charged Higgs mass limits do not apply here. Instead, a dilepton or trilepton search would be more suitable for such particles although the charged leptons originating solely from the gauge boson decays will be hard to distinguish from those coming from the SM. Constraints on the masses of ρ_2^0 and $\rho^\pm$ can be drawn from searches of wino-like neutralino and chargino in the context of supersymmetry [184, 185]. However, production cross-section of this pair at the LHC is smaller compared to the gauginos leading to weaker mass limits. Moreover, the decay pattern of ρ_2^0 is quite different from that of a wino-like neutralino. The most stringent gaugino mass bounds are derived from the trilepton final state analysis. Such a final state cannot be expected in our present scenario since ρ_2^0 dominantly decays into a $b\bar{b}$ pair along with ρ_1^0. However, $\rho^\pm$ always decays into ρ_1^0 associated with an on-shell or off-shell W-boson, similar to a wino-like chargino. Thus the bounds derived on the chargino masses in such cases [184, 185] can be applied to $m_{\rho^\pm}$ as well if appropriately scaled to its production cross-section and subjected to $m_{\rho_1^0}$. We have taken this constraint into account while constructing our benchmark points.

In this section, we discuss in detail the LHC phenomenology of the dark matter. The low mass dark matter can be copiously produced at LHC, either directly or from the decay of the its triplet partner.

4.8.1 Production cross-section and choice of benchmark points

For this we consider production of $\rho^\pm\rho_2^0$ which further decay into ρ_1^0 associated with quarks resulting in a multi-jet + $\not{E}_T$ signal. Similar collider signal can also arise from other production modes, namely, $\rho_2^0\rho_2^0$ and $\rho^+\rho^-$. While the ρ_2^0 pair production cross-section is smaller by orders of magnitude, the other two production channels have comparable cross-sections as shown in Fig. 4.11. For Fig. 4.11, we have kept the mass gap between ρ_2^0 and $\rho_\pm$ fixed at the pion mass and the cross-section is computed at 13 TeV

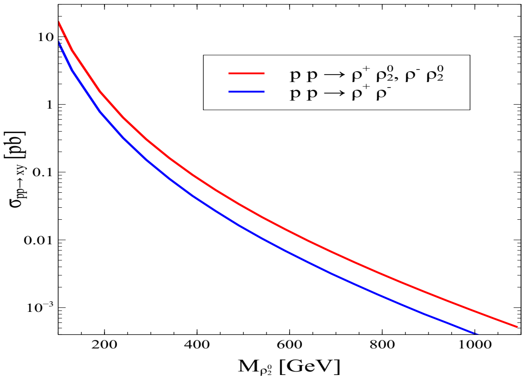

Figure 4.11: Variation of production cross section $\rho^\pm\rho_2^0$ and $\rho^\pm\rho^\mp$ with DM mass for 13 TeV run of LHC where we kept fixed $M_{\rho_2^0} - M_{\rho_1^0} = 20$ GeV, $M_{h_2} = M_{H^\pm} = 300$ GeV.

centre-of-mass energy. Clearly, $\sigma(pp \rightarrow \rho^\pm\rho_2^0)$ is almost twice to that of $\sigma(pp \rightarrow \rho^+\rho^-)$ making the former one the most favored production channel to probe for the present scenario. However, the latter one can also contribute significantly to boost the multi-jet + $\not{E}_T$ signal event rate given the fact that ρ_2^0 and $\rho^\pm$ are mass degenerate from the collider perspective. The degeneracy of ρ_2^0 and $\rho^\pm$ results in their decay products to have very similar kinematics. Therefore, in our study of the multi-jet final state we have included both the production channels $pp \rightarrow \rho_2^0\rho^\pm$ and $pp \rightarrow \rho^+\rho^-$. ρ_2^0 further decays into ρ_1^0 mostly via h_2 whereas $\rho^\pm$ also decays into ρ_1^0 via W-boson. Regardless of whether the intermediate scalar or the gauge bosons are on-shell or off-shell, we always consider their decays into pair of b-quarks or light quarks. In the former case, the decay of h_2 is likely to give rise to b-jets in the final state whereas the latter one results in light jets arising from W decay. Hence in order to combine the event rates arising from these two production channels, we do not demand any b-tagged jets in the final states. Besides, demanding b-tagged jets in the final state can also hinder the signal event rates specially for cases where the mass difference between ρ_2^0 and ρ_1^0, i.e., ΔM_{21} is small.

For detail collider simulation and analysis of the above mentioned final state, we have constructed few benchmark points representative of the available parameter space after imposing all the relevant constraints. We have presented our choice of benchmark points with all the relevant particle masses and DM constraints in Table 4.4. Note that, the mass

Parameters	$M_{\rho_1^0}$ [GeV]	$M_{\rho_2^0}$ [GeV]	M_{ρ^+} [GeV]	M_{h_2} [GeV]	$M_{H^\pm}$ [GeV]	σ_{SI} [pb]	Ωh^2
BP1	87.6	128.0	128.2	195.5	195.5	2.1×10^{-12}	0.1207
BP2	132.0	172.0	172.2	300.0	300.0	4.1×10^{-12}	0.1208
BP3	171.1	211.0	211.2	400.0	400.0	4.8×10^{-12}	0.1197
BP4	86.7	200.0	200.2	194.1	194.1	1.8×10^{-11}	0.1186
BP5	119.0	230.0	230.2	280.0	280.0	2.9×10^{-11}	0.1195

Table 4.4: Benchmark points to study LHC phenomenology. We fixed other BSM parameters as $\sin\alpha = 0.03$, $\sin\beta = 0.1$.

gap between ρ_2^0 (or $\rho\pm$) and ρ_1^0 (ΔM_{21}) can not be arbitrarily large for admissible values of β. Hence in some cases, these fermionic states can lie quite close together giving rise to a *compressed* scenario as depicted by, for example, BP1 in Table 4.4. However, the mass gap can be moderate to significantly large and our choice of the benchmark points encompasses all possible kind of DM mass regions and mass hierarchies.

4.8.2 Simulation details

As mentioned previously, the mass gap ΔM_{21} can be quite small in some cases, resulting in soft jets in the final state, which may escape detection. The standard procedure is to tag the radiation jets in order to look for such scenarios. For that, one needs to take into account production of the mother particles along with additional jets and perform a proper jet-parton matching [186, 187] in order to avoid double counting of jets. We have considered the above mentioned production channels associated with upto two additional jets at the parton level.

$$\begin{aligned} pp &\to XY \\ pp &\to XYj \\ pp &\to XYjj \end{aligned} \tag{4.30}$$

where {X Y} indicates any of the three pairs, $\{\rho_2^0\ \rho^+\}$, $\{\rho_2^0\ \rho^-\}$ and $\{\rho^+\ \rho^-\}$. The events have been generated at the parton level using MadGraph5(v2.4.3) [188, 189] with

CTEQ6L [190] parton distribution function (PDF). Events were then passed through PYTHIA(v6.4) [191] to perform showering and hadronisation effects. Matching between the shower jets and the parton level jets has been done using MLM [186, 187] matching scheme. We have subsequently passed the events through Delphes(v3.4.1) [192–194] for jet formation based on the anti-k_T jet clustering algorithm [195] via fastjet [196] and for detector simulation we used the default CMS detector cuts.

Since the number of hard jets obtained in the cascade are expected to vary for the different benchmark points depending on the choice of ΔM_{21}, we have chosen our final state with an optimal number of jet requirement along with missing energy: $\geq$ 2-jets + $\not{E}_T$. The dominant SM background contributions for such a signal can arise from QCD, V+ jets, $t\bar{t}$+ jets and VV + jets channels, where $V = W^{\pm}$ and Z. For collider analysis of this final state we have followed strategy similar to that adopted in, for example [197, 198].

Selection Cuts

We have used the following basic selection cuts (A0) to identify the charged leptons (e, μ), photon (γ) and jets in the final state:

- Leptons are selected with $p_T^l > 10$ GeV and the pseudorapidity $|\eta^{\ell}| < 2.5$, where $\ell = e, \mu$.
- We used $p_T^{\gamma} > 10$ GeV and psudorapidity $|\eta^{\gamma}| < 2.5$ as the basic cuts for photon.
- We have chosen the jets which satisfy $p_T^j > 40$ GeV and $|\eta^j| < 2.5$.
- We have considered the azimuthal separation between all reconstructed jets and missing energy must be greater than 0.2 i.e. $\Delta\phi(jet, \vec{\not{E}}_T) > 0.2$.

In Fig. 4.12, we have shown the distribution function of different kinematic variable for the illustrative benchmark points after applying the basic selection cuts (A0). In addition, we also show the distribution for the SM background events. The signal event

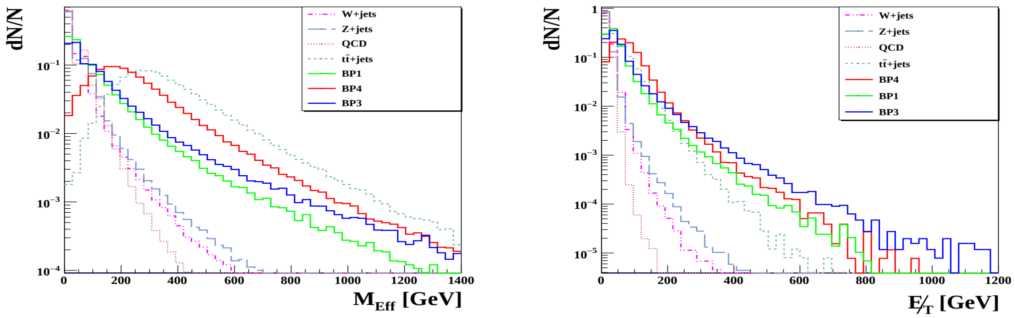

Figure 4.12: Normalised differential distribution with respect to the different cuts which we have used in our study. Besides the SM backgrounds we have also shown the distribution of three benchmark points BP1, BP4, BP3. All the kinematic variables have been addressed in text.

distributions shown here correspond to $\rho_2^0\rho^\pm$ production channel which is the dominant contributor to the final state.

Here we have shown the distribution corresponding to the effective mass (M_{Eff}) and missing energy ($\not{E}_T$) where the effective mass defined in the following way,

$$M_{Eff} = \sum_i |\vec{p}^{\,j}_{T_i}| + \sum_i |\vec{p}^{\,\ell}_{T_i}| + \not{E}_T . \tag{4.31}$$

These distributionis show some distinguishing features of the signal events from the SM backgrounds. Guided by these distributions we now proceed to device some appropriate kinematic cuts to optimise the signal to background events ratio in order to maximise the statistical significance of the signal.

A1: Since we are studying a hadronic final state, we have imposed a lepton and photon veto in the final state. This cut coupled with a large $\not{E}_T$ cut helps to reduce background events particularly arising from W + jets when W decays leptonically.

A2: p_T requirements on the hardest and second hardest jets: $p_T^{j_1} > 130$ GeV and $p_T^{j_2} > 80$ GeV. This cut significantly reduce the V + jets (where V = $W^\pm$, Z) and QCD backgrounds.

A3: The QCD multi-jet events have no direct source of missing energy. Therefore, any contribution to $\not{E}_T$ in these events must arise from the mismeasurement of the jet p_Ts. In order to minimise this effect, we have ensured that the $\vec{\not{E}}_T$ and the jets are well separated, i.e., $\Delta\phi(j_i,\vec{\not{E}}_T) > 0.4$ where i = 1, 2. For all the other jets, $\Delta\phi(j,\vec{\not{E}}_T) > 0.2$.

A4: We demand a hard cut on the effective mass variable, $M_{Eff} > 800$ GeV.

A5: We put the bound on the missing enrgy $\not{E}_T > 160$ GeV.

M_{Eff} and $\not{E}_T$ are the two most effective cuts to reduce SM background events for multi-jet analyses. As shown in Fig. 4.12, these variables clearly separates the signal kinematical region from most of the dominant backgrounds quite effectively and can reduce the backgrounds in a significant amount. Most importantly, these cuts along with A1 and A2, reduces the large QCD background to a neglible amount.

Results

In Table 4.5 and 4.6, we have shown numerical results of our collider analysis in production channels $\rho_2^0\rho^\pm$ and $\rho^+\rho^-$ respectively corresponding to the five choosen benchmark points (as shown in Table 4.4) which satisfy the present day accepted value of the DM relic density and are safe from the different ongoing direct detection experiment. We have studied the SM background in detail and in Table 4.7 we have shown the resulting cross sections after appyling the aforementioned cuts. Here, we have considered NLO cross section for all the SM background processes as provided in [188].

Signal at 13 TeV		Effective Cross section after applying cuts (fb)				
BP	Cross-section (pb)	A0 + A1	A2	A3	A4	A5
BP1	6.757	1005.05	175.08	138.45	22.02	19.15
BP2	2.279	385.22	69.16	56.51	11.87	10.85
BP3	1.052	189.71	34.63	29.19	7.36	6.82
BP4	1.296	1047.86	145.67	116.94	14.19	9.82
BP5	0.760	616.00	89.60	72.63	9.80	7.40

Table 4.5: Cut-flow table for the obtained signal cross section at 13 TeV LHC corresponding to $\rho_2^0\rho^\pm$ channel. The five benchmark points are referred as BP1-BP5. See the text for the details of the cuts A0-A5.

Signal at 13 TeV		Effective Cross section after applying cuts (fb)				
BP	Cross-section (pb)	A0 + A1	A2	A3	A4	A5
BP1	3.419	2639.30	74.36	59.18	8.54	7.31
BP2	1.156	880.60	28.77	23.87	4.95	4.43
BP3	0.532	402.24	14.80	12.62	3.18	2.95
BP4	0.652	446.80	63.99	45.54	5.72	3.76
BP5	0.380	258.55	34.40	28.07	3.99	3.08

Table 4.6: Cut-flow table for the obtained signal cross section at 13 TeV LHC corresponding to $\rho^+\rho^-$ channel. The five benchmark points are referred as BP1-BP5. See the text for the details of the cuts A0-A5.

SM Backgrounds at 13 TeV		Effective Cross section after applying cuts (pb)				
Channels	Cross-section (pb)	A0 + A1	A2	A3	A4	A5
$Z + \leq 4$ jets	5.7×10^4	5.5×10^3	361.90	241.60	11.40	2.20
$W^\pm + \leq 4$ jets	1.9×10^5	9.1×10^3	783.20	504.00	18.90	1.50
QCD (≤ 4 jets)	2.0×10^8	1.5×10^7	3.5×10^5	2.4×10^5	2.5×10^3	-
$t\bar{t} + \leq 2$ jets	722.94	493.73	171.46	120.63	13.89	1.94
$W^\pm Z + \leq 2$ jets	51.10	19.66	5.37	3.59	0.50	0.12
$ZZ + \leq 2$ jets	13.71	4.99	0.80	0.53	0.06	0.02
Total Backgrounds						5.78

Table 4.7: Cut-flow table for the obtained cross-sections corresponding to the relevant SM background channels for the cuts A0-A5 as mentioned in the text at the LHC with 13 TeV center-of-mass energy.

In order to compute statistical significance ($\mathcal{S}$) of our signal for the different benchmark points over the SM background we have used

$$\mathcal{S} = \sqrt{2 \times \left[(s+b)\ln\left(1+\frac{s}{b}\right) - s\right]}. \tag{4.32}$$

where s is the number of signal events and b that of the total SM background contribution. In Table 4.8, we have shown the statistical significance obtained for 100 fb^{-1} integrated luminosity ($\mathcal{L}$). In the last column we have also shown the required $\mathcal{L}$ to achieve 3σ statistical significance for our benchmark points at 13 TeV LHC.

Signal at 13 TeV		Statitical Significance ($\mathcal{S}$)	Required Luminosity $\mathcal{L}$ (fb^{-1})
BP	DM mass [GeV]	$\mathcal{L} = 100$ fb^{-1}	$\mathcal{S} = 3\sigma$
BP1	87.6	3.5	74.4
BP2	132.0	2.0	223.0
BP3	171.1	1.3	545.3
BP4	86.7	1.8	282.3
BP5	119.0	1.4	473.9

Table 4.8: Statistical significance of the multi-jet signal corresponding to different benchmark points for $\mathcal{L} = 100$ fb^{-1} integrated luminosity along with the required luminosity to achieve 3σ statistical significance at 13 TeV run of the LHC.

As evident from Table 4.5, 4.6, 4.7 and 4.8, the used kinematical cuts are efficient enough to reduce the SM background contributions to the multi-jet channel. At the same time sufficient number of signal events survive leading to discovery potential of such a scenario at the 13 TeV run of the LHC with realistic integrated luminosities. The cuts A2, A4 and A5 are particularly useful in reducing the dominant background constributions arising from W + jets, Z + jets and $t\bar{t}$ + jets. A combination of cuts A2-A5 has reduced the QCD contribution to a negligible amount. As the numbers indicate in Table 4.8, BP1 can be probed at the 13 TeV run of the LHC with 3σ statistical significance with relatively low luminosity owing to the large production cross-section. As expected, the signal significance declines as the mass of ρ_2^0 ($\rho^\pm$) is increased while its mass gap with ρ_1^0 is kept same as represented by the numbers corresponding to the two subsequent benchmark points (BP2 and BP3). The last two benchmark points, BP4 and BP5 represent the scenario when the parent particles have masses significantly higher than the DM candidate. As a result, one would expect the cut efficiencies to improve for these benchmark points. This is reflected for example in the case of BP5 which has a signal significance very similar to BP3 in spite of having the smallest production cross-section. It can be inferred from our analysis that ρ_2^0 ($\rho^\pm$) masses $\sim$ 250 GeV can easily be probed at the 13 TeV LHC with a reasonable luminosity.

5

Neutrino Mass, Leptogenesis and FIMP Dark Matter in a $\mathrm{U(1)_{B-L}}$ Model

5.1 Introduction

This chapter mostly covers the work [199] where we have extended the SM gauge group $\mathrm{SU(3)}_c \times \mathrm{SU(2)}_L \times \mathrm{U(1)}_Y$ by a local $\mathrm{U(1)_{B-L}}$ gauge group. The $\mathrm{B-L}$ extension of SM [94–97] has been studied earlier in the context of dark matter phenomenology [98–106, 200, 201] and baryogenesis in the early Universe in Refs. [107–109]. Since we have imposed a local U(1) symmetry, consequently an extra gauge boson (Z_{BL}) will arise. To cancel the anomaly due to this extra gauge boson we need to introduce three right-handed (RH) neutrinos (N_i, i = 1, 2, 3) to make the model anomaly free. Apart from the three RH neutrinos, we have also introduced two SM gauge singlet scalars namely ϕ_H and ϕ_{DM}, both of them are charged under the proposed $\mathrm{U(1)_{B-L}}$ gauge group. The $\mathrm{U(1)_{B-L}}$ symmetry is spontaneously broken when the scalar field ϕ_H takes a nonzero vacuum expectation value (VEV) and thereby generates the masses for the three RH neutrinos as well as the extra neutral gauge boson Z_{BL}, whose mass terms are forbidden initially due to the $\mathrm{U(1)_{B-L}}$ invariance of the Lagrangian. The other scalar ϕ_{DM} does not acquire any VEV and by choosing appropriate $\mathrm{B-L}$ charge ϕ_{DM} becomes naturally stable and therefore, can serve as a viable dark matter candidate. As mention above, anomaly cancellation requires the introduction of three RH neutrinos in the present model. Therefore we can easily generate the neutrino masses by the Type-I seesaw mechanism after B-L symmetry is broken. Diagonalising the light neutrino mass matrix (m_ν, for detail see Section 5.2.1), we determine the allowed parameter space by satisfying the 3σ bounds on the mass square differences (Δm^2_{12}, Δm^2_{atm}), the mixing angles ($\theta_{12}, \theta_{13}, \theta_{23}$) [89] and also the cosmological bound on the sum of three light neutrinos masses [20]. We also determine the effective mass $m_{\beta\beta}$ which is relevant for neutrino-less double beta decay and compare it against the current bound on $m_{\beta\beta}$ from GERDA phase I experiment [202].

Next, we explain the possible origin of the baryon asymmetry at the present epoch from an initially matter-antimatter symmetric Universe via leptogenesis. We first generate the lepton asymmetry (or $\mathrm{B}-\mathrm{L}$ asymmetry, Y_{B-L}) from the out of equilibrium, CP violating decays of RH neutrinos. The lepton asymmetry thus produced has been converted into the baryon asymmetry by the $(B+L)$ violating sphaleron processes which are effective before and during electroweak phase transition [203–205]. When the sphaleron processes are in thermal equilibrium ($10^{12}\,\mathrm{GeV} \lesssim T \lesssim 10^2$ GeV, T being the temperature of the Universe), the conversion rate is given by [206]

$$Y_B = -\frac{8N_f + 4N_{\phi_h}}{22N_f + 13N_{\phi_h}} Y_{B-L} \tag{5.1}$$

where $N_f = 3$ and $N_{\phi_h} = 1$, are the number of fermionic generations and number of Higgs doublet in the model, respectively.

Finally, in order to address the dark matter issue, we consider the singlet scalar ϕ_{DM} as a DM candidate. Since the couplings of this scalar to the rest of the particles of the model are free parameters, they could take any value. Depending on the value of these couplings, we could consider ϕ_{DM} as a WIMP or a FIMP. Detailed study on the WIMP type scalar DM in the present $\mathrm{U(1)_{B-L}}$ framework has been done in Refs. [93, 104, 105]. In most of the earlier works, it has been shown that the WIMP relic density is mainly satisfied around the resonance regions of the mediator particles. Moreover, the WIMP parameter space has now become severely constrained due to non-observation of any "real" signal in various direct detection experiments. Thus, as discussed earlier, in this situation the study of scalar DM other than WIMP is worthwhile. Therefore in this work, we consider the scalar field ϕ_{DM} as a FIMP candidate which, depending on its mass, is dominantly produced from the decays of heavy bosonic particles such as h_1, h_2, Z_{BL} and also from the annihilations of bosonic as well as fermionic degrees of freedom present in the model (e.g. N_i, Z_{BL}, h_i etc.). In the present work, we have extensively studied the FIMP DM production mechanism from all possible decays and annihilations other particles present in the model. Moreover, we have found that depending on our DM mass, a sharp correlation exists among the three puzzles of astroparticle physics namely neutrino mass generation, leptogenesis and DM.

In the non-thermal scenario, most of the production of the FIMP from the decay of a heavy particle occurs when $T \sim M$, where M is the mass of the decaying mother particle, which is generally assumed to be in thermal equilibrium. Therefore, the non-thermality condition of the FIMP demands that $\left.\frac{\Gamma}{H} < 1\right|_{T\sim M}$ [207], which in turn imposes a severe upper bound on the coupling strengths of the FIMP. Thus the non-thermality condition requires extremely small coupling of ϕ_{DM} with the thermal bath ($\lesssim 10^{-10}$) and hence, FIMP DM can easily evade all the existing bounds from DM direct detection experiments [115, 208, 209]. In this Chapter, we will not describe the model (particle spectrum and Lagrangian) because it is already described more elaborately in Chapter 2.

5.2 Results

5.2.1 Neutrino Masses and Mixing

As mentioned earlier, the cancellation of both axial vector anomaly [210, 211] and gravitational gauge anomaly [212, 213], in $\mathrm{U(1)_{B-L}}$ extended SM, requires the presence of extra chiral fermions. Hence, in the present model to cancel these anomalies we have introduced three right handed (RH) neutrinos (N_i, i=1 to 3). The Majorana masses for the RH neutrinos are generated only after spontaneous breaking of the proposed $\mathrm{B-L}$ symmetry by the VEV of ϕ_H. Also in the present scenario, as stated earlier, we are working in a basis where the Majorana mass matrix for the three RH neutrinos are diagonal i.e. $\mathcal{M}_{\mathcal{R}} = \mathrm{diag}(M_{N_1}, M_{N_2}, M_{N_3})$. The expression for the mass of ith RH neutrino (M_{N_i}) is given by,

$$M_{N_i} = \frac{y_{N_i}}{\sqrt{2}} v_{BL} \,. \tag{5.2}$$

On the other hand, the Dirac mass terms involving both left chiral and right chiral neutrinos, are originated when the electroweak symmetry is spontaneously broken by the VEV of SM Higgs doublet ϕ_h, giving rise to a 3×3 complex matrix $\mathcal{M}_{\mathcal{D}}$. In general, one can take all the elements of matrix $\mathcal{M}_{\mathcal{D}}$ as complex but for calculational simplicity and also keeping in mind that only three physical phases (one Dirac phase and two Majorana phases) exist for three light neutrinos (Majorana type), we have considered only three complex elements in the lower triangle part of the Dirac mass matrix $\mathcal{M}_{\mathcal{D}}$. However, the results we have presented later in this section will not change significantly if we consider all the elements of $\mathcal{M}_{\mathcal{D}}$ are complex. The Dirac mass matrix $\mathcal{M}_{\mathcal{D}}$ we assume has the following structure:

$$\mathcal{M}_D = \begin{pmatrix} y_{ee} & y_{e\mu} & y_{e\tau} \\ y_{\mu e} + i\,\tilde{y}_{\mu e} & y_{\mu\mu} & y_{\mu\tau} \\ y_{\tau e} + i\,\tilde{y}_{\tau e} & y_{\tau\mu} + i\,\tilde{y}_{\tau\mu} & y_{\tau\tau} \end{pmatrix}, \tag{5.3}$$

where $y_{ij} = \dfrac{y'_{ij}}{\sqrt{2}} v$ ($i, j = \mathrm{e}, \mu, \tau$) and the Yukawa coupling y'_{ij} has been defined in Eq. (2.1).

Now, with respect to the Majorana basis $\left(\overline{\nu_{\alpha L}}\ \ \overline{(N_{\alpha R})^c}\right)^T$ and $((\nu_{\alpha L})^c\ \ N_{\alpha R})^T$ one can write down the Majorana mass matrix for both left and right chiral neutrinos using $\mathcal{M_D}$ and $\mathcal{M_R}$ matrices in the following way,

$$M = \begin{pmatrix} 0 & \mathcal{M_D} \\ \mathcal{M_D}^T & \mathcal{M_R} \end{pmatrix}. \tag{5.4}$$

Since M_D and M_R are both 3×3 matrices (for three generations of neutrinos), the resultant matrix M will be of order 6×6 and also it is a complex symmetric matrix which reflects its Majorana nature. Therefore, after diagonalisation of the matrix M, we get three light and three heavy neutrinos, all of which are Majorana fermions. If we use the block diagonalisation technique, we can write the light and heavy neutrino mass matrices in the leading order as,

$$m_\nu \simeq -\mathcal{M_D}\,\mathcal{M_R}^{-1}\mathcal{M_D}^T\,, \tag{5.5}$$

$$m_N \simeq \mathcal{M_R}\,. \tag{5.6}$$

Here M_R is a diagonal matrix and the expression of all the elements of m_ν in terms of the elements of $\mathcal{M_D}$ and $\mathcal{M_R}$ matrices are given in Appendix of Ref. [199]. After diagonalising m_ν matrix we get three light neutrino masses (m_i, $i = 1, 2, 3$), three mixing angles (θ_{12}, θ_{13} and θ_{23}) and one Dirac CP phase δ.

We have used the Jarlskog Invariant $J_{\rm CP}$ [214] to determine the Dirac CP phase δ, which is defined as,

$$J_{\rm CP} = \frac{1}{8}\sin 2\theta_{12}\sin 2\theta_{23}\sin 2\theta_{13}\cos\theta_{13}\sin\delta. \tag{5.7}$$

Moreover, the quantity $J_{\rm CP}$ is related to the elements of the Hermitian matrix $h = m_\nu m_\nu^\dagger$ in the following way,

$$J_{CP} = \frac{\mathrm{Im}(h_{13}h_{23}h_{31})}{\Delta m^2_{21}\,\Delta m^2_{32}\,\Delta m^2_{31}} \tag{5.8}$$

where in the numerator Im(X) represents the imaginary part of X while in the denominator, $\Delta m^2_{ij} = m^2_i - m^2_j$. Once we determine the quantity $J_{\rm CP}$ (from Eq. (5.8)) and the intergenerational mixing angles of neutrinos then one can easily determine the Dirac CP phase using Eq. (5.7).

In the present scenario we have twelve independent parameters coming from the Dirac mass matrix. The RH neutrino mass matrix, in principle, should bring in three additional parameters. However, as we will discuss in details in Section 5.2.2, two of the RH neutrino masses is taken to be nearly degenerate. In particular, the condition of resonant leptogenesis requires that $M_{N_2} - M_{N_1} = \Gamma_1/2$, where Γ_1 is the tree level decay width of N_1 and is seen to be $\sim 10^{-11}$ GeV. Therefore, for all practical purposes we have $M_{N_1} \simeq M_{N_2}$, and the RH neutrino mass matrix only brings in two independent parameters, M_{N_1} and M_{N_3}. Thus, we have fourteen independent parameters which we vary in the following ranges,

$$\begin{array}{ccccc}
1~\text{TeV} & \leq & M_{N_1} & \leq & 3~\text{TeV}\,, \\
M_{N_1} & < & M_{N_3} & \leq & 15~\text{TeV}\,, \\
1 & \leq & \dfrac{\sqrt{2}\,y_{ij}}{v}\times 10^{8} & \leq & 1000 \quad (i,j=e,\mu,\tau, i=j\neq e)\,, \\
1 & \leq & \dfrac{\sqrt{2}\,y_{ee}}{v}\times 10^{10} & \leq & 100\,, \\
1 & \leq & \dfrac{\sqrt{2}\,\tilde{y}_{ij}}{v}\times 10^{8} & \leq & 1000 \quad (i=\tau, j=e,\mu)\,, \\
1 & \leq & \dfrac{\sqrt{2}\,\tilde{y}_{\mu e}}{v}\times 10^{9} & \leq & 1000\,.
\end{array} \tag{5.9}$$

We try to find the allowed parameter space which satisfy the following constraints on three mixing angles (θ_{ij}) and two mass square differences (Δm^2_{ij}), J_{CP} obtained from neutrino oscillation data and the cosmological bound on the sum of three light neutrino masses.

These experimental/observational results are listed below.

- Measured values of three mixing angles in 3σ range [89]:

  $30^\circ < \theta_{12} < 36.51^\circ$, $37.99^\circ < \theta_{23} < 51.71^\circ$ and $7.82^\circ < \theta_{13} < 9.02^\circ$.

- Allowed values of two mass squared differences in 3σ range [89]: $6.93 < \dfrac{\Delta m^2_{21}}{10^{-5}}\,\mathrm{eV}^2 < 7.97$ and $2.37 < \dfrac{\Delta m^2_{31}}{10^{-3}}\,\mathrm{eV}^2 < 2.63$ in 3σ range.

- Above mentioned values of the neutrino oscillation parameters also put an upper bound on the absolute value of J_{CP} from Eq. (5.7), which is $|J_{\mathrm{CP}}| \leq 0.039$.

- Cosmological upper bound on the sum of three light neutrino masses i.e. $\sum_i m_i < 0.23$ eV at 2σ C.L. [20].

While it is possible to obtain both normal hierarchy (NH) ($m_1 < m_2 < m_3$) and inverted hierarchy (IH) ($m_3 < m_1 < m_2$) in this scenario, we show our results only for NH for brevity. Similar results can be obtained for IH.

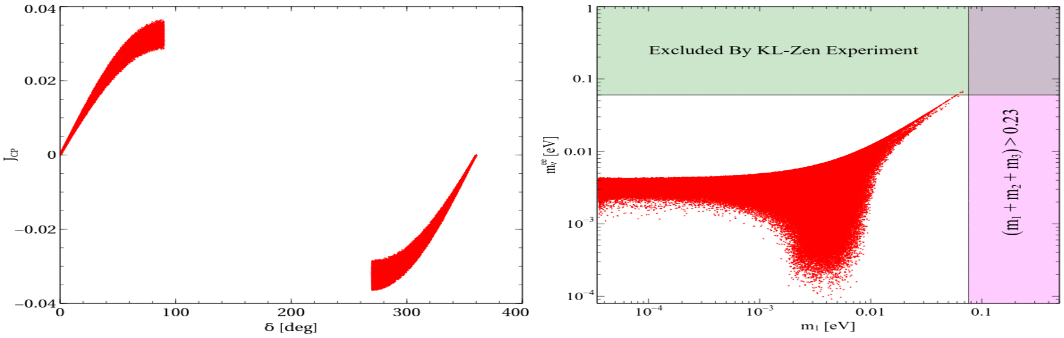

Figure 5.1: **LP:** Variation of J_{cp} with δ. **RP:** Variation of neutrino less double β decay parameter $m_{\beta\beta}$ with m_1

In the LP of Fig. 5.1, we have shown the variation of J_{CP} parameter (as defined in Eq. (5.7)) with the Dirac CP phase δ. From this plot one can easily notice that there are two allowed ranges of Dirac CP phase $0^\circ \leq \delta \leq 90^\circ$ and $270^\circ \leq \delta \leq 360^\circ$ respectively which can reproduce the neutrino oscillation parameters in 3σ range. Since the Jarlskog invariant J_{CP} is proportional to $\sin\delta$ (Eq. 5.7), hence we get both positive and negative values of J_{CP} symmetrically placed in the first and fourth quadrants. However, the absolute values of $J_{\rm CP}$ always lie below 0.039. Also, here we want to mention that from the recent results of T2K [215] experiment, values of δ lying in the fourth quadrant are favourable compared to those in first quadrant. In the RP of Fig. 5.1, we have shown the variation of neutrino less double β decay parameter $m_{\beta\beta}$ with the mass of lightest neutrino m_1. $m_{\beta\beta}$ is an important quantity for the study of neutrino less double β decay as the cross section of this process is proportional to $m_{\beta\beta} = \left|\sum_{i=1}^{3}(U_{\rm PMNS})^2_{ei}\, m_i\right| = (m_\nu)_{ee}$, where $(m_\nu)_{ee}$ (see Appendix of Ref. [199] for details.) is the (1,1) element of light neutrino mass matrix m_ν. The nature of this plot is very to similar to the usual plot in $m_{\beta\beta} - m_1$ plane for the normal hierarchical scenario [216]. In the same plot, we have also shown the current bound on $m_{\beta\beta}$ from KamLand-Zen experiment [217].

5.2.2 Baryogenesis via Resonant Leptogenesis

As we have three RH neutrinos in the present model, in this section we have studied the lepton asymmetry generated from the CP violating out of equilibrium decays of these heavy neutrinos at the early stage of the Universe. The $\rm B-L$ asymmetry thus produced is converted into the baryon asymmetry through sphaleron transitions which violate $\rm B+L$ quantum number while conserving the $\rm B-L$ charge. The sphaleron processes are active between temperatures of $\sim 10^{12}$ GeV to $\sim 10^{2}$ GeV in the early Universe. At high temperatures the sphalerons are in thermal equilibrium and subsequently they freeze-out at around $T \simeq 100-200$ GeV [218, 219], just before electroweak symmetry breaking (EWSB). To produce sufficient lepton asymmetry, which would eventually be converted into the observed baryon asymmetry, one requires RH neutrinos with masses $\gtrsim 10^8 - 10^9$ GeV [218, 220]. This is the well know scenario of the “normal” or “canonical" leptogenesis. However, detection of these very massive RH neutrinos is beyond the reach of LHC and other future colliders. Here we consider the RH neutrinos to be in TeV mass range to allow for their detection at collider experiments. It has been shown that with RH neu-

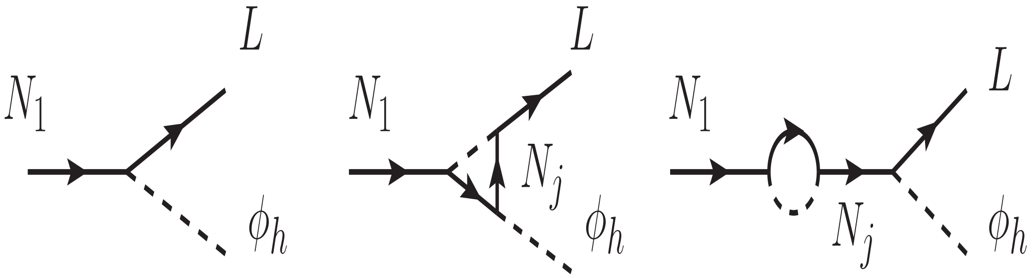

Figure 5.2: Feynmann diagrams for the decay of lightest RH neutrino N_1.

trinos in the TeV mass-scale range, it is possible to generate adequate lepton asymmetry by considering the two lightest RH neutrinos N_1 and N_2 to be almost degenerate. More specifically, we demand that $M_{N_2} - M_{N_1} \simeq \Gamma_1/2$, where Γ_1 [1] is the total decay width of the lightest RH neutrino N_1. This scenario is known as Resonant leptogenesis [219,221–223].

Fig. 5.2 shows the tree level as well as one loop decay diagrams of the lightest RH neutrino N_1. These diagrams are applicable for all the three RH neutrinos. Here L represents the SM lepton which can either be a charged lepton or a left chiral neutrino depending on the nature of the scalar field (charged [2] or neutral) associated in the vertex while N_j denotes the remaining two RH neutrinos, N_2 and N_3 for the case of N_1 decay. In order to produce baryon asymmetry in the Universe we need both C and CP violating interactions, which is one of the three necessary conditions (see Sakharov conditions [13] given in Section 5.1) for baryogenesis. Lepton asymmetry generated from the out of equilibrium decay of RH neutrinos is determined by the CP asymmetry parameter (ε_i), which is given

---

[1] The typical value of Γ_1 is $\sim 10^{-11}$ GeV (see Fig. 5.3) while $M_{N_i} \sim O(\mathrm{TeV})$. Hence we take $M_{N_1} = M_{N_2}$ throughout the work.

[2] Since these processes occurred before EWSB hence we have both charged as well as neutral scalars in the SM.

by (for details see Appendix of Ref. [199]),

$$\varepsilon_2 \simeq -\frac{1}{2}\frac{\mathrm{Im}\left[(\mathcal{M_D}\mathcal{M_D}^{\dagger})^2_{12}\right]}{(\mathcal{M_D}\mathcal{M_D}^{\dagger})_{11}\,(\mathcal{M_D}\mathcal{M_D}^{\dagger})_{22}}\,, \tag{5.10}$$

$$\varepsilon_1 \simeq -\frac{\Gamma_1\Gamma_2}{\Gamma_1^2+\Gamma_2^2}\frac{\mathrm{Im}\left[(\mathcal{M_D}\mathcal{M_D}^{\dagger})^2_{12}\right]}{(\mathcal{M_D}\mathcal{M_D}^{\dagger})_{11}\,(\mathcal{M_D}\mathcal{M_D}^{\dagger})_{22}}\,, \tag{5.11}$$

$$\simeq \frac{2\Gamma_1\Gamma_2}{\Gamma_1^2+\Gamma_2^2}\,\varepsilon_2\,. \tag{5.12}$$

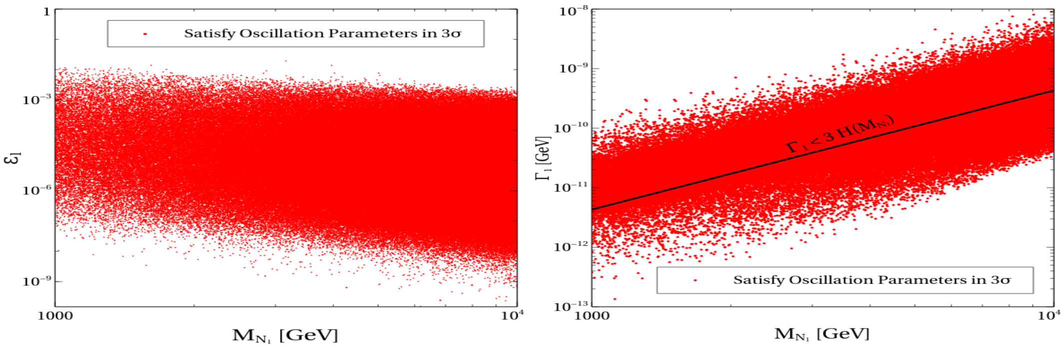

Figure 5.3: **LP:** Variation of CP asymmetry parameter ε_1 with the mass of N_1. **RP:** Variation of total decay width of N_1 with M_{N_1}. Black solid line represents the upper bound of Γ_1 coming from out of equilibrium condition of N_1. All the points in both plots satisfy the neutrino oscillation data in 3σ range.

In the LP of Fig. 5.3, we show the variation of CP asymmetry parameter ε_1, generated from the decay of RH neutrino N_1, with the mass of N_1. Here we see that for the considered ranges of M_{N_1} ($1000\,\mathrm{GeV} \le M_{N_1} \le 10000\,\mathrm{GeV}$) and other relevant Yukawa couplings (see Eq. (5.9)), the CP asymmetry parameter ε_1 can be as large as $\sim 10^{-2}$, which is significantly large compared to ε_1 in the "normal" Leptogenesis case ($\varepsilon_1 \sim 10^{-8}$ for $M_{N_1} \sim 10^{10}$ GeV) [218]. In the RP of Fig. 5.3, we plot the variation of total decay width of N_1 with M_{N_1}. From this plot, one can easily notice that in the present scenario, Γ_1 lies between $\sim 10^{-12}$ GeV to 10^{-9} GeV for the entire considered range of M_{N_1}. All the points in both panels satisfy the neutrino oscillations data in the 3σ range while the black solid line in the RP provides the upper bound on Γ_1, obtained from the out of equilibrium conditions for N_1 i.e. $\Gamma_1 < 3\,H(M_{N_1})$ [218] where H is Hubble parameter at $T = M_{N_1}$.

Next, we calculate the B – L asymmetry generated from the decays as well as the pair annihilations of the RH neutrinos N_1 and N_2. In order to calculate the net B – L asymmetry produced from the interactions of N_1 and N_2 at temperature of the Universe $T \simeq 150$ GeV (freeze-out temperature of sphaleron) we have to solve a set of three coupled Boltzmann equations. The relevant Boltzmann equations [218, 219] for calculating Y_{N_i} and Y_{B-L} are given below,

$$\begin{aligned}
\frac{dY_{N_1}}{dz} &= -\frac{M_{pl}}{1.66\,M_{N_1}^2}\frac{z\,\sqrt{g_\star(z)}}{g_{\rm s}(z)}\langle\Gamma_1\rangle\left(Y_{N_1}-Y_{N_1}^{\rm eq}\right)-\frac{2\pi^2}{45}\frac{M_{pl}\,M_{N_1}}{1.66}\frac{\sqrt{g_\star(z)}}{z^2}\times \\
&\quad \left(\langle\sigma{\rm v}\rangle_{N_1,Z_{BL}}+\langle\sigma{\rm v}\rangle_{N_1,t,H_{\rm BL}}\right)\left(Y_{N_1}^2-(Y_{N_1}^{\rm eq})^2\right), \qquad (5.13)\\
\frac{dY_{N_2}}{dz} &= -\frac{M_{pl}}{1.66\,M_{N_1}^2}\frac{z\,\sqrt{g_\star(z)}}{g_{\rm s}(z)}\langle\Gamma_2\rangle\left(Y_{N_2}-Y_{N_2}^{\rm eq}\right)-\frac{2\pi^2}{45}\frac{M_{pl}\,M_{N_1}}{1.66}\frac{\sqrt{g_\star(z)}}{z^2}\times \\
&\quad \left(\langle\sigma{\rm v}\rangle_{N_2,Z_{BL}}+\langle\sigma{\rm v}\rangle_{N_2,t,H_{\rm BL}}\right)\left(Y_{N_2}^2-(Y_{N_2}^{\rm eq})^2\right), \qquad (5.14)\\
\frac{dY_{B-L}}{dz} &= -\frac{M_{pl}}{1.66\,M_{N_1}^2}\frac{z\,\sqrt{g_\star(z)}}{g_{\rm s}(z)}\left[\sum_{j=1}^{2}\left(\frac{Y_{B-L}}{2}\frac{Y_{N_j^{eq}}}{Y_L^{\rm eq}}+\varepsilon_j\left(Y_{N_j}-Y_{N_j^{eq}}\right)\right)\langle\Gamma_j\rangle\right], \qquad (5.15)
\end{aligned}$$

where $Y_X = \dfrac{n_X}{\rm s}$ denotes the comoving number density of X, with n_X being the actual number density and $z = \dfrac{M_{N_1}}{T}$. Planck mass is denoted by M_{pl}. The quantity $g_\star(z)$ is a function of g_ρ and $g_{\rm s}$, the effective degrees of freedom related to the energy and entropy densities of the Universe respectively and defined in section 1.6. Before EWSB, the variation of $g_s(z)$ with respect to z is negligible compared to the first term within the brackets and hence one can use $\sqrt{g_\star(z)} \simeq \dfrac{g_{\rm s}(z)}{\sqrt{g_\rho(z)}}$. The equilibrium comoving number density of X ($X = N_i, L$), obeying the Maxwell Boltzmann distribution, is given by [30]

$$Y_X^{\rm eq}(z) = \frac{45\,g_X}{4\pi^4}\left(\frac{M_X\,z}{M_{N_1}}\right)^2\frac{{\rm K}_2\left(\frac{M_X}{M_{N_1}}\,z\right)}{g_s\left(\frac{M_{N_1}}{z}\right)}\,, \qquad (5.16)$$

where g_X and M_X are the internal degrees of freedom and mass of X respectively while $g_s\left(\frac{M_{N_1}}{z}\right)$ is the effective degrees of freedom related to the entropy density of the Universe at temperature $T = \dfrac{M_{N_1}}{z}$. ${\rm K}_2\left(\frac{M_X}{M_{N_1}}\,z\right)$ is the modified Bessel function of order 2. The

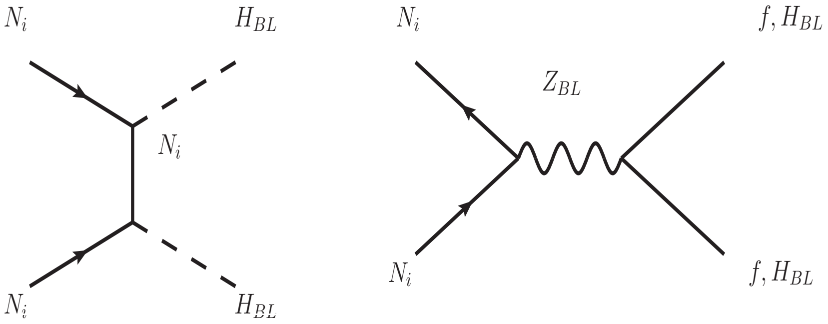

Figure 5.4: Feynman diagrams for the annihilations of RH neutrinos.

relevant Feynman diagrams including both decay and annihilation of N_i are shown in Figs. 5.2 and 5.4. The expression of thermal averaged decay width $\langle \Gamma_i \rangle$, which is related to total decay width Γ_i of N_i is given as

$$\langle \Gamma_i \rangle = \Gamma_i \; \frac{\mathrm{K}_1\left(\frac{M_{N_i}}{M_{N_1}}\, z\right)}{\mathrm{K}_2\left(\frac{M_{N_i}}{M_{N_1}}\, z\right)} . \tag{5.17}$$

The thermally average annihilation cross sections $\langle \sigma \mathrm{v} \rangle_{N_i, Z_{BL}}$ and $\langle \sigma \mathrm{v} \rangle_{N_i, Z_{BL}}$, appearing in Boltzmann equations (Eqs. (5.13) and (5.14)) for the processes shown in Fig. 5.4, can be defined in a generic form,

$$\langle \sigma \mathrm{v} \rangle_{N_i, x} = \frac{z}{16\, M_{N_i}^4\, M_{N_1}\, g_{N_i}^2\, \mathrm{K}_2\left(\frac{M_{N_i}}{M_{N_1}}\, z\right)^2} \int_{4\, M_{N_i}^2}^{\infty} \hat{\sigma}_{N_i, x}\, \mathrm{K}_1\left(\frac{\sqrt{s}}{M_{N_1}}\, z\right) \sqrt{s}\, ds \, , \tag{5.18}$$

where the $\hat{\sigma}_{N_i, x}$ is related to the actual annihilation cross section $\sigma_{N_i, x}$ by the following relation

$$\hat{\sigma}_{N_i, x} = 2\, g_{N_i}^2 \left(s - 4\, M_{N_1}^2\right) \sigma_{N_i, x} \, , \tag{5.19}$$

where $g_{N_i} = 2$ is the internal degrees of freedom of RH neutrino N_i. The expression of

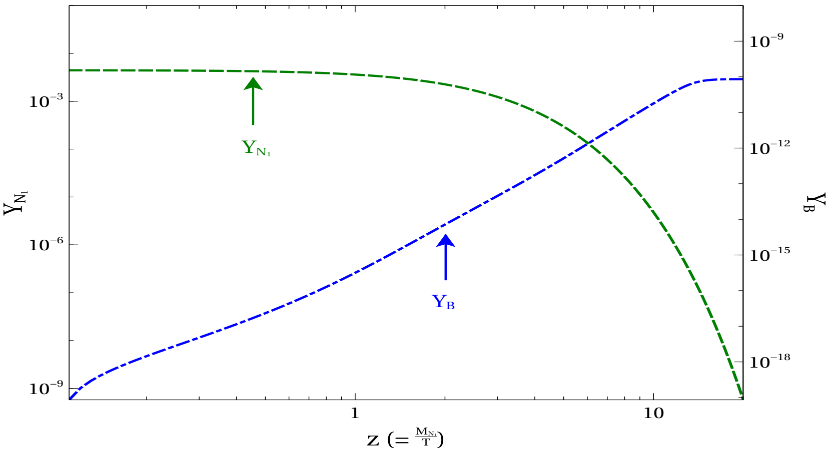

Figure 5.5: Variation of Y_{N_1} (Green dash line) and Y_{B-L} (blue dash-dot line) with z where other parameters have kept fixed at $M_{N_1} = 2000$ GeV, $\alpha_{BL}\left(= \frac{g_{BL}^2}{4\pi}\right) = 3\times10^{-4}$, $M_{Z_{BL}} = 3000$ GeV.

$\hat{\sigma}_{N_i,Z_{BL}}$ and $\hat{\sigma}_{N_i,t,H_{BL}}$ for the present model is given in Ref. [219].

To calculate the $\mathrm{B-L}$ asymmetry at around $T \simeq 150$ GeV, we have to numerically solve the set of three coupled Boltzmann equations (Eqs. (5.13)-(5.15)) using Eq. (1.82) and Eq. (5.19). However, we can reduce the two flavour analysis (when both N_2 and N_1 are separately considered) into one flavour case by considering the parameters of $\mathcal{M_D}$ matrix in such a way so that the decay widths of N_1 and N_2 are of the same order i.e. $\Gamma_1 \sim \Gamma_2$. Hence, the CP asymmetry generated from the decays of both N_1 and N_2 are almost identical ($\varepsilon_1 \sim \varepsilon_2$, see Eq. (5.10)-(5.11)). In this case, the net $\mathrm{B-L}$ asymmetry is equal to twice of that is being generated from the CP violating interactions of the lightest RH neutrino N_1 [219]. Hence instead of solving three coupled differential equations we now only need to solve Eqs. (5.13) and (5.15). The results we have found by numerically solving Eqs. (5.13) and (5.15) are plotted in Fig. 5.5. In this plot, we have shown the variation of Y_{N_1} and Y_{B-L} with z for $M_{N_1} = 2000$ GeV, $\alpha_{BL} = 3\times10^{-4}$ and $M_{Z_{BL}} = 3000$ GeV [3]. While solving the coupled Boltzmann equations we have considered the following initial conditions: $Y_{N_1}(T^B_{\rm in}) = Y^{\rm eq}_{N_1}$ and $Y_{B-L} = 0$ with $T^B_{\rm in}$ is the initial temperature which we have taken as 20 TeV. Thereafter, the evolutions of Y_{N_1} and Y_{B-L} are governed by

---

[3] The considered value of $M_{Z_{BL}}$ and the corresponding gauge coupling g_{BL} satisfy the upper bounds obtained from LEP [111, 112] and more recently from LHC [104] as well.

their respective Boltzmann equations. From Fig. 5.5, one can notice that initially upto $z \sim 1$ ($T \sim M_{N_1}$), the comoving number density of Y_{N_1} does not change much as a result of the $\mathrm{B-L}$ asymmetry produced from the decay, and the annihilation of N_1 is also less. However, as the temperature of the Universe drops below the mass of M_{N_1}, there is a rapid change in the number density of N_1, which changes around six orders of magnitude between $z = 1$ and $z = 20$. Consequently, the large change in Y_{N_1} significantly enhances the $\mathrm{B-L}$ asymmetry Y_{B-L} and finally Y_{B-L} saturates to the desired value around $\sim 10^{-10}$, when there are practically no N_1 left to produce any further $\mathrm{B-L}$ asymmetry.

The produced $B-L$ asymmetry is converted to net baryon asymmetry of the Universe through the sphaleron transitions while they are in equilibrium with the thermal bath. The quantities Y_{B-L} and Y_B are related by the following equation [206]

$$Y_B = -2 \times \frac{28}{79} Y_{B-L}(T_\mathrm{f}) , \tag{5.20}$$

where $T_\mathrm{f} \simeq 150$ GeV is the temperature of the Universe upto which the sphaleron process, converting $B-L$ asymmetry to a net B asymmetry, maintains its thermal equilibrium. The extra factor of two in the above equation is due to the equal contribution to Y_{B-L} arising from the CP violating interactions of N_2 as well. Finally, we calculate the net baryon asymmetry Y_B for three different masses of RH neutrino N_1 and CP asymmetry parameter ε_1. The results are listed in Table 5.1. In all three cases, the final baryon asymmetry lies within the experimentally observed range for Y_B i.e. $(8.239-9.375)\times 10^{-11}$ at 95% C.L. [12].

M_{N_1} [GeV]	ε_1	$Y_B = \frac{n_B}{S}$
1600	4.4×10^{-4}	8.7121×10^{-11}
1800	2.25×10^{-4}	8.7533×10^{-11}
2000	1.8×10^{-4}	8.5969×10^{-11}

Table 5.1: Baryon asymmetry of the Universe generated for three different values of M_{N_1} and ε_1.

5.2.3 FIMP Dark Matter

In the present section we explore the FIMP scenario for dark matter in the Universe, by considering the complex scalar field ϕ_{DM} as a corresponding candidate. As described in the Section 2.2, the residual $\mathbb{Z}_2$ symmetry of ϕ_{DM} makes the scalar field absolutely stable over the cosmological time scale and hence can play the role of a dark matter candidate. Since ϕ_{DM} has a nonzero $\mathrm{B-L}$ charge n_{BL}, therefore DM talks to the SM as well as the BSM particles through the exchange of extra neutral gauge boson Z_{BL} and two Higgs bosons present in the model, one is the SM-like Higgs h_1 while other one is the BSM Higgs h_2. The corresponding coupling strengths, in terms of gauge coupling g_{BL}, $\mathrm{B-L}$ charge n_{BL}, mixing angle α and λs, are listed in Table 5.2. As the FIMP never enters into thermal equilibrium, these couplings have to be extremely feeble in order to make the corresponding interactions nonthermal. For the case of $\phi_{DM}\phi^{\dagger}_{DM}Z_{BL\mu}$ coupling, we will make the $\mathrm{B-L}$ charge of ϕ_{DM} extremely tiny so that this interaction enters into the nonthermal regime. In principle, one can also choose the gauge coupling g_{BL} to be very small, however in the present case we will keep the values of g_{BL} and $M_{Z_{BL}}$ fixed at 0.07 and 3 TeV respectively as these values reproduce the observed baryon asymmetry of the Universe (see Section 5.2.2). Also, there is another advantage of choosing tiny n_{BL} as this will make only ϕ_{DM} out of equilibrium while keeping Z_{BL} in equilibrium with the thermal bath. Moreover, due to the nonthermal nature, the initial number density of FIMP is assumed to be negligible and as the temperature of the Universe begins to fall down, they start to be produced dominantly from the decays and annihilation of other heavy particles.

In the present scenario, we have considered all the particles except ϕ_{DM} to be in thermal equilibrium. Before EWSB, all the SM particles are massless[4]. In this regime, production of ϕ_{DM} occurs mainly from the decay and/or annihilation of BSM particles namely Z_{BL}, H_{BL}, and N_i. Also, before EWSB the annihilation of all four degrees of free-

---

[4] Although the SM particles acquire thermal masses before EWSB, we have neglected these masses, as in this regime this approximation will not affect the DM production processes significantly.

Vertex $a\,b\,c$	Vertex Factor g_{abc}
$\phi_{DM}\,\phi^{\dagger}_{DM}\,Z_{BL\mu}$	$g_{BL}\,n_{BL}(p_2-p_1)^{\mu}$
$\phi_{DM}\,\phi^{\dagger}_{DM}\,h_1$	$-(\lambda_{Dh}v\cos\alpha+\lambda_{DH}v_{BL}\sin\alpha)$
$\phi_{DM}\,\phi^{\dagger}_{DM}\,h_2$	$(\lambda_{Dh}v\sin\alpha-\lambda_{DH}v_{BL}\cos\alpha)$

Table 5.2: Couplings of FIMP (ϕ_{DM}) with Z_{BL}, h_1 and h_2.

dom of SM Higgs doublet ϕ_h can produce ϕ_{DM}. Feynman diagrams for all the production processes of ϕ_{DM} before EWSB are shown in Fig. 5.6.

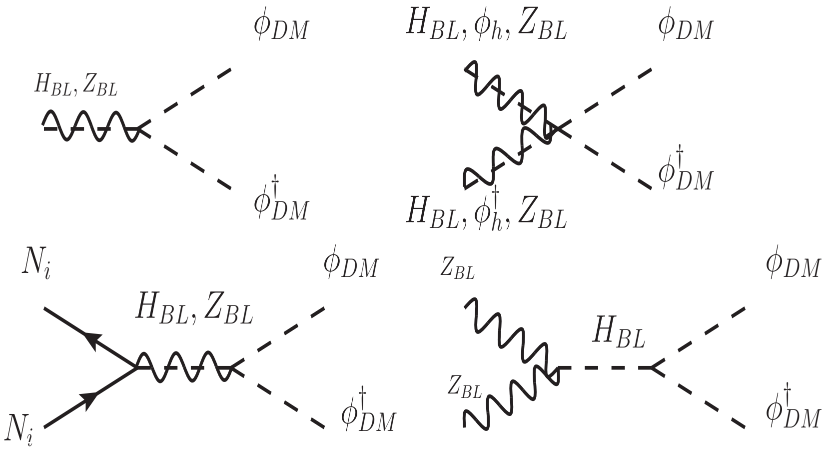

Figure 5.6: Feynman diagrams for the all possible production modes of ϕ_{DM} before EWSB.

After EWSB, all the SM particles become massive and consequently besides the BSM particles, ϕ_{DM} can now also be produced from the decay and/or annihilation of the SM particles as well. The corresponding Feynman diagrams are shown in Fig. 5.7. In generating the vertex factors for different vertices to compute the Feynman diagrams as listed in Fig. 5.6 and Fig. 5.7 we have used the LanHEP [120] package.

In order to compute the relic density of a species at the present epoch, one needs to study the evolution of the number density of the corresponding species with respect to the temperature of the Universe. The evolution of the number density of ϕ_{DM} is governed by the Boltzmann equation containing all possible number changing interactions of ϕ_{DM}.

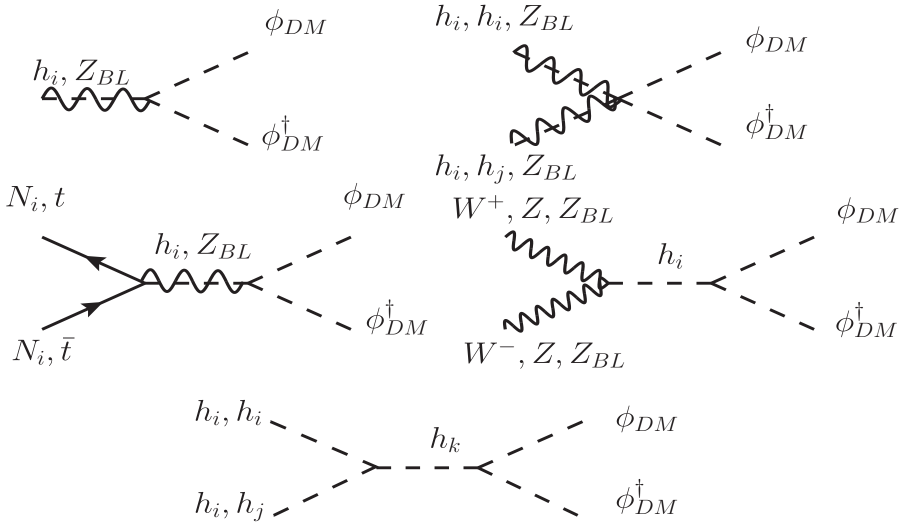

Figure 5.7: Production processes of ϕ_{DM} from both SM as well as BSM particles after EWSB.

The Boltzmann equation of ϕ_{DM} in terms of its comoving number density $Y_{\phi_{DM}} = \frac{n_{\phi_{DM}}}{\mathrm{s}}$, where n and s are actual number density and entropy density of the Universe is given by

$$\begin{aligned}\frac{dY_{\phi_{DM}}}{dz} &= \frac{2M_{pl}}{1.66M_{h_1}^2}\frac{z\sqrt{g_\star(z)}}{g_{\mathrm{s}}(z)}\left[\sum_{X=Z_{BL},h_1,h_2}\langle\Gamma_{X\to\phi_{DM}\phi_{DM}^\dagger}\rangle(Y_X^{\mathrm{eq}}-Y_{\phi_{DM}})\right]\\ &+\frac{4\pi^2}{45}\frac{M_{pl}M_{h_1}}{1.66}\frac{\sqrt{g_\star(z)}}{z^2}\left[\sum_p\langle\sigma\mathrm{v}_{p\bar{p}\to\phi_{DM}\phi_{DM}^\dagger}\rangle(Y_p^{\mathrm{eq}\,2}-Y_{\phi_{DM}}^2)\right.\\ &\left.+\langle\sigma\mathrm{v}_{h_1h_2\to\phi_{DM}\phi_{DM}^\dagger}\rangle(Y_{h_1}^{\mathrm{eq}}Y_{h_2}^{\mathrm{eq}}-Y_{\phi_{DM}}^2)\right],\end{aligned}\tag{5.21}$$

where $z = \frac{M_{h_1}}{T}$, while $\sqrt{g_\star(z)}$, $g_{\mathrm{s}}(z)$ and M_{pl} are same as those in Eqs. (5.13)–(5.15) of Section 5.2.2. In the above equation (Eq. (5.21)), first term represents the contribution coming from the decays of Z_{BL}, h_1 and h_2. The expressions of equilibrium number density $Y_X^{\mathrm{eq}}(z)$ (X is any SM or BSM particle expect ϕ_{DM}) and the thermal averaged decay width $\langle\Gamma_{X\to\phi_{DM}\phi_{DM}}\rangle$ can be obtained from Eqs. (5.16) and (5.17), respectively by only replacing M_{N_1} with M_X, the mass of decaying mother particle. As mentioned above, before EWSB, the summation in the first terms is over h_2 and Z_{BL} only, as there will be no contribution from the SM Higgs decay as such trilinear vertex ($h_1\phi_{DM}\phi_{DM}^\dagger$) is absent before EWSB and after EWSB there will be contributions to the relic density of ϕ_{DM} from all there decaying particles. The dark matter production from the pair annihilations of SM and BSM particles are described by the second term of the Boltzmann equation. Here, summation over p includes all possible pair annihilation channels namely W^+W^-, ZZ, $Z_{BL}Z_{BL}$, N_iN_i, h_ih_i, $t\bar{t}$. However before EWSB, pair annihilations of the BSM particles and SM Higgs doublet ϕ_h contribute to the production processes (i.e. $p = Z_{BL}, N_i, H_{BL}, \phi_h$, see Fig. 5.6). The third term, which is present only after EWSB, is another the production mode of ϕ_{DM} from the annihilation of h_1 and h_2. The expressions of all the relevant cross sections and decay widths for computing the DM number density are given in Appendix of Ref. [199]. The most general form of thermally averaged annihilation cross section for two different annihilating particles of mass M_A and M_B is given by Eq. (1.76).

Finally, as defined in Eq. (1.85) the relic density of ϕ_{DM} is obtained using the following relation between Ωh^2 and $Y_{\phi_{DM}}(0)$ [224, 225],

$$\Omega h^2 = 2.755 \times 10^8 \left(\frac{M_{DM}}{\text{GeV}}\right) Y_{\phi_{DM}}(0)\,, \tag{5.22}$$

where $Y_{\phi_{DM}}(0)$ is the value of comoving number density at the present epoch, which can be obtained by solving the Boltzmann equation.

The contribution to dark matter production processes from decays as well as annihilations of various SM and BSM particles depend on the mass of ϕ_{DM}. Accordingly, We have divided our rest of the dark matter analysis into four different regions depending on M_{DM} and the dominant production modes of ϕ_{DM}.

$M_{DM} < \frac{M_{h_1}}{2}, \frac{M_{h_2}}{2}, \frac{M_{Z_{BL}}}{2}$, SM and BSM particles decay dominated region.

In this case DM is dominantly produced from the decays of all three particles namely h_1, h_2 and Z_{BL}. Therefore, in this case $\mathrm{U(1)_{B-L}}$ part of the present model directly enters into the dark matter production. Moreover in this mass range, ϕ_{DM} can also be produced from the annihilations of SM and BSM particles, however, we find that their contributions are not as significant as those from the decays of h_1, h_2 and Z_{BL}. In the left panel (LP) and right panel (RP) of Fig. 5.8, we have shown the variation of DM relic density with z. In LP, we have shown the dependence of DM relic density with the initial temperature T_{in}. Initial temperature (T_{in}) is the temperature upto which we have assumed that the number density of DM is zero and its production processes start thereafter. We can clearly see from the figure that as long as the initial temperature is above the mass of BSM Higgs ($M_{h_2} \sim 500$ GeV), the final relic density does not depend on the choice of the initial temperature and reproduces the observed DM relic density of the Universe for the chosen values of model parameters as written in the caption of Fig. 5.8. If we reduce the initial

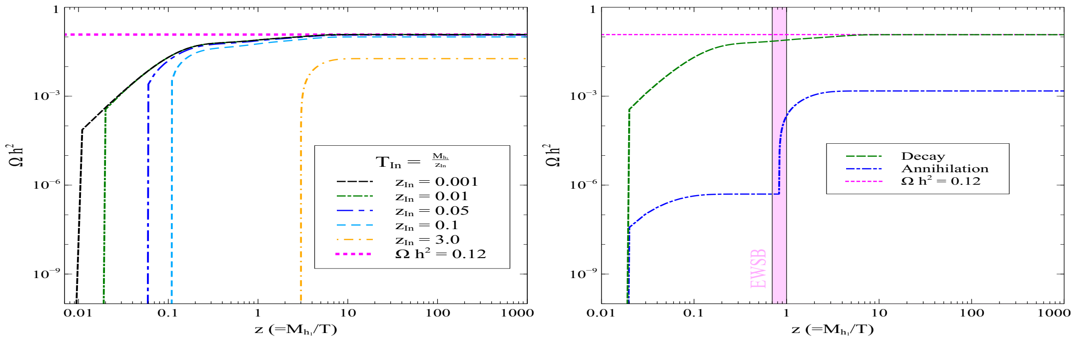

Figure 5.8: Left (Right) panel: Variation of relic density Ωh^2 with z for different initial temperature (Contributions to Ωh^2 coming from decay and annihilation), where other parameters are fixed at $\lambda_{Dh} = 8.75 \times 10^{-13}$, $\lambda_{DH} = 5.88 \times 10^{-14}$, $n_{BL} = 1.33 \times 10^{-10}$, M_{DM} = 50 GeV, $M_{Z_{BL}} = 3000$ GeV, $g_{BL} = 0.07$, $M_{h_1} = 125.5$ GeV and $M_{h_2} = 500$ GeV, $\alpha = 10^{-4}$.

temperature from 500 GeV, i.e. for $T_{in} = 251$ GeV, the decay contribution of BSM Higgs h_2 becomes less since corresponding the number density of h_2 for $T_{in} < M_{h_2}$ is Boltzmann suppressed (exponentially suppressed), which is clearly shown by the blue dashed-dotted line. Hence, if we reduce the initial temperature (T_{in}) further i.e. $T_{in} < M_{h_2}, M_{h_1} \sim 42$ GeV then the number densities of both SM-like Higgs h_1 as well as BSM Higgs h_2 become Boltzmann suppressed and hence, less amount of DM production will take place which is evident from the LP of Fig. 5.8 (represented by the yellow dashed-dot line). On the other hand in the RP of Fig. 5.8, we have shown the contributions to DM relic density coming from decay and annihilation. Magenta dotted horizontal line represents the present day observed DM relic density of the Universe. Green dashed line represents the total decay

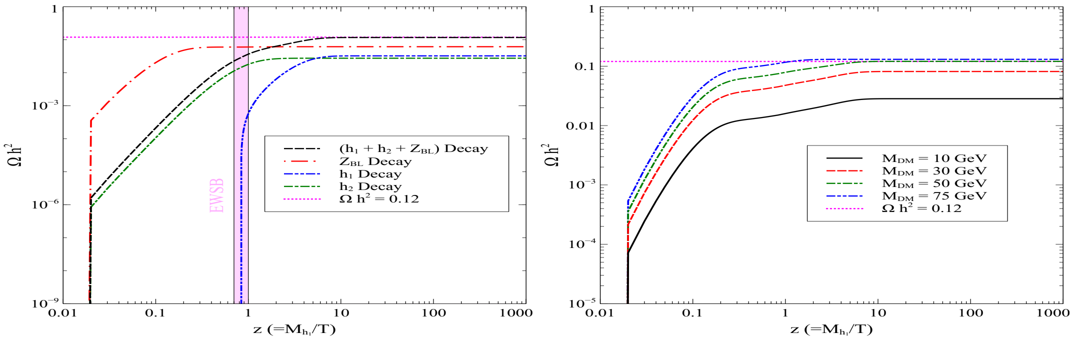

Figure 5.9: Left panel: Showing variation of decay contributions of both the Higgs bosons to Ωh^2 separately with z. Right panel: Variation of relic density Ωh^2 with z for different values of DM mass M_{DM}. Other parameters value have been kept fixed at $\lambda_{Dh} = 8.75 \times 10^{-13}$, $\lambda_{DH} = 5.88 \times 10^{-14}$, $n_{BL} = 1.33 \times 10^{-10}$, $M_{DM} = 50$ GeV (for LP), $M_{Z_{BL}} = 3000$ GeV, $g_{BL} = 0.07$, $M_{h_1} = 125.5$ GeV and $M_{h_2} = 500$ GeV, $\alpha = 10^{-4}$.

contribution arising from the decays of both h_1, h_2 and Z_{BL} whereas the net annihilation contribution coming from the annihilation of all the SM as well as BSM particles has been shown by the blue dashed-dotted line. There is a sudden rise in the annihilation contribution which occurs around the Universe temperature $T \sim 154$ GeV (i.e. EWSB temperature). After the EWSB temperature, all the SM particles become massive and hence the sudden rise in the annihilation part because of the appearance of the following annihilation channels W^+W^-, ZZ, h_1h_1, h_1h_2. The plot clearly implies that the lion share of the contribution comes from the decay of both Higgses h_1, h_2 and Z_{BL}, while for the considered values of model parameters the annihilation contribution is subdominant. Moreover, in this case we cannot enhance the annihilation contribution by increasing parameters λ_{Dh}, λ_{DH} and n_{BL} as these changes will result in the over production of dark matter from the decays of h_1, h_2 and Z_{BL}.

In the LP of Fig. 5.9, we have shown how the individual decay contribution from each scalar varies with z. Here we consider the following values of the scalar quartic couplings $\lambda_{Dh} = 8.75 \times 10^{-13}$ and $\lambda_{DH} = 5.88 \times 10^{-14}$ and the $(B-L)$ charge of ϕ_{DM} $n_{BL} = 1.33 \times 10^{-10}$. From this plot we can see that before EWSB SM-like Higgs h_1 cannot decay to a pair of ϕ_{DM} as in this epoch it has no coupling with the latter. In this regime the decay of BSM Higgs h_2 and Z_{BL} contribute, while after EWSB even the SM-like Higgs starts contributing to the DM production and hence we get an increased relic density (right side of EWSB). Its worth mentioning here that while generating the plot in the LP of Fig. 5.9, we have taken the scalar quartic couplings λ_{Dh}, λ_{DH} and $\mathrm{B-L}$ charge of ϕ_{DM} n_{BL} of different strengths such that the contributions of both the scalars (h_1 and h_2) and the extra gauge boson to the DM relic density are of equal order. This is because for the case of BSM Higgs h_2 decay the coupling λ_{DH} multiplied by the $\mathrm{B-L}$ symmetry breaking VEV v_{BL} is relevant, while for the decay of the SM-like Higgs h_1, the product of the parameter λ_{Dh} and the EWSB VEV v is relevant and the contribution from the decay of Z_{BL}, DM charge n_{BL} is relevant. Since in the present case $v_{BL} > v$, the magnitudes of the two quartic couplings λ_{Dh} and λ_{DH} are of different order (see Table 5.2). On the other hand, in the RP of Fig. 5.9, we have shown the variation of the relic density with z for four different values of the DM mass M_{DM}. From Eq. (5.22), one can see that the DM relic density is directly proportional to the mass M_{DM} and as a result when other relevant couplings remain unchanged Ωh^2 increases with M_{DM}. This feature is clearly visible in the RP for the cases with M_{DM} = 10 GeV (black solid line), M_{DM} = 30 GeV (red dashed line) and 50 GeV (green dashed line) respectively. However for M_{DM} = 75 GeV (blue dashed dot line) Ωh^2 does not rise equally because for this value of DM mass the decay of h_1 to a pair of ϕ_{DM} and $\phi^{\dagger}_{DM}$ becomes kinematically forbidden and hence, there is no equal increment in this case.

In LP and RP of Fig. 5.10, we have shown how the relic density varies with z for different values of scalar quartic couplings λ_{Dh} and λ_{DH}, respectively. In each panel, one can easily notice that there exists a kink around the EWSB region. However in the LP, the kink occurs for a higher value of λ_{Dh} while in the RP, the situation is just opposite. We have already seen in the LP of Fig. 5.9 that before EWSB only h_2 decay is contributing to DM relic density and at the EWSB region SM-like Higgs h_1 also starts contributing. A kink will always appear in the relic density curve when contribution of the SM-like Higgs boson h_1 to Ωh^2 is larger compared to that of the BSM Higgs h_2 and extra gauge boson Z_{BL} i.e. $\Gamma_{h_1\to\phi_{DM}\phi^{\dagger}_{DM}} > \Gamma_{h_2\to\phi_{DM}\phi^{\dagger}_{DM}}, \Gamma_{Z_{BL}\to\phi_{DM}\phi^{\dagger}_{DM}}$. The values of scalar quartic

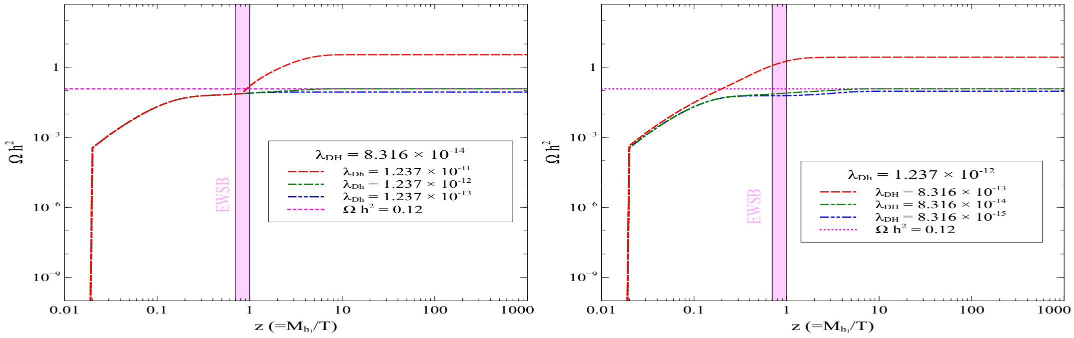

Figure 5.10: Left (Right) panel: Variation of relic density Ωh^2 with z for three different values of λ_{Dh} (λ_{DH}), where other parameters are fixed at $\lambda_{DH} = 5.88 \times 10^{-14}$ ($\lambda_{Dh} = 8.75 \times 10^{-13}$), $n_{BL} = 1.33 \times 10^{-10}$, M_{DM} = 50 GeV, $M_{Z_{BL}}$ = 3000 GeV, $g_{BL} = 0.07$, M_{h_1} = 125.5 GeV and M_{h_2} = 500 GeV, $\alpha = 10^{-4}$.

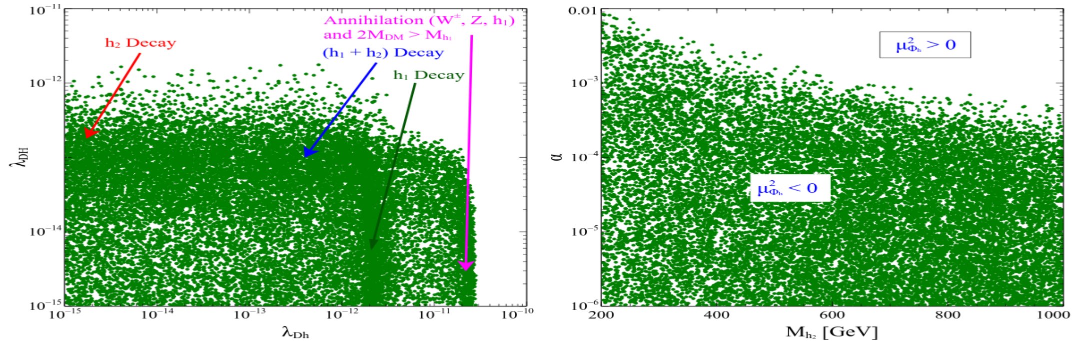

Figure 5.11: Left (Right) panel: Allowed region in the $\lambda_{Dh} - \lambda_{DH}$ ($M_{h_2} - \alpha$) plane where other parameters are fixed at $M_{Z_{BL}}$ = 3000 GeV, $g_{BL} = 0.07$, $n_{BL} = 1.33 \times 10^{-10}$, M_{h_1} = 125.5.

couplings λ_{Dh} and λ_{DH} in the LP of Fig. 5.9 are such that $\Gamma_{h_2 \to \phi_{DM}\phi^{\dagger}_{DM}}$ and $\Gamma_{Z_{BL} \to \phi_{DM}\phi^{\dagger}_{DM}}$ always remain large compared to $\Gamma_{h_1 \to \phi_{DM}\phi_{DM}}$ and hence no kink is observed in the total relic density curve. However, in the present figure (in the left panel of Fig. 5.10) we do have kinks around the EWSB region, because in the LP with $\lambda_{DH} = 8.316 \times 10^{-14}$ and $n_{BL} = 1.33 \times 10^{-10}$, $\Gamma_{h_1 \to \phi_{DM}\phi^{\dagger}_{DM}} > \Gamma_{h_2 \to \phi_{DM}\phi^{\dagger}_{DM}}, \Gamma_{Z_{BL} \to \phi_{DM}\phi^{\dagger}_{DM}}$ condition is satisfied only for the case with larger value of $\lambda_{Dh} = 1.237 \times 10^{-11}$ ($\lambda_{Dh} >> \lambda_{DH}$) while in the RP with a fixed value of $\lambda_{Dh} = 1.237 \times 10^{-12}$, the above condition is not maintained because Z_{BL} decay channel dominates.

In the LP of Fig. 5.11, we have shown the allowed region in the coupling plane ($\lambda_{Dh} - \lambda_{DH}$) which reproduces the observed DM relic density ($0.1172 \leq \Omega h^2 \leq 0.1226$). In this figure, we have clearly indicated the dominant DM production processes when

M_{DM} varies between 10 GeV to 100 GeV i.e. DM production from the decays of h_1, h_2 or both or entirely from the annihilations of SM particles like $W^{\pm}$, Z, h_1 etc. The parameters which are related to the Z_{BL} decay (g_{BL}, n_{BL}) have been kept fixed at 0.07 and 1.33×10^{-10} respectively, so at every time an equal amount of Z_{BL} decay contribution remains present. As illustrated in the figure, when the parameter λ_{Dh} is small compared to the other parameter λ_{DH} then among the two scalars it is the BSM Higgs h_2 which is mainly contributing to the DM production while for the opposite case, the production of ϕ_{DM} becomes h_1 dominated and in between both the scalars contribute equally. Apart from that, if the mass of ϕ_{DM} is greater than the half of the SM-like Higgs mass (i.e. $M_{DM} > \frac{M_{h_1}}{2}$) then DM production from h_1 decay becomes kinematically forbidden. In this case, however, the production from the decays of h_2 and Z_{BL} are still possible. Now, the deficit in DM production can be compensated by the production from self annihilation of SM particles like h_1, $W^{\pm}$ and Z and for this we need to increase the parameter λ_{Dh}. Moreover, by increasing λ_{Dh} (decreasing λ_{DH} simultaneously) we can arrive a situation where DM production is entirely dominated by the annihilations of SM particles and this situation has been indicated by a pink coloured arrow in the LP of Fig. 5.11. On the other hand, in the RP of Fig. 5.11 we have presented the allowed region in $M_{h_2} - \alpha$ plane which satisfies the relic density bound. From this figure one can see that with the increase of M_{h_2}, the allowed values of mixing angle α decrease. The reason behind this decrement is related to the vacuum stability conditions as given in the Eq. (2.13). The region satisfying both the relic density bound as well as the vacuum stability conditions is shown by the green dots while in the other part of $M_{h_2} - \alpha$ plane the quantity $\mu^2_{\phi_h}$ becomes positive which is undesirable in the context of the present model (see Eq. (2.13)).

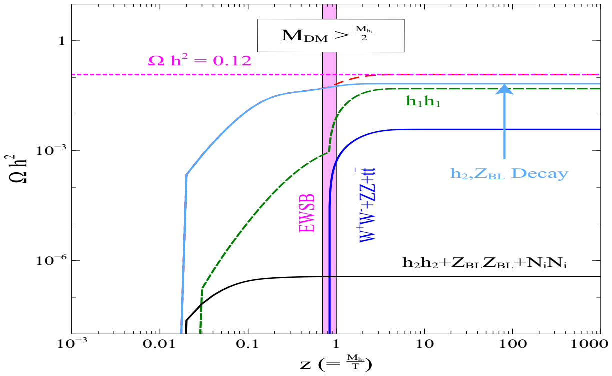

Figure 5.12: Variation of DM relic density Ωh^2 with z. Other parameters value have been kept fixed at $\lambda_{Dh} = 6.364 \times 10^{-12}$, $\lambda_{DH} = 7.637 \times 10^{-14}$, $n_{BL} = 8.80 \times 10^{-11}$, $M_{DM} = 70$ GeV, $M_{Z_{BL}} = 3000$ GeV, $g_{BL} = 0.07$, $M_{h_1} = 125.5$ GeV, $M_{h_2} = 500$ GeV, $\alpha = 10^{-5}$, $M_{N_2} \approx M_{N_1} = 2000$ GeV and $M_{N_3} = 2500$ GeV.

$\frac{M_{h_1}}{2} < M_{\phi_{DM}} < \frac{M_{h_2}}{2}, \frac{M_{Z_{BL}}}{2}$**, BSM particles decay and SM particles annihilation dominated region.**

Clearly in this mass region, DM production from the decay of SM-like Higgs h_1 is kinematically forbidden and hence DM has been produced from the decays of h_2, Z_{BL} only. However, unlike the previous case, here we find significant contribution to DM relic density arising from the self annihilation of the SM particles namely, h_1, $W^\pm$, Z and t. On the other hand, the annihilations of BSM particles like Z_{BL}, h_2 and N_i have negligible effect on DM production processes. In Fig. 5.12, we have shown the variation of DM relic density with z for $\frac{M_{h_1}}{2} < M_{\phi_{DM}} < \frac{M_{h_2}}{2}, \frac{M_{Z_{BL}}}{2}$. Since now the decay of the h_1 to $\phi_{DM}{\phi_{DM}}^\dagger$ is kinematically forbidden, hence we can increase the parameter λ_{Dh} safely and this will not overproduce DM in the Universe. Due to this moderately large value of λ_{Dh}, the annihilation channels become important. From Fig. 5.12 it is clearly seen that in this case the annihilation channel $h_1h_1 \to \phi_{DM}\phi^\dagger_{DM}$ (Green dashed line) contributes significantly to the DM production. Therefore in the present case, production of DM has been controlled by the decays of h_2, Z_{BL} and the self annihilations of the SM particles and thus directly relates to the $\mathrm{U(1)_{B-L}}$ sector of this model.

$\frac{M_{h_1}}{2}, \frac{M_{h_2}}{2} < M_{\phi_{DM}} < \frac{M_{Z_{BL}}}{2}$**, BSM particles decay and annihilation dominated region.**

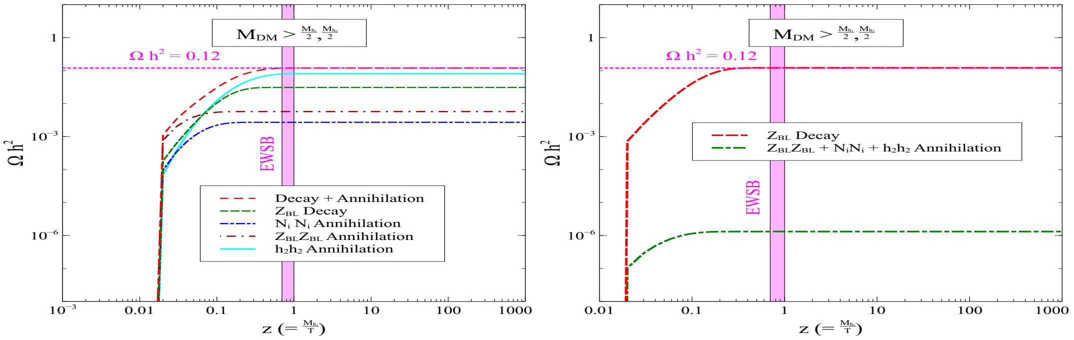

Figure 5.13: Left (Right) panel: Variation of DM relic density Ωh^2 with z. Other parameters value have been kept fixed at $\lambda_{Dh} = 2.574 \times 10^{-12}$ (7.212×10^{-14}), $\lambda_{DH} = 3.035 \times 10^{-11}$ (8.316×10^{-14}), $n_{BL} = 3.4 \times 10^{-11}$ (6.2×10^{-11}), $M_{DM} = 450$ GeV (600 GeV), $M_{Z_{BL}} = 3000$ GeV, $g_{BL} = 0.07$, $M_{h_1} = 125.5$ GeV, $M_{h_2} = 500$ GeV, $\alpha = 10^{-5}$, $M_{N_2} \approx M_{N_1} = 2000$ GeV and $M_{N_3} = 2500$ GeV.

In this regime of the DM mass, the only surviving decay mode is the decay of $\mathrm{B-L}$ gauge boson Z_{BL} to a pair of ϕ_{DM}. Apart from that, depending on the choice of mass of ϕ_{DM} a significant fraction of DM has been produced from the self annihilation of either BSM Higgs h_2. In other word, we can say that in this region the production of DM is BSM particles dominated. In LP of Fig. 5.13 we show the relative contribution of dominant production modes of DM to Ωh^2 for a chosen value of $M_{DM} = 450$ GeV. From this plot one can easily notice that in the case when $M_{DM} < M_{h_2}$, the almost entire fraction of DM is produced from the decay of Z_{BL} (green dashed line) and self annihilation of BSM Higgs h_2 (solid turquoise line). This is because, as in this case the production of ϕ_{DM} from h_2 decay is kinematically forbidden hence one can increase the parameter λ_{DH} so that the annihilation channel $h_2 h_2 \rightarrow \phi_{DM} \phi_{DM}^{\dagger}$, which is mainly proportional to λ_{DH}^2 (due to four point interaction) becomes significant.

On the other hand, in the RP we have considered a situation where almost the entire DM has been produced from the decay of $\mathrm{B-L}$ gauge boson. For this, we have chosen $M_{DM} > M_{h_2}$ and a larger value of $n_{BL} = 6.2 \times 10^{-11}$. Similar to the previous case (i.e. $M_{DM} < M_{h_2}$) here also, the production of ϕ_{DM} from h_2 decay still remains forbidden.

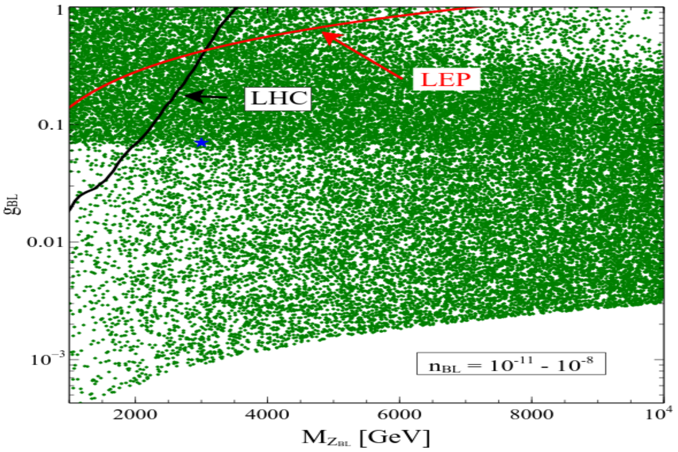

Figure 5.14: Allowed region in $M_{Z_{BL}} - g_{BL}$ plane which produces observed DM relic density. Solid lines (black and red) are the upper limits on the gauge coupling g_{BL} for a particular mass of Z_{BL} obtained from LHC and LEP respectively. Other relevant parameters used in this plot are $250\,\text{GeV} \le M_{DM} \le 5000\,\text{GeV}$, $\lambda_{Dh} = 7.212 \times 10^{-14}$, $\lambda_{DH} = 8.316 \times 10^{-14}$, $M_{h_2} = 500$ GeV, $\alpha = 10^{-5}$, $M_{N_2} \approx M_{N_1} = 2000$ GeV and $M_{N_3} = 2500$ GeV.

However, as the sum of final state particles masses are larger than that of initial state hence, in this case $h_2 h_2$ annihilation mode becomes suppressed. Moreover, to make the contribution of h_2 annihilation even more suppressed we have reduced the quartic couplings λ_{Dh} and λ_{DH} accordingly. As a result other annihilation channels e.g. $Z_{BL} Z_{BL}$, $N_i N_i$ also become inadequate as these channels are mediated by the exchange of h_1 and h_2. Although, RH neutrinos can annihilate to $\phi_{DM} \phi_{DM}{}^\dagger$ via Z_{BL}, we cannot increase the contribution of Z_{BL} mediated diagrams because for that one has to further increase the $\mathrm{B-L}$ charge of ϕ_{DM} (n_{BL}), which results in an over production of DM in the Universe from Z_{BL} decay. From the RP of Fig. 5.13, one can easily notice that in this situation Z_{BL} decay is the most dominant DM production channel (red dashed line) while the total contributions from the annihilations of h_2, Z_{BL} and N_i are negligible. Therefore, for the entire mass range of ϕ_{DM} i.e. $\frac{M_{h_1}}{2}, \frac{M_{h_2}}{2} < M_{\phi_{DM}} < \frac{M_{Z_{BL}}}{2}$, the DM production processes are always related to the $\mathrm{U(1)_{B-L}}$ sector of the present model by receiving a sizeable contribution from Z_{BL} decay.

In Fig. 5.14, we have shown the allowed region (green coloured points) in $M_{Z_{BL}} - g_{BL}$ plane which reproduces the observed DM relic density. While generating this plot we have varied $250\,\mathrm{GeV} \leq M_{DM} \leq 5000$ GeV and $10^{-11} \leq n_{BL} \leq 10^{-8}$. In this region as mentioned above dominant contributions to DM relic density arise from Z_{BL} decay and annihilation of BSM Higgs h_2. In this figure, the black solid line represents the current upper bound [104,113,226] on g_{BL} for a particular mass of Z_{BL} from LHC [5] while the limit [111,112,227] from LEP [6] has been indicated by the red solid line respectively. Therefore, the region below the red and black solid line is allowed by the collider experiments like LHC and LEP. The benchmark value of g_{BL}, $M_{Z_{BL}}$ (= 0.07, 3000 GeV) for which we have computed the baryon asymmetry in the previous section (Section 5.2.2) is highlighted by a blue coloured star. Hence, in this regime the extra gauge boson Z_{BL} immensely takes part in achieving the correct ballpark value of the DM relic density and also at the same time Z_{BL} plays a significant role to obtain the observed value of the matter-antimatter asymmetry of the Universe.

$M_{\phi_{DM}} > \frac{M_{h_1}}{2}, \frac{M_{h_2}}{2}, \frac{M_{Z_{BL}}}{2}$**, BSM particles annihilation dominated region.**

Finally, in this range of DM mass the entire production of ϕ_{DM} from the decays of h_1, h_2 and Z_{Bl} become kinematically inaccessible. Therefore, in this case all three parameters namely λ_{Dh}, λ_{DH} and n_{BL} become free and we can make sufficient increment to these parameters so that either scalar medicated (h_1, h_2) or gauge boson mediated (Z_{BL}) annihilation processes of N_i, Z_{BL} or both can be the dominant contributors in DM production.

Similarly, in the LP and RP of Fig. 5.15, we have shown two different situations where the DM production are dominated by scalar (h_1, h_2) mediated diagrams and gauge boson Z_{BL} mediated diagrams respectively. In the LP, by keeping the n_{BL} value low and adjusting the parameters λ_{Dh} and λ_{DH} one can achieve the correct value DM relic density and on

---

[5] To get the bound in $M_{Z_{BL}} - g_{BL}$ plane from LHC, ATLAS and CMS collaborations consider the Drell-Yan processes ($p\,p \to Z_{BL} \to \bar{l}\,l$, with l = e or μ) and by searching the dilepton resonance they put lower bound on $M_{Z_{BL}}$ for a particular value of extra gauge coupling g_{BL}.

[6] LEP consider the processes $e^+e^- \to \bar{f}\,f$ $(f \neq e)$ above the Z-pole mass and by measuring its cross section they put lower limit on the ratio between the gauge boson mass and guage coupling, which is $\frac{M_{Z_{BL}}}{g_{BL}} \geq 6-7$ TeV.

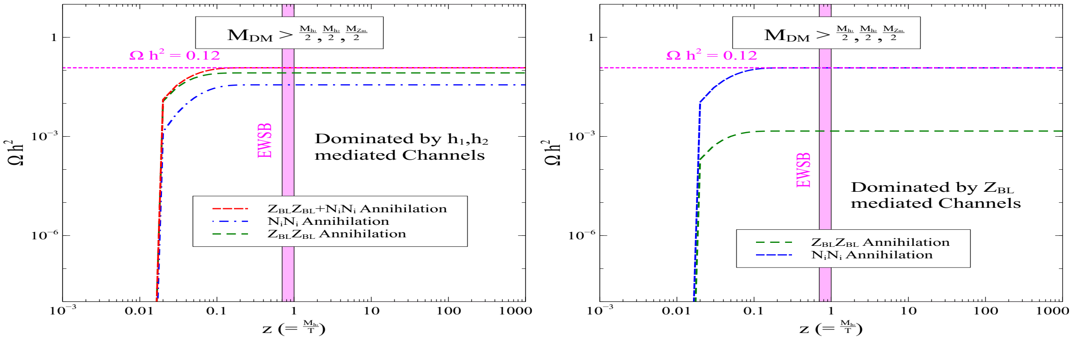

Figure 5.15: Left (Right) Panel: Variation of DM relic density Ωh^2 with z when dominant contributions are coming from scalar h_i, (gauge boson Z_{BL}) mediated annihilation channels. Other relevant parameters value have been kept fixed at $\lambda_{Dh} = 7.017\times10^{-12}$ (7.212×10^{-13}), $\lambda_{DH} = 6.307\times10^{-11}$ (8.316×10^{-12}), $n_{BL} = 1.0\times10^{-10}$ (1.34×10^{-8}), $M_{DM} = 1600$ GeV, $M_{Z_{BL}} = 3000$ GeV, $g_{BL} = 0.07$, $M_{h_1} = 125.5$ GeV, $M_{h_2} = 500$ GeV, $\alpha = 10^{-5}$, $M_{N_2} \approx M_{N_1} = 2000$ GeV and $M_{N_3} = 2500$ GeV.

the other hand, in the RP we have kept the values of λ_{Dh} and λ_{DH} sufficiently low and by suitably adjusting the DM charge n_{BL} we have achieved the correct value of the DM relic density. Therefore, in this region, a strong correlation exists among the neutrino sector, $\mathrm{U(1)_{B-L}}$ sector and DM sector as the entire DM is now being produced from N_iN_i and $Z_{BL}Z_{BL}$ annihilations.

In Fig. 5.16, we have shown the allowed parameter space in $M_{DM} - M_{N_1}$ plane by DM relic density. In order to generate this plot we have varied DM mass in the range $1500\,\mathrm{GeV} \leq M_{DM} \leq 3000\,\mathrm{GeV}$, RH neutrino masses $1500\,\mathrm{GeV} \leq M_{N_i} \leq 10000\,\mathrm{GeV}$ $(i = 1,2)$, $M_{N_1} < M_{N_3} \leq M_{N_1} + 5000$ GeV and $10^{-10} \leq n_{BL} \leq 10^{-8}$. Other relevant parameters have been kept fixed at $\lambda_{Dh} = 7.212\times10^{-13}$, $\lambda_{DH} = 8.316\times10^{-12}$, $M_{Z_{BL}} = 3000$ GeV, $g_{BL} = 0.07$, $M_{h_2} = 500$ GeV, $\alpha = 10^{-5}$ As discussed above, in this regime ($M_{DM} > \frac{M_{h_1}}{2}, \frac{M_{h_2}}{2}, \frac{M_{Z_{BL}}}{2}$) ϕ_{DM} is dominantly produced from the annihilations of Z_{BL} and RH neutrinos. From this plot one can observe that in this high DM mass range to obtain the observed DM relic density, the mass of the lightest RH neutrino cannot be larger than ~ 6000 GeV. Analogous to the Fig. 5.14, here also we have indicated the benchmark point for which we have computed baryon asymmetry in the previous section (Section 5.2.2) by a blue coloured star. Therefore, in this case RH neutrinos are very actively taking part

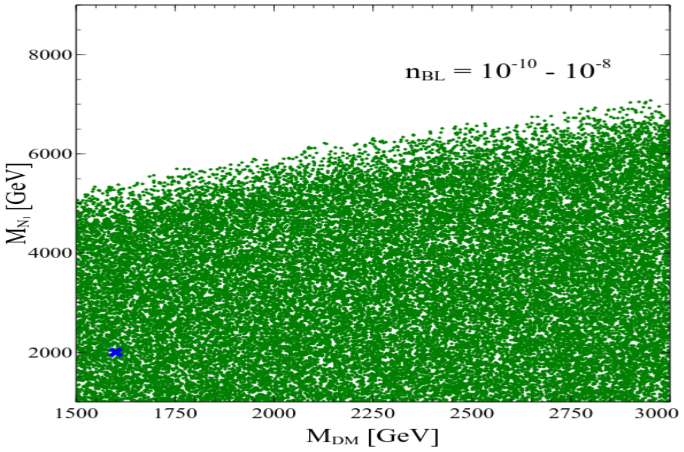

Figure 5.16: Allowed region in $M_{DM} - M_{N_1}$ plane which mimics the observed DM relic density. The blue coloured star represent our benchmark point (M_{DM} = 1600 GeV, M_{N_1} = 2000 GeV).

in all three processes we have considered in this work namely DM production processes, tiny neutrino mass generation and also the generation of required lepton asymmetry to reproduce the observed baryon asymmetry of the Universe.

From the above four regions, which are based on the mass of our FIMP DM, it is evident that in the first region DM production mainly happens from the decay of h_1, h_2 and Z_{BL} and all annihilations are subdominant. Therefore, in this region only the extra neutral gauge boson (Z_{BL}), BSM Higgs (h_2) and SM-like Higgs (h_1) are taking part in the DM relic density estimates and there is no significant role of the RH neutrinos. In the second region, SM-like Higgs decay does not contribute to DM production processes, hence one can safely increase the quartic coupling λ_{Dh} and consequently $h_1 h_1$ annihilation contribution increases. Similar to the previous regime, here also RH neutrinos have less importance in determining the DM relic density. In the third region, the only decay mode that involves in DM production is $Z_{BL} \to \phi_{DM} {\phi_{DM}}^\dagger$. Since all other decay modes correspond to h_1 and h_2 are kinematically forbidden, hence we can increase both the quartic couplings λ_{Dh} and λ_{DH} appropriately which eventually enhance the annihilation contribution from the BSM Higgs significantly. Moreover, due to the increment of quartic couplings in this region $Z_{BL} Z_{BL}$ and $N_i N_i$ annihilation channels start contributing in the

DM production processes. Lastly in region four, due to the high value of the DM mass no decay process contributes to DM relic density and only the BSM particles annihilation contributes. Therefore, in this region by properly adjusting the extra gauge coupling g_{BL}, one can get a sizeable fraction of DM production from the annihilation of RH neutrinos. Since apart from the masses of the involving particles, the annihilation of RH neutrinos mediated by Z_{BL} depends on the extra (B-L) gauge coupling g_{BL} solely. Thus, depending on the mass range of our FIMP DM, we can say that the different model parameters and the additional BSM particles (e.g. Z_{BL}, N_i, h_2) are fully associated to the DM production processes in the early Universe.

Analytical Estimates

So far, we have solved the full Boltzmann equation (Eq. 5.21) for a FIMP ϕ_{DM} numerically. Apart from this, one can estimate the FIMP relic density (or comoving number density) by using the approximate analytical formula. Let us consider a FIMP (ϕ_{DM}) which is produced from the decay of a particle A *i.e.*, $A \to \phi_{DM} {\phi_{DM}}^\dagger$, where A in the present model can be h_1, h_2 or Z_{BL}. The contribution of A to the FIMP relic density at the present epoch, considering the effect of both ϕ_{DM} and ${\phi_{DM}}^\dagger$, is given by [34],

$$\Omega^{FIMP} h^2 \simeq \frac{2.18 \times 10^{27} g_A}{g_s \sqrt{g_\rho}} \frac{M_{DM} \Gamma_A}{M_A^2}\,, \tag{5.23}$$

where M_A and g_A are mass and internal degrees of freedom of the mother particle A, respectively, while Γ_A is the decay width of the process $A \to \phi_{DM} {\phi_{DM}}^\dagger$. The analytic expressions for Γ_A corresponding to h_2, h_1 and Z_{BL} are given in the Appendix of Ref. [199]. Moreover, g_ρ and g_s, as define earlier, are the degrees of freedom related to the energy and entropy densities of the Universe, respectively. Let us now compare the analytical result with the numerical value which we obtain by solving the Boltzmann equation Eq. (5.21).

For this, let us consider a situation when a significant fraction of our FIMP candidate (ϕ_{DM}) is produced from the decay mode of BSM Higgs *i.e.*, $h_2 \to \phi_{DM}\phi_{DM}^{\dagger}$. Substituting the values of model parameters given in the caption of Fig. 5.9 to Eq. (5.23), we get the contribution of h_2 to DM relic density, which is

$$\Omega^{FIMP}h^2 \simeq 0.027, \tag{5.24}$$

where we consider $g_\rho = g_s \approx 100$ and $g_A = 1$. This can be compared to the contribution of h_2 obtained from exact numerical estimate shown in the LP of Fig. 5.9 which is,

$$\Omega_{h_2 \to \phi_{DM}\phi_{DM}^{\dagger}} h^2 = 0.0276. \tag{5.25}$$

Therefore, from the above two estimates it is clearly evident that the analytical result agrees well with the full numerical result. Similarly, for the other decay modes also (*i.e.* h_1, Z_{BL}) one can match the analytical and numerical results.

6

FIMP and Muon $(g-2)$ in a $\mathrm{U}(1)_{L_\mu-L_\tau}$ Model

6.1 Introduction

This chapter is based on [228] and discuss the extension of SM gauge group by a local $\mathrm{U}(1)_{L_\mu-L_\tau}$ symmetry [126, 139, 229]. Therefore, the complete gauge group in this model is $\mathrm{SU}(3)_c\times\mathrm{SU}(2)_L\times\mathrm{U}(1)_Y\times\mathrm{U}(1)_{L_\mu-L_\tau}$. Since we are increasing the SM gauge group by a local $\mathrm{U}(1)_{L_\mu-L_\tau}$ symmetry, we must check the cancellation of axial vector anomaly [210, 211] and mixed gravitational-gauge anomaly [212, 213]. The advantage of the $\mathrm{U}(1)_{L_\mu-L_\tau}$ extension is that these anomalies cancel automatically between the second and third generations [230–232] of SM fermions.

We also extend the particle content of the SM and include three right-handed neutrinos and two SM gauge singlet scalars. The new particles are given appropriate $\mathrm{U}(1)_{L_\mu-L_\tau}$ charge. One of the scalars picks up a Vacuum Expectation Value (VEV) breaking $\mathrm{U}(1)_{L_\mu-L_\tau}$ symmetry spontaneously, while the other does not take any VEV. The $\mathrm{U}(1)_{L_\mu-L_\tau}$ charge $n_{\mu\tau}$ of the other scalar ϕ_{DM} is chosen in such a way that it remains stable even after $\mathrm{U}(1)_{L_\mu-L_\tau}$ breaking and becomes a dark matter candidate. The new gauge boson $Z_{\mu\tau}$ after spontaneous breaking of $\mathrm{U}(1)_{L_\mu-L_\tau}$ becomes massive and gives additional contribution to the muon $(g-2)$, helping reconcile the observed data with the theoretical prediction in this model. The three right-handed neutrinos carry Majorana masses and give rise to light neutrino mass matrix via the Type-I seesaw mechanism. In our earlier work in Ref. [126], we showed that our model can explain the nonzero neutrino masses and their intergenerational mixing angles. Also in that work, we considered the scalar field ϕ_{DM} as a WIMP type dark matter candidate and checked its viability in various direct detection experiments. We found that all the existing constraints are satisfied around the resonance regions, where the mediator mass is nearly equal to twice of dark matter mass. The model for the present work is exactly similar to the model as discussed in Chapter 3, hence we will not describe the model here.

In this work, we show that ϕ_{DM} could serve as a FIMP type dark matter candidate in this $\mathrm{U}(1)_{L_\mu - L_\tau}$ extension of the SM. All particles of our model including the additional scalar h_2, $Z_{\mu\tau}$ and the three right-handed neutrinos are in thermal equilibrium in the early Universe except ϕ_{DM}. In order to make this possible, ϕ_{DM} must be feebly interacting with other particles. We choose its couplings with the visible sector to be extremely small (see Section 3.2 and 6.3 for detailed discussions) such that it remains out of equilibrium throughout its evolution in the early Universe [1]. We compute the relic density of ϕ_{DM} by solving the Boltzmann equation where we consider all the possible production modes of ϕ_{DM} from the decays as well as the annihilations of SM and BSM particles. We find that in our model, ϕ_{DM} is produced not only from the decays of h_1 and h_2, but also from the pair annihilation of N_i ($i = 2, 3$) mediated by the extra neutral gauge boson $Z_{\mu\tau}$. Therefore, the dark matter phenomenology is intricately intertwined with the phenomenology of neutrino masses and muon $(g-2)$.

6.2 Muon $(g-2)$ and neutrino mass

In our previous work [126] we studied in detail the muon $(g-2)$ and neutrino mass phenomenology in the framework of present model. The difference here with the previous

---

[1] $\Gamma < H$ where Γ is the dark matter production rate and H is the Hubble parameter [207]

work is that here we wish to produced the dark matter via the freeze-in mechanism instead of freeze-out, as in [126]. Our aim is to simultaneously explain the dark matter relic abundance as well as the muon $(g-2)$. The region of the $g_{\mu\tau}$ - $M_{Z_{\mu\tau}}$ parameter space that can explain the muon $(g-2)$ has been shown in [233]. This allowed region is seen to be very small and mostly constrained by the neutrino trident process experiments such as CHARM-II, CCFR [145, 146] and 4-leptons decay [233]. In determining the allowed parameter space for the present model, we have considered the relic density constraint [20] and also the bound on invisible decay width of SM-like Higgs [170]. The one loop contribution [127, 144] to muon $(g-2)$ for the U$(1)_{L_\mu - L_\tau}$ gauge boson $Z_{\mu\tau}$ mediated diagram is given in Eq. (3.23). In Fig. 6.1 we show the allowed and disfavoured regions in the $g_{\mu\tau}$-$M_{Z_{\mu\tau}}$ plane. The region above the green dashed line is ruled out by the neutrino trident experiment CCFR [233]. The grey region inside the blue dashed-dotted line and black dashed line can explain the $(g-2)$ anomaly in $\pm 2\sigma$ range [233]. As will be discussed in much detail later, the red dots in this figure span the parameter region which can satisfy the dark matter relic abundance (cf. Eq. (1.85)). We see that for $g_{\mu\tau} \geq 3 \times 10^{-3}$ no red points exist because the contribution from the $Z_{\mu\tau}$ mediated diagram to the relic abundance becomes too large. See Appendix of Ref. [228], for the expression of cross section of $\bar{N}_i N_i \to \phi^\dagger_{DM} \phi_{DM}$, $i = 2, 3$. The region of the parameter space compatible with both the dark matter relic abundance and muon $(g-2)$ lies in the narrow overlapping zone. The benchmark point (values of $g_{\mu\tau}$ and $M_{Z_{\mu\tau}}$) used in all further results shown in this work

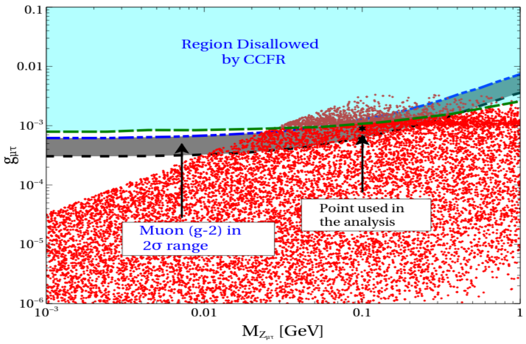

Figure 6.1: Bounds in the $g_{\mu\tau}$ - $M_{Z_{\mu\tau}}$ plane from different experiments and allowed region to satisfy relic density (red dots) and muon $(g-2)$ excess in $2\,\sigma$ range (grey shaded region).

is marked by the star in Fig. 6.1 and corresponds to $M_{Z_{\mu\tau}} = 100$ MeV and $g_{\mu\tau} = 9 \times 10^{-4}$. Such low mass $Z_{\mu\tau}$ gauge boson can be searched by looking $2\mu + \not{E}_T$ final states in LHC or future collider experiments [234,235]. For these values of the parameters, the contribution to muon $(g-2)$ from Eq. (3.23) comes out to be

$$\Delta a_\mu = 22.6 \times 10^{-10}, \tag{6.1}$$

which lies within the $\pm 2\sigma$ range of the observed value [233]. The neutrino mass in the context of the present model has been discussed in detail in section 3.4.

6.3 FIMP Dark Matter and Boltzmann Equation

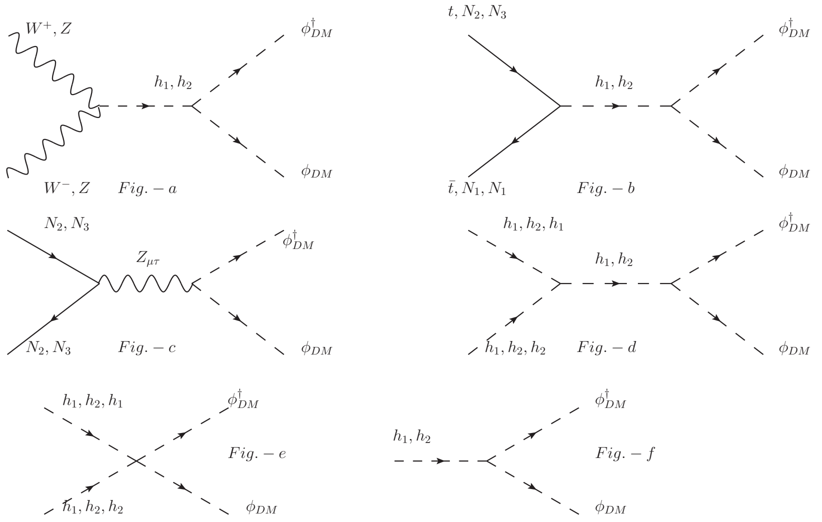

Figure 6.2: Feynman diagrams for the dark matter production processes from the annihilations and decays of different SM and BSM particles.

Vertex $a\,b\,c$	Vertex Factor g_{abc}
$\phi_{DM}\,\phi^\dagger_{DM}\,h_1$	$-(\lambda_{Dh} v \cos\alpha + \lambda_{DH} v_{\mu\tau} \sin\alpha)$
$\phi_{DM}\,\phi^\dagger_{DM}\,h_2$	$(\lambda_{Dh} v \sin\alpha - \lambda_{DH} v_{\mu\tau} \cos\alpha)$
$\phi_{DM}\,\phi^\dagger_{DM}\,Z^\rho_{\mu\tau}$	$n_{\mu\tau} g_{\mu\tau} (p_2 - p_1)^\rho$
$\bar{N}_i\,N_i\,Z^\rho_{\mu\tau}$	$\frac{g_{\mu\tau}}{2} \gamma^\rho \gamma^5$

Table 6.1: Relevant couplings required to compute Feynman diagrams given in Fig. 6.2.

As can be seen from the Eqs. (3.1–3.4), the dark matter particle can interact with the thermal bath containing both SM as well as BSM particles only via h_1, h_2 and $Z_{\mu\tau}$. The Feynman diagrams relevant for the production of dark matter are shown in Fig. 6.2. The corresponding couplings are listed in Table 6.1. From Table 6.1, one can see that the couplings of ϕ_{DM} with scalar bosons h_1 and h_2 depend on the parameters λ_{Dh} and λ_{DH}, while that with extra neutral gauge boson $Z_{\mu\tau}$ involves $g_{\mu\tau}$ and $n_{\mu\tau}$. For the dark matter to be a suitable FIMP candidate, the cross section of the diagrams listed in Fig. 6.2 should be very small. The complete expressions for the contribution from each of the diagrams is given in the Appendix of Ref. [228]. The processes involving h_1 and h_2 can be easily made feeble enough by taking λ_{Dh} and $\lambda_{DH} \sim 10^{-12}$. As we will see later, the other important production mechanism of ϕ_{DM} is shown by the Feynman diagram where N_2 and N_3 annihilate to ϕ_{DM} via the new gauge boson $Z_{\mu\tau}$. The expression for the cross section of this process is given in the Appendix of Ref. [228]. We see that the cross section for this process is proportional to $\sim g^4_{\mu\tau} n^2_{\mu\tau}/10^2$. Since we fix $g_{\mu\tau} = 9 \times 10^{-4}$ to explain the anomalous muon $(g-2)$, we take $n_{\mu\tau} \sim 10^{-5}$ to keep $\sigma_{N_j N_j \to \phi^\dagger_{DM} \phi_{DM}}$ small enough so that ϕ_{DM} stays out of chemical equilibrium. This choice for $n_{\mu\tau}$ also ensures that there is a remnant Z_2 symmetry even when $\mathrm{U}(1)_{L_\mu - L_\tau}$ symmetry is broken spontaneously, which enables ϕ_{DM} to be stable. Thus, ϕ_{DM} behaves as a FIMP dark matter, it stays out of thermal equilibrium at all times, and is produced by the freeze-in mechanism.

The evolution of comoving number density of FIMP produced from the decays as well as annihilations of the SM and BSM particles is governed by the Boltzmann equation. The Boltzmann equation in terms of the comoving number density of ϕ_{DM} is given below. This equation contains both decay as well as annihilation terms. While deriving the Boltzmann equation for the FIMP ϕ_{DM}, we have taken all the particles except ϕ_{DM} in thermal equilibrium and hence their number densities follow the Maxwell-Boltzmann distribution function.

$$
\begin{aligned}
\frac{dY_{\phi_{DM}}}{dz} &= \frac{2M_{pl}}{1.66M_{h_2}^2}\frac{z\sqrt{g_\star(z)}}{g_s(z)}\left[\sum_{i=1,2}\langle\Gamma_{h_i\to\phi_{DM}^\dagger\phi_{DM}}\rangle(Y_i^{eq}-Y_{\phi_{DM}})\right] \\
&+\frac{4\pi^2}{45}\frac{M_{pl}M_{h_2}}{1.66}\frac{\sqrt{g_\star(z)}}{z^2}\left[\sum_{p=W,Z,h_1,h_2,f}\langle\sigma\mathrm{v}_{p\bar{p}\to\phi_{DM}^\dagger\phi_{DM}}\rangle(Y_p^{eq\,2}-Y_{\phi_{DM}}^2)\right. \\
&\left.+\sum_{i=1,j=2,3}\langle\sigma\mathrm{v}_{N_iN_j\to\phi_{DM}^\dagger\phi_{DM}}\rangle(Y_{N_i}^{eq}Y_{N_j}^{eq}-Y_{\phi_{DM}}^2)+\langle\sigma\mathrm{v}_{h_1h_2\to\phi_{DM}^\dagger\phi_{DM}}\rangle(Y_{h_1}^{eq}Y_{h_2}^{eq}-Y_{\phi_{DM}}^2)\right].
\end{aligned}
\tag{6.2}
$$

In the above equation $Y_{\phi_{DM}} = \dfrac{n_{\phi_{DM}}}{\mathrm{s}}$ is the comoving number density, $n_{\phi_{DM}}$ represents the actual number density of the dark matter candidate ϕ_{DM} while s is the entropy of the Universe. The quantity $z = \dfrac{\Lambda}{T}$, where Λ is some mass scale and here it corresponds to the mass of the second Higgs h_2 ($\Lambda \sim M_{h_2}$). The temperature of the Universe is denoted by T and $M_{pl} = 1.22 \times 10^{19}$ GeV is the Planck mass. The functions $g_\star(z)$, $g_s(z)$ and $g_\rho(z)$ are defined in section 1.6. If the decaying particles (h_1, h_2) are in thermal equilibrium [2] then the thermal average of the decay width can be calculated by using the Eq. (5.17).

Next we explain the Boltzmann equation given in Eq. (6.2) term by term. The first term on the R.H.S represents the contribution to $Y_{\phi_{DM}}$ arising from the decays of h_1 and h_2 and it is proportional to the equilibrium comoving number density of the decaying particle. On the other hand, the inverse decay term proportional to the comoving number density of ϕ_{DM} occurs with a negative sign as it *washes out* the ϕ_{DM} number density. However, as we have mentioned before that the initial number density of ϕ_{DM} is extremely small due to its non-thermal origin and hence the negative feedback coming from the inverse processes can be safely neglected.

Similarly, the second, third and fourth terms in the R.H.S of Eq. (6.2) indicate the net contribution to $Y_{\phi_{DM}}$ coming from the annihilations of SM and BSM particles at the early stage of the Universe. Unlike the first term (decay term) of Eq. (6.2) these terms are

---

[2] If they are not in thermal equilibrium then we have to find their non-thermal momentum distribution functions by solving the appropriate Boltzmann equations which will be discussed in Chapter 7.

proportional to the second power of the comoving number densities of relevant particles. The term proportional to Y_p^2 $(p = W, Z, h_1, h_2, f)$ (in the second term of the Boltzmann equation) represents the increment of $Y_{\phi_{DM}}$ from the pair annihilation of p and its antiparticle while the feedback arising from the inverse process $\phi_{DM}\phi_{DM}^\dagger \to p\bar{p}$ is proportional to $Y_{\phi_{DM}}^2$ and comes with a negative sign. The rest of the annihilation terms represent the production processes of ϕ_{DM} from the annihilations of two different particles such as (N_i, N_j), (h_1, h_2) and consequently these terms are proportional to the comoving number densities of two different initial state particles. The terms indicating the inverse processes $(\phi_{DM}\phi_{DM}^\dagger \to N_iN_j,\ h_ih_j,\ i \neq j)$ are proportional to $Y_{\phi_{DM}}^2$, as in the second term of the Boltzmann equation. All the annihilation terms of Eq. (6.2) are proportional to the thermal averaged annihilation cross sections of relevant processes and if all the other particles (except ϕ_{DM}) involved in the annihilation processes are in thermal equilibrium then the general expression of thermally averaged annihilation cross section of a process $A\,B \to \phi_{DM}^\dagger\phi_{DM}$ is given in Eq. (1.76). In order to get the comoving number density $(Y_{\phi_{DM}})$ of the DM particle ϕ_{DM}, we have to solve the Boltzmann equation numerically. After determining the comoving number density $Y_{\phi_{DM}}$ of dark matter particle ϕ_{DM} at the present epoch, we can determine the relic density [224, 225] as defined in Eq. (1.84),

$$\Omega_{\phi_{DM}}h^2 = 2.755\times 10^8 \left(\frac{M_{\phi_{DM}}}{\mathrm{GeV}}\right) Y_{\phi_{DM}}(T_0)\,, \tag{6.3}$$

where M_{DM} is in GeV. In this work we have used the relic density bound as given in Eq. (1.85).

6.4 Results

We have implemented our model in LanHEP [120] to generate all the vertex factors which are required to calculate the relevant annihilation cross sections and decay widths. Corresponding Feynman diagrams are shown in Fig. 6.2. After putting all the cross sections

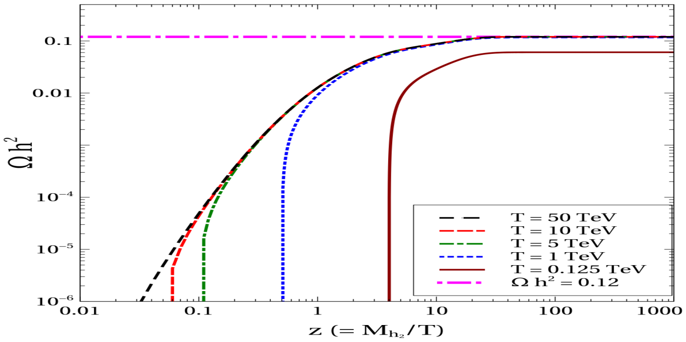

Figure 6.3: Variation of relic density for different choices of initial temperature while the other parameters have been kept fixed at, $M_{Z_{\mu\tau}} = 0.1$ GeV, $g_{\mu\tau} = 9.0 \times 10^{-4}$, $\alpha = 0.01$, $\lambda_{Dh} = 9.8 \times 10^{-13}$, $\lambda_{DH} = 1.3 \times 10^{-11}$, $M_{DM} = 50.0$ GeV, $n_{\mu\tau} = 5.5 \times 10^{-5}$.

and decay widths (as listed in Appendix of Ref. [228]) in Eq. (6.2), we solve the Boltzmann equation numerically and study the related phenomenology of FIMP dark matter. Throughout this analysis we keep the extra Higgs mass fixed at $M_{h_2} = 500$ GeV. In Fig. 6.3, we show the variation of the dark matter relic density with z for different choices of the initial temperature. From the figure, it is clear that if the initial temperature is greater $T_{\text{in}} \geq 1$ TeV, then there is no dependence of the final relic density on the value of the initial temperature. This can be explained in the following way. As the heavy Higgs h_2 is in thermal equilibrium with the cosmic soup, hence the maximum production of ϕ_{DM} from the decay of h_2 occurs around a temperature of the Universe (T) ~ M_{h_2} i.e. 500 GeV. However, as the temperature of the Universe drops below M_{h_2}, the number density of the extra Higgs boson (h_2) becomes exponentially suppressed (or Boltzmann suppressed), which in turn reduces the final abundance of ϕ_{DM}. This case is shown by the choice $T_{\text{in}} = 125$ GeV in the figure. Hence in what follows, we take a fixed $T_{\text{in}} = 1$ TeV.

In the left panel of Fig. 6.4, we show the relative contributions of two different types of production processes (decay and annihilation) to Ωh^2. The red dotted line represents the contribution from the decay of SM-like Higgs boson h_1 and extra Higgs boson h_2, while the black dashed line corresponds to the contribution from the all possible annihilation channels of SM and BSM particles (see Fig. 6.2 for the corresponding Feynman diagrams). The total contribution towards the relic density of ϕ_{DM} coming from the

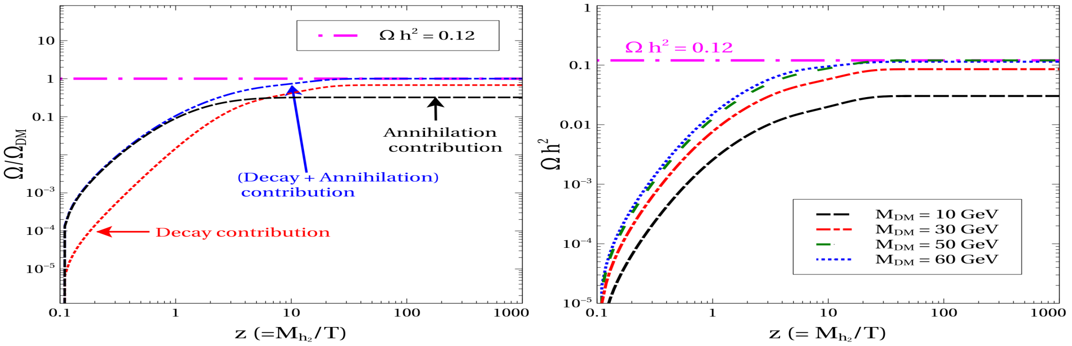

Figure 6.4: Left panel showing the contributions of decay and annihilation in the total relic density. Right panel: Variation of dark matter relic density with z for four different values of dark matter mass M_{DM}. The other parameters are kept fixed at $M_{Z_{\mu\tau}} = 0.1$ GeV, $g_{\mu\tau} = 9.0 \times 10^{-4}$, $\alpha = 0.01$, $\lambda_{Dh} = 9.8 \times 10^{-13}$, $\lambda_{DH} = 1.3 \times 10^{-11}$, $M_{DM} = 50.0$ GeV (LP), $n_{\mu\tau} = 5.5 \times 10^{-5}$.

decay as well as annihilation of different particles is represented by blue dashed-dotted line. The horizontal magenta line indicates the observed value of dark matter relic density ($\Omega h^2 \sim 0.12$ [20]) at the present epoch. From this plot, it can be seen clearly that for our chosen set of model parameters ($M_{Z_{\mu\tau}} = 0.1$ GeV, $g_{\mu\tau} = 9.0 \times 10^{-4}$, $\alpha = 0.01$, $\lambda_{Dh} = 9.8 \times 10^{-13}$, $\lambda_{DH} = 1.3 \times 10^{-11}$, $M_{DM} = 50.0$ GeV, $n_{\mu\tau} = 5.5 \times 10^{-5}$), the decay processes contribute $\sim 67\%$ of dark matter production while rest of the dark matter particles are produced from the annihilations of different SM as well as BSM particles. In the right panel of Fig. 6.4, the variation of relic density with z (i.e. with respect to the inverse of temperature T) has been shown for four different values of dark matter mass M_{DM}. For M_{DM} = 10 GeV, 30 GeV and 50 GeV, the relic density is seen to rise with M_{DM}. This agrees with the expression for relic density given in Eq. (6.3). However, if we take a slightly higher value of dark matter mass, M_{DM} = 60 GeV (blue dotted line), the relic density decreases instead of increasing. This is because M_{DM} = 60 GeV is very close to half of the SM like Higgs boson mass ($\sim M_{h_1}/2$) and the decay mode $h_1 \to \phi_{DM}\phi^\dagger_{DM}$ becomes phase space suppressed. Therefore, it reduces the contribution arising from h_1 decay and hence the final relic density of dark matter.

The contributions to Ωh^2 arising from the decays of h_1, h_2 and the annihilations of SM as well as BSM particles are shown respectively in left and right panels of Fig. 6.5. Here

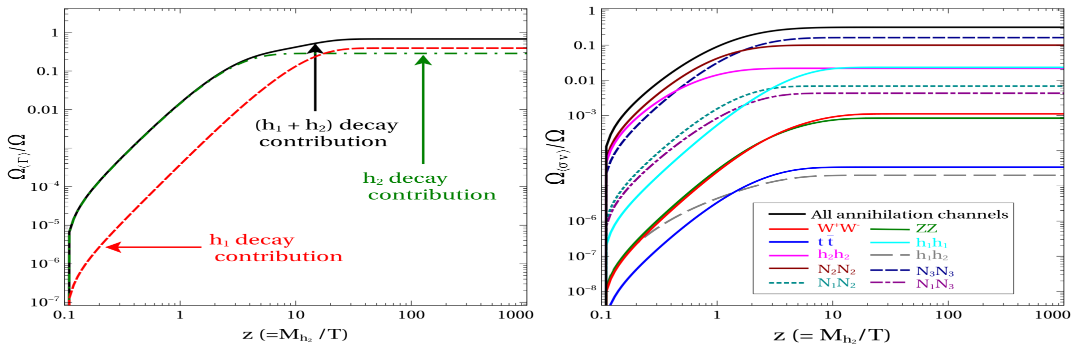

Figure 6.5: Left Panel: Relative contributions of two decay modes in relic density. Right Panel: Relative contributions of different annihilation channels towards Ωh^2. Other parameters are kept fixed at $M_{Z_{\mu\tau}} = 0.1$ GeV, $g_{\mu\tau} = 9.0\times10^{-4}$, $\alpha = 0.01$, $\lambda_{Dh} = 9.8\times10^{-13}$, $\lambda_{DH} = 1.3\times10^{-11}$, $M_{DM} = 50.0$ GeV, $n_{\mu\tau} = 5.5\times10^{-5}$.

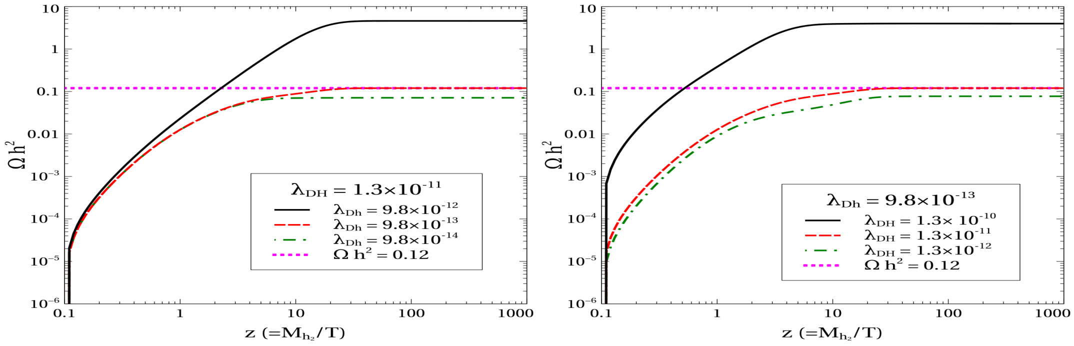

Figure 6.6: Left (Right) Panel: Variation of relic density with z for three different values of λ_{Dh} (λ_{DH}). Other parameters are kept fixed at $M_{Z_{\mu\tau}} = 0.1$ GeV, $g_{\mu\tau} = 9.0\times10^{-4}$, $\alpha = 0.01$, $\lambda_{Dh} = 9.8\times10^{-13}$, $\lambda_{DH} = 1.3\times10^{-11}$, $M_{DM} = 50.0$ GeV, $n_{\mu\tau} = 5.5\times10^{-5}$.

we define a quantity $\frac{\Omega_{\langle\Gamma\rangle}}{\Omega}$ ($\frac{\Omega_{\langle\sigma v\rangle}}{\Omega}$) which represents the fractional contribution of a particular decay (annihilation) channel to dark matter relic density. In the left-panel of Fig. 6.5, the contribution from h$_2$ decay has been shown by the green dashed-dotted line and that from h$_1$ decay has been shown by the red dashed line, while the total decay contribution to the dark matter relic density is represented by the black solid line. From this plot one can see that, initially for low values of z ($z < 10$, corresponding to higher temperatures), the extra Higgs contribution to Ωh^2 is more because of its high mass. On the other hand, for higher values of z ($z > 10$), the SM-like Higgs decay contribution starts dominating. In the right panel of Fig. 6.5, we show the contribution coming from different annihilation channels. The total contribution from all the annihilation channels is represented by the black solid line while the other lines show the contribution of individual channels. From this plot it is clearly seen that, the two dominating annihilation channels are $N_2 N_2$ and $N_3 N_3$. Annihilation channels $h_1 h_1$ and $h_2 h_2$ also have significant role in the production processes of dark matter, while the effect of other channels are sub dominant. In the left-panel of Fig. 6.6, variation of relic density with z for three different value of λ_{Dh} have been shown. The red dashed line for $\lambda_{Dh} = 9.8 \times 10^{-13}$ gives the correct relic density. In the right-panel of Fig. 6.6 we show the variation of relic density for different values of the other quartic coupling λ_{DH}. It is clear from Fig. 6.6 that the relic density increases with both λ_{Dh} and λ_{DH} as the production modes of ϕ_{DM} are proportional to these quartic couplings. However, the increment of Ωh^2 with respect to increasing λ_{Dh} or λ_{DH} is not uniform. When we decrease λ_{Dh} (λ_{DH}) from 9.8×10^{-13} (1.3×10^{-11}) by one order of magnitude, the decrease in Ωh^2 is very small because in this regime we have dominant contribution from the $Z_{\mu\tau}$ mediated right-handed neutrino annihilation channel. However, if we increase λ_{Dh} (λ_{DH}) from 9.8×10^{-13} (1.3×10^{-11}) by one order of magnitude, Ωh^2 increases by more than order of magnitude since in this case the contribution from decay channels become dominant.

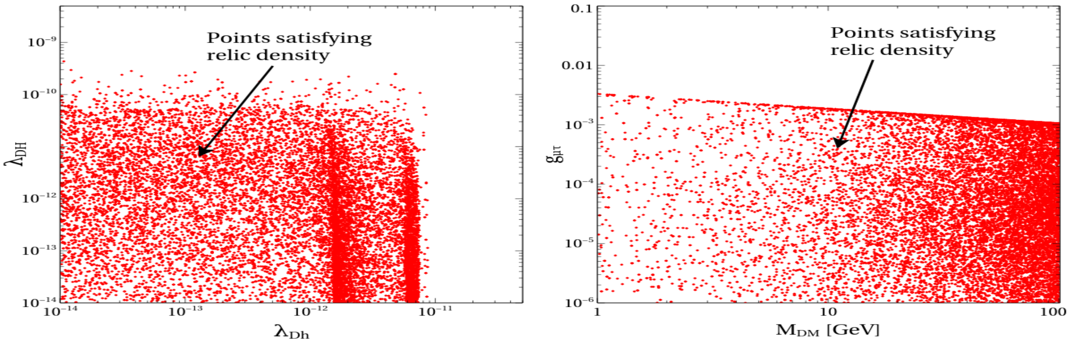

Figure 6.7: Left panel: Allowed parameter space in λ_{Dh} - λ_{DH} plane. Right panel: Allowed parameter space in M_{DM} - $g_{\mu\tau}$ plane. In both the plots red points satisfy the relic density bound.

In the left-panel of Fig. 6.7, we have shown the allowed regions in the λ_{Dh} - λ_{DH} plane. The red points in the plane satisfy the relic density bound. Both the parameters λ_{Dh} and λ_{DH} have been varied from 10^{-14} to 10^{-8}. We see from the figure that for $\lambda_{Dh} \geq 8 \times 10^{-11}$ and $\lambda_{Dh} \geq 3 \times 10^{-10}$ no red points exist, and therefore these regions are disallowed by the relic density bound. One can also notice that there is no lower bound on λ_{Dh} and λ_{DH}.

This is because for lower values of λ_{Dh} and λ_{DH}, even though the Higgs mediated annihilation and decay contributions become very less, the $Z_{\mu\tau}$ mediated annihilation channels ($N_i N_i \to \phi^{\dagger}_{DM} \phi_{DM}$, $i = 2, 3$ see Appendix of Ref. [228]) contribute fully and hence can explain the relic density bound. In the right-panel of Fig. 6.7, we show the allowed regions in the M_{DM} - $g_{\mu\tau}$ plane. Here we have varied dark matter mass M_{DM} from 1 GeV to 100 GeV and the $\mathrm{U}(1)_{L_\mu - L_\tau}$ gauge coupling $g_{\mu\tau}$ from 10^{-6} to 0.1. The figure shows that the whole range of dark matter mass M_{DM} can satisfy the relic density bound. However, the gauge coupling $g_{\mu\tau} \geq 3 \times 10^{-3}$ does not satisfy the relic density bound as over production of ϕ_{DM} occurs through the annihilation channel $N_i N_i \to \phi^{\dagger}_{DM} \phi_{DM}$, $i = 2, 3$.

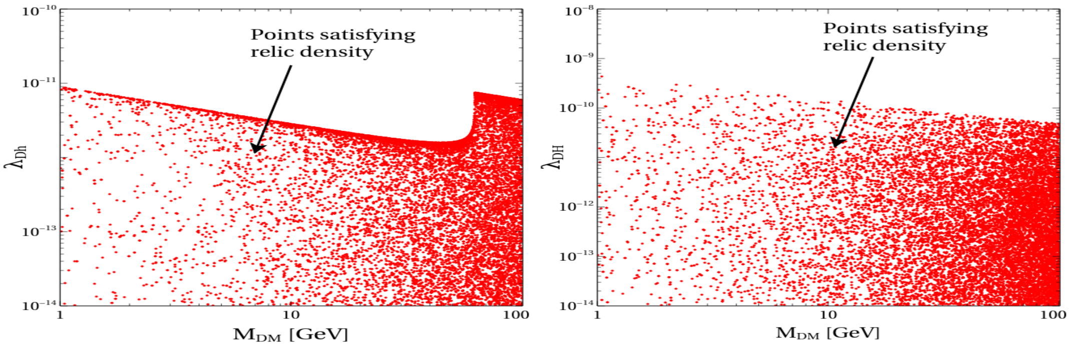

Figure 6.8: Left panel: Allowed parameter space in M_{DM} - λ_{Dh} plane. Right panel: Allowed parameter space in M_{DM} - λ_{DH} space. In both the plots red points satisfy the relic density bound.

In Fig. 6.8, we show the allowed parameter space in the $M_{DM} - \lambda_{Dh}$ and $M_{DM} - \lambda_{DH}$ planes in the left and right panels respectively. As it was seen earlier, here too the whole range of considered dark matter mass [3] is allowed. However, there is an upper limit on both λ_{Dh} and λ_{DH}. In both the panels, there exist an anti-correlation between the dark matter mass and the quartic coupling $\lambda_{Dh(H)}$ since the relic density is proportional to the dark matter mass M_{DM} as well as the coupling constant. Hence, if we increase M_{DM} then to satisfy the relic density, $\lambda_{Dh(H)}$ must decrease. In the left-panel we observe that around $M_{DM} \sim 62$ GeV, there is a rise in λ_{Dh}. This happens because this is the resonance region for the SM-like Higgs and as a result there is little contribution from the decay

---

[3] In all the plots the allowed red points in the M_{DM} appear more dense on the right since we have generated the random number in linear scale but plotted the figures in the log scale.

of SM-like Higgs (phase space suppression). Hence, to satisfy the relic density bound, there is a sudden rise in λ_{Dh} to increase the contribution arising from the decay as well as annihilation processes involving h_1. Beyond $M_{DM} \sim 62.5$ GeV, there is no contribution from the SM-like Higgs. Hence, the coupling λ_{Dh} again starts behaving in the normal way (anti-correlation). No such peculiar behaviour is seen for λ_{DH} because this parameter is important for the decay of h_2 and the chosen mass range of the dark matter is not in the resonance region of the extra Higgs h_2 ($M_{h_2} \sim 500$ GeV). Therefore, for the quartic coupling λ_{DH}, the anti-correlation exists for the entire range of dark matter mass M_{DM} (1-100 GeV).

7

Explaining the 3.5 keV X-ray Line in a $L_\mu - L_\tau$ Extension of the Inert Doublet Model

7.1 Introduction

This chapter reflects the work [236] where we address the issue of the observed neutrino masses and mixing, dark matter abundance of the universe and the 3.5 keV line within a BSM (Beyond SM) model, where we have naturally a two component Dark Matter and a nearly degenerate long-lived state. We extend the SM gauge group by an anomaly free local $U(1)_{L_\mu - L_\tau}$ symmetry [139, 230–232]. We break this gauge symmetry spontaneously by introducing in the model a SM singlet scalar charged under $U(1)_{L_\mu - L_\tau}$. The mass of the resultant neutral gauge boson is given in terms of the new gauge coupling and vacuum expectation value (VEV) of this scalar. Also included in the model are three RH neutrinos and a SM (inert) doublet scalar, both of which carry -1 charge with respect to an additional Z_2 symmetry, while all other particles carry charge $+1$. This forbids all Yukawa couplings of this doublet with the SM fermions (thereby earning the name, inert doublet) and the only Yukawa term where it appears is the one with the RH neutrinos. The Z_2 symmetry also forbids the normal Yukawa coupling involving the lepton doublets, RH neutrinos and the SM Higgs doublet. On the other hand, the allowed Yukawa coupling between the lepton doublets, RH neutrinos and the inert doublet does not lead to a Dirac-like mass term since the inert doublet does not take a VEV. As a result, light neutrino masses via Type-I seesaw is forbidden. However, the light neutrinos get mass radiatively at one-loop, where the RH neutrinos and the inert doublet run in the loop [90]. The RH neutrinos protected by the Z_2 symmetry become the dark matter of the universe. The Z_2 symmetry allows the RH neutrinos to be coupled only to the Higgs sector and the $Z_{\mu\tau}$. We invoke a non-thermal production mechanism for the generation of DM in the early universe via the freeze-in mechanism [34] wherein the RH neutrinos are mainly produced by out-of-equilibrium decays of $Z_{\mu\tau}$ gauge bosons.

The 3.5 keV γ line can be explained by the decay of a heavy RH neutrino to another RH neutrino if the two states are nearly degenerate and the mass splitting is 3.5 keV [237, 238]. Moreover the lifetime of the next-to-lightest neutrino has to be sufficiently long. Both conditions are naturally realised in our scenario. Indeed we will see that in the $U(1)_{L_\mu - L_\tau}$ symmetric limit, the $L_\mu - L_\tau$ symmetry enforces two completely degenerate states and one heavier state for the RH mass spectrum in our model. The two lighter degenerate RH neutrino states play the role of a two-component dark matter. The spontaneous breaking of $U(1)_{L_\mu - L_\tau}$ results in a small mass splitting between the two degenerate RH neutrinos, determined by the symmetry breaking scale and Yukawa couplings of the RH neutrinos. The lifetime of the heavier state is longer than the age of the Universe due both to the phase-space suppression and to the small parameters needed to explain the light neutrino masses.

7.2 Model

The complete gauge group in our model is, $\mathrm{SU}(3)_c \times \mathrm{SU}(2)_L \times \mathrm{U}(1)_Y \times U(1)_{L_\mu - L_\tau}$. In addition to the SM particles, we augment our model with a SM scalar doublet, a SM scalar singlet and three RH neutrinos. We also impose a $\mathbb{Z}_2$ symmetry to make the additional doublet inert. The $\mathbb{Z}_2$ charge of the RH neutrinos are also taken to be -1 to keep them stable, such that they could be dark matter candidates. The complete fermionic and scalar particle content of the model and their corresponding charges under the different symmetry groups are shown in Tables 7.1 and 7.2:

Gauge Group	Baryon Fields			Lepton Fields			Scalar Fields		
	$Q_L^i = (u_L^i, d_L^i)^T$	u_R^i	d_R^i	$L_L^i = (\nu_L^i, e_L^i)^T$	e_R^i	N_R^i	ϕ_h	ϕ_H	η
$\mathrm{SU(2)_L}$	2	1	1	2	1	1	2	1	2
$\mathrm{U(1)_Y}$	1/6	2/3	−1/3	−1/2	−1	0	1/2	0	1/2
$\mathbb{Z}_2$	+	+	+	+	+	−	+	+	−

Table 7.1: Particle contents and their corresponding charges under SM gauge group and discrete group $\mathbb{Z}_2$.

Gauge Group	Baryonic Fields	Lepton Fields			Scalar Fields		
	(Q_L^i, u_R^i, d_R^i)	(L_L^e, e_R, N_R^e)	$(L_L^\mu, \mu_R, N_R^\mu)$	$(L_L^\tau, \tau_R, N_R^\tau)$	ϕ_h	ϕ_H	η
$\mathrm{U(1)}_{L_\mu - L_\tau}$	0	0	1	−1	0	1	0

Table 7.2: Particle contents and their corresponding charges under $\mathrm{U(1)}_{L_\mu - L_\tau}$.

The complete Lagrangian $\mathcal{L}$ for the present model is as follows,

$$\begin{aligned}\mathcal{L} &= \mathcal{L}_{SM} + \mathcal{L}_N + (D_\mu \phi_H)^\dagger (D^\mu \phi_H) + (D_\mu \eta)^\dagger (D^\mu \eta) + \sum_{j=\mu,\tau} Q^j \bar{L}_j \gamma_\rho L_j Z^\rho_{\mu\tau} \\ &\quad - \frac{1}{4} F_{\mu\tau_{\rho\sigma}} F_{\mu\tau}{}^{\rho\sigma} - V(\phi_h, \phi_H, \eta)\,, \end{aligned} \tag{7.1}$$

where ϕ_h and η are two $\mathrm{SU(2)}_L$ doublets while ϕ_H is a scalar singlet. Moreover, $Q^j = 1(-1)$ for $j = \mu(\tau)$ where $L_j = \begin{pmatrix} \nu_j & j \end{pmatrix}^T$. Here, one of the scalar doublets namely η which is odd under $\mathbb{Z}_2$ symmetry, does not have any Yukawa interaction involving only SM fermions and acts like an inert doublet. For the same symmetry reason it does not have any VEV. The field strength tensor for the extra neutral gauge field $Z_{\mu\tau}$ corresponding to gauge group $\mathrm{U(1)}_{L_\mu - L_\tau}$ is denoted by $F_{\mu\tau}$. In principle we should include a mixing term between the SM neutral gauge boson Z and the new neutral gauge boson $Z_{\mu\tau}$. The experimental bound restricts this mixing to be $< 10^{-3}$ br the LEP II [111, 239]. In this work we assume no mixing between the neutral gauge bosons of SM and $U(1)_{L_\mu - L_\tau}$. Indeed, if such mixing is generated at the loop level, we expect it to be suppressed not only by loop factors, but also by the gauge coupling $g_{\mu\tau}$[1] rendering it negligible in our

---

[1] In this work, to maintain the nonthermal nature of our DM candidates we consider $g_{\mu\tau} \sim 10^{-11}$ (see Section 7.5).

discussion. The Lagrangian for the three RH neutrinos $\mathcal{L}_N$ after obeying all the symmetry has the following form,

$$\begin{aligned}
\mathcal{L}_N &= \sum_{i=e,\mu,\tau} \frac{i}{2}\bar{N}_i\gamma^\mu D_\mu N_i - \frac{1}{2} M_{ee}\,\bar{N}^c_e N_e - \frac{1}{2} M_{\mu\tau}\,(\bar{N}^c_\mu N_\tau + \bar{N}^c_\tau N_\mu) \\
&\quad -\frac{1}{2} h_{e\mu}(\bar{N}^c_e N_\mu + \bar{N}^c_\mu N_e)\phi^\dagger_H - \frac{1}{2} h_{e\tau}(\bar{N}^c_e N_\tau + \bar{N}^c_\tau N_e)\phi_H \\
&\quad - \sum_{\alpha=e,\mu,\tau} h_\alpha \bar{L_\alpha}\tilde{\eta} N_\alpha + h.c.,
\end{aligned} \tag{7.2}$$

where $\tilde{\eta} = i\sigma_2\eta^*$. The potential $V(\phi_h,\phi_H,\eta)$ in Eq. (7.1) contains all possible interaction terms involving the two SM scalar doublets and one SM scalar singlet,

$$\begin{aligned}
V(\phi_h,\phi_H,\eta) &= -\mu^2_H\phi^\dagger_H\phi_H - \mu^2_h\phi^\dagger_h\phi_h + \mu^2_\eta\eta^\dagger\eta + \lambda_1(\phi^\dagger_h\phi_h)^2 + \lambda_2(\eta^\dagger\eta)^2 + \lambda_3(\phi^\dagger_H\phi_H)^2 \\
&\quad +\lambda_{12}(\phi^\dagger_h\phi_h)(\eta^\dagger\eta) + \lambda_{13}(\phi^\dagger_h\phi_h)(\phi^\dagger_H\phi_H) + \lambda_{23}(\phi^\dagger_H\phi_H)(\eta^\dagger\eta) + \lambda_4(\phi^\dagger_h\eta)(\eta^\dagger\phi_h) \\
&\quad +\frac{1}{2}\lambda_5\left((\phi^\dagger_h\eta)^2 + h.c.\right).
\end{aligned} \tag{7.3}$$

After spontaneous breaking of $\mathrm{U}(1)_{L_\mu - L_\tau}$ and $\mathrm{SU}(3)_c\times\mathrm{SU}(2)_L\times\mathrm{U}(1)_Y$, the scalars take the following form,

$$\phi_h = \begin{pmatrix} 0 \\ \dfrac{v+H}{\sqrt{2}} \end{pmatrix},\ \ \phi_H = \left(\frac{v_{\mu\tau}+H_{\mu\tau}}{\sqrt{2}}\right),\ \ \eta = \begin{pmatrix} \eta^+ \\ \dfrac{\eta^0_R + i\eta^0_I}{\sqrt{2}} \end{pmatrix}. \tag{7.4}$$

There is mixing between the neutral components of ϕ_h and ϕ_H, and the off diagonal elements of the mass matrix are proportional to the parameter λ_{13}. After diagonalising the mass matrix one obtains two physical scalar states h_1 and h_2. Masses of h_1, h_2 and mixing angle α are given by

$$M^2_{h_1} = \lambda_1 v^2 + \lambda_3 v^2_{\mu\tau} - \sqrt{(\lambda_3 v^2_{\mu\tau} - \lambda_1 v^2)^2 + (\lambda_{13}\, v\, v_{\mu\tau})^2}\,, \tag{7.5}$$

$$M^2_{h_2} = \lambda_1 v^2 + \lambda_3 v^2_{\mu\tau} + \sqrt{(\lambda_3 v^2_{\mu\tau} - \lambda_1 v^2)^2 + (\lambda_{13}\, v\, v_{\mu\tau})^2}\,, \tag{7.6}$$

$$\tan 2\alpha = \frac{\lambda_{13}\, v_{\mu\tau}\, v}{\lambda_3 v^2_{\mu\tau} - \lambda_1 v^2}\,. \tag{7.7}$$

The lighter Higgs state h_1, for small mixing angle α and $v_{\mu\tau} \gg v$, behaves as the Standard Model Higgs observed at the LHC [140, 141] and therefore we will take its mass to be 125.5 GeV. From the above Eq. (7.5)-(7.7), we can also write down the quartic couplings in terms of the physical masses of the Higgses M_{h_1} and M_{h_2} and the mixing angle α. The expressions are as follows,

$$\begin{aligned} \lambda_3 &= \frac{M_{h_1}^2 + M_{h_2}^2 + (M_{h_2}^2 - M_{h_1}^2)\cos 2\alpha}{4\,v_{\mu\tau}^2}\,, \\ \lambda_1 &= \frac{M_{h_1}^2 + M_{h_2}^2 + (M_{h_1}^2 - M_{h_2}^2)\cos 2\alpha}{4\,v^2}\,, \\ \lambda_{13} &= \frac{(M_{h_2}^2 - M_{h_1}^2)\cos\alpha \sin\alpha}{v\,v_{\mu\tau}}\,, \end{aligned} \tag{7.8}$$

In order to obtained a stable *vacuum*, the quartic couplings need to satisfy the following inequalities,

$$\begin{aligned} &\lambda_1 \geq 0, \lambda_2 \geq 0, \lambda_3 \geq 0, \\ &\lambda_{12} \geq -2\sqrt{\lambda_1 \lambda_2}, \\ &\lambda_{13} \geq -2\sqrt{\lambda_1 \lambda_3}, \\ &\lambda_{23} \geq -2\sqrt{\lambda_2 \lambda_3}, \\ &\lambda_{12} + \lambda_4 - |\lambda_5| \geq -2\sqrt{\lambda_1 \lambda_2}, \\ &\sqrt{\lambda_{13} + 2\sqrt{\lambda_1 \lambda_3}}\sqrt{\lambda_{23} + 2\sqrt{\lambda_2 \lambda_3}}\sqrt{\lambda_{12} + \lambda_4 - |\lambda_5| + 2\sqrt{\lambda_1 \lambda_2}} \\ &+2\sqrt{\lambda_1\lambda_2\lambda_3} + \lambda_{13}\sqrt{\lambda_2} + \lambda_{23}\sqrt{\lambda_1} + (\lambda_{12} + \lambda_4 - |\lambda_5|)\sqrt{\lambda_3} \geq 0\ , \\ &\sqrt{\lambda_{13} + 2\sqrt{\lambda_1 \lambda_3}}\sqrt{\lambda_{23} + 2\sqrt{\lambda_2 \lambda_3}}\sqrt{\lambda_{12} + 2\sqrt{\lambda_1 \lambda_2}} \\ &+2\sqrt{\lambda_1\lambda_2\lambda_3} + \lambda_{13}\sqrt{\lambda_2} + \lambda_{23}\sqrt{\lambda_1} + \lambda_{12}\sqrt{\lambda_3} \geq 0\ . \end{aligned} \tag{7.9}$$

As we will see in the result section (Section 7.5), in our analysis the value of the extra singlet scalar *vev* is around 10^{14} GeV, mass of BSM Higgs M_{h_2} = 5 TeV and the mixing angle between the neutral components of Higgses $\alpha = 0.01$. Hence, we get the following values for the quartic couplings by using the Eq. (7.8),

$$\lambda_1 = 0.15,\ \lambda_3 = 1.25 \times 10^{-21} \text{ and } \lambda_{13} = 1.01 \times 10^{-11}\,. \tag{7.10}$$

All the values of the quartic couplings as shown above are positive and in the present case the quartic couplings which are related to the inert doublet are free parameters (except λ_5, which we have considered $\sim 10^{-3}$ to obtain light neutrino masses in sub-eV range), hence all the inequalities as prescribed in Eq. (7.9) are inevitably satisfied.

On the other hand the masses of the inert doublet components after symmetry breaking can be expressed in the following form,

$$\begin{aligned} M^2_{\eta^\pm} &= \mu^2_\eta + \frac{1}{2}\left(\lambda_{12} v^2 + \lambda_{23} v^2_{\mu\tau}\right), \\ M^2_{\eta^0_R} &= \mu^2_\eta + \frac{1}{2}\lambda_{23}\, v^2_{\mu\tau} + \frac{1}{2}(\lambda_{12} + \lambda_4 + \lambda_5)\, v^2\,, \\ M^2_{\eta^0_I} &= \mu^2_\eta + \frac{1}{2}\lambda_{23}\, v^2_{\mu\tau} + \frac{1}{2}(\lambda_{12} + \lambda_4 - \lambda_5)\, v^2\,, \end{aligned} \tag{7.11}$$

The mass term for the extra neutral gauge boson $Z_{\mu\tau}$ is also generated when ϕ_H acquires a nonzero VEV $v_{\mu\tau}$ such that

$$M_{Z_{\mu\tau}} = g_{\mu\tau}\, v_{\mu\tau}\,, \tag{7.12}$$

where $g_{\mu\tau}$ is the gauge coupling corresponding to gauge group $\mathrm{U}(1)_{L_\mu - L_\tau}$. In this model all three RH neutrinos are odd under the $\mathbb{Z}_2$ symmetry. However, the mass of N_1 comes out to be higher than that of N_2 and N_3, so that N_1 can decay to the lighter RH neutrinos. Also, we will see in Section 7.3 that the masses of N_2 and N_3 are nearly degenerate because of the $L_\mu - L_\tau$ symmetry, so that both can play the role of dark matter candidate. Furthermore, in Section 7.4 we will show that the RH neutrinos can be produced by the freeze-in mechanism in the early Universe, which requires a tiny gauge coupling $g_{\mu\tau} \sim \mathcal{O}(10^{-11})$. Thus, in order to have a TeV scale gauge boson $Z_{\mu\tau}$ we need large $v_{\mu\tau}$.

Therefore, by choosing appropriate values of the relevant model parameters we can make the masses of inert doublet components higher than the reheat temperature of the universe so that their effect on the production of N_2 and N_3 can be safely neglected.

7.3 Heavy and Light Neutrino Masses

In this section we will show how the $\mathrm{U}(1)_{L_\mu - L_\tau}$ symmetry determines the mass spectrum and mixing angles of all the six neutrinos, the three heavy ones as well as the three light ones. The relevant part of the Lagrangian was given in Eq. (7.2) where the first term gives the kinetic part while the rest give the mass terms and Yukawa terms involving the neutrinos. After $\mathrm{U}(1)_{L_\mu - L_\tau}$ and electroweak symmetry breaking the mass matrix for the RH neutrinos is given by

$$\mathcal{M}_R = \begin{pmatrix} M_{ee} & \frac{v_{\mu\tau}}{\sqrt{2}} h_{e\mu} & \frac{v_{\mu\tau}}{\sqrt{2}} h_{e\tau} \\ \frac{v_{\mu\tau}}{\sqrt{2}} h_{e\mu} & 0 & M_{\mu\tau}\, e^{i\xi} \\ \frac{v_{\mu\tau}}{\sqrt{2}} h_{e\tau} & M_{\mu\tau}\, e^{i\xi} & 0 \end{pmatrix}, \tag{7.13}$$

where the terms involving the VEV $v_{\mu\tau}$ appear after $\mathrm{U}(1)_{L_\mu - L_\tau}$ breaking. In the limit that $\mathrm{U}(1)_{L_\mu - L_\tau}$ is unbroken, the RH neutrino mass matrix is given by

$$\mathcal{M}_R = \begin{pmatrix} M_{ee} & 0 & 0 \\ 0 & 0 & M_{\mu\tau}\, e^{i\xi} \\ 0 & M_{\mu\tau}\, e^{i\xi} & 0 \end{pmatrix}. \tag{7.14}$$

Eigenvalues of Eq. (7.14) are

$$\begin{aligned} M'_{2/3} &= \pm M_{\mu\tau} e^{i\xi} \\ M'_1 &= M_{ee}, \end{aligned} \tag{7.15}$$

giving very naturally two degenerate RH neutrinos with opposite parity. The $\mathrm{U}(1)_{L_\mu - L_\tau}$ breaking terms in Eq. (7.13) brings corrections to the RH neutrino mass spectrum, breaking the degeneracy between N_2 and N_3. The mass splitting between them is given at first order for $M_{ee} \gg M_{\mu\tau}$ by

$$\Delta M_{23} = \frac{(h_{e\mu} + h_{e\tau})^2 v_{\mu\tau}^2}{2M_{ee}}. \tag{7.16}$$

Hence, the mass splitting between N_2 and N_3 depends on the $\mathrm{U}(1)_{L_\mu - L_\tau}$ breaking VEV $v_{\mu\tau}$ and the Yukawa couplings $h_{e\mu}$ and $h_{e\tau}$. In what follows, we will see that $v_{\mu\tau}$ will be determined by the choice of the $Z_{\mu\tau}$ gauge boson. However, the Yukawa couplings $h_{e\mu}$ and $h_{e\tau}$ can be suitably adjusted to yield a mass splitting of 3.5 keV, needed to explain the 3.5 keV X-ray line from $N_2 \to N_3 \gamma$ decay.

Despite having the RH neutrinos in this model, the masses for light neutrinos cannot be generated by the Type-I seesaw mechanism since the normal Yukawa term involving the RH neutrinos, lepton doublets and the standard model Higgs ϕ_h is forbidden by the $\mathbb{Z}_2$ symmetry. The other Yukawa term between the RH neutrinos, lepton doublets and inert doublet η is allowed, but η does not take any VEV. Hence, there is no mass term for the light neutrinos at the tree-level. However, masses for the light neutrinos gets generated radiatively at the one-loop level [90] through the diagram shown in Fig. 7.1, giving the following mass matrix for the light neutrinos [90]

$$M^{\nu}_{ij} = \sum_k \frac{y_{ik} y_{jk} M_k}{16\pi^2} \left[\frac{M^2_{\eta^0_R}}{M^2_{\eta^0_R} - M^2_k} \ln \frac{M^2_{\eta^0_R}}{M^2_k} - \frac{M^2_{\eta^0_I}}{M^2_{\eta^0_I} - M^2_k} \ln \frac{M^2_{\eta^0_I}}{M^2_k} \right], \tag{7.17}$$

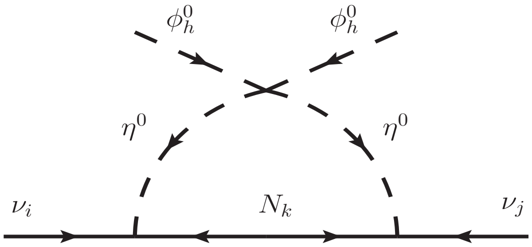

Figure 7.1: Radiative neutrino mass generation by one loop.

where M_k is the mass of k^{th} RH neutrino while $M_{\eta_R^0,\eta_I^0}$ is the mass of $\eta_{R,I}^0$. The quantities $y_{ji} = h_j U_{ji}$, where h_j are the Yukawa couplings in the last term of Eq. (7.2) and U_{ji} are the elements of the RH neutrino mixing matrix since the flavour basis (N_α, $\alpha = 1, 2, 3$) of the RH neutrinos and their mass basis (N_i, $i = 1, 23$) are related by a unitary transformation, $N_\alpha = \sum U_{\alpha i} N_i$. If we put this relation into the last term of Eq. (7.2), one can write the Yukawa term involving SM leptons and RH neutrinos in the following way

$$\mathcal{L}_N \supset h_j \bar{L}_j \tilde{\eta} U_{ji} N_i = y_{ji} \bar{L}_j \tilde{\eta} N_i \,. \tag{7.18}$$

If we consider the mass square difference between η_R^0 and η_I^0 i.e. $M^2_{\eta_R^0} - M^2_{\eta_I^0} = \lambda_5 v^2 << M_0^2$ where $M_0^2 = (M^2_{\eta_R^0} + M^2_{\eta_I^0})/2$ then the above expression reduces to the following form,

$$M_{ij}^{\nu} = \frac{\lambda_5 v^2}{16\pi^2} \sum_k \frac{y_{ik}\, y_{jk}\, M_k}{M_0^2 - M_k^2} \left[1 - \frac{M_k^2}{M_0^2 - M_k^2} \ln \frac{M_0^2}{M_k^2} \right] . \tag{7.19}$$

In this work we have considered the masses of inert scalars greater than the reheat temperature of the Universe, i.e. $M_{\eta^0_{R,I}} \sim 10^6$ GeV. The masses of RH neutrinos we consider to be around ~ 100 GeV. If we take the parameter $\lambda_5 \sim 10^{-3}$ and $v = 246$ GeV, then to obtain the neutrino masses of the order of $M_\nu \sim 10^{-11}$ GeV, we need $y_{ji}^2 \sim 10^{-1}$ which can be easily obtained. The $\mathrm{U}(1)_{L_\mu - L_\tau}$ breaking ensures that the mixing angle θ_{13} is non-zero and θ_{23} is non-maximal.

7.4 Production of Dark Matter

We consider the non-thermal production of dark matter candidates. Hence, the initial number densities of these particles are assumed to be negligibly small and their interactions with the particles in the thermal bath are also extremely feeble. As mentioned before, the lighter RH neutrino states N_2 and N_3 are our dark matter candidates, stabilised by the Z_2 symmetry. Because of their gauge and Z_2 charges they could be produced only through the decay of $Z_{\mu\tau}$ and h_1 [2] and h_2 bosons. In what follows, we will see that the dominant production channel for the RH neutrinos is via the decay of $Z_{\mu\tau}$. In order for the total abundances of N_2, N_3 to match the observed DM relic density at the present epoch, the gauge coupling has to be small $g_{\mu\tau} \lesssim 10^{-11}$. Since all the interactions of $Z_{\mu\tau}$ are proportional to the gauge coupling $g_{\mu\tau}$, the requirement of such a tiny gauge coupling makes the additional neutral gauge boson $Z_{\mu\tau}$ also decoupled from the thermal bath. Therefore, before computing the DM number density we first need to know the distribution function of mother particle $Z_{\mu\tau}$ by solving the relevant Boltzmann equation. The most general form of the Boltzmann equation describing the distribution function of any species can be expressed as,

$$\hat{L}[f] = C[f] \tag{7.20}$$

where $\hat{L}$ is the Liouville operator and f is the distribution function which we want to compute while in the RHS the term C contains interaction processes which are responsible for changing the number density of the species under considering. C is known as the collision term. If one considers an isotropic and homogeneous Universe then using the

---

[2] Since the mass of the SM-like Higgs has to be kept at 125.5 GeV, the decay channel $h_1 \to N_i N_j$ will be kinematically allowed only for lighter N_i/N_j masses.

FRW metric, the Liouville operator [3] takes the following form,

$$\hat{L} = \frac{\partial}{\partial t} - H\,p\,\frac{\partial}{\partial p}\,, \tag{7.21}$$

where p is magnitude of three momentum and H is the Hubble parameter. Now, we change the variables (p, t) to a new set of variables (ξ_p, r) using a transformation as mentioned in Ref. [240]

$$r = \frac{M_{sc}}{T},\;\; \xi_p = \left(\frac{g_s(T_0)}{g_s(T)}\right)^{1/3} \frac{p}{T}\,. \tag{7.22}$$

M_{sc} is some reference mass scale. Using the time-Temperature relationship $\frac{dT}{dt} = -HT\left(1 + \frac{T\,g_s'(T)}{3\,g_s(T)}\right)^{-1}$, the Liouville operator defined in Eq. (7.21) can be reduced to the following form containing a derivative with respect to a single variable, i.e.

$$\hat{L} = r\,H\left(1 + \frac{T g_s'}{3 g_s}\right)^{-1} \frac{\partial}{\partial r} \tag{7.23}$$

where $g_s(T)$ and $g_s'(T)$ are the effective number of degrees of freedom (d.o.f) related to entropy of the Universe and its derivative with respect to the temperature T.

The Boltzmann equation to determine the distribution function ($f_{Z_{\mu\tau}}$) of $Z_{\mu\tau}$ is then given by,

$$\hat{L} f_{Z_{\mu\tau}} = \sum_{i=1,2} C^{h_i \to Z_{\mu\tau} Z_{\mu\tau}} + C^{Z_{\mu\tau} \to\, all}\,, \tag{7.24}$$

where the first term in the RHS represents the production of $Z_{\mu\tau}$ from the decays of scalars h_1 and h_2 while the second term describing the depletion of $Z_{\mu\tau}$ due to its all possible decay modes. The expressions of collision terms $C^{h_i \to Z_{\mu\tau} Z_{\mu\tau}}$ and $C^{Z_{\mu\tau} \to\, all}$ are given in Appendix of Ref. [236]. Note that generically also scattering processes, which change

---

[3] General form of the Liouville operator is, $\hat{L} = p^\alpha \frac{\partial}{\partial x^\alpha} - \Gamma^\alpha_{\beta\gamma} p^\beta p^\gamma \frac{\partial}{\partial p^\alpha}$ where p^α is the four momentum and $\Gamma^\alpha_{\beta\gamma}$ is the affine connection by which gravitational interaction enters in the equation.

the $Z_{\mu\tau}$ number, are present, but those give a subleading contribution compared to the decay (see e.g. the Appendix of [241] for a discussion).

Once we numerically evaluate the non thermal momentum distribution of the gauge boson $Z_{\mu\tau}$, we can easily determine the number density of $Z_{\mu\tau}$ using following relation

$$n_{Z_{\mu\tau}}(r) = \frac{g\,T^3}{2\pi^2}\,\mathcal{B}(r)^3 \int d\xi_p\, \xi_p^2\, f_{Z_{\mu\tau}}(\xi_p, r)\,, \tag{7.25}$$

where

$$\mathcal{B}(r) = \left(\frac{g_s(T_0)}{g_s(T)}\right)^{1/3} = \left(\frac{g_s(M_{sc}/r)}{g_s(M_{sc}/r_0)}\right)^{1/3}. \tag{7.26}$$

Here T_0 is the initial temperature and M_{sc} is some reference mass scale. In this work we take $T_0 = 10$ TeV and $M_{sc} = M_{h_1} = 125.5$ GeV, the mass of SM Higgs boson. The entropy density of the Universe is given by [242],

$$s = \frac{2\pi^2}{45}\, g_s(T)\, T^3\,. \tag{7.27}$$

Therefore, after determining the number density of $Z_{\mu\tau}$ and the entropy of the Universe one can determine the comoving number density using the following relation,

$$Y_{Z_{\mu\tau}} = \frac{n_{Z_{\mu\tau}}}{s}\,. \tag{7.28}$$

Finally, to determine the comoving number densities of DM components N_2 and N_3, we need to solve the relevant Boltzmann equation for N_2 and N_3, which can be written in a generic form,

$$\begin{aligned}\frac{dY_{N_j}}{dr} &= \frac{V_{ij}\, M_{pl}\, r\, \sqrt{g_\star(r)}}{1.66\, M_{sc}^2\, g_s(r)} \left[\sum_{k=1,2}\sum_{i=1,2,3} \langle\Gamma_{h_k\to N_j N_i}\rangle (Y_{h_k} - Y_{N_j} Y_{N_i})\right] \\ &\quad + \frac{V_{ij}\, M_{pl}\, r\, \sqrt{g_\star(r)}}{1.66\, M_{sc}^2\, g_s(r)} \sum_{i=1,2,3} \langle\Gamma_{Z_{\mu\tau}\to N_j N_i}\rangle_{NTH} (Y_{Z_{\mu\tau}} - Y_{N_j} Y_{N_i})\,, \end{aligned} \tag{7.29}$$

where M_{pl} is the Planck mass while $g_\star(r) = \frac{g_s(r)}{\sqrt{g_\rho(r)}}\left(1 - \frac{1}{3}\frac{d\ln g_s(r)}{d\ln r}\right)$ is a function of $g_\rho(r)$ and $g_s(r)$. The parameter $V_{ij} = 2$ for $i = j$ and equal to 1 otherwise. The first term in the above equation represents the production of N_j from the decays of scalar fields h_1 and h_2. Since these scalar fields remain in thermal equilibrium throughout their cosmological evolution, one can consider their distribution function as Maxwell-Boltzmann distribution. Therefore the thermal averaged decay width for a process $h_(k) \to N_j N_i$ is given by [30]

$$\langle \Gamma_{h_k \to N_j N_i} \rangle = \Gamma_{h_k \to N_j N_i} \frac{K_1\left(r\frac{M_{h_k}}{M_{sc}}\right)}{K_2\left(r\frac{M_{h_k}}{M_{sc}}\right)}, \tag{7.30}$$

where K_i is the Modified Bessel function of i^{th} kind. As the neutral gauge boson $Z_{\mu\tau}$ is not in thermal equilibrium (due to very small value of $g_{\mu\tau}$), one cannot assume a Maxwell-Boltzmann distribution function for $Z_{\mu\tau}$. The distribution $f_{Z_{\mu\tau}}$ of $Z_{\mu\tau}$ can be found by solving Eq. (7.24) and we have shown it in Fig. 7.2. Although the shape of the distribution is similar in both cases but they differ by magnitude because in the current case $Z_{\mu\tau}$

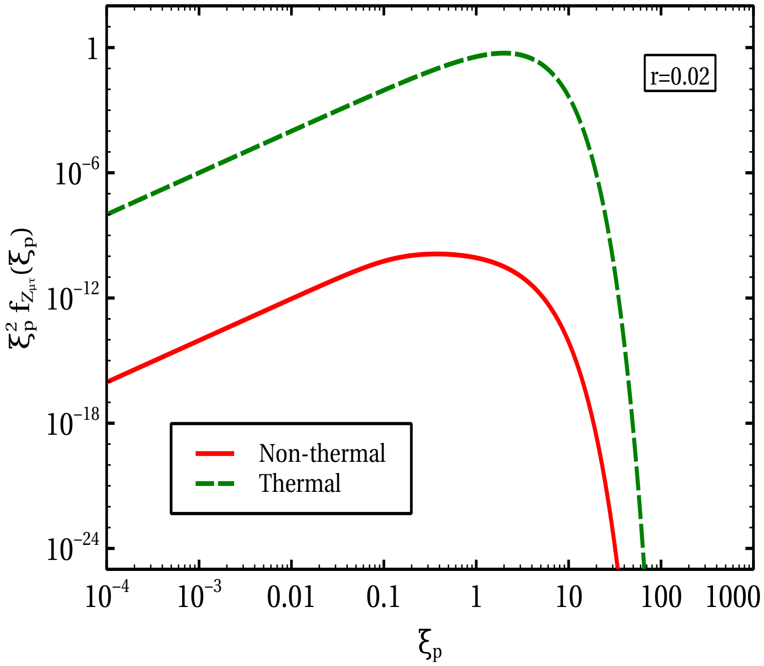

Figure 7.2: Thermal and Non-thermal distribution function of $Z_{\mu\tau}$ gauge boson.

is always out of equilibrium and never attains equilibrium value. Once we get the distribution function $f_{Z_{\mu\tau}}$ the non-thermal average of decay width for the process $Z_{\mu\tau} \to N_j N_i$ can be computed as follows

$$\langle \Gamma_{Z_{\mu\tau}\to N_j N_i} \rangle_{NTH} = M_{Z_{\mu\tau}} \Gamma_{Z_{\mu\tau}\to N_j N_i} \frac{\int \frac{f_{Z_{\mu\tau}}(p)}{\sqrt{p^2+M^2_{Z_{\mu\tau}}}} d^3p}{\int f_{Z_{\mu\tau}}(p) d^3p} \,. \tag{7.31}$$

All the relevant decay widths of h_2 and $Z_{\mu\tau}$ needed in Eq. (7.29) are given in Appendix of Ref. [236] in detail. After solving the above Boltzmann equations for j=2 and j=3, we can determine the comoving number density of the DM candidates N_2 and N_3. Therefore, one can easily determine the total DM relic density for N_2 and N_3 candidates by using the following relation [224],

$$\Omega_{DM}h^2 \;=\; 2.755 \times 10^8 \left(\frac{M_{N_2}}{\text{GeV}}\right) Y_{N_2}(T_{\text{Now}}) + 2.755 \times 10^8 \left(\frac{M_{N_3}}{\text{GeV}}\right) Y_{N_3}(T_{\text{Now}}) \,. \tag{7.32}$$

7.5 Results

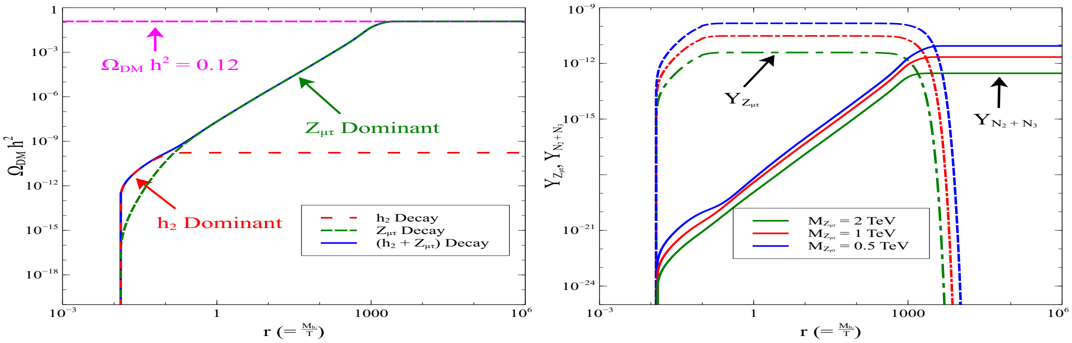

Figure 7.3: Left panel: Variation of relic density with r and contributions from h_2 and $Z_{\mu\tau}$ in the DM production. Right panel: Variation of comoving number density of $Z_{\mu\tau}$ and N_2, N_3 with r for three different values of gauge boson mass. Other parameters have been kept fixed at $g_{\mu\tau} = 1.01 \times 10^{-11}$, mixing angle $\alpha = 0.01$, gauge boson mass $M_{Z_{\mu\tau}} = 1$ TeV, DM mass $M_{DM} = 100$ GeV, BSM Higgs mass $M_{h_2} = 5$ TeV and RH neutrinos masses $M_{N_1} = 150$ GeV and $M_{DM} = M_{N_2} \simeq M_{N_3} = 100$ GeV.

Using Eqs. (7.29), (7.30), (7.31) and (7.32) we numerically compute the DM abundance. In the left panel of Fig. 7.3 we show the time evolution of the DM relic density with $r(= M_{h_1}/T)$. The left panel of the this figure shows the comparative contribution for the two DM production channels, $Z_{\mu\tau} \to N_i N_j$ and $h_2 \to N_i N_j$. We have taken masses of the RH neutrinos N_2 and N_3 as 100 GeV and hence the decay of SM-like Higgs h_1 to a pair of RH neutrinos is kinematically forbidden. From the left panel we see that for the large value of BSM Higgs mass ($M_{h_2} \sim 5$ TeV), the DM production at low r (which corresponds to high T) is dominated by h_2 decay. However, as the temperature of the universe falls and goes below the mass of the $Z_{\mu\tau}$ gauge bosons, they get produced, and for high value of r (which corresponds to comparably lower temperature of the universe), the DM production via the $Z_{\mu\tau}$ decay channel dominates. The reason for this dominance can be understood as follows. We see that the decay width $\Gamma_{Z_{\mu\tau}\to N_i N_j} \propto M_{Z_{\mu\tau}} g_{\mu\tau}^2$ while $\Gamma_{h_2 \to N_i N_j} \propto M_{h_2} h_{e\alpha} h_{e\beta}$ (as given in Appendix of Ref. [236]), where $h_{e\alpha} h_{e\beta}$ are products of two any of the Yukawa couplings $h_{e\mu}$ and $h_{e\tau}$ that appeared in Eq. (7.2). Since we have chosen $M_{Z_{\mu\tau}} \sim M_{h_2}$ we can write

$$\frac{\Gamma_{Z_{\mu\tau}\to N_i N_j}}{\Gamma_{h_2 \to N_i N_j}} \propto \frac{g_{\mu\tau}^2}{h_{e\alpha} h_{e\beta}}, \tag{7.33}$$

Since the Yukawa couplings $h_{e\alpha}$ appear as the $\mathrm{U}(1)_{L_\mu - L_\tau}$ breaking terms in the RH neutrino mass matrix which instruments the splitting of 3.5 keV between N_2 and N_3 we have from Eq. (7.13)

$$V_{e\alpha} = \frac{h_{e\alpha} v_{\mu\tau}}{\sqrt{2}} \sim 0.1\ \mathrm{GeV}. \tag{7.34}$$

Inserting this in Eq. (7.33) and using the relation $M_{Z_{\mu\tau}} = g_{\mu\tau} v_{\mu\tau}$ we get

$$\frac{\Gamma_{Z_{\mu\tau}\to N_i N_j}}{\Gamma_{h_2 \to N_i N_j}} \propto \frac{M_{Z_{\mu\tau}}^2}{V_{e\alpha}^2}, \tag{7.35}$$

explaining the dominance of the $Z_{\mu\tau}$ decay channel.

In the right panel of Fig. 7.3 we show the variation of the comoving number densities of the $Z_{\mu\tau}$ gauge boson *vis-a-vis* that of the sum of N_2 and N_3. We show this as function of r for three different values of the gauge boson mass $M_{Z_{\mu\tau}}$.

The abundance $Y_{Z_{\mu\tau}}$ (indicated by the dash line) has an initial rise, then flattens and finally decays. One can see from Eq. (7.24) that there are two collision terms in the Boltzmann Equation, one for $Z_{\mu\tau}$ production and another one for its decay to all possible channels and they are active at different times. Note that the maximal abundance of $Z_{\mu\tau}$ can be easily estimated also by the analytic formula for FIMP production, i.e. for $M_{Z_{\mu\tau}} \ll M_{h_2}$

$$\Omega^{FI} h^2 = 1.09 \times 10^{27} \frac{g}{g_S^{3/2}} \frac{M_{Z_{\mu\tau}}}{M_{h_2}^2} \Gamma_{h_2 \to Z_{\mu\tau} Z_{\mu\tau}} \sim 2.18 \times 10^{24} \frac{g_{\mu\tau}^2 M_{h_2}}{32\pi M_{Z_{\mu\tau}}} = 8.54;, \tag{7.36}$$

where g counts the number of internal degrees of freedom of the mother particle. According to eq. (7.32) this corresponds to $Y_{Z_{\mu\tau}} = 0.3 \times 10^{-10}$ and is in perfect agreement with the plateau in Fig. 7.3. One interesting point to note is that as we increase the $Z_{\mu\tau}$ mass $M_{Z_{\mu\tau}}$, keeping $g_{\mu\tau}$ fixed, the DM abundance decreases instead of increasing, as explained by the relation above. In the same figure also the production of dark matter as a result of the out-of-equilibrium decay of $Z_{\mu\tau}$ can be seen beautifully. Less production of $Z_{\mu\tau}$ results in lower DM abundance, since practically every $Z_{\mu\tau}$ produces two Dark Matter particles.

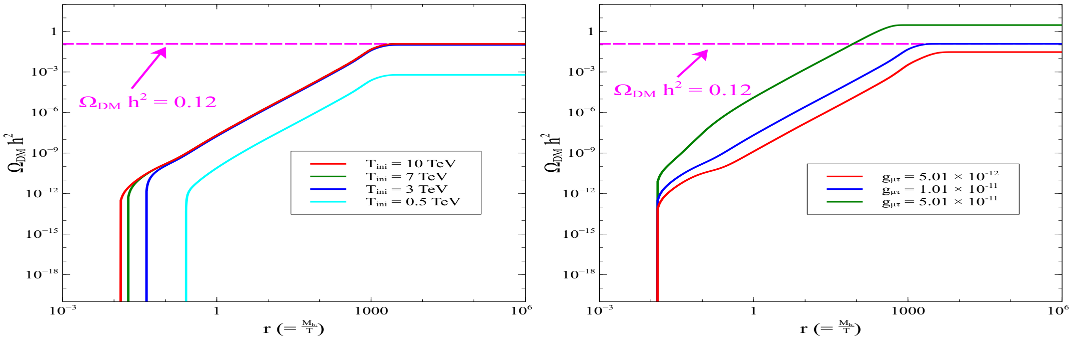

Figure 7.4: Left (Right) panel: Variation of relic density with r for different initial temperature (for different gauge coupling values), while the other parameters have been kept fixed at $g_{\mu\tau} = 1.01 \times 10^{-11}$ ($T_{ini} = 10$ TeV), mixing angle $\alpha = 0.01$, gauge boson mass $M_{Z_{\mu\tau}} = 1$ TeV, BSM Higgs mass $M_{h_2} = 5$ TeV and RH neutrinos masses $M_{N_1} = 150$ GeV, $M_{N_2} \simeq M_{N_3} = 100$ GeV.

The left panel of Fig. 7.4 shows the variation of relic density with the parameter r for different initial temperature T_{ini} (temperature where DM relic density is taken as zero). Important point to note here that as long as the initial temperature is above the mass of the gauge boson $Z_{\mu\tau}$, final relic density remains the same. However, when we reduce the initial temperature below the $Z_{\mu\tau}$ mass (shown by the cyan color curve) then final abundance reduces significantly due to the Boltzmann suppression factor. In the right panel we show the variation of DM relic density with r for different gauge coupling values ($g_{\mu\tau}$). One can see from the figure that if we increase the value of the gauge coupling, the DM production rate as well as the total DM abundance increases. The reason can be understood easily if we see the expression of DM production rate (as given in Appendix of Ref. [236]), which is almost the same as the $Z_{\mu\tau}$ decay rate, is proportional to the second power of $g_{\mu\tau}$. In the present model for $g_{\mu\tau} = 1.01 \times 10^{-11}$ we achieve the correct DM relic density value of the universe. In both the panels of Fig. 7.4, the horizontal magenta line corresponds to the present day correct DM relic density value of the universe. For the rest of the analysis, we have fixed the initial temperature of the universe at 10 TeV.

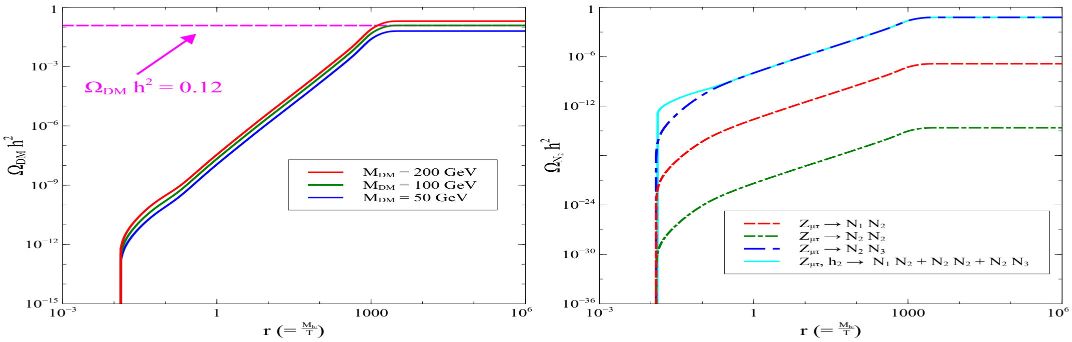

Figure 7.5: Left (Right) panel: Variation of relic density with r for different values of DM mass (Contributions in the relic density of DM from different channels of $Z_{\mu\tau}$), while the other parameters have been kept fixed at $g_{\mu\tau} = 1.01 \times 10^{-11}$, mixing angle $\alpha = 0.01$, gauge boson mass $M_{Z_{\mu\tau}} = 1$ TeV ($M_{DM} = 100$ GeV), BSM Higgs mass $M_{h_2} = 5$ TeV and RH neutrinos masses $M_{N_1} = 150$ GeV, $M_{DM} = M_{N_2} \simeq M_{N_3} = 100$ GeV.

In the left panel of Fig. 7.5, we present the variation of the DM relic density for three different values of the DM mass M_{DM} ($=M_{N_2}, M_{N_3}$). As shown in Eq. (7.32) that DM relic density is proportional to the DM mass M_{N_2} and M_{N_3} and this dependence is evident in the left panel of Fig. 7.5. For the chosen value of the parameters (mentioned in the caption), we have obtained correct relic density value (indicated by the horizontal line) of the universe for DM mass value $M_{DM} = M_{N_2} \simeq M_{N_3} = 100$ GeV, this value will be different for different set of values of the other parameters. In the right panel of Fig. 7.5, we show the decay contributions of $Z_{\mu\tau}$ in different channels. The relative contributions among the different channels is seen to differ significantly and the decay rate into N_2N_3 dominates naturally producing equal populations of the two Dark Matter candidates. Indeed, to produce degenerate neutrinos i.e. $M_{N_2} \simeq M_{N_3}$, we have considered relatively small values of $\frac{h_{e\mu}v_{\mu\tau}}{\sqrt{2}}$ and $\frac{h_{e\tau}v_{\mu\tau}}{\sqrt{2}}$ (~ 0.1), as discussed before. Therefore, the elements of the unitary matrix which relate the flavour and mass basis of the RH neutrinos take the following form, $U_{11} \sim 1$, $U_{12}, U_{13}, U_{21}, U_{31} \sim 0.01$, $U_{22} = U_{23} = \frac{1}{\sqrt{2}}$ and $U_{32} = -U_{33} = -\frac{1}{\sqrt{2}}$. Therefore, it is clear from the couplings (as listed in Appendix of Ref. [236]) that the dominant channel for DM production is $Z_{\mu\tau} \to N_2N_3$, while the other channels will be suppressed which is clearly visible in the right panel of Fig. 7.3. Similar considerations will also be true for the N_3 DM production channels.

7.6 3.5 keV γ ray line

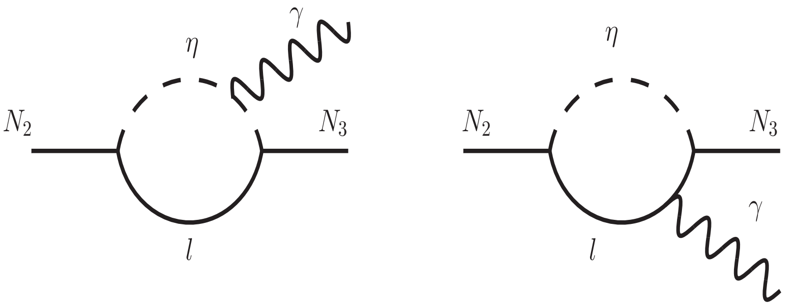

Figure 7.6: Radiative decay of RH neutrino ($N_2 \to N_3\gamma$) and 3.55 keV γ-line.

Finally, we come to the explanation of the 3.5 keV γ-ray line from the RH neutrino radiative decay $N_2 \to N_3\gamma$. Since the photon flux for a decaying Dark Matter candidate is given by

$$\Phi = \frac{1}{4\pi M_{N_2}\tau_{N_2}}\int_{l.o.s.}\rho_{N_2}(\vec{r})d\vec{r} \tag{7.37}$$

where the last integral over the N_2 density is computed along the line of sight and τ_{N_2} is the lifetime of the heavier DM particle N_2. In order to explain the 3.5 keV line from a decay such as $N_2 \to N_3\gamma$, we need not only a mass splitting between the two fermion states of $\sim$ 3.5 keV, but also a decay width of the unstable DM given as,

$$\Gamma(N_2 \to N_3\gamma) = (0.72-6.6)\times 10^{-52}\,\text{GeV}\left(\frac{M_{N_2}}{3.5\,\text{keV}}\right) = (0.2-1.9)\times 10^{-44}\,\text{GeV}\left(\frac{M_{N_2}}{100\,\text{GeV}}\right) \tag{7.38}$$

Here we are assuming that the density of N_2 is approximately half of the DM density and rescaled the result of [47] accordingly.

The relevant decay diagrams for N_2 are shown in Fig. 7.6. We consider N_2 to be slightly heavier than N_3 ($\sim$ 3.5 keV) so that it can produce the 3.5 keV γ-ray line. As discussed before, the 3.5 keV mass splitting between nearly-degenerate N_2 and N_3 can be easily achieved in our model via the $\text{U}(1)_{L_\mu-L_\tau}$ symmetry and its breaking parameters. So we take $V_{e\alpha} = \frac{h_{e\alpha}v_{\mu\tau}}{\sqrt{2}} \sim 0.1$ GeV ($\alpha = \mu, \tau$) and by suitably adjusting the $V_{e\alpha}$ parameters we can generate the 3.5 keV mass gap between N_2 and N_3. For the $\text{U}(1)_{L_\mu-L_\tau}$ conserving leading terms in Eq. (7.13) we take the values M_{ee} = 11 TeV and $M_{\mu\tau}$ = 100 GeV which gives us M_{N_2} and $M_{N_3} \sim 100$ GeV with opposite CP parities [243]. Ref. [243] has pointed out that if N_2 and N_3 have opposite CP, then the transition from N_2 to N_3 is governed only by the magnetic moment term (μ_{23}), generated at one loop level as shown in Figure 7.6. Therefore, the effective Lagrangian for the decay process $N_2 \to N_3\gamma$ is given as

$$\mathcal{L}_{eff} \approx i\frac{\mu_{23}}{2}\bar{N}_2\sigma^{\mu\nu}N_3F_{\mu\nu}\,. \tag{7.39}$$

In determining the expression for the above decay process we consider the ratio of lepton mass to RH neutrino mass to be very small ($\frac{M_l}{M_{N_2}} \ll 1$). Also, the ratio of the RH neutrino mass and the inert doublet mass is very small i.e. $\frac{M_{N_2}}{M_\eta} \ll 1$. The decay width of N_2 comes out as [244],

$$\Gamma(N_2 \to N_3\gamma) = \frac{\mu_{23}^2}{4\pi}\,\delta^3 \left(1 - P\,\frac{M_{N_3}}{M_{N_2}}\right)^2 , \tag{7.40}$$

where $\delta = \frac{M_{N_2}}{2}(1 - \frac{M_{N_3}^2}{M_{N_2}^2})$, P gives the relative CP of the two neutrino states, which in the present model is $P = -1$. The magnetic moment coefficient μ_{23} in our model is given by

$$\mu_{23} = \sum_i \frac{e}{2}\frac{1}{(4\pi)^2}\frac{M_{N_2}}{M_\eta^2}(y_{i2}y_{i3}), \tag{7.41}$$

where $y_{ij} = h_i U_{ij}$ being the derived Yukawa couplings given in Eq. (7.18) . The values of the parameters appearing in the N_2 decay width are intimately related with those that determine the light neutrino masses. In Section 7.3, we had set the parameter values to explain the tiny neutrino mass in the following order,

$$M_\eta = 10^6\,\text{GeV}, M_{N_2} = 100\,\text{GeV}, (y_{ij})^2 = 10^{-1}\,. \tag{7.42}$$

Using these in the Eq. (7.18) we get $\mu_{23} \sim \mathcal{O}(10^{-14})$ GeV^{-1}. Using Eq. (7.40), for DM mass around 100 GeV, $\delta \simeq 3.5$ keV and $\mu_{23} \sim 10^{-14}$ GeV^{-1}, we get the lifetime of N_2 of the order $\mathcal{O}(10^{-44})$ GeV, which is exactly what is needed to give the 3.5 keV line. Note that the lifetime of N_2 is then around 10^{19} sec and hence greater than the age of the universe (10^{17} sec). Hence the present model can naturally explain the origin of the claimed 3.5 keV line.

8

Conclusion

In this thesis, we have mainly studied two well known beyond standard model puzzles which are dark matter and neutrino mass. In describing them we have extended the SM gauge group as well as the particle spectrum. We will summarize the whole thesis in chapter wise.

8.1 Galactic Gamma Ray Excess and Dark Matter Phenomenology in a $U(1)_{B-L}$ Model

In Chapter 2, the $U(1)_{\mathrm{B-L}}$ symmetry that we impose is local, there is an additional gauge boson Z_{BL} in this model. Three right handed neutrinos also have to included in the model to make it anomaly free. In order to break the $U(1)_{\mathrm{B-L}}$ symmetry spontaneously, one introduces an extra SM singlet scalar ϕ_H which carries a nontrivial $\mathrm{B-L}$ charge. The $\mathrm{B-L}$ charge of this scalar can be arranged in such a way that the right handed neutrinos pick up Majorana masses when ϕ_H gets a VEV, breaking the $U(1)_{\mathrm{B-L}}$ symmetry spontaneously. As a result the Z_{BL} gauge boson also becomes massive. This extra neutral gauge boson has been searched for at collider experiments which put a stringent bound on the combination of the new $U(1)_{\mathrm{B-L}}$ gauge coupling and the mass of Z_{BL}. We extended this gauged $U(1)_{\mathrm{B-L}}$ model further by adding another complex SM scalar ϕ_{DM} which is charged under $U(1)_{\mathrm{B-L}}$ and arranged its $U(1)_{\mathrm{B-L}}$ charge in such away that all decays of ϕ_{DM} are forbidden making it a stable DM candidate. We imposed constraints coming from vacuum stability, LEP bound on $M_{Z_{BL}}/g_{BL}$, LHC bounds on signal strength of the SM-like Higgs and invisible decay width of the SM-like Higgs, and found the regions of the model parameter space which can simultaneously explain the observed DM relic density as well as the Fermi-LAT GC gamma ray excess and at the same time evaded the bounds from the direct detection experiments such as LUX. We showed that for DM masses in the range 40-55 GeV and for a wide range of $U(1)_{\mathrm{B-L}}$ gauge boson masses, one can satisfy all these constraints if the additional neutral Higgs scalar has a mass around the resonance region.

8.2 Neutrino Mass, Dark Matter and Anomalous Magnetic Moment of Muon in a $\mathrm{U}(1)_{L_\mu - L_\tau}$ Model

In Chapter 3, we propose a gauged $L_\mu - L_\tau$ extension of the SM with two additional scalars and three additional right-handed neutrinos. Since we require $U(1)_{L_\mu - L_\tau}$ to be local, we get an extra gauge boson, $Z_{\mu\tau}$. One of the most appealing aspects of the gauged $U(1)_{L_\mu - L_\tau}$ extension of the SM is that it does not introduce any anomaly in the theory [230–232]. This model can explain the anomalous muon $(g-2)$ data, small neutrino masses and peculiar mixing pattern, and provides a viable dark matter candidate. It can explain the relic abundance as well as the galactic centre gamma ray excess while satisfying all other experimental bounds. It also predict no CP violation in neutrino oscillation experiments. This model is phenomenologically rich and predictive and should be testable in forthcoming high energy physics experiments, including collider experiments, dark matter experiments as well as neutrino oscillation experiments.

8.3 Singlet-Triplet Fermionic Dark Matter and LHC Phenomenology

In Chapter 4, we study WIMP-type DM and shown that its relic density, detection at direct and indirect detection experiments, and detection at collider experiments are intimately inter-related. In this work we have proposed a fermion DM model that can successfully explain the DM relic density, can be tested in future direct detection experiments, and can be produced and tested at the 13 TeV run of the LHC. The present model allows for low mass fermionic DM that satisfactorily produces the observed relic density of the universe. It can be tested at the current and next-generation DM direct detection experiments. More importantly the 100 GeV mass range of the DM candidate in this model allows its production and detection at the LHC. The 13 TeV LHC can discover this fermionic DM candidate for with more than 3σ statistical significance with reasonable luminosity.

8.4 Neutrino Mass, Leptogenesis and FIMP Dark Matter in a $\mathrm{U(1)_{B-L}}$ Model

In Chapter 5, we study the spontaneously broken local $\mathrm{U(1)_{B-L}}$ extension of the SM with three additional RH and two additional scalars can explain the three main evidences for physics beyond the SM, *viz.*, small neutrino masses, matter-antimatter asymmetry of the Universe and dark matter. Tiny neutrino masses and all mixing angles can be obtained via Type I seesaw mechanism where we chose a certain pattern for the real and complex Yukawa couplings. The model gave a definite prediction for the CP violating phase to be measured in the next generation long baseline experiments. The dark matter candidate is a scalar which is neutral under the SM gauge group and has a nonzero $\mathrm{B-L}$ charge. DM is made stable by virtue of a remnant $\mathbb{Z}_2$ symmetry arises after the spontaneous breaking of $\mathrm{U(1)_{B-L}}$ gauge symmetry. This can be achieved by imposing a suitable $\mathrm{B-L}$ charge on

ϕ_{DM} so that the Lagrangian does not contain any odd term of ϕ_{DM}. This scalar DM can easily be taken as a FIMP candidate which is produced from the decays and annihilations of SM and BSM particles. Therefore, even if the WIMP type DM is ruled out in near future from direct detection experiments this present variant of $\mathrm{U(1)_{B-L}}$ scenario with FIMP DM will still survive. Further, since g_{BL} is of the order of SM gauge couplings, this model has the potential to be tested in the LHC or in other future collider experiments by detecting $\mathrm{B-L}$ gauge boson Z_{BL} from its SM decay products. Moreover, considering the masses of RH neutrinos in TeV scale allow us to simultaneously explain the baryon asymmetry of the Universe from resonant leptogenesis, FIMP DM production via Freeze-in mechanism and also neutrino masses and mixing from TeV scale Type-I seesaw. Thus, all three phenomena addressing in this article are interconnected to each other.

8.5 FIMP and Muon $(g-2)$ in a $\mathrm{U}(1)_{L_\mu-L_\tau}$ Model

This section will summarize Chapter 6. Our proposed $\mathrm{U}(1)_{L_\mu-L_\tau}$ extension of the SM can explain the three main puzzles that demand beyond Standard Model physics. First, it can successfully explain the smallness of neutrino masses via the Type-I seesaw mechanism as well as the peculiar mixing pattern of the neutrinos via the $\mathrm{U}(1)_{L_\mu-L_\tau}$ gauge symmetry that also acts on the lepton flavours, thereby giving a pattern to the light neutrino mass matrix. Second, the additional one loop contribution of the extra neutral gauge boson $Z_{\mu\tau}$ can successfully satisfy the muon $(g-2)$ data. And finally, the model has a SM singlet scalar with non-zero $\mathrm{U}(1)_{L_\mu-L_\tau}$, that makes it stable and which acts as a non-thermal dark matter candidate, thereby satisfying constraint on the relic abundance and at the same time evading all bounds coming from direct and indirect dark matter detection experiments.

8.6 Explaining the 3.5 keV X-ray Line in a $L_\mu - L_\tau$ Extension of the Inert Doublet Model

Chapter 7 deals with the extension of the SM gauge group by a local $U(1)_{L_\mu - L_\tau}$ gauge group and a $\mathbb{Z}_2$ discrete symmetry. The particles spectrum was extended by three RH neutrinos, one inert doublet and one SM gauge singlet scalar. We showed that this model explains the observed 3.5 keV line consistently with the relic dark matter abundance in the framework of a model that generates light neutrino masses radiatively. The Type I seesaw in this model is forbidden by the $\mathbb{Z}_2$ symmetry but tiny neutrino masses are generated via a one-loop diagram involving the RH neutrino and the inert doublet which does not take any VEV. We considered inert scalar masses $\sim 10^6$ GeV, which is higher than the reheat temperature, and RH neutrino masses ~ 100 GeV. Then for parameter choices $\lambda_5 \sim 10^{-3}$ and Yukawa couplings $y^2_{ji} \sim 10^{-1}$ we can get light neutrino masses $M_\nu \sim 0.01$ eV. The RH neutrino mass matrix in our model is non-diagonal and carries the $L_\mu - L_\tau$ flavour structure which ensures that two of the RH neutrino remain degenerate in the $U(1)_{L_\mu - L_\tau}$ symmetric limit. The spontaneous breaking of the $U(1)_{L_\mu - L_\tau}$ gauge symmetry generates terms in the RH neutrino mass matrix that splits the two degenerate RH neutrinos by 3.5 keV, while the third one remains heavier. The two nearly degenerate neutrinos form the two-component DM in our model. We showed that the RH neutrinos are predominately produced by the decay of the extra neutral gauge boson $Z_{\mu\tau}$, which are taken in the 1 TeV mass range in our model. The production of RH neutrinos from decay of the additional scalar h_2 is subdominant, while the annihilation channels have negligible effect. We showed that the peculiar structure of the unitary matrix (U) which relates the flavour and mass basis of the RH neutrinos ensures that the decay mode $Z_{\mu\tau} \to N_2 N_3$ is the dominant one among the other channels. Since the associated gauge coupling $g_{\mu\tau}$ is taken to be very small here, the $Z_{\mu\tau}$ stays out of equilibrium in the early universe and the RH neutrinos are produced by the freeze-in mechanism. We solved the coupled Boltzmann equation numerically and showed the dependence of the DM relic abundance on initial temperature T_{ini}, $g_{\mu\tau}$, $M_{Z_{\mu\tau}}$

and M_{DM}. Finally, we showed that the heavier of the two DM component N_2 can decay into the lighter N_3 ($N_2 \rightarrow N_3\gamma$) through one loop diagram, thus producing the 3.5 keV X-ray line that was observed by Chandra satellite. The model parameter values which determine the lifetime of N_2 were obtained through constraints from the light neutrino mass sector and gave a decay rate of 10^{-44} GeV for N_2. So the lifetime of the heavier Dark Matter particle is consistent with both the age of the universe as well as the strength of the observed 3.5 keV line.

Bibliography

[1] B. W. Lee, C. Quigg and H. B. Thacker, *Weak Interactions at Very High-Energies: The Role of the Higgs Boson Mass*, *Phys. Rev.* **D16** (1977) 1519.

[2] Super-Kamiokande collaboration, *Evidence for oscillation of atmospheric neutrinos*, *Phys. Rev. Lett.* **81** (1998) 1562 [`hep-ex/9807003`].

[3] SNO collaboration, *Direct evidence for neutrino flavor transformation from neutral current interactions in the Sudbury Neutrino Observatory*, *Phys. Rev. Lett.* **89** (2002) 011301 [`nucl-ex/0204008`].

[4] KamLAND collaboration, *First results from KamLAND: Evidence for reactor anti-neutrino disappearance*, *Phys. Rev. Lett.* **90** (2003) 021802 [`hep-ex/0212021`].

[5] Daya Bay collaboration, *Measurement of the Reactor Antineutrino Flux and Spectrum at Daya Bay*, *Phys. Rev. Lett.* **116** (2016) 061801 [`1508.04233`].

[6] RENO collaboration, *Observation of Energy and Baseline Dependent Reactor Antineutrino Disappearance in the RENO Experiment*, *Phys. Rev. Lett.* **116** (2016) 211801 [`1511.05849`].

[7] Double Chooz collaboration, *Improved measurements of the neutrino mixing angle θ_{13} with the Double Chooz detector*, *JHEP* **10** (2014) 086 [1406.7763].

[8] T2K collaboration, *Measurements of neutrino oscillation in appearance and disappearance channels by the T2K experiment with 6.6×10^{20} protons on target*, *Phys. Rev.* **D91** (2015) 072010 [1502.01550].

[9] T2K collaboration, *Anti-neutrino oscillations with T2K*, 1508.06153.

[10] NOvA collaboration, *First measurement of electron neutrino appearance in NOvA*, *Phys. Rev. Lett.* **116** (2016) 151806 [1601.05022].

[11] NOvA collaboration, *First measurement of muon-neutrino disappearance in NOvA*, *Phys. Rev.* **D93** (2016) 051104 [1601.05037].

[12] Particle Data Group collaboration, *Review of Particle Physics*, *Chin. Phys.* **C40** (2016) 100001.

[13] A. D. Sakharov, *Violation of CP Invariance, C asymmetry, and baryon asymmetry of the universe*, *Pisma Zh. Eksp. Teor. Fiz.* **5** (1967) 32.

[14] F. Zwicky, *On the Masses of Nebulae and of Clusters of Nebulae*, *Astrophys. J.* **86** (1937) 217.

[15] Y. Sofue and V. Rubin, *Rotation curves of spiral galaxies*, *Ann. Rev. Astron. Astrophys.* **39** (2001) 137 [astro-ph/0010594].

[16] D. Clowe, A. Gonzalez and M. Markevitch, *Weak lensing mass reconstruction of the interacting cluster 1E0657-558: Direct evidence for the existence of dark matter*, *Astrophys. J.* **604** (2004) 596 [astro-ph/0312273].

[17] D. Harvey, R. Massey, T. Kitching, A. Taylor and E. Tittley, *The non-gravitational interactions of dark matter in colliding galaxy clusters*, *Science* **347** (2015) 1462 [1503.07675].

[18] M. Bartelmann and P. Schneider, *Weak gravitational lensing*, *Phys. Rept.* **340** (2001) 291 [`astro-ph/9912508`].

[19] WMAP collaboration, *Nine-Year Wilkinson Microwave Anisotropy Probe (WMAP) Observations: Cosmological Parameter Results*, *Astrophys. J. Suppl.* **208** (2013) 19 [`1212.5226`].

[20] PLANCK collaboration, *Planck 2015 results. XIII. Cosmological parameters*, *Astron. Astrophys.* **594** (2016) A13 [`1502.01589`].

[21] M. Milgrom, *A Modification of the Newtonian dynamics as a possible alternative to the hidden mass hypothesis*, *Astrophys. J.* **270** (1983) 365.

[22] A. Almog and D. Garlaschelli, *Binary versus non-binary information in real time series: empirical results and maximum-entropy matrix models*, *New J. Phys.* **16** (2014) 093015 [`1404.7275`].

[23] EROS-2 collaboration, *Limits on the Macho Content of the Galactic Halo from the EROS-2 Survey of the Magellanic Clouds*, *Astron. Astrophys.* **469** (2007) 387 [`astro-ph/0607207`].

[24] MACHO collaboration, *MACHO project limits on black hole dark matter in the 1-30 solar mass range*, *Astrophys. J.* **550** (2001) L169 [`astro-ph/0011506`].

[25] S. M. Koushiappas and A. Loeb, *Dynamics of Dwarf Galaxies Disfavor Stellar-Mass Black Holes as Dark Matter*, *Phys. Rev. Lett.* **119** (2017) 041102 [`1704.01668`].

[26] T. D. Brandt, *Constraints on MACHO Dark Matter from Compact Stellar Systems in Ultra-Faint Dwarf Galaxies*, *Astrophys. J.* **824** (2016) L31 [`1605.03665`].

[27] MACHO collaboration, *The MACHO project: Microlensing results from 5.7 years of LMC observations*, *Astrophys. J.* **542** (2000) 281 [`astro-ph/0001272`].

[28] R. Magee, A.-S. Deutsch, P. McClincy, C. Hanna, C. Horst, D. Meacher et al., *Methods for the detection of gravitational waves from subsolar mass ultracompact binaries*, *Phys. Rev.* **D98** (2018) 103024 [`1808.04772`].

[29] M. Taoso, G. Bertone and A. Masiero, *Dark Matter Candidates: A Ten-Point Test*, *JCAP* **0803** (2008) 022 [`0711.4996`].

[30] P. Gondolo and G. Gelmini, *Cosmic abundances of stable particles: Improved analysis*, *Nucl. Phys.* **B360** (1991) 145.

[31] G. Belanger, F. Boudjema, A. Pukhov and A. Semenov, *MicrOMEGAs 2.0: A Program to calculate the relic density of dark matter in a generic model*, *Comput. Phys. Commun.* **176** (2007) 367 [`hep-ph/0607059`].

[32] G. Belanger, F. Boudjema, A. Pukhov and A. Semenov, *Dark matter direct detection rate in a generic model with micrOMEGAs 2.2*, *Comput. Phys. Commun.* **180** (2009) 747 [`0803.2360`].

[33] G. Belanger, F. Boudjema, A. Pukhov and A. Semenov, *micrOMEGAs*$_3$*: A program for calculating dark matter observables*, *Comput. Phys. Commun.* **185** (2014) 960 [`1305.0237`].

[34] L. J. Hall, K. Jedamzik, J. March-Russell and S. M. West, *Freeze-In Production of FIMP Dark Matter*, *JHEP* **03** (2010) 080 [`0911.1120`].

[35] T. Marrodán Undagoitia and L. Rauch, *Dark matter direct-detection experiments*, *J. Phys.* **G43** (2016) 013001 [`1509.08767`].

[36] J. Cooley, *Overview of Non-Liquid Noble Direct Detection Dark Matter Experiments*, *Phys. Dark Univ.* **4** (2014) 92 [`1410.4960`].

[37] J. Cooley, *Overview of Non-Liquid Noble Direct Detection Dark Matter Experiments*, *Phys. Dark Univ.* **4** (2014) 92 [`1410.4960`].

[38] C. Weniger, *A Tentative Gamma-Ray Line from Dark Matter Annihilation at the Fermi Large Area Telescope*, *JCAP* **1208** (2012) 007 [`1204.2797`].

[39] L. Goodenough and D. Hooper, *Possible Evidence For Dark Matter Annihilation In The Inner Milky Way From The Fermi Gamma Ray Space Telescope*, `0910.2998`.

[40] D. Hooper and L. Goodenough, *Dark Matter Annihilation in The Galactic Center As Seen by the Fermi Gamma Ray Space Telescope*, *Phys. Lett.* **B697** (2011) 412 [`1010.2752`].

[41] FERMI-LAT collaboration, *The Large Area Telescope on the Fermi Gamma-ray Space Telescope Mission*, *Astrophys. J.* **697** (2009) 1071 [`0902.1089`].

[42] S. K. Lee, M. Lisanti, B. R. Safdi, T. R. Slatyer and W. Xue, *Evidence for Unresolved γ-Ray Point Sources in the Inner Galaxy*, *Phys. Rev. Lett.* **116** (2016) 051103 [`1506.05124`].

[43] R. Bartels, S. Krishnamurthy and C. Weniger, *Strong support for the millisecond pulsar origin of the Galactic center GeV excess*, *Phys. Rev. Lett.* **116** (2016) 051102 [`1506.05104`].

[44] A. W. Strong, I. V. Moskalenko and V. S. Ptuskin, *Cosmic-ray propagation and interactions in the Galaxy*, *Ann. Rev. Nucl. Part. Sci.* **57** (2007) 285 [`astro-ph/0701517`].

[45] PAMELA collaboration, *An anomalous positron abundance in cosmic rays with energies 1.5-100 GeV*, *Nature* **458** (2009) 607 [`0810.4995`].

[46] D. Hooper, I. Cholis, T. Linden and K. Fang, *HAWC Observations Strongly Favor Pulsar Interpretations of the Cosmic-Ray Positron Excess*, *Phys. Rev.* **D96** (2017) 103013 [`1702.08436`].

[47] E. Bulbul, M. Markevitch, A. Foster, R. K. Smith, M. Loewenstein and S. W. Randall, *Detection of An Unidentified Emission Line in the Stacked X-ray spectrum of Galaxy Clusters*, *Astrophys. J.* **789** (2014) 13 [`1402.2301`].

[48] A. Boyarsky, O. Ruchayskiy, D. Iakubovskyi and J. Franse, *Unidentified Line in X-Ray Spectra of the Andromeda Galaxy and Perseus Galaxy Cluster*, *Phys. Rev. Lett.* **113** (2014) 251301 [`1402.4119`].

[49] N. Cappelluti, E. Bulbul, A. Foster, P. Natarajan, M. C. Urry, M. W. Bautz et al., *Searching for the 3.5 keV Line in the Deep Fields with Chandra: the 10 Ms observations*, *Astrophys. J.* **854** (2018) 179 [`1701.07932`].

[50] V. Brdar, J. Kopp, J. Liu and X.-P. Wang, *X-Ray Lines from Dark Matter Annihilation at the keV Scale*, *Phys. Rev. Lett.* **120** (2018) 061301 [`1710.02146`].

[51] A. Biswas, S. Ganguly and S. Roy, *Fermionic dark matter via UV and IR freeze-in and its possible X-ray signature*, `1907.07973`.

[52] R. Davis, Jr., D. S. Harmer and K. C. Hoffman, *Search for neutrinos from the sun*, *Phys. Rev. Lett.* **20** (1968) 1205.

[53] B. T. Cleveland, T. Daily, R. Davis, Jr., J. R. Distel, K. Lande, C. K. Lee et al., *Measurement of the solar electron neutrino flux with the Homestake chlorine detector*, *Astrophys. J.* **496** (1998) 505.

[54] J. N. Bahcall, W. A. Fowler, I. Iben, Jr. and R. L. Sears, *Solar neutrino flux*, *Astrophys. J.* **137** (1963) 344.

[55] J. N. Bahcall, M. H. Pinsonneault and S. Basu, *Solar models: Current epoch and time dependences, neutrinos, and helioseismological properties*, *Astrophys. J.* **555** (2001) 990 [`astro-ph/0010346`].

[56] KAMIOKANDE-II collaboration, *Observation of B-8 Solar Neutrinos in the Kamiokande-II Detector*, *Phys. Rev. Lett.* **63** (1989) 16.

[57] KAMIOKANDE-II collaboration, *Results from one thousand days of real time directional solar neutrino data*, *Phys. Rev. Lett.* **65** (1990) 1297.

[58] KAMIOKANDE-II collaboration, *Constraints on neutrino oscillation parameters from the Kamiokande-II solar neutrino data*, *Phys. Rev. Lett.* **65** (1990) 1301.

[59] KAMIOKANDE collaboration, *Solar neutrino data covering solar cycle 22*, *Phys. Rev. Lett.* **77** (1996) 1683.

[60] SUPER-KAMIOKANDE collaboration, *Solar B-8 and hep neutrino measurements from 1258 days of Super-Kamiokande data*, *Phys. Rev. Lett.* **86** (2001) 5651 [`hep-ex/0103032`].

[61] SUPER-KAMIOKANDE collaboration, *Constraints on neutrino oscillations using 1258 days of Super-Kamiokande solar neutrino data*, *Phys. Rev. Lett.* **86** (2001) 5656 [`hep-ex/0103033`].

[62] GALLEX collaboration, *Solar neutrinos observed by GALLEX at Gran Sasso.*, *Phys. Lett.* **B285** (1992) 376.

[63] GALLEX collaboration, *GALLEX solar neutrino observations: Results for GALLEX IV*, *Phys. Lett.* **B447** (1999) 127.

[64] GNO collaboration, *GNO solar neutrino observations: Results for GNO I*, *Phys. Lett.* **B490** (2000) 16 [`hep-ex/0006034`].

[65] GNO collaboration, *Complete results for five years of GNO solar neutrino observations*, *Phys. Lett.* **B616** (2005) 174 [`hep-ex/0504037`].

[66] SAGE collaboration, *Results from SAGE*, *Phys. Lett.* **B328** (1994) 234.

[67] SAGE collaboration, *Measurement of the solar neutrino capture rate with gallium metal*, *Phys. Rev.* **C60** (1999) 055801 [`astro-ph/9907113`].

[68] SAGE collaboration, *Measurement of the solar neutrino capture rate by SAGE and implications for neutrino oscillations in vacuum*, Phys. Rev. Lett. **83** (1999) 4686 [`astro-ph/9907131`].

[69] SAGE collaboration, *Solar neutrino flux measurements by the Soviet-American Gallium Experiment (SAGE) for half the 22 year solar cycle*, J. Exp. Theor. Phys. **95** (2002) 181 [`astro-ph/0204245`].

[70] SNO collaboration, *Measurement of the rate of* $\nu_e + d \to p + p + e^-$ *interactions produced by* ^8B *solar neutrinos at the Sudbury Neutrino Observatory*, Phys. Rev. Lett. **87** (2001) 071301 [`nucl-ex/0106015`].

[71] SNO collaboration, *Measurement of day and night neutrino energy spectra at SNO and constraints on neutrino mixing parameters*, Phys. Rev. Lett. **89** (2002) 011302 [`nucl-ex/0204009`].

[72] KamLAND collaboration, *Measurement of neutrino oscillation with KamLAND: Evidence of spectral distortion*, Phys. Rev. Lett. **94** (2005) 081801 [`hep-ex/0406035`].

[73] KamLAND collaboration, *Precision Measurement of Neutrino Oscillation Parameters with KamLAND*, Phys. Rev. Lett. **100** (2008) 221803 [`0801.4589`].

[74] Borexino collaboration, *First real time detection of Be-7 solar neutrinos by Borexino*, Phys. Lett. **B658** (2008) 101 [`0708.2251`].

[75] Borexino collaboration, *Direct Measurement of the Be-7 Solar Neutrino Flux with 192 Days of Borexino Data*, Phys. Rev. Lett. **101** (2008) 091302 [`0805.3843`].

[76] Super-Kamiokande collaboration, *Study of the atmospheric neutrino flux in the multi-GeV energy range*, Phys. Lett. **B436** (1998) 33 [`hep-ex/9805006`].

[77] SUPER-KAMIOKANDE collaboration, *Measurement of the flux and zenith angle distribution of upward through going muons by Super-Kamiokande*, *Phys. Rev. Lett.* **82** (1999) 2644 [`hep-ex/9812014`].

[78] T. J. Haines et al., *Calculation of Atmospheric Neutrino Induced Backgrounds in a Nucleon Decay Search*, *Phys. Rev. Lett.* **57** (1986) 1986.

[79] D. Casper et al., *Measurement of atmospheric neutrino composition with IMB-3*, *Phys. Rev. Lett.* **66** (1991) 2561.

[80] R. Becker-Szendy et al., *The Electron-neutrino and muon-neutrino content of the atmospheric flux*, *Phys. Rev.* **D46** (1992) 3720.

[81] KAMIOKANDE-II collaboration, *Experimental Study of the Atmospheric Neutrino Flux*, *Phys. Lett.* **B205** (1988) 416.

[82] KAMIOKANDE collaboration, *Atmospheric muon-neutrino / electron-neutrino ratio in the multiGeV energy range*, *Phys. Lett.* **B335** (1994) 237.

[83] K2K collaboration, *Measurement of Neutrino Oscillation by the K2K Experiment*, *Phys. Rev.* **D74** (2006) 072003 [`hep-ex/0606032`].

[84] MINOS collaboration, *Observation of muon neutrino disappearance with the MINOS detectors and the NuMI neutrino beam*, *Phys. Rev. Lett.* **97** (2006) 191801 [`hep-ex/0607088`].

[85] MINOS collaboration, *Measurement of Neutrino Oscillations with the MINOS Detectors in the NuMI Beam*, *Phys. Rev. Lett.* **101** (2008) 131802 [`0806.2237`].

[86] B. Pontecorvo, *Mesonium and anti-mesonium*, *Sov. Phys. JETP* **6** (1957) 429.

[87] B. Pontecorvo, *Inverse beta processes and nonconservation of lepton charge*, *Sov. Phys. JETP* **7** (1958) 172.

[88] Z. Maki, M. Nakagawa and S. Sakata, *Remarks on the unified model of elementary particles*, *Prog. Theor. Phys.* **28** (1962) 870.

[89] F. Capozzi, E. Lisi, A. Marrone, D. Montanino and A. Palazzo, *Neutrino masses and mixings: Status of known and unknown* 3ν *parameters*, *Nucl. Phys.* **B908** (2016) 218 [`1601.07777`].

[90] E. Ma, *Verifiable radiative seesaw mechanism of neutrino mass and dark matter*, *Phys. Rev.* **D73** (2006) 077301 [`hep-ph/0601225`].

[91] A. Zee, *A Theory of Lepton Number Violation, Neutrino Majorana Mass, and Oscillation*, *Phys. Lett.* **93B** (1980) 389.

[92] S. Khan, M. Mitra and A. Patra, *Neutrino and Collider Implications of a Left-Right Extended Zee Model*, *Phys. Rev.* **D98** (2018) 115038 [`1805.09844`].

[93] A. Biswas, S. Choubey and S. Khan, *Galactic gamma ray excess and dark matter phenomenology in a* $U(1)_{B-L}$ *model*, *JHEP* **08** (2016) 114 [`1604.06566`].

[94] R. N. Mohapatra and R. E. Marshak, *Local B-L Symmetry of Electroweak Interactions, Majorana Neutrinos and Neutron Oscillations*, *Phys. Rev. Lett.* **44** (1980) 1316.

[95] H. M. Georgi, S. L. Glashow and S. Nussinov, *Unconventional Model of Neutrino Masses*, *Nucl. Phys.* **B193** (1981) 297.

[96] C. Wetterich, *Neutrino Masses and the Scale of B-L Violation*, *Nucl. Phys.* **B187** (1981) 343.

[97] M. Lindner, D. Schmidt and T. Schwetz, *Dark Matter and neutrino masses from global* $U(1)_{B-L}$ *symmetry breaking*, *Phys. Lett.* **B705** (2011) 324 [`1105.4626`].

[98] T. Mondal and T. Basak, *Class of Higgs-portal Dark Matter models in the light of gamma-ray excess from Galactic center*, *Phys. Lett.* **B744** (2015) 208 [`1405.4877`].

[99] N. Okada and O. Seto, *Higgs portal dark matter in the minimal gauged* $U(1)_{B-L}$ *model*, *Phys. Rev.* **D82** (2010) 023507 [1002.2525].

[100] N. Okada and Y. Orikasa, *Dark matter in the classically conformal B-L model*, *Phys. Rev.* **D85** (2012) 115006 [1202.1405].

[101] L. Basso, O. Fischer and J. J. van der Bij, *Natural* Z' *model with an inverse seesaw mechanism and leptonic dark matter*, *Phys. Rev.* **D87** (2013) 035015 [1207.3250].

[102] T. Basak and T. Mondal, *Constraining Minimal* $U(1)_{B-L}$ *model from Dark Matter Observations*, *Phys. Rev.* **D89** (2014) 063527 [1308.0023].

[103] B. L. Sánchez-Vega, J. C. Montero and E. R. Schmitz, *Complex Scalar DM in a B-L Model*, *Phys. Rev.* **D90** (2014) 055022 [1404.5973].

[104] J. Guo, Z. Kang, P. Ko and Y. Orikasa, *Accidental dark matter: Case in the scale invariant local B-L model*, *Phys. Rev.* **D91** (2015) 115017 [1502.00508].

[105] W. Rodejohann and C. E. Yaguna, *Scalar dark matter in the* $B-L$ *model*, *JCAP* **1512** (2015) 032 [1509.04036].

[106] N. Okada and S. Okada, Z'_{BL} *portal dark matter and LHC Run-2 results*, *Phys. Rev.* **D93** (2016) 075003 [1601.07526].

[107] W. Buchmuller and T. Yanagida, *Baryogenesis and the scale of B-L breaking*, *Phys. Lett.* **B302** (1993) 240.

[108] W. Buchmuller and M. Plumacher, *Baryon asymmetry and neutrino mixing*, *Phys. Lett.* **B389** (1996) 73 [hep-ph/9608308].

[109] T. R. Dulaney, P. Fileviez Perez and M. B. Wise, *Dark Matter, Baryon Asymmetry, and Spontaneous B and L Breaking*, *Phys. Rev.* **D83** (2011) 023520 [1005.0617].

[110] F. Calore, I. Cholis, C. McCabe and C. Weniger, *A Tale of Tails: Dark Matter Interpretations of the Fermi GeV Excess in Light of Background Model Systematics*, *Phys. Rev.* **D91** (2015) 063003 [`1411.4647`].

[111] M. Carena, A. Daleo, B. A. Dobrescu and T. M. P. Tait, *Z' gauge bosons at the Tevatron*, *Phys. Rev.* **D70** (2004) 093009 [`hep-ph/0408098`].

[112] G. Cacciapaglia, C. Csaki, G. Marandella and A. Strumia, *The Minimal Set of Electroweak Precision Parameters*, *Phys. Rev.* **D74** (2006) 033011 [`hep-ph/0604111`].

[113] ATLAS collaboration, *Search for high-mass dilepton resonances in pp collisions at $\sqrt{s} = 8$ TeV with the ATLAS detector*, *Phys. Rev.* **D90** (2014) 052005 [`1405.4123`].

[114] LUX collaboration, *First results from the LUX dark matter experiment at the Sanford Underground Research Facility*, *Phys. Rev. Lett.* **112** (2014) 091303 [`1310.8214`].

[115] LUX collaboration, *Improved Limits on Scattering of Weakly Interacting Massive Particles from Reanalysis of 2013 LUX Data*, *Phys. Rev. Lett.* **116** (2016) 161301 [`1512.03506`].

[116] J. M. Cline, K. Kainulainen, P. Scott and C. Weniger, *Update on scalar singlet dark matter*, *Phys. Rev.* **D88** (2013) 055025 [`1306.4710`].

[117] Particle Data Group collaboration, *Review of Particle Physics*, *Chin. Phys.* **C38** (2014) 090001.

[118] P. Bechtle, S. Heinemeyer, O. Stål, T. Stefaniak and G. Weiglein, *Probing the Standard Model with Higgs signal rates from the Tevatron, the LHC and a future ILC*, *JHEP* **11** (2014) 039 [`1403.1582`].

[119] G. Belanger, B. Dumont, U. Ellwanger, J. F. Gunion and S. Kraml, *Status of invisible Higgs decays*, *Phys. Lett.* **B723** (2013) 340 [`1302.5694`].

[120] A. Semenov, *LanHEP - a package for automatic generation of Feynman rules from the Lagrangian. Updated version 3.1*, `1005.1909`.

[121] M. Cirelli, G. Corcella, A. Hektor, G. Hutsi, M. Kadastik, P. Panci et al., *PPPC 4 DM ID: A Poor Particle Physicist Cookbook for Dark Matter Indirect Detection*, *JCAP* **1103** (2011) 051 [`1012.4515`].

[122] J. F. Navarro, C. S. Frenk and S. D. M. White, *A Universal density profile from hierarchical clustering*, *Astrophys. J.* **490** (1997) 493 [`astro-ph/9611107`].

[123] J. Einasto, *On the Construction of a Composite Model for the Galaxy and on the Determination of the System of Galactic Parameters*, *Trudy Astrofizicheskogo Instituta Alma-Ata* **5** (1965) 87.

[124] L. Bergstrom, P. Ullio and J. H. Buckley, *Observability of gamma-rays from dark matter neutralino annihilations in the Milky Way halo*, *Astropart. Phys.* **9** (1998) 137 [`astro-ph/9712318`].

[125] B. Moore, T. R. Quinn, F. Governato, J. Stadel and G. Lake, *Cold collapse and the core catastrophe*, *Mon. Not. Roy. Astron. Soc.* **310** (1999) 1147 [`astro-ph/9903164`].

[126] A. Biswas, S. Choubey and S. Khan, *Neutrino Mass, Dark Matter and Anomalous Magnetic Moment of Muon in a* $U(1)_{L_\mu - L_\tau}$ *Model*, *JHEP* **09** (2016) 147 [`1608.04194`].

[127] S. Baek, N. G. Deshpande, X. G. He and P. Ko, *Muon anomalous g-2 and gauged L(muon) - L(tau) models*, *Phys. Rev.* **D64** (2001) 055006 [`hep-ph/0104141`].

[128] Muon g-2 collaboration, *Measurement of the negative muon anomalous magnetic moment to 0.7 ppm*, *Phys. Rev. Lett.* **92** (2004) 161802 [`hep-ex/0401008`].

[129] S. Mohanty, S. Rao and D. P. Roy, *Reconciling the muon $g-2$ and dark matter relic density with the LHC results in nonuniversal gaugino mass models*, *JHEP* **09** (2013) 027 [`1303.5830`].

[130] S. P. Das, M. Guchait and D. P. Roy, *Testing SUSY models for the muon g-2 anomaly via chargino-neutralino pair production at the LHC*, *Phys. Rev.* **D90** (2014) 055011 [`1406.6925`].

[131] W. Altmannshofer, C.-Y. Chen, P. S. Bhupal Dev and A. Soni, *Lepton flavor violating Z' explanation of the muon anomalous magnetic moment*, *Phys. Lett.* **B762** (2016) 389 [`1607.06832`].

[132] S. Baek, H. Okada and K. Yagyu, *Flavour Dependent Gauged Radiative Neutrino Mass Model*, *JHEP* **04** (2015) 049 [`1501.01530`].

[133] S. Baek, *Dark matter and muon $(g-2)$ in local $U(1)_{L_\mu - L_\tau}$-extended Ma Model*, *Phys. Lett.* **B756** (2016) 1 [`1510.02168`].

[134] Z.-z. Xing and Z.-h. Zhao, *A review of $\mu-\tau$ flavor symmetry in neutrino physics*, *Rept. Prog. Phys.* **79** (2016) 076201 [`1512.04207`].

[135] P. Minkowski, *$\mu \to e\gamma$ at a Rate of One Out of 10^9 Muon Decays?*, *Phys. Lett.* **67B** (1977) 421.

[136] T. Yanagida, *Horizontal gauge symmetry and masses of neutrinos*, Conf. Proc. **C7902131** (1979) 95.

[137] R. N. Mohapatra and G. Senjanovic, *Neutrino Mass and Spontaneous Parity Nonconservation*, *Phys. Rev. Lett.* **44** (1980) 912.

[138] J. Schechter and J. W. F. Valle, *Neutrino Masses in SU(2) x U(1) Theories*, *Phys. Rev.* **D22** (1980) 2227.

[139] S. Choubey and W. Rodejohann, *A Flavor symmetry for quasi-degenerate neutrinos: L(mu) - L(tau)*, *Eur. Phys. J.* **C40** (2005) 259 [`hep-ph/0411190`].

[140] ATLAS collaboration, *Observation of a new particle in the search for the Standard Model Higgs boson with the ATLAS detector at the LHC*, *Phys. Lett.* **B716** (2012) 1 [`1207.7214`].

[141] CMS collaboration, *Observation of a New Boson at a Mass of 125 GeV with the CMS Experiment at the LHC*, *Phys. Lett.* **B716** (2012) 30 [`1207.7235`].

[142] N. Chakrabarty, D. K. Ghosh, B. Mukhopadhyaya and I. Saha, *Dark matter, neutrino masses and high scale validity of an inert Higgs doublet model*, *Phys. Rev.* **D92** (2015) 015002 [`1501.03700`].

[143] F. Jegerlehner and A. Nyffeler, *The Muon g-2*, *Phys. Rept.* **477** (2009) 1 [`0902.3360`].

[144] S. N. Gninenko and N. V. Krasnikov, *The Muon anomalous magnetic moment and a new light gauge boson*, *Phys. Lett.* **B513** (2001) 119 [`hep-ph/0102222`].

[145] CHARM-II collaboration, *First observation of neutrino trident production*, *Phys. Lett.* **B245** (1990) 271.

[146] CCFR collaboration, *Neutrino tridents and W Z interference*, *Phys. Rev. Lett.* **66** (1991) 3117.

[147] B. Adhikary, M. Chakraborty and A. Ghosal, *Masses, mixing angles and phases of general Majorana neutrino mass matrix*, *JHEP* **10** (2013) 043 [`1307.0988`].

[148] A. Semenov, *LanHEP: A Package for the automatic generation of Feynman rules in field theory. Version 3.0*, *Comput. Phys. Commun.* **180** (2009) 431 [`0805.0555`].

[149] XENON collaboration, *Physics reach of the XENON1T dark matter experiment*, *JCAP* **1604** (2016) 027 [`1512.07501`].

[150] DARWIN collaboration, *DARWIN: towards the ultimate dark matter detector*, *JCAP* **1611** (2016) 017 [`1606.07001`].

[151] F. Calore, I. Cholis and C. Weniger, *Background Model Systematics for the Fermi GeV Excess*, *JCAP* **1503** (2015) 038 [1409.0042].

[152] S. Choubey, S. Khan, M. Mitra and S. Mondal, *Singlet-Triplet Fermionic Dark Matter and LHC Phenomenology*, *Eur. Phys. J.* **C78** (2018) 302 [1711.08888].

[153] Fermi-LAT collaboration, *Updated search for spectral lines from Galactic dark matter interactions with pass 8 data from the Fermi Large Area Telescope*, *Phys. Rev.* **D91** (2015) 122002 [1506.00013].

[154] P. Chardonnet, P. Salati and P. Fayet, *Heavy triplet neutrinos as a new dark matter option*, *Nucl. Phys.* **B394** (1993) 35.

[155] C. Biggio and F. Bonnet, *Implementation of the Type III Seesaw Model in FeynRules/MadGraph and Prospects for Discovery with Early LHC Data*, *Eur. Phys. J.* **C72** (2012) 1899 [1107.3463].

[156] M. Hirsch, R. A. Lineros, S. Morisi, J. Palacio, N. Rojas and J. W. F. Valle, *WIMP dark matter as radiative neutrino mass messenger*, *JHEP* **10** (2013) 149 [1307.8134].

[157] A. Chaudhuri, N. Khan, B. Mukhopadhyaya and S. Rakshit, *Dark matter candidate in an extended type III seesaw scenario*, *Phys. Rev.* **D91** (2015) 055024 [1501.05885].

[158] S. Bhattacharya, N. Sahoo and N. Sahu, *Singlet-Doublet Fermionic Dark Matter, Neutrino Mass and Collider Signatures*, *Phys. Rev.* **D96** (2017) 035010 [1704.03417].

[159] M. Frigerio and T. Hambye, *Dark matter stability and unification without supersymmetry*, *Phys. Rev.* **D81** (2010) 075002 [0912.1545].

[160] Y. Mambrini, N. Nagata, K. A. Olive and J. Zheng, *Vacuum Stability and Radiative Electroweak Symmetry Breaking in an SO(10) Dark Matter Model*, *Phys. Rev.* **D93** (2016) 111703 [`1602.05583`].

[161] M. Cirelli, N. Fornengo and A. Strumia, *Minimal dark matter*, *Nucl. Phys.* **B753** (2006) 178 [`hep-ph/0512090`].

[162] E. Ma and D. Suematsu, *Fermion Triplet Dark Matter and Radiative Neutrino Mass*, *Mod. Phys. Lett.* **A24** (2009) 583 [`0809.0942`].

[163] J. Erler and P. Langacker, *Electroweak model and constraints on new physics*, `hep-ph/0407097`.

[164] J. Erler and P. Langacker, *Electroweak Physics*, *Acta Phys. Polon.* **B39** (2008) 2595 [`0807.3023`].

[165] M.-C. Chen, S. Dawson and C. B. Jackson, *Higgs Triplets, Decoupling, and Precision Measurements*, *Phys. Rev.* **D78** (2008) 093001 [`0809.4185`].

[166] A. Abada, C. Biggio, F. Bonnet, M. B. Gavela and T. Hambye, *mu —> e gamma and tau —> l gamma decays in the fermion triplet seesaw model*, *Phys. Rev.* **D78** (2008) 033007 [`0803.0481`].

[167] LUX collaboration, *Results from a search for dark matter in the complete LUX exposure*, *Phys. Rev. Lett.* **118** (2017) 021303 [`1608.07648`].

[168] XENON collaboration, *First Dark Matter Search Results from the XENON1T Experiment*, *Phys. Rev. Lett.* **119** (2017) 181301 [`1705.06655`].

[169] PandaX-II collaboration, *Dark Matter Results From 54-Ton-Day Exposure of PandaX-II Experiment*, *Phys. Rev. Lett.* **119** (2017) 181302 [`1708.06917`].

[170] ATLAS, CMS collaboration, *Measurements of the Higgs boson production and decay rates and constraints on its couplings from a combined ATLAS and CMS*

analysis of the LHC pp collision data at $\sqrt{s} = 7$ and 8 TeV, JHEP **08** (2016) 045 [`1606.02266`].

[171] A. Alloul, N. D. Christensen, C. Degrande, C. Duhr and B. Fuks, *FeynRules 2.0 - A complete toolbox for tree-level phenomenology*, Comput. Phys. Commun. **185** (2014) 2250 [`1310.1921`].

[172] Fermi-LAT collaboration, *Search for Gamma-ray Spectral Lines with the Fermi Large Area Telescope and Dark Matter Implications*, Phys. Rev. **D88** (2013) 082002 [`1305.5597`].

[173] H.E.S.S. collaboration, *Search for Photon-Linelike Signatures from Dark Matter Annihilations with H.E.S.S.*, Phys. Rev. Lett. **110** (2013) 041301 [`1301.1173`].

[174] S. Profumo, F. S. Queiroz and C. E. Yaguna, *Extending Fermi-LAT and H.E.S.S. Limits on Gamma-ray Lines from Dark Matter Annihilation*, Mon. Not. Roy. Astron. Soc. **461** (2016) 3976 [`1602.08501`].

[175] L. Bergstrom and P. Ullio, *Full one loop calculation of neutralino annihilation into two photons*, Nucl. Phys. **B504** (1997) 27 [`hep-ph/9706232`].

[176] Z. Bern, P. Gondolo and M. Perelstein, *Neutralino annihilation into two photons*, Phys. Lett. **B411** (1997) 86 [`hep-ph/9706538`].

[177] ATLAS collaboration, *Search for heavy resonances decaying into WW in the $e\nu\mu\nu$ final state in pp collisions at $\sqrt{s} = 13$ TeV with the ATLAS detector*, Eur. Phys. J. **C78** (2018) 24 [`1710.01123`].

[178] ATLAS collaboration, *Search for heavy ZZ resonances in the $\ell^+\ell^-\ell^+\ell^-$ and $\ell^+\ell^-\nu\bar{\nu}$ final states using proton–proton collisions at $\sqrt{s} = 13$ TeV with the ATLAS detector*, Eur. Phys. J. **C78** (2018) 293 [`1712.06386`].

[179] ATLAS collaboration, *Search for new phenomena in high-mass diphoton final states using 37 fb^{-1} of proton–proton collisions collected at* $\sqrt{s} = 13$ *TeV with the ATLAS detector*, *Phys. Lett.* **B775** (2017) 105 [1707.04147].

[180] CMS collaboration, *Search for a charged Higgs boson in pp collisions at* $\sqrt{s} = 8$ *TeV*, *JHEP* **11** (2015) 018 [1508.07774].

[181] CMS collaboration, *Search for a light charged Higgs boson decaying to* $c\bar{s}$ *in pp collisions at* $\sqrt{s} = 8$ *TeV*, *JHEP* **12** (2015) 178 [1510.04252].

[182] CMS collaboration, *Search for Charged Higgs boson to* $c\bar{b}$ *in lepton+jets channel using top quark pair events*, .

[183] ATLAS collaboration, *Search for charged Higgs bosons in the* $H^{\pm} \rightarrow tb$ *decay channel in pp collisions at* $\sqrt{s} = 13$ *TeV using the ATLAS detector*, .

[184] ATLAS collaboration, *Search for electroweak production of supersymmetric particles in the two and three lepton final state at* $\sqrt{s} = 13$ *TeV with the ATLAS detector*, .

[185] ATLAS collaboration, *Search for the direct production of charginos and neutralinos in final states with tau leptons in* $\sqrt{s} = 13$ *TeV pp collisions with the ATLAS detector*, *Eur. Phys. J.* **C78** (2018) 154 [1708.07875].

[186] M. L. Mangano, M. Moretti, F. Piccinini and M. Treccani, *Matching matrix elements and shower evolution for top-quark production in hadronic collisions*, *JHEP* **01** (2007) 013 [hep-ph/0611129].

[187] S. Hoeche, F. Krauss, N. Lavesson, L. Lonnblad, M. Mangano, A. Schalicke et al., *Matching parton showers and matrix elements*, in *HERA and the LHC: A Workshop on the implications of HERA for LHC physics: Proceedings Part A*, pp. 288–289, 2005, hep-ph/0602031, DOI.

[188] J. Alwall, R. Frederix, S. Frixione, V. Hirschi, F. Maltoni, O. Mattelaer et al., *The automated computation of tree-level and next-to-leading order differential cross sections, and their matching to parton shower simulations*, *JHEP* **07** (2014) 079 [`1405.0301`].

[189] J. Alwall, M. Herquet, F. Maltoni, O. Mattelaer and T. Stelzer, *MadGraph 5 : Going Beyond*, *JHEP* **06** (2011) 128 [`1106.0522`].

[190] J. Pumplin, D. R. Stump, J. Huston, H. L. Lai, P. M. Nadolsky and W. K. Tung, *New generation of parton distributions with uncertainties from global QCD analysis*, *JHEP* **07** (2002) 012 [`hep-ph/0201195`].

[191] T. Sjostrand, S. Mrenna and P. Z. Skands, *PYTHIA 6.4 Physics and Manual*, *JHEP* **05** (2006) 026 [`hep-ph/0603175`].

[192] DELPHES 3 collaboration, *DELPHES 3, A modular framework for fast simulation of a generic collider experiment*, *JHEP* **02** (2014) 057 [`1307.6346`].

[193] M. Selvaggi, *DELPHES 3: A modular framework for fast-simulation of generic collider experiments*, *J. Phys. Conf. Ser.* **523** (2014) 012033.

[194] A. Mertens, *New features in Delphes 3*, *J. Phys. Conf. Ser.* **608** (2015) 012045.

[195] M. Cacciari, G. P. Salam and G. Soyez, *The anti-k_t jet clustering algorithm*, *JHEP* **04** (2008) 063 [`0802.1189`].

[196] M. Cacciari, G. P. Salam and G. Soyez, *FastJet User Manual*, *Eur. Phys. J.* **C72** (2012) 1896 [`1111.6097`].

[197] ATLAS collaboration, *Search for squarks and gluinos with the ATLAS detector in final states with jets and missing transverse momentum using $\sqrt{s} = 8$ TeV proton–proton collision data*, *JHEP* **09** (2014) 176 [`1405.7875`].

[198] J. Dutta, P. Konar, S. Mondal, B. Mukhopadhyaya and S. K. Rai, *A Revisit to a Compressed Supersymmetric Spectrum with 125 GeV Higgs*, *JHEP* **01** (2016) 051 [`1511.09284`].

[199] A. Biswas, S. Choubey and S. Khan, *Neutrino mass, leptogenesis and FIMP dark matter in a* $\mathrm{U}(1)_{B-L}$ *model*, *Eur. Phys. J.* **C77** (2017) 875 [`1704.00819`].

[200] S. Patra, W. Rodejohann and C. E. Yaguna, *A new* $B-L$ *model without right-handed neutrinos*, *JHEP* **09** (2016) 076 [`1607.04029`].

[201] N. Okada and S. Okada, Z'*-portal right-handed neutrino dark matter in the minimal* $U(1)_X$ *extended Standard Model*, *Phys. Rev.* **D95** (2017) 035025 [`1611.02672`].

[202] GERDA collaboration, *Results on Neutrinoless Double-*β *Decay of* ^{76}*Ge from Phase I of the GERDA Experiment*, *Phys. Rev. Lett.* **111** (2013) 122503 [`1307.4720`].

[203] N. S. Manton, *Topology in the Weinberg-Salam Theory*, *Phys. Rev.* **D28** (1983) 2019.

[204] F. R. Klinkhamer and N. S. Manton, *A Saddle Point Solution in the Weinberg-Salam Theory*, *Phys. Rev.* **D30** (1984) 2212.

[205] V. A. Kuzmin, V. A. Rubakov and M. E. Shaposhnikov, *On the Anomalous Electroweak Baryon Number Nonconservation in the Early Universe*, *Phys. Lett.* **155B** (1985) 36.

[206] S. Yu. Khlebnikov and M. E. Shaposhnikov, *The Statistical Theory of Anomalous Fermion Number Nonconservation*, *Nucl. Phys.* **B308** (1988) 885.

[207] G. Arcadi and L. Covi, *Minimal Decaying Dark Matter and the LHC*, *JCAP* **1308** (2013) 005 [`1305.6587`].

[208] XENON1T collaboration, *The XENON1T Dark Matter Search Experiment*, *Springer Proc. Phys.* **148** (2013) 93 [`1206.6288`].

[209] CDMS-II collaboration, *Results from a Low-Energy Analysis of the CDMS II Germanium Data*, *Phys. Rev. Lett.* **106** (2011) 131302 [`1011.2482`].

[210] S. L. Adler, *Axial vector vertex in spinor electrodynamics*, *Phys. Rev.* **177** (1969) 2426.

[211] W. A. Bardeen, *Anomalous Ward identities in spinor field theories*, *Phys. Rev.* **184** (1969) 1848.

[212] R. Delbourgo and A. Salam, *The gravitational correction to pcac*, *Phys. Lett.* **40B** (1972) 381.

[213] T. Eguchi and P. G. O. Freund, *Quantum Gravity and World Topology*, *Phys. Rev. Lett.* **37** (1976) 1251.

[214] C. Jarlskog, *Commutator of the Quark Mass Matrices in the Standard Electroweak Model and a Measure of Maximal CP Violation*, *Phys. Rev. Lett.* **55** (1985) 1039.

[215] T2K collaboration, *Measurement of neutrino and antineutrino oscillations by the T2K experiment including a new additional sample of ν_e interactions at the far detector*, *Phys. Rev.* **D96** (2017) 092006 [`1707.01048`].

[216] S. Dell'Oro, S. Marcocci, M. Viel and F. Vissani, *Neutrinoless double beta decay: 2015 review*, *Adv. High Energy Phys.* **2016** (2016) 2162659 [`1601.07512`].

[217] KamLAND-Zen collaboration, *Search for Majorana Neutrinos near the Inverted Mass Hierarchy Region with KamLAND-Zen*, *Phys. Rev. Lett.* **117** (2016) 082503 [`1605.02889`].

[218] M. Plumacher, *Baryogenesis and lepton number violation*, *Z. Phys.* **C74** (1997) 549 [`hep-ph/9604229`].

[219] S. Iso, N. Okada and Y. Orikasa, *Resonant Leptogenesis in the Minimal B-L Extended Standard Model at TeV*, *Phys. Rev.* **D83** (2011) 093011 [`1011.4769`].

[220] W. Buchmuller, P. Di Bari and M. Plumacher, *Cosmic microwave background, matter - antimatter asymmetry and neutrino masses*, *Nucl. Phys.* **B643** (2002) 367 [`hep-ph/0205349`].

[221] A. Pilaftsis, *CP violation and baryogenesis due to heavy Majorana neutrinos*, *Phys. Rev.* **D56** (1997) 5431 [`hep-ph/9707235`].

[222] A. Pilaftsis and T. E. J. Underwood, *Resonant leptogenesis*, *Nucl. Phys.* **B692** (2004) 303 [`hep-ph/0309342`].

[223] J. Heeck and D. Teresi, *Leptogenesis and neutral gauge bosons*, *Phys. Rev.* **D94** (2016) 095024 [`1609.03594`].

[224] J. Edsjo and P. Gondolo, *Neutralino relic density including coannihilations*, *Phys. Rev.* **D56** (1997) 1879 [`hep-ph/9704361`].

[225] A. Biswas and D. Majumdar, *The Real Gauge Singlet Scalar Extension of Standard Model: A Possible Candidate of Cold Dark Matter*, *Pramana* **80** (2013) 539 [`1102.3024`].

[226] CMS collaboration, *Search for Heavy Narrow Dilepton Resonances in pp Collisions at $\sqrt{s} = 7$ TeV and $\sqrt{s} = 8$ TeV*, *Phys. Lett.* **B720** (2013) 63 [`1212.6175`].

[227] ALEPH, DELPHI, L3, OPAL, LEP ELECTROWEAK collaboration, *Electroweak Measurements in Electron-Positron Collisions at W-Boson-Pair Energies at LEP*, *Phys. Rept.* **532** (2013) 119 [`1302.3415`].

[228] A. Biswas, S. Choubey and S. Khan, *FIMP and Muon $(g-2)$ in a $U(1)_{L_\mu - L_\tau}$ Model*, *JHEP* **02** (2017) 123 [`1612.03067`].

[229] W. Altmannshofer, S. Gori, S. Profumo and F. S. Queiroz, *Explaining dark matter and B decay anomalies with an $L_\mu - L_\tau$ model*, *JHEP* **12** (2016) 106 [1609.04026].

[230] X. G. He, G. C. Joshi, H. Lew and R. R. Volkas, *NEW Z-prime PHENOMENOLOGY*, *Phys. Rev.* **D43** (1991) 22.

[231] X.-G. He, G. C. Joshi, H. Lew and R. R. Volkas, *Simplest Z-prime model*, *Phys. Rev.* **D44** (1991) 2118.

[232] E. Ma, D. P. Roy and S. Roy, *Gauged L(mu) - L(tau) with large muon anomalous magnetic moment and the bimaximal mixing of neutrinos*, *Phys. Lett.* **B525** (2002) 101 [hep-ph/0110146].

[233] W. Altmannshofer, S. Gori, M. Pospelov and I. Yavin, *Neutrino Trident Production: A Powerful Probe of New Physics with Neutrino Beams*, *Phys. Rev. Lett.* **113** (2014) 091801 [1406.2332].

[234] F. Elahi and A. Martin, *Constraints on $L_\mu - L_\tau$ interactions at the LHC and beyond*, *Phys. Rev.* **D93** (2016) 015022 [1511.04107].

[235] K. Harigaya, T. Igari, M. M. Nojiri, M. Takeuchi and K. Tobe, *Muon g-2 and LHC phenomenology in the $L_\mu - L_\tau$ gauge symmetric model*, *JHEP* **03** (2014) 105 [1311.0870].

[236] A. Biswas, S. Choubey, L. Covi and S. Khan, *Explaining the 3.5 keV X-ray Line in a $L_\mu - L_\tau$ Extension of the Inert Doublet Model*, *JCAP* **1802** (2018) 002 [1711.00553].

[237] C.-W. Chiang and T. Yamada, *3.5-keV X-ray line from nearly-degenerate WIMP dark matter decays*, *JHEP* **09** (2014) 006 [1407.0460].

[238] A. Falkowski, Y. Hochberg and J. T. Ruderman, *Displaced Vertices from X-ray Lines*, *JHEP* **11** (2014) 140 [1409.2872].

[239] T. Appelquist, B. A. Dobrescu and A. R. Hopper, *Nonexotic Neutral Gauge Bosons*, *Phys. Rev.* **D68** (2003) 035012 [`hep-ph/0212073`].

[240] J. König, A. Merle and M. Totzauer, *keV Sterile Neutrino Dark Matter from Singlet Scalar Decays: The Most General Case*, *JCAP* **1611** (2016) 038 [`1609.01289`].

[241] G. Arcadi, L. Covi and F. Dradi, *3.55 keV line in Minimal Decaying Dark Matter scenarios*, *JCAP* **1507** (2015) 023 [`1412.6351`].

[242] E. W. Kolb and M. S. Turner, *The Early Universe*, *Front. Phys.* **69** (1990) 1.

[243] P. B. Pal and L. Wolfenstein, *Radiative Decays of Massive Neutrinos*, *Phys. Rev.* **D25** (1982) 766.

[244] M. Garny, A. Ibarra, D. Tran and C. Weniger, *Gamma-Ray Lines from Radiative Dark Matter Decay*, *JCAP* **1101** (2011) 032 [`1011.3786`].